Statistical mechanics of immunity from genes to populations

Hurry, Christian

Awarding institution:
King's College London

Statistical mechanics of immunity from genes to populations

Christian John Hurry

Department of Mathematics

King's College London

Under the supervision of Dr. Alessia Annibale

A thesis submitted for the degree of

Doctor of Philosophy in Applied Mathematics

September 2022

I dedicate this thesis to my Mum and Dad, who were stood in the room at the University of Manchester where, unbeknownst to us, I would receive my first offer to study Physics.

Acknowledgements

First and foremost I would like to thank my supervisor Dr. Alessia Annibale, who has patiently provided technical and moral support throughout my doctoral training. Her wide expertise, dedication to rigour, and creative problem solving has been a constant source of inspiration over the years. Secondly, I would like to thank Dr. Alexander Mozeika, with whom Alessia and I have worked closely for the duration of my studies. His insight, suggestions and mentorship were invaluable to me. The weekly discussions between the three of us were one of the most enjoyable parts of my studies and solidified my passion for research. I am indebted to you both. I would also like to thank Professor Franca Fraternali, who as my secondary supervisor provided a great deal of support during my studies, and with whom we had many useful discussions.

I thank the ESPRC Centre for Doctoral Training in Cross-Disciplinary Approaches to Non-Equilibrium Systems (CANES, EP/L015854/1), which supported my doctoral training. In particular I would like to thank Dr. Joe Bhaseen, Professor Chris Lorenz, and Professor Reimer Kühn for conversations regarding research, industry and career development over the years. The CANES CDT provided a unique environment where I was exposed to many strands of research across different disciplines and contributed greatly to my development as an interdisciplinary scientist. I also thank the Disordered Systems group, who's research continues to fascinate me, and the wider Department of Mathematics at King's College London.

On a personal note, I would like to thank my peers in Cohort IV of the CANES CDT. We were close at the start of our studies - literally, that office was tiny - and have remained close since. In particular, Giuseppe, Joe, Matt, Grisha, thank you for your friendship, and good luck for the future. I thank my friends in room K4L.12, and urge them to keep up the Friday night pints. I would also like to thank Rory, my friend of many years, for being a great flatmate throughout my studies.

Lastly, I would like to thank my Mum and Dad, Joanne and Peter, my sister, Bethany, my Grandma, Helen, and my Nana and Grandad, Mercia and John - each of whom has provided endless love and support.

Publications contributing to the thesis

During the production of this thesis, work was submitted for publication in academic journals. The publications are as follows:

1. CJ Hurry, Alexander Mozeika, Alessia Annibale, *Modelling the interplay between the $CD4^+/CD8^+$ T-cell ratio and the expression of MHC-I in tumours*, J. Math. Biol. 83, 2 (2021)
2. CJ Hurry, Alexander Mozeika, Alessia Annibale, *Vaccination with partial transmission and social distancing on contact networks*, J. Stat. Mech. (2022) 033302
3. CJ Hurry, Alexander Mozeika, Alessia Annibale, *Dynamics of sparse Boolean networks with multi-node and self-interactions*, (accepted for publication in the Journal of Physics A: Mathematical and Theoretical, 2022)

Articles 1, 2 and 3 contain work described in chapters 2, 3 and 4, respectively.

Abstract

In this thesis we provide three different models of processes related to immunity. Firstly, we describe a model of the T-cell mediated anti-tumour immune response. We describe the anti-tumour immune response as a set of cellular kinetic rate equations. T-cells are assumed to act as binary agents (active/inactive) that evolve with time according to a noisy linear threshold function. Using the Kramers-Moyal expansion of the master equation, we are able to describe the system as a closed set of ordinary differential equations. We find that there is a critical value of the ratio of helper to cytotoxic T-cells that depends on the expression of MHC-I in tumour cells. We demonstrate the effect that this interplay has on the efficacy of the helper/cytotoxic T-cell ratio and MHC-I expression as prognostic markers.

Secondly, we model infectious disease outbreak in populations where individuals are vaccinated with a vaccine that reduces the likelihood to transmit the disease to a small but finite value. We study the SIR model on networks with nodes that belong to one of several sub-populations with different individual transmissibility and apply the cavity method to derive equations for the risk that a node in a network will cause outbreak. We show that the threshold for outbreak in populations split into vaccinated and unvaccinated sub-populations, will depend upon the proportion of the population that is vaccinated, as well as the density of links between the vaccinated and unvaccinated sub-populations. Furthermore, we show that the cavity method can be used to derive the distribution of risk in populations with heterogeneity in individual transmissibility, and in some cases provide an exact expression for this distribution.

The immune system is comprised of many different cell types, with different functions. Within an organism, different cell types have the same genetic make-up, but they differ in the set of genes that are expressed. The last model presented in this thesis is concerned

with determining the conditions that are necessary for gene regulatory networks to support a diverse set of stable gene expression profiles, corresponding to different cell types. We consider a bipartite model of gene regulatory networks consisting of genes and transcription factors. Gene expression is modelled as a Boolean variable (on/off), that evolves according to synchronous Glauber dynamics. Genes receive regulatory signals from transcription factors which are in turn synthesised by expressed genes. Our work focuses particularly on self-regulation, where genes that contribute to the synthesis of a transcription factor may be regulated by that same transcription factor. We extend the dynamical cavity method for systems with self-interactions and multi-node interactions to derive a computationally feasible scheme for the dynamical analysis of our model. We show that networks with bidirectional, multi-node interactions support multiple diverse gene expression profiles, suggesting that self-regulation is an important feature of multi-cellular life.

Contents

1 Introduction

Immunity is achieved through the interactions of many different types of cells, each with their own distinct function. The immune system can therefore be seen as a complex network of interactions, one that produces many interesting phenomena. Immune cells work to locate sites of infection, recruit further immune cells to help manage infection, and eliminate foreign pathogens. A range of biological agents (attenuated microorganisms, surface proteins associated with pathogens, mRNA etc) can be administered to a patient, to stimulate the immune response, and provide immunity from particular infectious diseases. Collectively, this broad range of pharmaceuticals are referred to as vaccines.

Vaccines have transformed efforts to prevent the spread of infectious diseases, and they have a long and storied history. The term vaccine originates from the cowpox serum, used as an inoculation against smallpox, studied by Edward Jenner in the late 18^{th} century, who's work is seen as a significant step in the development of modern vaccination campaigns (1, 2). To understand the impact that the advent of modern vaccination has had on society, one

only needs to consider the eradication of smallpox, as declared by the World Health Organisation (WHO) in 1980 (3, 4, 5). This demonstrated the feasibility of disease eradication by vaccination, and is a stark reminder of how the importance of vaccination goes beyond the health of any one individual. On the other hand, to understand the fragility of progress against infectious diseases, one only needs to consider measles. As a result of vaccination there was a 74% reduction in the global incidence of measles in the period 2000-2015 (6). Eradicating measles was deemed to be feasible by the WHO, since humans are the only hosts of the disease, measles is genetically stable, and all geneotypes of measles are recognised by the same immune cells (7). This led to the goal of the elimination of measles by 2020 in several WHO regions (8). Despite these goals, the number of people who had received a first dose of vaccine remains below the estimated vaccine coverage of 95% needed to prevent disease outbreak. This can be attributed to a number of limiting factors such as a lack of political resources, as well as the increased incidence of "vaccine hesitancy" (7, 9). The increase in skepticism, fueled by misinformation, has been a cause of concern for the progress against measles, in particular due to the outbreak of the disease in regions which had previously prevented transmission, including within the UK, and strategies to counter this misinformation are seen as an important tool in the steps towards the elimination of measles (9, 10).

A further difficulty in the control of infectious disease outbreaks is the ability of infectious diseases to mutate and adapt when passing from host to host, hampering vaccine effectiveness in the process. This was acutely demonstrated by the alpha, delta and omicron variants that have spread glob-

ally since the beginning of the COVID-19 pandemic (11, 12, 13) . The volatility of the spread of COVID-19, in part due to the incidence of new variants, limits the comparison to more genetically stable diseases such as polio and measles, and makes any discussion of a future steady-state of the pandemic highly speculative. Possible end states of any infectious disease outbreak could range from global eradication, regional elimination, endemicity (as the disease becomes predictable and health systems adapt to cope with this additional pressure), to a more permanently unpredictable scenario (14, 15). Recently, the quantitative evidence that would indicate these different phases was discussed (15). The fragile progress that has been made against diseases that expert opinion deems eradicable, and the overwhelming challenges posed by the pandemic of a mutating disease which risks immune evasion, highlights the limits of vaccination campaigns. However, a quantitative assessment of these challenges is feasible, and is surely necessary in the step towards their solution.

Of course, the developments in the production of safe and effective vaccines is in part due to the increased understanding of the mechanisms that govern the immune system. The immune system can be split into innate and adaptive immunity. Innate immunity includes anatomical barriers that physically impede foreign pathogens from infecting the host (16). It is also mediated by a number of immune cells which coordinate an immune response against foreign pathogens. One example, of the many, innate immune cells is macrophages, primarily known for their ability to engulf and kill foreign pathogens, in a process known as phagocytosis (16). They also invoke inflammation, recruiting further immune cells to the site of infection (16). This

includes cells that comprise the adaptive immune system, which differ from innate immune cells by mediating an immune response that, unlike the innate response, is *specific* to particular foreign pathogens.

The primary cells of the adaptive immune system are two distinct lineages of lymphocytes, B-cells and T-cells, discovered in the 1960s (17, 18, 19). The discovery of these cells and the molecular analysis of their receptors (20, 21) complemented an early theory of how adaptive immunity mounts a specific response to pathogens, known as clonal selection. This early theory, posited by Burnet, suggested that cells of the adaptive immune system were divided into many groups of cells of the same type, known as clones, with each clone being specific to a particular pathogen. When exposed to that pathogen, the cells of the clone would proliferate and coordinate the immune response against that pathogen, whilst the other clones would not (22). The receptors of T and B cells were found to bind to molecules associated with specific pathogens, providing evidence of how the immune system recognises pathogens.

When the receptors of B-cells and T-cells bind to these molecules, they can differentiate into effector cells, which perform a myriad of functions in the adaptive immune response. The primary response of B-cells is to differentiate into antibody producing cells (23). These antibodies circulate in the host, binding to the antigen which invoked the production of antibodies. Antibodies neutralise the ability of viruses to infect host cells, and mark bacteria as a target for phagocytosis by, for example, macrophages (16, 23). This is just one way in which the cells of the adaptive immune system and innate immune system co-operate to mount an effective immune response.

T-cells differentiate into various effector cells, the majority of which are categorised as helper and cytotoxic T-cells. Helper T-cells produce cytokines that enhance the function of many immune cells, including the activation of cytotoxic T cells and the proliferation of B-cells (16, 24). The main function of cytotoxic T-cells is to kill cells infected with viruses which display the antigen that invoked the T-cell response (16, 25). There is also a sub-population of T-cells, regulatory T-cells, which have the opposite role, suppressing the activity of immune cells, preventing damage caused by the immune response such as autoimmunity (16, 26). In auto-immune conditions, such as coeliac disease, diabetes and inflammatory bowel disease, the immune system targets normal, healthy cells, leading to a detrimental impact on health.

Another example of the immune system having a deleterious effect on health is the immune response against cancer, first documented in the 19^{th} century (27, 28). It is now known that tumours produce antigens, proteins which are recognised by immune cells, and that these trigger an anti-tumour immune response mediated by T cells (29). The picture is complicated, however, as tumour cells are not equally immunogenic. For example, some tumour cells show a loss of surface molecules which cytotoxic T-cells are required to bind to if they are to eliminate tumour cells (30, 31). This creates a selective pressure as the immune system preferentially kills tumour cells with higher immunogenicity, allowing less immunogenic tumour cells to thrive. Due to their high level of mutation, tumour cells from the same tumour are known to be genetically diverse, and this provides many criteria for which selective pressures may emerge, via interactions between tumour cells and their environment (32, 33). It is not only the ability of tumours to evolve to avoid

the anti-tumour immune response that complicates the immune response to cancer. Some subsets of immune cells, such as macrophages and regulatory T cells have an explicitly pro-tumour function and are recruited to form part of the tumour environment and aid tumour growth (34, 35, 36, 37, 38). Therefore, although there is an immune response that eliminates tumour cells, the affect on cancer progression is unclear. In spite of this, modern therapeutics have been developed that are designed to augment tumour immunity. A significant example is CAR T-cell therapy, during which a sample of T-cells is taken from a patient and is used to produce genetically modified T-cells *in vitro*, which are then injected into the patient. These modified T-cells express a receptor that can bind to tumour cells without the aid of a surface molecule, MHC-I, which is often down regulated in the progression of cancer (39). These therapies have seen success in the treatment of blood cancers, (40, 41, 42), but their efficacy against solid tumours is mixed, which shows that it is not the recognition of antigens alone that dampens anti-tumour immunity, but also the interactions with the complex tumour environment (43). This is evidenced by the improved efficacy of CAR T-cell therapy in combination with checkpoint blockers, another immunotherapy which targets mechanisms of tumour immune evasion (44, 45). The challenge is to build a quantitative and systemic view of the interactions between the constituent parts of the immune system and the tumour environment in order to develop immunotherapies to their full potential.

Understanding the system-wide behaviour of the immune response is complicated by the diversity of immune cells, since there are many types of immune cells, each with their own function that may vary with their en-

vironment. As a result of this, the immune response is a highly dynamic set of processes, which can be experimentally resolved when focusing on just a few interactions, but becomes more intractable when focusing on system wide behaviour. The advent of single cell RNA technologies, which allow experimentalists to categorise cells via the expression of different genes, has given insight into the diversity of immune cells and its connection with system wide function, since the activation of immune cells is modulated by gene transcription (46, 47). For example, it was recently found that macrophages in the lungs of mice differed in function, depending on whether the cells were localised near nerve tissue or blood vessels (48). This demonstrates how single cell studies, in combination with studies of cell function and spatial position, can be used to deduce the relationship between heterogeneity in cells and immune function. In some sense the immune system is a model system to study cell differentiation, since the molecular reaction that triggers differentiation is sometimes well known; for example, the differentiation of a naive T or B cell to an activated cell is caused by the binding of their receptor to its cognate antigen (49). Immune cells that partially share the same developmental lineage, may have drastically different function due to differences in gene expression. It remains one of the key challenges in molecular biology to understand how differences in gene transcription lead to differences in the physiology and function of cell types, sometimes called the genotype-phenotype relationship. To understand how immune cells interact with their environment and with each other to control the immune response, it will be necessary to improve our understanding of the genotype-phenotype relationship. Understanding this relationship may also reveal new therapeutic targets. Achieving this goal

will require the integration of data at multiple scales - transcriptomics, proteomics, metabolomics, physiology - and mathematical modelling (50, 51, 52).

Our understanding of immunity has made serious positive changes to society. Vaccinations provide us with the best tools to control infectious disease outbreaks. Underpinning this is an increased understanding of the immune system at the cellular and molecular level, which has only improved since the advent of modern single cell analyses. The challenges, however, are clear. How best to design vaccination campaigns against disease and population behaviours that are unpredictable is an open question. Despite success in the technology behind vaccine development, it is also clear that the clinical use of the immune system is yet to reach its full potential, with the anti-tumour immune response being just one example of this. More fundamentally, improvements in the understanding of gene regulation are necessary to understand immune cell diversity and for the identification of new therapeutic targets. Due to the amount known about molecular causes for cellular differentiation, the study of gene regulation in the immune system may also elucidate the genotype-phenotype relationship. Each of these challenges can be understood as complex systems of interacting agents.

To elucidate the mechanisms that govern key phenomena related to each of these challenges, we shall require methods from statistical mechanics. Statistical mechanics is comprised of many techniques developed to analyse the behaviour of large systems of many interacting agents. Traditionally, these agents were particles, and statistical mechanics was used to understand the emergence of the macroscopic behaviour of materials from the microscopic behaviour of atoms. Over time, statistical mechanics has been shown to be

a more encompassing scientific field of study, providing deep insight into phenomena in, for example, economics, social sciences, and the biological sciences. In this thesis we propose a model of (i) the T-cell mediated anti-tumour immune response, (ii) the spread of epidemics in populations which are inoculated with a vaccine which reduces the transmissibility of an individual, and (iii) gene expression dynamics with self-regulation. Each of these models makes use of techniques from statistical mechanics and in several cases we are required to extend these techniques in order to handle the novel features of the systems we consider. Additionally, these phenomena act at different biological scales; cell-to-cell interactions, person-to-person disease transmission, and intracellular gene regulation. In studying these distinct phenomena this thesis demonstrates the wide applicability of statistical mechanics.

Chapter 2 details the model of the T-cell mediated anti-tumour immune response. Looking at the literature we identified an apparent contradiction in the reported efficacy of $CD4^+/CD8^+$ as a biomarker for prognosis in cancer (53, 54, 55). This biomarker has seen success as a prognostic marker in diseases associated with poor immune function (56, 57, 58, 59). An additional marker for prognosis in cancer that has been of recent interest is MHC-I. As we detail in Chapter 2, T-cells bind to this molecule on the surface of tumour cells and trigger apoptosis (60). Measurements of MHC-I have shown success as an independent marker for prognosis in cancer (61, 62). Our hypothesis was that since there is a mechanistic interplay between helper T-cells, an important subset of $CD4^+$ cells, cytotoxic T-cells, an important subset of $CD8^+$ cells, and MHC-I, incorrect conclusions about the efficacy of these markers may be drawn when they are considered separately. To demonstrate this, we

proposed a minimal model of the interplay between the helper/cytotoxic T-cell ratio and MHC-I expression in tumour cells. We describe the adaptive immune response as a set of cellular reactions, and use the principals of rate kinetics to derive a set of ODEs describing the change of cell concentrations with time. Where our work differs from earlier work of the anti-tumour immune response (63, 64) is that we describe T-cells as stochastic agents, discrete variables which update their state based upon the concentration of other cells which comprise the stimuli for T-cell activation. To study the dynamics of this system we use non-equilibrium statistical mechanics to derive closed expressions for the average activation of T-cells. We find that in our model statistical fluctuations about the average may be neglected, such that our model is described by a closed set of ODEs. When studying the long-time dynamics of this system, we derive a condition for the elimination of tumours, which states that there is a critical value of MHC-I expression, below which a tumour is eliminated. This critical value depends on the helper/cytotoxic T-cell ratio, and provides an explanation for how contradictions in the reported efficacy of MHC-I and $CD4^+/CD8^+$ may be affected by their use as independent markers.

In Chapter 3 we investigate the spread of epidemics in populations inoculated with a vaccine that reduces transmissibility of infected individuals. Previously, the spread of infectious diseases has been studied as a percolation process on networks of social contacts (65, 66). The theory of percolation considers removing nodes (or edges) from a network at random with some probability, and studies the effect that this has on the collective properties of the network (67). In particular, it has been shown that if nodes (edges)

are removed with high enough probability, the network will become disconnected, such that the network will not contain a set of connected nodes whose size is a finite fraction of the number of nodes in the network N in the limit $N \to \infty$ (67). This set of nodes is known as a giant connected component (GCC), and the theory of percolation has derived conditions for the existence of a GCC for networks drawn from different random graph ensembles (67). In the Susceptible-Infected-Recovered (SIR) model of epidemics, which we study in Chapter 3, infections pass from one node to another, and when nodes recover from an infection, the nodes are assumed to have immunity from future infections. This creates a unidirectional dynamics which is inherently out-of-equilibrium. In a similar vein to the derivation of the condition for the existence of GCC in graph ensembles, an epidemic threshold can be derived for networks in which nodes follow SIR dynamics (and other similar models where nodes can not become susceptible after recovery) (65, 66). This is a critical value of the transmissibility of the disease, below which the infection of an individual will not cause an outbreak across the network.

One can consider vaccination in the SIR model on networks by studying node deletion; a vaccinated node is removed from the network, such that the disease may not be transmitted along any of its links in the network. One can then show how vaccinating individuals affects the epidemic threshold, and hence understand the proportion of individuals that must be vaccinated to prevent further outbreak, demonstrating the principles of herd immunity. These models are also used for the design of vaccination strategies, comparing different methods of selecting which nodes should be vaccinated given a finite vaccine supply (68, 69, 70, 71). Since the original pioneering work, focus has

been on increasing the realism of such models. Often this involves considering more realistic network structures, such as networks with power law degree distribution, which have been shown to lack a percolation threshold, and are in fact always susceptible to outbreak (72, 73, 74). More recently, focus has been given to competitive and cooperative disease dynamics (75, 76, 77), percolation on multiplex networks which encode higher order structure (78, 79), and differences in the predicted epidemic threshold from contact tracing and reality (80).

In this chapter we study how the probability that a single infected node causes an outbreak can be computed in the presence of node heterogeneities. Namely, nodes may recover at different rates. This calculation is non-trivial, due to the dependence on all possible routes that an infection may travel along the network. For sparsely connected networks, which social networks are often observed to be, the calculation may be computed using message-passing or cavity methods. The cavity method originates in statistical physics and, in brief, it uses a recursive argument to derive a set of equations that describe the properties of nodes. It does so by considering how the properties of a given node are influenced by its neighbouring nodes. This reasoning is applied in a recursive fashion: the properties of the neighbouring nodes will depend on their neighbours, and so on. A general introduction to the cavity method, which details this argument, is provided in Appendix A. While previous works have studied the effect of heterogeneity in the recovery/infection rates on the risk of epidemics (see e.g (65, 81)), in this chapter we demonstrate how these methods may be applied to networks with node heterogeneities *and* strong degree correlations. We consider a population split into groups of

different transmissibility, and define a random graph ensemble from which networks can be drawn with strong degree correlations, where correlations are driven by differences in the transmissibility of nodes. This allows us to study the effect of degree correlations between groups of nodes with different rates of recovery. For such networks, we can derive new expressions for the epidemic threshold and the average probability that a node causes an outbreak, and show how they change with node heterogeneities and degree correlations. Extending more recent methods, we also demonstrate how the cavity method can be used to compute the distribution of these probabilities. In some cases, it is possible to yield a closed expression for this distribution, such that one can explore how differences in the transmissibility of individuals in the network, and the correlations between individuals of different transmissibility, affect the shape of the distribution. Our methods provide a theoretical framework to compare the efficacy of vaccination strategies when a vaccine can not prevent infection, but can reduce the overall transmissibility of infectious individuals.

After developing techniques for the steady-state analysis of complex networks, in Chapter 4 we study their dynamics. In particular we study a model of gene regulatory networks (GRNs). In our model the expression of genes is a Boolean variable, such that a gene is is either expressed or not. Randomly connected Boolean networks as models of gene regulation date back to the pioneering work of Kauffman (82, 83). In our case, the state of the genes evolve synchronously in discrete time steps such that all genes update their current state simultaneously, based upon the state of the genes at the previous time step. The expression of a gene at a given time point is determined

by some noisy function of the states of genes responsible for its regulation. Earlier studies of Boolean networks in the field of cybernetics, (84), focused on simple topologies and have remained influential during a resurgence of interest in the behaviour of complex networks (85). In our case, we consider a network with a large number of nodes, and heterogeneity in the number of genes that regulate each gene. Due to the many degrees of freedom that characterise complex systems such as this, a statistical approach is necessary to obtain analytical results. The dynamical analysis of complex systems is an open area of research, however, several techniques have been developed for the study of large many-body systems including dynamical mean field theory (86, 87, 88), dynamical replica theory (89, 90, 91, 92), generating functional analysis (93, 94, 95) and the dynamical cavity method (87, 96, 97, 98). The networks we consider are directed and sparsely connected, which earlier work has shown can be analysed using the dynamical cavity method (98). This work studied GRNs with bidirectional links *or* multi-node interactions, where the state of a node depends on the combined state of nodes it interacts with. In Chapter 4 we provide two new developments to the study of sparse, directed networks by considering (i) systems with self-interactions, and (ii) systems with bidirectional links *and* multi-node interactions. The dynamical cavity method can be used to provide a set of equations which approximate the dynamics of our model. We demonstrate the regimes where this approximation is accurate, and where this approximation breaks down. As a result of our study we are able to show that networks with bidirectional and multi-node interactions support a diverse set of multiple stable gene expression profiles, as observed in multi-cellular life.

In the fifth and final chapter, we provide a summary of the thesis. In doing so, we highlight areas of outlook for potential future investigations, in some cases providing initial formulae. Lastly, we provide an introduction to the cavity method, which several results in this thesis rely on, in an appendix to the thesis. In this appendix we apply the cavity method to simpler problems than discussed in the main chapters of the thesis, to provide a general overview of both the static and dynamical cavity method. References cited in all chapters are listed in the bibliography at the end of the thesis.

2 A model of the T-cell mediated anti-tumour immune response

2.1 Introduction

It is now known that tumours evoke an immune response, which can alter the growth and makeup of a tumour. Greater understanding of the anti-tumour immune response has led to the development of immunotherapies, which have seen some degree of success in clinical trials, particularly in cancers of the blood (42, 99, 100, 101, 102). However, the use of these therapies in solid cancers and conversion to the clinic still remains a challenge as was pointed out by (103).

The immune system can be seen as a network of interacting cells, with many different cell types working together to perform a wide-ranging and robust function against pathogens. In addition to this, tumours are rapidly evolving parts of this network. A systemic understanding of the mechanisms of the anti-tumour immune response is, therefore, vital in the development of immunotherapies. The sheer complexity, however, of the immune response

to tumours necessitates focusing on just a subset of processes. With this in mind this chapter seeks to address the adaptive, T-cell dependent anti-tumour immune response.

T-cells are lymphocytes, a group of white blood cells, distinguished from other lymphocytes by their unique receptor known as the T-cell receptor (TCR). TCRs are specific to foreign antigens (a part of a protein recognised by a TCR) such that they typically do not bind with molecules associated with healthy cells. A given TCR can recognise many different antigens, a property known as the cross-reactivity of T-cells (104, 105). If an antigen is recognsied by a TCR, we say that TCR is specific to that antigen. T-cells can be split into two main sub-types: helper and cytotoxic T-cells. Antigens are taken up and processed by professional antigen presenting cells (APCs) which present them as a peptide on the surface molecule MHC-II. Helper T-cells can then activate by binding to MHC-II which displays the antigen that the TCR is specific to. Activated helpers can then activate cytotoxic T-cells which eliminate cells that present a cognate antigen (an antigen that is recognised by the TCR) via MHC-I. The T-cell dependent response eliminates infected cells, but is also invoked by tumours (106).

A common experimental technique in immunology is immunostaining, which uses antibodies that bind to specific proteins, to sort cells. Helper T-cells are known for their high expression of the protein CD4, and cytotoxic cells for high CD8. For this reason, they are commonly referred to as $CD4^+$ and $CD8^+$ cells, respectively. A decrease in the $CD4^+/CD8^+$ ratio , measured from blood samples, is considered to be a good prognostic marker for conditions associated with immunodeficiency such as HIV (56, 57), and

aging (58, 59). It should be noted that subsets of T-cells other than helper and cytotoxic T-cells contribute to the $CD4^+$ and $CD8^+$ sub-populations. For example, in blood, regulatory T-cells account for $5-10\%$ of $CD4^+$ T-cells (107). In cancer, regulatory T-cells are typically more prevalent, making up $20-50\%$ of $CD4^+$ cells in some tumours (108). For this reason, changes in the $CD4^+/CD8^+$ ratio in these two contexts are not directly comparable.

Indeed, there are many different subsets of $CD4^+$ and $CD8^+$ cells involved in the immune response to tumours, as has been previously reviewed (109). The majority of $CD8^+$ T-cells in tumours are cytotoxic T-cells. In human tumour cultures, high levels of cytotoxic T-cell activity have been shown against tumours derived from the same host as the T-cells, but not against tumours from different hosts, due to the highly specific cytotoxic T-cell mediated response (110, 111). Indeed, studies in lung cancer (112) and melanoma (113) have shown that the presence of cytotoxic T-cells is associated with longer survival and tumour regression. For these reasons, cytotoxic $CD8^+$ T-cells play a major role in anti-tumour immunity and have formed the basis of many immunotherapies (114).

In addition to $CD8^+$, there are several subsets of $CD4^+$ T-cells which are major contributors to tumour immunity, some of which contribute to the anti-tumour immune response, other which suppress anti-tumour immunity, and some with a more ambiguous role (109). A clear contributor to anti-tumour immunity are Th1 cells. These cells are distinguished by their secretion of the cytokines IFN-γ and TNF-α, generally seen to promote anti-tumour immunity (115). The main mechanism for this is the interaction between Th1 and cytotoxic T-cells. This was demonstrated by adoptive cell therapies, where

the transfer of Th1 cells was unsuccessful in tumour rejection unless $CD8^+$ cells were also transferred (116). Additionally, IFN-γ is a cytokine associated with inflammation, such that it induces the recruitment of leukocytes to the site of immunosurveillance - indeed patients treated with IFN-γ have shown increased counts of total leukocytes (117, 118).

In contrast to the Th1, regulatory T-cells (Tregs) are more clearly associated with pro-tumour immune function. These cells are distinguished by the expression of the biomarkers $CD4^+CD25^+FoxP3^+$ (119, 120). Experimentally, the effect of transferring $CD8^+$ T-cells either with or without CD25+ T-cells (the original biomarker used to classify Tregs) in mice with melanoma has been studied (106, 121). In these studies, $CD8^+$ mediated anti-tumour immunity was suppressed when $CD4^+CD25^+$ T-cells were absent, demonstrating the functional link between Tregs and the $CD8^+$ mediated immunity. It was later shown that Tregs produce cytokines which promote the exhaustion of $CD8^+$ T-cells (such that they lose their ability to function) in the tumour environment, and hence suppress anti-tumour immunity (122). In addition to the exhaustion of T-cells, Tregs have a myriad of other immunosuppressant functions such as the suppression of antigen presentation in DCs, and the suppression of helper T-cell function (123). Although the mechanisms of Treg cells are suppressive, there are, however, studies which show that high levels of Tregs are associated with good prognosis, potentially due to the inhibition of other suppressive T-cells (120).

Th2 and Th17 cells have a more ambiguous role in the tumour immune response. Adoptive cell therapy with Th2 cells has been shown to invoke inflammation leading to tumour cell eradication (124). Th2 cells also pro-

duce cytokines which both promote and inhibit tumour immunity: they activate suppressive immune cells, inhibit antigen presenting cells, and recruit eosinophils (which kill tumour cells) to the tumour site (125). Th17 cells are distinguished by their high levels of the the excretion of cytokine IL-17. Increased levels of Th17 have been seen across cancers and were shown to stimulate the proliferation of naive T-cells, suggesting that Th17 have an anti-tumour function (126). However, the role of Th17 is heavily context dependent: it has been shown that they have pro- and anti-tumour function in different cancers. Pro-tumour function includes increased tumour cell proliferation and recruitment of immune cells. Conversely, anti-tumour function is seen in the enhancement of the cytotoxic and natural killer response (127).

The myriad of functions that different sub-types of $CD4^+$ cells have shows how the value of $CD4^+/CD8^+$ is heavily context dependent. Solid tumours are a porous mixture of tumour cells, immune cells and healthy tissue cells. T-cells can infiltrate tumours and the $CD4^+/CD8^+$ ratio of infiltrating T-cells can be measured from tumour samples. A low $CD4^+/CD8^+$ of infiltrating T-cells has been considered as a marker for prognosis across several cancer types including: cervical (128), breast (129, 130), lung, liver, testicular and colorectal cancers (53). Tumours from a cohort of breast, lung, colorectal, liver and testicular cancers, were surveyed (53) and it was found that low intra-epithelial $CD4^+/CD8^+$ was associated with early stage cancer due to an expanded $CD8^+$ population, and that later stage cancers were associated with low $CD4^+/CD8^+$ due to a loss of the $CD4^+$ population. In addition to these results in solid cancers, a low $CD4^+/CD8^+$ ratio in the blood correlated with poor survival in chronic lymphocytic leukemia (CLL) (131). Despite

the evidence that across cancer types a low $CD4^+/CD8^+$ ratio is a sign of poor prognosis, patients with low $CD4^+/CD8^+$ ratio of tumour infiltrating T-cells were found to have significantly improved survival in separate studies of colorectal cancer (54) and ovarian cancer (55), contradicting these studies.

There are many factors, biological and immunological, which could account for the prognostic variability in the $CD4^+/CD8^+$ ratio. Overall T-cell infiltration, i.e the density of T-cells in a tumour, may account for this variability in tumours, as the absolute number of T-cells will affect the strength of the immune response. As one would expect, the density of T-cells has also been shown to correlate with prognosis in cancer (132, 133). However, recent results have shown that the tumour reactivity of infiltrating T-cells, which reflects the proportion of TCRs that are specific to tumour associated antigens, is low in cancers where infiltration is a marker for prognosis (134). Therefore, the infiltration of specific T-cells may also lead to variability in prognostic markers.

A key stage in the progression of tumours is the down-expression of MHC-I, a cell surface molecule with which immune cells interact (60). Despite evidence for MHC-I expression correlating with prognosis, the relationship with tumour growth is less clear. The total absence of MHC-I in breast tumours has been shown to activate a group of innate immune cells, natural killer (NK) cells, which can kill cells without MHC-I recognition (135). However, studies of colorectal cancer showed that tumours with high MHC-I were found in patients with longer survival times and that MHC-I could be used as an independent marker of prognosis (61, 62). To complement the results seen with breast cancer, the total absence of MHC-I in colorectal cancer also showed

longer patient survival times compared with low MHC-I expression, due to the activation of NK cells (61). To summarise, MHC-I expression impacts the growth of tumours *in vivo*, with low expression favouring tumour growth, while high expression leading to longer patient survival. The exception is tumours with an absence of MHC-I which trigger an innate immune response from NK cells. This stresses the importance of tumour heterogeneity: low MHC-I expression, due to a large proportion of cells down-expressing MHC-I, will prevent a sufficient T-cell response, but the low level of MHC-I will also interrupt the response from NK cells.

There is a mechanistic interplay between the $CD4^+/CD8^+$ ratio and MHC-I expression. This is because cytotoxic cells, which form the majority of $CD8^+$ cells, bind to MHC-I in order to eliminate tumour cells. In spite of this fact there is a lack of data measuring the $CD4^+/CD8^+$ ratio and MHC-I together. One study has shown that the prognostic value of T-cell markers improves when MHC-I expression is also considered (136). Additionally, the loss of MHC-I in pancreatic cancer has been shown to lead to a lower level of infiltration by cytotoxic T-cells (133). Cytotoxic T-cell infiltration was found to be a marker of prognosis, however, MHC-I alone was not. Our hypothesis is that the interplay between $CD4^+/CD8^+$, T-cell infiltration, and MHC-I could explain the differences in prognostic value for these parameters across individual tumours and different cancers. To address this we create a mathematical model, starting from known cellular processes to derive system-wide behaviour. The aim is to see if such a model captures this interplay and explains potential variation in the prognostic value of $CD4^+/CD8^+$ and MHC-I.

As research has turned towards systemic modelling of the immune system

there has been an increase in mathematical and computational approaches to modelling challenges in immunology. Mathematical models used are mainly *deterministic*, comprised of ordinary differential equations (ODEs). Such models usually fall into two extremes: either, the model is low dimensional, 'macroscopic', and does not fully capture the systemic behaviour of the system; or it is high dimensional, 'microscopic', with a large number of unknown parameters; usually this makes statistical evaluation of these models with real data difficult. Furthermore, ODE models also fail to capture the inherent *stochasticity* of biological processes. In this paper we consider a model that lies between these two approaches, keeping the model to a few key parameters, whilst also including inherent stochasticity of microscopic behaviour.

Anti-tumour immunity has been a popular subject of mathematical modelling, as recently reviewed by (137). Models of the T-cell mediated immune response to tumours can be categorised by the sub-populations of T-cells that they consider. The pioneering work of (63) modelled the cytotoxic T-cell population interacting with immunogenic tumour cells in a predator-prey type model, and is a work that has continued to influence more recent modelling efforts (138, 139, 140). Similarly, more recent work has also focused on a model of tumour cells and immune cells which limit the growth of tumour cells, assumed to be mostly comprised of cytotoxic T-cells (141). This work differs significantly from (63) by modelling competition between immunogenic and immunoresistant sub-populations of tumour cells. Recent work has also extended the approach of (63) to model the explicit interaction between helper and cytotoxic T-cells (64, 142). Both works focus on analytical results, and are perhaps most in common with the research presented in this chapter. They

are, however, both deterministic models, and our work deviates from them in this respect.

Previous work has also accounted for the interaction between the helper, cytotoxic *and* regulatory T-cell subsets (143). However, analytical results were found to be intractable due to the complexity of the model, and the results rely instead on numerical simulation. More recently, a model of the interaction between helper, regulatory, and cytotoxic T-cells has been studied via fixed point analysis (144). This model considers how the over stimulation of the helper T-cell response can enhance the response of regulatory T-cells, and in turn limit the cytotoxic response. The interaction between effector $CD8^+$ T-cells and regulatory T-cells have also been modelled to produce a probabilistic model that determines prognosis based on the ratio of these T-cell subsets (145).

In our work we model the interplay between the helper/cytotoxic T-cell ratio and the expression of MHC-I in tumours explicitly. Although our model is also a system of ODEs which describe the change in concentration of cells, our model differs from previous efforts by including the stochastic dynamics of T-cell activation. The latter is used in the derivation of our model, but our analysis is based on non-equilibrium statistical mechanics, as similarly implemented by (146) to study the role of the helper/suppressive T-cell ratio in the B-cell response to antigens, allowing us to describe the macroscopic behaviour of the system deterministically. The work contained in this chapter differs from (146) as it focuses explicitly on the helper/cytotoxic ratio and its interplay with MHC-I, including the effect of time-dependent MHC-I expression. Statistical mechanics has a rich recent history in modelling the immune

system (147, 148, 149, 150, 151, 152) and here we use it to address the unique modelling challenges that tumour immunology poses. In doing so we derive a condition for the eradication of tumours which reveals a critical threshold of MHC-I expression. This threshold is found to depend on the helper/cytotoxic T-cell ratio, T-cell infiltration, and T-cell specificity.

In this work, we exclude the effects of NK cells and macrophages, focusing exclusively on the T-cell dependent response. This allows our model to be kept to a few key parameters that can be analysed in full. As previously discussed, NK cells play a dominant role when MHC-I is totally *absent*, a case which is less relevant for our model. The role of macrophages in the tumour is a double edged sword, with macrophages eliminating tumour cells, and also forming part of the bulk tumour, and has been modelled previously (153). It has been shown empirically that the presence of macrophages in tumours impedes cytotoxic T-cells in reaching tumour cells (154) and hence macrophages may affect the prognostic value of the helper/cytotoxic T-cell ratio. In this work we focus on the interactions between helper and cytotoxic T-cells, and do not model macrophages explicitly. We note, however, that the presence of macrophages would not alter the interactions between helper T-cells, cytotoxic T-cells, and tumour cells that we consider in our model. Additionally, while we do not focus on the interaction of helper and regulatory T-cells, we note that our model can implicitly account for immunosuppressive effects, that will include the function of regulatory T-cells. The result of this work is a low dimensional model with just a few important parameters, derived from known immunological and biological mechanisms.

The remaining sections of this chapter will be organised as follows: in

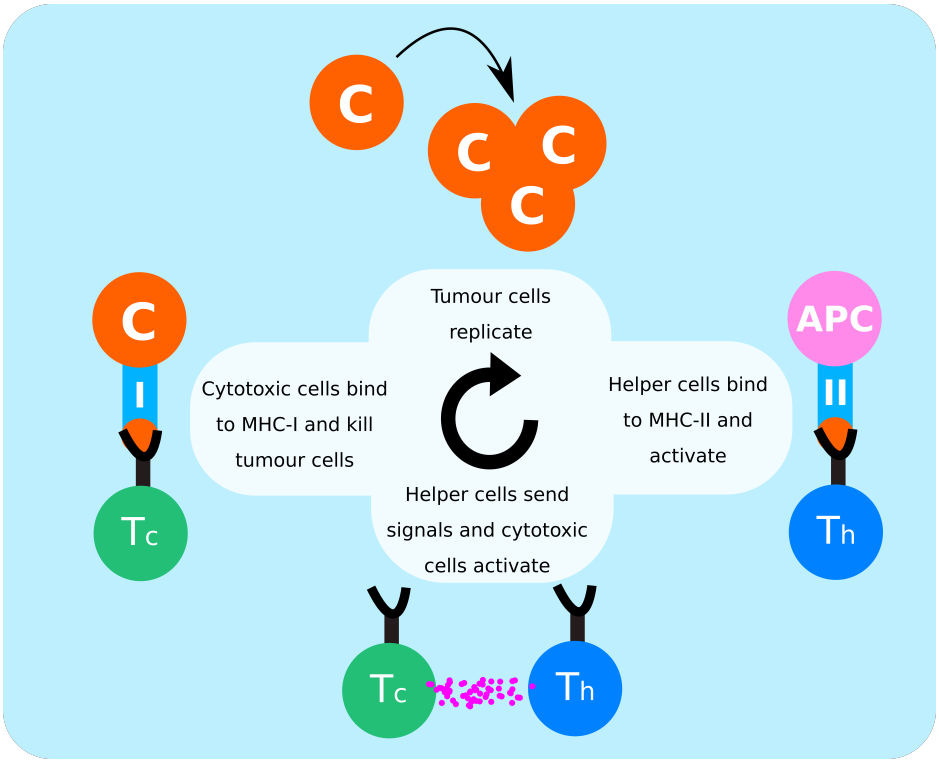

Figure 2.1: Summary of cellular interactions between tumour cells (C), antigen presenting cells (APCs), helper T cells (Th) and cytotoxic T cells (Tc) in anti-tumour immune response.

Sec. 2.2 we will introduce our mathematical model for tumour-immune interactions, in Sec. 2.3 we will present four key results that are of biological relevance and we will provide a discussion that assesses how our results fit in with the questions raised by the literature. We will discuss benefits and limitations of our modelling approach as well as pathways for future work in Sec. 2.4. Technical details are described in the appendices at the end of this chapter.

2.2 Constructing a mathematical model

2.2.1 The adaptive anti-tumour immune response

Tumour cells express antigens that are recognised by the immune system. Tumour antigens are typically the result of a mutation that leads to a change in the peptide presented in complex with MHC-I, but may also be proteins, associated with normal cells, with aberrant high expression on tumour cells (155). In both cases, the antigens distinguish the tumour cell from normal cells and can invoke an immune response. As tumour cells grow and divide, they may undergo apoptosis and release antigenic material into the tumour environment which is then taken up and processed by antigen presenting cells (156). Additionally, living tumour cells can release antigens in extracellular vesicles, which may also be taken up and processed by antigen presenting cells to stimulate other immune cells (157, 158) (although recently these have been shown to contribute to the inhibition of anti-tumour immunity and hence exhibit a dual role in tumour immunity (159, 160, 161)).

Antigen presenting cells, such as dendritic cells (162, 163, 164, 165) and B-cells (166, 167, 168), migrate to the tumour environment, take up antigens, process them internally into peptides, and display them on their surface in complex with MHC-II. Naive $CD4^+$ cells which have not been exposed to antigen may bind to this peptide-MHC complex via their TCR, if their TCR is specific to that antigen, and will differentiate into various effector T-cells, including Th1, Th2, Th17 and Treg cells (162, 165, 166, 169). In our model we focus on the Th1 lineage. Th1 cells have two important functions. Firstly, Th1 cells secrete cytokines that induce the increase in number of APCs. This

includes cytokines that stimulate the proliferation B-cells (23, 170) and cytokines which stimulate the maturation of DCs which then recruit further DCs (24, 164, 171, 172, 173). Secondly, and most crucially, Th1 cells also secrete cytokines that provide help to activate cytotoxic T-cells (116, 174). Finally, $CD8^+$ cells must bind with MHC-I to differentiate into cytotoxic T-cells which may then induce tumour cell death via cytolysis. (116, 163, 175).

The interactions in the anti-tumour immune response that we have described can be written as a series of cellular kinetic rate reactions. Here we list the full set of reactions that we model. By describing the immune response in this way, we can use the law of mass action to write a series of ODEs for further analysis. In our model we consider a population of the following cells: i) tumour cells, C, ii) antigen presenting cells, which we separate into two states, either without tumour antigen presented on MHC-II, B, or with tumour antigen presented on MHC-II, P, and iii) T-cells which we split into cytotoxic, T_c, and helper T-cells, T_h, which may be active or inactive, where we indicate the active populations by T_c^* and T_h^*. When we refer to helpers, we are considering the Th1 subset of T-cells, as it is these cells that mediate T-cell help for cytotoxic T-cells. The interactions between these cells, summarised in Figure 2.1, are described by the following reactions:

- Tumour cells, C, replicate at a constant rate r ,

$$C \xrightarrow{r} 2C. \tag{2.1}$$

- Tumour cells compete for resources such that there is a maximum con-

centration of tumour cells, ρ_c, in a finite volume

$$C + C \xrightarrow{r/\rho_c} C. \tag{2.2}$$

- Professional antigen presenting cells, B, such as dendritic cells (162, 163, 164, 165) and B-cells (166, 167, 168), capture antigens, process them into peptides, and display them in complex with surface molecules MHC-II, P ,

$$B + C \underset{\pi^-}{\overset{\pi^+}{\rightleftarrows}} P + C. \tag{2.3}$$

- Helper T-cells, T_h, bind to MHC-II molecules which present a tumour associated peptide antigen and activate (162, 165, 166, 169),

$$T_h + P \xrightarrow{W} T_h^* + P. \tag{2.4}$$

- Cytotoxic T-cells, T_c, are activated, T_c^*, by binding to MHC-I molecules on the surface of tumour cells that displays a peptide antigen, with the help of cytokines secreted by activated helpers (116, 174),

$$T_c + T_h^* + C \xrightarrow{W'} T_c^* + T_h^* + C. \tag{2.5}$$

- Activated helpers induce an increase in the number of antigen presenting cells. For example, activated helper T-cells stimulate the proliferation of B-cells (23, 170), and also stimulate the maturation of DCs which

then release cytokines that recruit further DCs (24, 164, 171, 172, 173)

$$T_h^* + B \xrightarrow{\lambda} T_h^* + 2B \tag{2.6}$$

- To ensure that there is a finite pool of APCs in our model, we assume that professional antigen presenting cells maintain homeostasis by competing at rate δ for the same resources,

$$B + B \xrightarrow{\delta} B. \tag{2.7}$$

- Activated cytotoxic T-cells eliminate tumour cells after docking to an MHC-I molecule which presents a tumour associated peptide antigen (116, 163, 175),

$$T_c^* + C \xrightarrow{\kappa} T_c^*. \tag{2.8}$$

The 'killing' rate, κ, is proportional to the rate at which cytotoxic cells bind and induce cytotoxic death, k, and the expression of MHC-I, γ, which can decrease throughout the development of the tumour. This is such that $\kappa = k\gamma$. For the remainder of this paper we set $k = 1$ and, without loss of generality, focus on the expression of MHC-I, $\gamma \in [0, 1]$, with $\gamma = 0$ corresponding to no tumour cells expressing MHC-I and $\gamma = 1$ corresponding to maximum MHC-I expression in the tumour. In principle, γ will vary with time, but to simplify the analysis we assume for now that it is constant and comment later on the effect of time-dependent γ. We note that γ is, specifically, the expression of MHC-I in tumour cells i.e. molecules which are bound to tumour associated

antigens and thus involved in the interaction with cytotoxic T cells, as oppose to bulk expression of MHC in the tumor environment. We would expect, however, these two quantities to be proportional to each other.

2.2.2 A statistical mechanics description of the immune system

We consider a solid tumour to occupy a space of fixed volume V. This volume is comprised of cells including helper and cytotoxic T-cells, professional antigen presenting cells and tumour cells. We represent the number of tumour cells, antigen presenting cells, and antigen presenting cells with MHC-II peptide complex, by the variables $[C]$, $[B]$ and $[P]$, respectively. We then choose to present our model in terms of the concentration of these cells, as experimentally raw cell counts are collected for a given volume or sample. The concentration of each of these cells is simply given by their number over the volume of the solid tumour, $c = [C]/V$, $b = [B]/V$ and $p = [P]/V$. The volume is permeable such that T-cells can move freely from the periphery into the solid tumour. We consider there to be a large population of T-cells, each labelled by an index $i = 1, \ldots, N$, such that the density of T-cells, $\rho = N/V$, is finite. T-cells can be divided in two sub-types: helper and cytotoxic. We describe the sub-type of each T-cell i by a binary variable η_i,

$$\eta_i = \begin{cases} 1, \text{ if T-cell } i \text{ is a helper T-cell} \\ 0, \text{ if T-cell } i \text{ is a cytotoxic T-cell} \end{cases} \tag{2.9}$$

that we regard as random, with distribution

$$\mathrm{P}(\eta) = \epsilon\delta_{\eta,1} + (1-\epsilon)\delta_{\eta,0} \tag{2.10}$$

where the parameter $\epsilon \in [0,1]$ controls the proportion of helper and cytotoxic T-cells, such that if $\epsilon = 0$ all T-cells are cytotoxic, while if $\epsilon = 1$ all T-cells are helpers. The helper/cytotoxic ratio is given by $R = \epsilon/(1-\epsilon)$. In principle this ratio should be time-dependent, as one would expect the number of helper and cytotoxic T-cells in the tumour environment to vary with time. However, in our model we consider a large population of T-cells with a fixed helper/cytotoxic ratio, and instead consider the dynamics of T-cell activation, as we detail later.

Each T-cell has receptors known as T-cell receptors (TCRs). If a TCR can bind an antigen peptide it is said to be specific to that antigen. If a TCR is not specific to a tumour associated antigen, the T-cell will not form part of the anti-tumour immune response. Indeed, it is not necessary that all T-cells in the tumour environment are specific to tumour associated antigens, and so the density of T-cells alone is not sufficient to describe the level of T-cell mediated anti-tumour immunity. To account for this we introduce a binary random variable ξ_i

$$\xi_i = \begin{cases} 1, \text{ if T-cell } i \text{ is specific to tumour antigen} \\ 0, \text{ otherwise} \end{cases} \tag{2.11}$$

drawn from the distribution

$$\mathrm{P}(\xi|\eta) = \left[A_\eta \delta_{\xi,1} + \left(1 - A_\eta\right) \delta_{\xi,0}\right] \tag{2.12}$$

such that $A_\eta \in [0,1]$ controls the fraction of T-cells of type η that are specific to tumour associated antigens. This is such that A_0 describes the fraction of cytotoxic T-cells that bind to MHC-I with tumour antigen peptide, and A_1 the fraction of helper T-cells that bind to MHC-II with tumour antigen peptide. In general there may be differences in the size of the helper and cytotoxic pools of T-cells that are specific to tumour antigens, however, in the lack of detailed knowledge about such differences, we assume statistical independence of η and ξ such that $A_\eta = A \; \forall \eta = 0, 1$.

The evolution of T-cells is described in Section 2.2.1 by equations (2.4) and (2.5). As these are cellular kinetic rate equations we could derive a set of ODEs that describe the change in concentration of the active and inactive cytotoxic T-cells, T_c and T_c^*, and the active and inactive helper T-cells T_h and T_h^*. However, we shall take an alternative approach, and derive equations for the fraction of cytotoxic and helper T-cells that are active at a given point in time. As it shall later turn out, this approach will lead to a lower dimensional system of equations than if we derived ODEs from each of the cellular kinetic rate equations in Section 2.2.1. Since the activation of T-cells evolves with time over the course of the immune response, each T-cell can be described by

a time-dependent state variable $\sigma_i(t)$ where,

$$\sigma_i(t) = \begin{cases} 1, \text{ if T-cell } i \text{ is activated at time } t \\ 0, \text{ otherwise.} \end{cases} \tag{2.13}$$

During the immune response, T-cell activation occurs through a TCR-dependent pathway. The TCR of cytotoxic and helper T-cells bind to the peptide complex of MHC-I and MHC-II, respectively. Upon binding, some condition is met such that the T-cell activates. The precise nature of the activation of T-cells is debated, but there is evidence to suggest that sufficient binding time is required for activation (176, 177, 178, 179, 180). Due to noise, inherent in biological systems, T-cells are likely to bind and unbind in a stochastic manner, therefore we treat T-cell activation as a stochastic process, following previous studies of T-cell activation in the literature (146, 151, 181, 182).

For simplicity, we assume that T-cells update their activation state at regular time intervals of duration Δ (while it is unlikely that T-cells update at regular time intervals, this choice is temporary, as we will eventually send $\Delta \to 0$ to retrieve continuous time dynamics), according to a linear threshold function,

$$\sigma_i(t+\Delta) = \theta\left(\eta_i \xi_i p(t) + (1-\eta_i)\xi_i c(t) \frac{1}{V} \sum_{j=1}^{N} \sigma_j(t) \eta_j \xi_j - \phi(t) - T z_i(t)\right), \tag{2.14}$$

where $\theta(x) = 1$ for $x > 0$ and 0 otherwise, and $z_i(t)$ is a zero-averaged random variable with suitably normalised variance mimicking fast noise in the

biological environment or stochasticity in T-cell activation. This modelling choice for the activation of T-cells is a coarse-grained description, which neglects details of specific molecular interactions involving TCRs, opting instead to represent such details as source of stochasiticity. The parameter T controls the noise level, such that the activation dynamics is fully stochastic for $T \to \infty$ and it is deterministic for $T = 0$. In the absence of noise ($T = 0$), equation (2.14) states that a T-cell i will activate if it receives a strong enough activation signal from the environment, i.e. if the activation signal is above a certain threshold $\phi(t)$. The activation signal depends on the nature of the T-cell, helper or cytotoxic, and it is given by the first and second term in the round brackets, respectively. According to the interactions described in equations (2.4) and (2.5) a helper T-cell i (i.e. $\eta_i = 1$) will activate if it is specific to tumour antigens (i.e. $\xi_i = 1$) and there is a sufficient concentration $p(t)$ of antigen presenting cells with tumour associated antigens, while a cytotoxic T-cell ($\eta_i = 0$) will activate if it is specific to tumour antigens (i.e. $\xi_i = 1$) and it is sufficiently co-stimulated by tumour cells and active, tumour specific helpers, whose concentrations are $c(t)$ and $V^{-1}\sum_{j=1}^{N}\sigma_j(t)\eta_j\xi_j$, respectively. The threshold $\phi(t)$ mimics any barrier that T-cells need to overcome to activate, including immunosuppressive effects due to T-cell exhaustion and inactivation via Treg cells. Noise (i.e. $T > 0$) can be interpreted as the amount that T-cells deviate from their deterministic activation rules. In addition to the binding and unbinding of T-cells to MHC-I, noise may also account for alternative activation pathways. For example, cytotoxic T-cells may not necessarily need helper T-cells to activate, they can be directly activated by APCs.

We note that equation (2.14) models reactions (2.4) and (2.5) in the pres-

ence of noise, at the *microscopic* level of individual T-cells. As we previously mentioned, alternatively one could model (2.4) and (2.5) at population level, via reaction kinetics (i.e. ODE) equations for the densities of active and inactive T-cells, valid under the assumptions of a well-mixed system and negligible fluctuations due to discreteness of cells. Noise could be included at population level, by introducing a reaction for spontaneous activation and deactivation of T-cells, whose rates would lead to additional free parameters in the model. Our approach starts instead from stochastic equations for the microscopic cell states, which do not require the above assumptions and keep the number of free parameters to a minimum. Macroscopic cell densities, such as those involved in reaction kinetics, can be obtained within our approach, as sums of microscopic variables, e.g. the density of active T-cells that are specific to tumour antigens can be retrieved as $V^{-1}\sum_{i=1}^{N}\xi_i\sigma_i$.

Next, we write differential equations for the concentrations of tumour and antigen presenting cells in the local environment, by modelling the cellular reactions in (2.1)-(2.8) at population level. Their evolution can be written in the following way,

$$\frac{\mathrm{d}c}{\mathrm{d}t} = \left[r - \gamma\frac{1}{V}\sum_{i=1}^{N}\sigma_i(1-\eta_i)\xi_i\right]c - \frac{rc^2}{\rho_c} \tag{2.15}$$

$$\frac{\mathrm{d}b}{\mathrm{d}t} = b\left(\lambda\frac{1}{V}\sum_{i=1}^{N}\sigma_i\eta_i\xi_i - \delta b\right) \tag{2.16}$$

$$\frac{\mathrm{d}p}{\mathrm{d}t} = \pi^{+}bc - \pi^{-}p. \tag{2.17}$$

We see here that the dependence on T-cell activation, described by the stochas-

tic variable $\sigma_i(t)$, means that the concentrations c, b and p are also subject to stochastic fluctuations.

Equation (2.15) contains three terms describing the change in tumour cell concentration with time, $\frac{\mathrm{d}c}{\mathrm{d}t}$. The first term states that c will increase at a rate r proportionally with c, corresponding to equation (2.1). The second term describes the effect of the T-cells on the tumour cells as in equation (2.8): a sum is taking over all the T-cells, and a non-zero contribution is only made by T-cells which are cytotoxic, specific to tumour cells and active, i.e. when $\sigma_i = 1 - \eta_i = \xi_i = 1$. Therefore, the second term states that tumour cells will be killed at a rate $\kappa = \gamma$ and proportionally with the concentration of tumour cells and the fraction of active, specific cytotoxic T-cells. Finally, the third term states that in the absence of the second term, i.e the T-cell response, the tumour cells will reach a carrying capacity concentration ρ_c, as described in equation (2.2).

The equations for $\frac{\mathrm{d}b}{\mathrm{d}t}$ can similarly be annotated. The first term states that antigen presenting cells will proliferate due to the presence of active helper T-cells at rate λ, as in equation (2.6). The second term describes competition at constant rate δ, as described in equation (2.7). We note that one could rewrite equation (2.16) in the following way,

$$\frac{\mathrm{d}b}{\mathrm{d}t} = Kb\left(1 - \frac{b}{N_b}\right) \tag{2.18}$$

$$K = \lambda \frac{1}{V} \sum_{i=1}^{N} \sigma_i \eta_i \xi_i \tag{2.19}$$

$$N_b = \frac{\lambda}{\delta} \frac{1}{V} \sum_{i=1}^{N} \sigma_i \eta_i \xi_i \tag{2.20}$$

such that b follows a logistic growth model with replication rate K and carrying capacity N_b. We highlight that the replication rate and carrying capacity of the APCs is not fixed, but dependent on the level of immune activity, in this case the fraction of active helper T-cells. The first and second terms in $\frac{\mathrm{d}p}{\mathrm{d}t}$ correspond to the reactions described in (2.3) and account for the antigen uptake and presentation by antigen presenting cells at rate π^+, and the reverse process where a receptor is freed for the uptake of new antigen, at rate π^-, respectively. When a cell from our naive APC population, B, engages with an antigen, it is still able to uptake further antigen. Hence, cells from our activated population of APCs, P, are still effectively cells in the naive population, B, but with less capacity to uptake further antigen. In principle, this means that equation (2.16) should contain a term reflecting the loss of naive APCs becoming activated APCs, $-\frac{1}{n}\pi^+ bc$, where n is the total number of antigens that APCs can present, and a gain term reflecting the reverse process $+\frac{1}{n}\pi^- p$. The capacity of APCs to present antigen on MHC-II is reportedly large. For DCs the number of MHC-II molecules is $\mathcal{O}(10^6)$ (162, 183) (although we note the number of MHC-II molecules that display a specific antigen has been estimated to be a small fraction of this, 0.1% (184)), and for B-cells the number of antigen receptors is $\mathcal{O}(10^5)$ (185). For our purposes, we consider n to be large, such that terms $\mathcal{O}(1/n)$ can be neglected. We note that in what follows we focus on the steady state of our model, and as it turns out these terms would vanish anyway in the steady state. This is because equation (2.17) would also have to include terms $+\frac{1}{n}\pi^+ bc$ and $-\frac{1}{n}\pi^- p$, which cancel the respective terms in equation (2.16) at the fixed point.

2.3 Results

2.3.1 Macroscopic dynamics of T-cell activation

From a set of cellular reactions we have started to build a set of differential equations, with the inclusion of a microscopic description of T-cells. As they stand we can not solve equations (2.15)-(2.17) directly, due to the dependence on the stochastic variables $\sigma_i(t)$. To make analytical progress we define the macroscopic observables,

$$m(\boldsymbol{\sigma}) = \frac{1}{V}\sum_{i=1}^{N}\sigma_i\eta_i\xi_i \tag{2.21}$$

$$a(\boldsymbol{\sigma}) = \frac{1}{V}\sum_{i=1}^{N}\sigma_i\xi_i, \tag{2.22}$$

where $\boldsymbol{\sigma} \in \{0,1\}^N$, representing the density of active, specific helpers and the density of active, specific T-cells, respectively. With these definitions equations (2.15)-(2.17) can be written as follows,

$$\begin{aligned}
\frac{\mathrm{d}c}{\mathrm{d}t} &= \left[r - \gamma\left(a(\boldsymbol{\sigma}) - m(\boldsymbol{\sigma})\right) - \frac{rc}{\rho_c}\right]c \\
\frac{\mathrm{d}b}{\mathrm{d}t} &= b\left(\lambda m(\boldsymbol{\sigma}) - \delta b\right) \\
\frac{\mathrm{d}p}{\mathrm{d}t} &= \pi^{+}bc - \pi^{-}p.
\end{aligned} \tag{2.23}$$

We now seek to derive the time evolution of the macroscopic observables $a(\boldsymbol{\sigma})$ and $m(\boldsymbol{\sigma})$. To this purpose, we must specify the statistical properties of the activation noise. Information about the latter is very scarce in biological literature (181, 186, 187). A natural choice would be to assume a Gaussian

distribution of noise however, for convenience of analysis and without loss of generality, we consider a distribution of noise more common in statistical physics (see 2.A for details).

While our expressions for c, b and p evolve in continuous time, equation (2.14) shows that T-cells evolve in discrete time steps of duration Δ. However, from equation (2.14) one can derive the continuous time master equation for time-dependent probability $\mathrm{P}_t(\sigma)$. To do so, one assumes that T-cells are updated sequentially, where in a given time step Δ, a T-cell is selected from the population with uniform probability. Formally, one then sets the magnitude of the time step to $\Delta = 1/N$ in equation (2.14), and takes the limit $N \to \infty$ as detailed in 2.A. Biologically, this means that we assume that the population of T-cells is sufficiently large, such that the state of the population of T-cells, σ, evolves continuously, i.e in any infinitesimal duration of time we expect that at least one T-cell to update its activation state. Equations for the time evolution of the macroscopic observables $a(\sigma)$ and $m(\sigma)$ are also derived in 2.A. It will turn out that fluctuations of these quantities around their averages, $m(t) = \sum_\sigma \mathrm{P}_t(\sigma)m(\sigma)$ and $a(t) = \sum_\sigma \mathrm{P}_t(\sigma)a(\sigma)$, vanish as the number of T-cells, N, is sent to infinity and that the evolution of these averages is governed by the equations

$$\begin{aligned} \frac{\mathrm{d}m}{\mathrm{d}t} &= -m + \frac{\rho}{2}\left\langle \eta\xi\left[1+\tanh\left(\frac{\beta}{2}\left(\eta\xi p + (1-\eta)\xi c m - \phi(t)\right)\right)\right]\right\rangle_{\eta,\xi} \\ \frac{\mathrm{d}a}{\mathrm{d}t} &= -a + \frac{\rho}{2}\left\langle \xi\left[1+\tanh\left(\frac{\beta}{2}\left(\eta\xi p + (1-\eta)\xi c m - \phi(t)\right)\right)\right]\right\rangle_{\eta,\xi}. \end{aligned} \tag{2.24}$$

In the above the density of T-cells $\rho = \frac{N}{V}$ is assumed to be finite when $N \to \infty$

and $\langle \dots \rangle_{\eta,\xi}$ denotes the average over the joint distribution,

$$\mathrm{P}(\eta,\xi) = \lim_{N\to\infty} \frac{1}{N} \sum_i \delta_{\eta,\eta_i} \delta_{\xi,\xi_i}. \tag{2.25}$$

As stated earlier, we assume that $\mathrm{P}(\eta,\xi) = \mathrm{P}(\eta)\mathrm{P}(\xi)$, i.e. the probability of a T-cell having a cognate receptor to the tumour associated antigens is not dependent on whether T-cell i is helper or cytotoxic. Equations (2.10) and (2.12) may then be used to compute the averages in (2.24).

Finally, we take equations (2.23) and replace $m(\sigma)$ and $a(\sigma)$ with their thermodynamic averages m and a, which is equivalent to a mean-field approximation, that we show in the appendix to be exact in the limit $N \to \infty$. This allows us to get a small, closed system of ODEs,

$$\begin{aligned}
\frac{\mathrm{d}c}{\mathrm{d}t} &= \left[r - \gamma(a-m) - \frac{rc}{\rho_c} \right] c \\
\frac{\mathrm{d}b}{\mathrm{d}t} &= b\left(\lambda m - \delta b\right) \\
\frac{\mathrm{d}p}{\mathrm{d}t} &= \pi^+ bc - \pi^- p \\
\frac{\mathrm{d}m}{\mathrm{d}t} &= -m + \frac{\epsilon A \rho}{2}\left[1 + \tanh\left(\frac{\beta}{2}\left(p - \phi(t)\right)\right)\right] \\
\frac{\mathrm{d}a}{\mathrm{d}t} &= -a + \frac{A\rho}{2}\left[1 + \epsilon \tanh\left(\frac{\beta}{2}\left(p - \phi(t)\right)\right) + (1-\epsilon)\tanh\left(\frac{\beta}{2}\left(cm - \phi(t)\right)\right)\right].
\end{aligned} \tag{2.26}$$

By describing the T-cell dependent anti-tumour immune response with ODEs we have neglected the role of spatial heterogeneity in the evolution of tumours. This was done in the spirit of capturing the interplay between the $\mathrm{CD4}^+/\mathrm{CD8}^+$ T-cell ratio and MHC-I expression with a simple model, amenable to analytical solution. In principle one could model spatial heterogeneity in

the T-cell dependent immune response by making the variables ϵ and A functions of spatial position. This would result in c, b and p becoming spatially-dependent. However, further considerations would need to be made to account for cellular drift in space. By neglecting spatial dependencies, our approach is equivalent to modelling a small, macroscopic region of a solid tumour where spatially-dependent variables can be regarded as uniform.

2.3.2 Conditions for tumour eradication

We use the system of equations (2.26) to derive a set of conditions which will qualitatively describe how the anti-tumour immune response changes with parameters of the model. First, we write the system of equations in a more compact way by defining the vector $\mathbf{x} = (c, b, p, m, a)$ such that $\dot{\mathbf{x}} = \mathbf{F}(\boldsymbol{x})$, where each component of the vector $\mathbf{F}$ is the RHS of the corresponding ODE. Second, we find fixed points of the dynamics from $\dot{\mathbf{x}} = \mathbf{0}$ and analyse their stability by inspecting the eigenvalues of the Jacobian $\partial\mathbf{F}/\partial\mathbf{x}$. The system will allow for fixed points if the activation threshold $\phi(t)$, accounting for immunosuppressive effects, is stationary. In the remainder of this work, we will focus on a vanishing stationary threshold $\phi(t) = 0\ \forall t$. In this case our model will provide a lower limit on the size of the tumour, as immunosuppressive signals reduce the anti-tumour immune response. We find that there are two fixed points which, subject to some condition, are stable. There are two other fixed points but they are always unstable. The potentially stable fixed points are given by,

$$\mathbf{x}_1 = (0, \frac{\lambda m^*}{\delta}, 0, m^*, a^*), \tag{2.27}$$

where $m^* = \frac{\epsilon A\rho}{2}$ and $a^* = \frac{A\rho}{2}$ and

$$\mathbf{x}_2 = (c^*, \frac{\lambda m^*}{\delta}, \frac{\pi^+\lambda}{\pi^-\delta}c^*m^*, m^*, a^*) \tag{2.28}$$

where c^*, m^* and a^* are the solution to the system of equations

$$c^* = \frac{\rho_c(r - \gamma(a^* - m^*))}{r} \tag{2.29}$$

$$m^* = \frac{\epsilon A\rho}{2}\left(1 + \tanh\left(\frac{\beta\pi^+\lambda}{2\pi^-\delta}c^*m^*\right)\right) \tag{2.30}$$

$$a^* = \frac{A\rho}{2}\left(1 + \epsilon\tanh\left(\frac{\beta\pi^+\lambda}{2\pi^-\delta}c^*m^*\right) + (1-\epsilon)\tanh\left(\frac{\beta}{2}c^*m^*\right)\right). \tag{2.31}$$

The fixed point $\mathbf{x}_1$ corresponds to tumour eradication, $c^* = 0$, whereas $\mathbf{x}_2$ corresponds to tumour escape, $c^* \neq 0$. The size of the tumour at $\mathbf{x}_2$ varies with the parameters of the system. When T-cells are all cytotoxic, $\epsilon = 0$, there is no signal from helper cells $m^* = 0$, and all T-cell signal comes from cytotoxic cells, $a^* = \frac{A\rho}{2}$, resulting in a tumour below the carrying capacity, $c^* = \rho_c\left(1 - \frac{\gamma A\rho}{2}\right)$. However, when all T-cells are helpers, $\epsilon = 1$, we have that the net T-cell signal is equivalent to the helper T-cell signal, $m^* = a^*$, and that the tumour reaches the carrying capacity, $c^* = \rho_c$. From analysis of the eigenvalues of the Jacobian $\partial\mathbf{F}/\partial\mathbf{x}$ we find that $\mathbf{x}_1$ is stable when,

$$\gamma > \gamma_c = \frac{2r}{A\rho}(1 + R) \tag{2.32}$$

when this condition is not met $\mathbf{x}_1$ is unstable. To assess the stability of $\mathbf{x}_2$ we should analyse the eigenvalues of the Jacobian evaluated at $\mathbf{x}_2$, however the eigenvalues are found to be non-trivial and a condition for stability based on

a single parameter as in (2.32) is not tractable.

To make progress analytically, we shall reduce the dimensionality of our system by considering the timescales at which the different processes in our model occur. To begin we define $\tilde{r} = r\tau_c$ and $\tilde{\gamma} = \gamma\tau_c$ where τ_c is a constant that will set the relative rate of reactions that govern tumour cell concentration, and $\tilde{r}$ and $\tilde{\gamma}$ are the redefined rate of tumour replication and MHC-I expression, respectively. Substituting our expressions for r and γ into our expression for $\frac{\mathrm{d}c}{\mathrm{d}t}$ in (2.26), we can write,

$$\tau_c \frac{\mathrm{d}c}{\mathrm{d}t} = \left[\tilde{r} - \tilde{\gamma}(a - m) - \frac{\tilde{r}c}{\rho_c}\right] c. \tag{2.33}$$

Similarly, we may define $\tilde{\lambda} = \lambda\tau_p$, $\tilde{\delta} = \delta\tau_p$ and $\tilde{\pi}^{\pm} = \pi^{\pm}\tau_p$ where τ_p is a constant that will set the relative rate of reactions that govern antigen presentation. Our expressions for $\frac{\mathrm{d}b}{\mathrm{d}t}$ and $\frac{\mathrm{d}p}{\mathrm{d}t}$ in (2.26) may then be written,

$$\tau_p \frac{\mathrm{d}b}{\mathrm{d}t} = b\left(\tilde{\lambda}m - \tilde{\delta}b\right) \tag{2.34}$$

$$\tau_p \frac{\mathrm{d}p}{\mathrm{d}t} = \tilde{\pi^+}bc - \tilde{\pi^-}p. \tag{2.35}$$

We now scale time such that our equations evolve on the timescale defined by

$t = \tau\tau_c$. In this case the system of equations (2.26) becomes,

$$\frac{\mathrm{d}c}{\mathrm{d}\tau} = \left[\tilde{r} - \tilde{\gamma}(a-m) - \frac{\tilde{r}c}{\rho_c}\right] c \tag{2.36}$$

$$\frac{\tau_p}{\tau_c}\frac{\mathrm{d}b}{\mathrm{d}\tau} = b\left(\tilde{\lambda}m - \tilde{\delta}b\right) \tag{2.37}$$

$$\frac{\tau_p}{\tau_c}\frac{\mathrm{d}p}{\mathrm{d}\tau} = \tilde{\pi^+}bc - \tilde{\pi^-}p. \tag{2.38}$$

$$\frac{1}{\tau_c}\frac{\mathrm{d}m}{\mathrm{d}\tau} = -m + \frac{\epsilon A\rho}{2}\left[1 + \tanh\left(\frac{\beta}{2}p\right)\right] \tag{2.39}$$

$$\frac{1}{\tau_c}\frac{\mathrm{d}a}{\mathrm{d}\tau} = -a + \frac{A\rho}{2}\left[1 + \epsilon\tanh\left(\frac{\beta}{2}p\right) + (1-\epsilon)\tanh\left(\frac{\beta}{2}cm\right)\right]. \tag{2.40}$$

We now assume that $\tau_c \gg \tau_p$ such that the processing and presentation of antigens is fast relative to the replication and cell-mediated death of tumour cells. To support this assumption, we refer to the immunological literature. Firstly, it has been shown that the rate at which surface MHC-II is endocytosed in immature and mature DCs is on the timescale of about an hour: a study found immature DCs to endocytose 70% of their MHC-II surface molecules in 80 minutes, with mature DCs only endocytosing 15% in the same time period, as MHC-II half-life is known to be longer in the mature state (188). While this may suggest that mature DCs lose the ability to take up and present fresh antigen, it has been shown, in mice, that both immature and mature DCs take up and present fresh antigen *in vivo* after just 30 minutes of exposure to antigen (189). To assess the timescale at which the concentration of tumour cells evolves, we note that in solid cancers, tumour cell doubling times *in vitro* are approximately 30 hours, as has been measured in ovarian (190) as well as breast and lung cancer (191) cancer cell lines. With this in mind, we consider antigen presentation to be a fast process relative

to the evolution of tumour cell concentration, and take $\frac{\tau_p}{\tau_c} \to 0$. This implies that equations (2.37) and (2.38) reach their stable nullcline, $b = \frac{\tilde{\lambda} m}{\tilde{\delta}} = \frac{\lambda m}{\delta}$ and $p = \frac{\pi^+ \lambda m c}{\pi^- \delta}$ which we note depend on the original, unscaled, parameters. Consequently, our system of equations is reduced to,

$$\frac{\mathrm{d}c}{\mathrm{d}t} = \frac{1}{\tau_c}\left[\tilde{r} - \tilde{\gamma}(a-m) - \frac{\tilde{r}c}{\rho_c}\right] c \tag{2.41}$$

$$\frac{\mathrm{d}m}{\mathrm{d}t} = -m + \frac{\epsilon A \rho}{2}\left[1 + \tanh\left(\frac{\beta}{2} p\right)\right] \tag{2.42}$$

$$\frac{\mathrm{d}a}{\mathrm{d}t} = -a + \frac{A\rho}{2}\left[1 + \epsilon \tanh\left(\frac{\beta}{2} p\right) + (1-\epsilon)\tanh\left(\frac{\beta}{2} cm\right)\right] \tag{2.43}$$

with $p = \frac{\pi^+ \lambda m c}{\pi^- \delta}$.

At this stage we are faced with one of two options: either the evolution of tumour cell concentration is faster than T-cell activation or vice versa. In the literature, it has been shown that a single DC can interact with 5000 T-cells an hour (192). This suggests that our variables describing the fraction of T-cells that are active, m and a, will evolve on a much faster timescale than the tumour cell concentration. If we accept this, and consider the case that T-cell activation is faster than tumour cell division, we shall formally send $\frac{1}{\tau_c} \to 0$. We can study the solution to this system of equations (2.41)-(2.43) under the assumption that $\frac{1}{\tau_c} \ll 1$ via singular perturbation theory. The "inner" solution to these equations, where it is assumed $t = \mathcal{O}(1)$, is found by sending $\frac{1}{\tau_c} \to 0$ such that from equation (2.41),

$$\frac{\mathrm{d}c}{\mathrm{d}t} = 0 \tag{2.44}$$

$$\implies c = c(t=0) = c_0 \tag{2.45}$$

and the system of equations is reduced to,

$$\frac{\mathrm{d}m}{\mathrm{d}t} = -m + \frac{\epsilon A\rho}{2}\left[1 + \tanh\left(\frac{\beta}{2}p_0\right)\right] \tag{2.46}$$

$$\frac{\mathrm{d}a}{\mathrm{d}t} = -a + \frac{A\rho}{2}\left[1 + \epsilon\tanh\left(\frac{\beta}{2}p_0\right) + (1-\epsilon)\tanh\left(\frac{\beta}{2}c_0 m\right)\right]. \tag{2.47}$$

with $p_0 = \frac{\pi^+\lambda m c_0}{\pi^-\delta}$. On the other hand, the "outer" solution in singular perturbation theory is found by rescaling time such that $t = \tau\tau_c$, assuming $\tau = \mathcal{O}(1)$ (i.e. $t = \mathcal{O}(\frac{1}{\tau_c})$), and sending $\tau_c \to \infty$. After rescaling time, equations (2.41)-(2.43) become,

$$\frac{\mathrm{d}c}{\mathrm{d}\tau} = \left[\tilde{r} - \tilde{\gamma}(a-m) - \frac{\tilde{r}c}{\rho_c}\right]c \tag{2.48}$$

$$\frac{1}{\tau_c}\frac{\mathrm{d}m}{\mathrm{d}\tau} = -m + \frac{\epsilon A\rho}{2}\left[1 + \tanh\left(\frac{\beta}{2}p\right)\right] \tag{2.49}$$

$$\frac{1}{\tau_c}\frac{\mathrm{d}a}{\mathrm{d}\tau} = -a + \frac{A\rho}{2}\left[1 + \epsilon\tanh\left(\frac{\beta}{2}p\right) + (1-\epsilon)\tanh\left(\frac{\beta}{2}cm\right)\right]. \tag{2.50}$$

In the limit $\tau_c \to \infty$ we find that $\frac{1}{\tau_c}\frac{\mathrm{d}m}{\mathrm{d}\tau} = 0$ and $\frac{1}{\tau_c}\frac{\mathrm{d}a}{\mathrm{d}\tau} = 0$ such that m and a reach their nullclines

$$a = \frac{A\rho}{2}\left[1 + \epsilon\tanh\left(\frac{\beta}{2}p\right) + (1-\epsilon)\tanh\left(\frac{\beta}{2}cm\right)\right] \tag{2.51}$$

$$m = F^{-1}(c) \tag{2.52}$$

where

$$F(m) = \frac{2\pi^-\delta}{\beta\pi^+\lambda m}\tanh^{-1}\left(\frac{2m}{\epsilon A\rho} - 1\right). \tag{2.53}$$

Hence, the outer solution is reduced to a single ODE,

$$\frac{\mathrm{d}c}{\mathrm{d}\tau} = \left[\tilde{r} - \frac{\tilde{\gamma}A\rho}{2}(1-\epsilon)\left[1+\tanh\left(\beta c F^{-1}(c)/2\right)\right] - \frac{\tilde{r}c}{\rho_c}\right] c = f(c). \tag{2.54}$$

Formally, the inner solution at $t \to \infty$ should be equivalent to the outer solution at $\tau \to 0$. If we consider the inner solution, equations (2.45)-(2.47), at $t \to \infty$ we find that m and a will reach the fixed points of equations (2.46) and (2.47) which are given by,

$$a = \frac{A\rho}{2}\left[1+\epsilon\tanh\left(\frac{\beta}{2}p_0\right)+(1-\epsilon)\tanh\left(\frac{\beta}{2}c_0 m\right)\right] \tag{2.55}$$

$$m = F^{-1}(c_0). \tag{2.56}$$

If we consider the outer solution at $\tau \to 0$, from equation (2.54) we have that c will simply be set at its initial condition

$$\lim_{\tau\to 0} c = c(\tau = 0) = c_0. \tag{2.57}$$

If we then substitute c_0 into the outer solution for a and m, given by equations (2.51) and (2.52), we find that they are equivalent to the inner solution for a and m in the limit $t \to \infty$, given by equations (2.55) and (2.56). Hence, it is the case that the inner solution at $t \to \infty$ and the outer solution at $\tau \to 0$ are equivalent. One then expects that the inner and outer solutions match at some intermediate timescale τ^* where $1 \ll \tau^* \ll \frac{1}{\tau_c}$ i.e. $\tau^* = \frac{1}{\sqrt{\tau_c}}$.

As we are interested in the long time dynamics of our system, we consider the outer solution at $\tau \to \infty$. In this case the tumour cell concentration c will

reach one of two fixed points of equation (2.54), given by,

$$c^* = 0 \tag{2.58}$$

$$c^* = \rho_c \left(1 - \frac{\gamma A \rho}{2r}(1-\epsilon)\left[1 + \tanh\left(\beta c^* F^{-1}(c^*)/2\right)\right]\right) \tag{2.59}$$

corresponding to tumour eradication and large stable tumour formation, respectively. The non-trivial fixed point, $c^* > 0$, can be found using the relation $F^{-1}(c^*) = m^*$ via the numerical solution of (2.29)-(2.31).

To inspect the stability of the fixed points we evaluate the derivative $f'(c)$ of the 'velocity' function defined in (2.54). The fixed point $c^* = 0$ is stable when $f'(0) < 0$ giving us the condition $\gamma > \gamma_c = \frac{2r}{A\rho}\frac{1}{1-\epsilon}$ which is equivalent to (2.32). The non-trivial fixed point $c^* > 0$ will be stable when $f'(c^*) < 0$, yielding

$$\gamma < \gamma^* = \frac{2r}{A\rho}(1+R)\left\{1 - \frac{\beta}{2}c^*\left[m^* + \frac{c^*}{F'(m^*)}\right]\cosh^{-2}\left(\beta c^* m^*/2\right)\right\}^{-1}. \tag{2.60}$$

We now have an expression for the critical value of MHC-I where the fixed point $c^* \neq 0$ becomes unstable, γ^*, given by equation (2.60), and an expression for the critical value of MHC-I where $c^* = 0$ becomes unstable, γ_c, given by equation (2.32). Since it is not necessary that $\gamma_c = \gamma^*$, there is a possibility that either i) $\gamma^* < \gamma < \gamma_c$ and both fixed points are unstable or ii) $\gamma_c < \gamma < \gamma^*$ and both fixed points are stable; this would suggest that the dynamics are non-trivial and can not be analysed through linear stability analysis alone. To investigate which, if any, of the two scenarios is taking place, we perform limiting analysis of the stability condition. We

first note that for meaningful values of m i.e $0 < m < \epsilon A\rho$ which must be, by definition, at most of order $\mathcal{O}(1)$, we can show that $F'(m) > 0$. The term $\frac{\beta}{2}c^*\left[m^* + \frac{c^*}{F'(m^*)}\right]\cosh^{-2}(\beta c^* m^*/2) \sim \mathcal{O}(\frac{c^{*2}}{\exp(c^*)}) < 1$ which vanishes at both $c^* \to 0$ and $c^* \to \infty$. It then follows from equations (2.59) and (2.60) that,

$$\text{as } \gamma \to 0^+, \quad c^* \to \rho_c^- \quad \Longrightarrow \quad \gamma^* \geq \gamma_c^+ \tag{2.61}$$

with equality at $\rho_c \to \infty$. We can also look at the limit that the γ approaches its critical value to find,

$$\text{as } \gamma \to \gamma_c^-, \quad c^* \to 0^+ \quad \text{and} \quad \gamma^* \to \gamma_c^+. \tag{2.62}$$

However, the exact value of γ^* can only be found through numerical solution of equations (2.29) and (2.30). We note that γ^* can be written as function of γ through its dependence on c^*. In the left panel of Figure 2.2 we plot γ^* as a function of γ and find that,

$$\gamma > \gamma_c \implies \gamma > \gamma^* \tag{2.63}$$

$$\gamma < \gamma_c \implies \gamma < \gamma^* \tag{2.64}$$

which implies that the fixed points exchange stability as $\gamma \to \gamma_c$.

From the analysis of the long time dynamics of the system (2.26), and by taking into account different timescales of processes, we have shown that there are two fixed points where $c = 0$ or $c = c^*$. If the MHC-I expression is above some critical value, $\gamma > \gamma_c$, the fixed point $c = 0$ is stable and $c = c^*$ is unstable, whereas the reverse is true if $\gamma < \gamma_c$. In doing so we have assumed

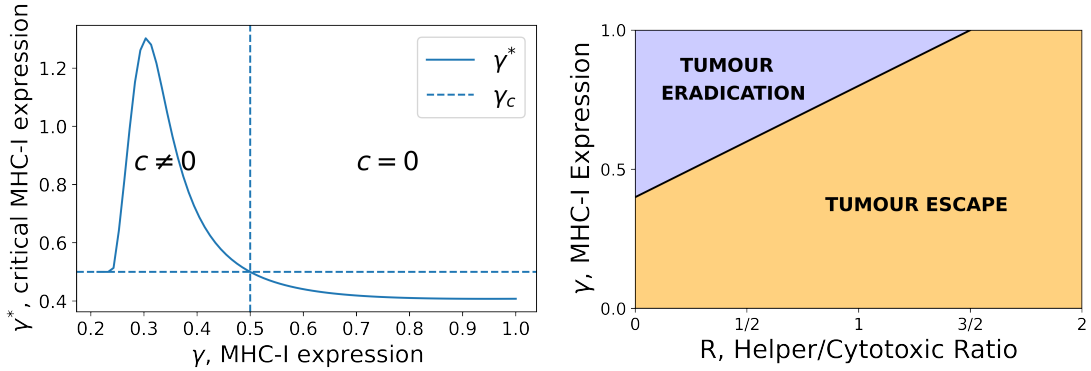

Figure 2.2: Left: Critical value of MHC-I, γ^* given by equation (2.60), where the non-zero fixed point of equation (2.54) becomes stable/unstable. From equation (2.60) γ^* depends on γ through c^*, and so we plot this as a function of γ. Dashed lines indicate the critical value of MHC-I, γ_c, where the fixed point $c = 0$ of equation (2.54) becomes stable/unstable. The model parameters used are: tumour replication rate $r = 0.15$, helper/cytotoxic ratio $R = 1/3$, and specific T-cell density $A\rho = 0.8$. All other parameters are set to 1. Right: γ is plotted against the helper/cytotoxic ratio R. Tumour cells are removed above the critical line indicated by the solid line $\gamma = \gamma_c$. The model parameters used are: tumour replication rate $r = 0.2$, specificity of T-cells $A = 1$ and density of T-cells $\rho = 1.0$. Parameters have been chosen to clearly delineate the different regions of interest i.e tumour escape $c \neq 0$ and tumour eradication $c = 0$.

that $\tau_c \gg 1$. However, we find in 2.B that the fixed points of the system are the same if we assume the reverse $\tau_c \ll 1$ (although the transient dynamics will differ).

This shows that there is a critical value of MHC-I expression, above which the tumour will be eradicated, and below which it will reach some stable tumour size. Furthermore, the critical value of MHC-I depends linearly through the helper/cytotoxic ratio R. To remove tumour cells a large population of cytotoxic T-cells is required and this depends on the expression of MHC-I. This is illustrated in Figure 2.2 (right panel). This implies that measuring $CD4^+/CD8^+$ alone may yield incorrect understanding of tumour progression *in vivo* since it also depends on the expression of MHC-I. With a low MHC-I

expression, a $CD4^+/CD8^+$ ratio that would have been considered healthy for high MHC-I expression would not lead to complete tumour eradication. We note that this figure shows that higher CD8 and higher MHC-I are associated with lower tumour size, consistent with current data (136).

The stability of the fixed points does not depend on the T-cell activation noise level, $\beta^{-1} = T$. The noise does however affect the size of the escaped tumour as shown in Figure 2.3, obtained by solving together equations (2.29) and (2.30) numerically. In this figure we set $r = 0.5$ and $A = \rho = \gamma = 1$ to ensure that the fixed point $c = c^*$ is stable. We also set $\rho_c = 1000$, but in this case the choice is arbitrary as ρ_c will not affect the stability of c^*, only its size and the time it takes for the fixed point to be reached. For $\beta > 10^1$ the change in the tumour cell concentration becomes negligible due to the hyperbolic tangent function that appears in (2.30) which saturates for large values of β. An additional observation is the dependence of γ_c on the parameters A and ρ in (2.32). These parameters, respectively, represent the specificity and density of T-cells in the tumour. We refer to the product $A\rho$ as the specific infiltration of T-cells, as in combination these parameters describe the density of T-cells that are involved in the anti-tumour immune response. We find that γ_c is proportional to $(A\rho)^{-1}$ which suggests that small changes in the specific infiltration of T-cells may correspond to large changes in stable tumour cell concentration.

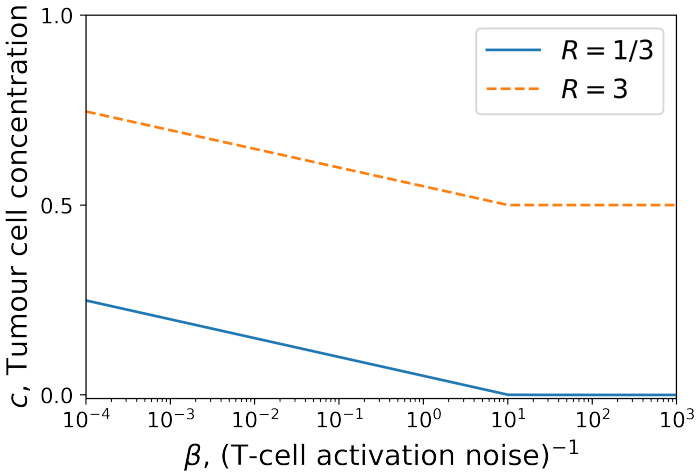

Figure 2.3: Equilibrium tumour concentration plotted as a function of inverse T-cell activation noise β. Activation noise is increasing from right to left. The tumour replication rate is $r = 0.5$, the carrying capacity concentration is $\rho_c = 1000$, and the MHC-I expression and specific tumour density are set to $\gamma = A = \rho = 1$. The tumour cell concentration is normalised with respect to the carrying capacity ρ_c.

2.3.3 Tumour size with immune parameters

This model provides predictions for the dependence of the size of the tumour, given by equations (2.29) and (2.30), on different immune parameters. Figure 2.4 shows how the size of the tumour varies with MHC-I expression (left panel) and infiltration of specific T-cells $A\rho$ (right panel) and it shows that it increases when the helper/cytotoxic ratio is larger. For a low helper/cytotoxic ratio we see a discontinuity in the stable tumour size. This is due to the figure showing the tumour size dynamically reached at equilibrium. Above the critical value of infiltration, which can also be found from (2.32), there are enough T-cells to remove tumour cells, but below this value the tumour can grow to a stable size that depends on all other parameters of the system. We note that similar behaviour is seen in the left and right panels of 2.4. This is due to

the parameters γ, A and ρ appearing as a product in the expression (2.59) for the stable tumour cell concentration, suggesting that these parameters have a functionally equivalent effect on the stable tumour cell concentration (indeed, in section 2.3.6, we quantify the sensitivity of the stable tumour cell concentration to each of these parameters, and show that they have similar impact).

A common problem with ODE models of immunology is that they require temporal data for validation - which can be hard to come by for both practical and ethical reasons. Our model is based upon immune dynamics but can be used to produce predictions not based on time as in the case with the figures discussed in this section. Concurrent measurements of MHC-I, T-cell infiltration and $CD4^+/CD8^+$ are lacking in the literature (exceptions include (136, 193)), but are examples of data which could be used to validate this model.

2.3.4 Optimal helper/cytotoxic ratio

Another feature of this model is the ability to predict an optimal helper/cytotoxic ratio R. Here we define optimal to mean yielding the lowest stable tumour size when equation (2.54) equilibrates to the fixed point $c = c^*$. We parameterised the system such that the fixed point $c = c^*$ was always stable and considered the numerical solution for the stable tumour cell concentration, (2.29)-(2.31), for different values of R as shown in Figure 2.5. As the cytotoxic T-cell pool decreases the tumour cell concentration increases, as expected. However, if there are not enough helper cells to activate the cytotoxic pop-

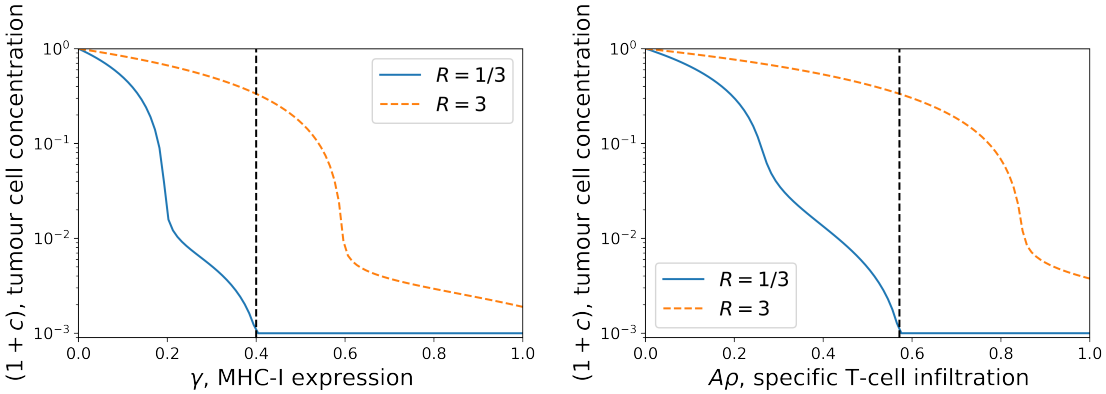

a) **b)**

Figure 2.4: Stable tumour cell concentration, c, against MHC-I expression, γ, in (**a**) and against specific tumour T-cell infiltration, $A\rho$, in (**b**), displayed for two different helper/cytotoxic T-cell ratios, R. To plot this on a logarithmically scaled y-axis, we have plotted $(1+c)/\rho_c$. Here the tumour replication rate is $r = 0.15$, the activation noise is $\beta^{-1} = 1$, T-cell density is $\rho = 1$, the specificity in (**a**) is set to $A = 1$, the MHC-I expression in (**b**) is $\gamma = 0.7$, and the carrying capacity is set to $\rho_c = 1000$. The dashed vertical line indicates, for the case $R = 1/3$, the critical value, predicted by equation (2.32), where the stable tumour cell concentration in the long time limit becomes non-zero.

ulation, the tumour reaches a large size, corresponding to the peak around $R = 0$. Note that even in absence of helper T-cells, cytotoxic T-cells may still activate at finite noise levels (corresponding to activation via pathways independent of helper cells.) This explains why at $R = 0$ the tumour cell concentration is still below the carrying capacity ρ_c in Figure 2.5. An interesting feature of this model is that it shows that there is a range of values of R for which the tumour size is relatively small. This suggests that the immune system is robust to changes in the helper/cytotoxic ratio. While we consider this parameter fixed in our model, in principle it is a dynamic quantity. If the helper/cytotoxic ratio varied dynamically within this region of of parameter space, the variation in the stable tumour cell concentration would be negligible.

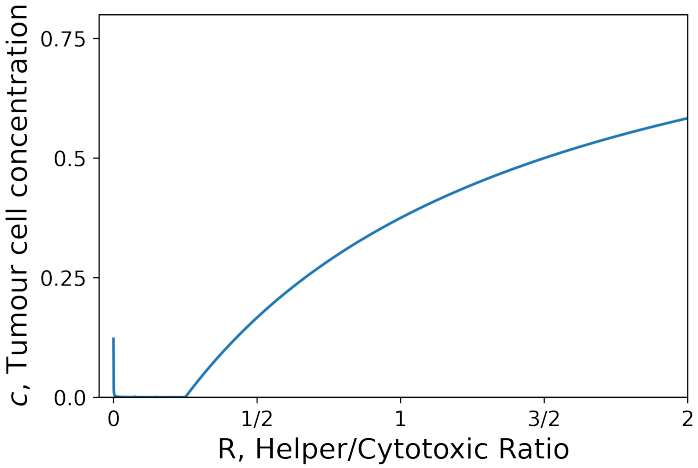

Figure 2.5: Cell concentration of a tumour which has escaped plotted as a function of the helper/cytotoxic T-cell ratio R for $\beta = 100$, $r = 0.8$, $A = \gamma = \rho = 1$, $\rho_c = 1000$. The tumour cell concentration has been normalised with the carrying capacity ρ_c.

2.3.5 Time variation of MHC-I expression

In our model we have treated the expression of MHC-I, γ, as a constant, however in principle it should evolve with time, $\gamma = \gamma(t)$. As the tumour progresses, tumour cells with low expression of MHC-I will evade the immune response and will have an advantage over tumour cells that have high MHC-I expression. This selective pressure means that the MHC-I expression in the bulk tumour will decrease over time. Analytical progress with time dependent MHC-I expression $\gamma(t)$ is difficult, so to achieve this we reduce our system of equations by assuming *all* T-cells are active i.e $a = A\rho/2$ and $m = \epsilon A\rho/2$. By fixing a and m to their maximum physical values, the system of equations reduces to a single equation for the tumour cell concentration,

$$\frac{\mathrm{d}c}{\mathrm{d}t} = \left[r - \bar{A}\gamma(t) - \frac{rc}{\rho_c} \right] c, \tag{2.65}$$

with

$$\bar{A} = \frac{A\rho(1-\epsilon)}{2}. \tag{2.66}$$

We refer to this limit as a "best-case" scenario, since if a and m are allowed to vary below their maximum value, the tumour concentration will be higher than if locked at their maximum value. The solution of the above equation, which we discuss in 2.C, is given by

$$c(t) = \frac{c_0\rho_c \mathrm{e}^{\int_0^t (r-\bar{A}\gamma(s))ds}}{\rho_c + c_0 r \int_0^t \mathrm{e}^{\int_0^s (r-\bar{A}\gamma(s'))ds'}ds}, \tag{2.67}$$

where c_0 is the initial condition $c(t=0) = c_0$. This solution requires knowledge of $\gamma(t)$. The latter has not been studied in the literature, however, we can bound the solution for a family of $\gamma(t)$ functions if we assume that the maximum, $\gamma_{\max}$, and minimum, $\gamma_{\min}$, values of the function are known. We find the upper bound to be

$$c(t) \leq \frac{c_0\rho_c \mathrm{e}^{t(r-\bar{A}\gamma_{\min})}}{\rho_c + \frac{c_0 r}{r-\bar{A}\gamma_{\max}}\left(\mathrm{e}^{t(r-\bar{A}\gamma_{\max})} - 1\right)}. \tag{2.68}$$

The long-time behaviour of the upper bound in the above depends on $\gamma_{\min}$ as follows

$$c(\infty) \leq \begin{cases} 0, & \text{if} \quad \gamma_{\min} > \frac{r}{\bar{A}} = \gamma_c \\ \infty & \text{otherwise,} \end{cases} \tag{2.69}$$

where we have recovered that for the tumour to be eradicated as $t \to \infty$ we require that $\gamma > \gamma_c$.

A tighter bound on $c(t)$ can be found with a specific form of $\gamma(t)$. In particular, if we assume that the expression of MHC-I decays exponentially,

$$\gamma(t) = \mathrm{e}^{-\frac{t}{\tau_\gamma}} \tag{2.70}$$

where τ_γ is the timescale of MHC-I decay, the solution can be bound as follows,

$$\frac{c_0\rho_c \mathrm{e}^{\bar{A}\tau_\gamma\left(\mathrm{e}^{-\frac{t}{\tau_\gamma}}-1\right)}}{\rho_c \mathrm{e}^{-rt} + c_0\left(1-\mathrm{e}^{-rt}\right)} \leq c(t) \leq \frac{c_0\rho_c \mathrm{e}^{\bar{A}\tau_\gamma \mathrm{e}^{-\frac{t}{\tau_\gamma}}}}{\rho_c \mathrm{e}^{-rt+\bar{A}\tau_\gamma} + c_0\left(1-\mathrm{e}^{-rt}\right)} \tag{2.71}$$

where in the above we have used $\int_0^t \mathrm{e}^{rs} ds \leq \int_0^t \mathrm{e}^{rs+\tau_\gamma \bar{A}\mathrm{e}^{-\frac{s}{\tau_\gamma}}} ds \leq \int_0^t \mathrm{e}^{rs+\tau_\gamma \bar{A}} ds$. If we now consider the long-time behaviour of $c(t)$ we find that

$$\rho_c \mathrm{e}^{-\bar{A}\tau_\gamma} \leq c(\infty) \leq \rho_c. \tag{2.72}$$

The upper bound is now finite in the long time limit, and is equal to the carrying capacity concentration, as would be expected. We see that the lower bound of $c(t)$ is also finite. The latter is due to $\gamma_{\min} < \gamma_c$. Therefore, according to this model the exponential decay of MHC-I prohibits the eradication of tumours. However, it is important to stress that if the decay rate is sufficiently slow, the tumour cell concentration can become very small. All calculations have been made under the assumption that $\rho = \frac{N}{V} = \mathcal{O}(1)$. We show in the appendix that in this regime stochastic fluctuations are suppressed as $V \to \infty$.

However, for finite N, fluctuations become of the same order as the mean, and can remove a small number of tumour cells in a finite time. Additionally, as discussed in the introduction, we neglect the role of NK cells to focus on the T-cell dependent response. However, at low MHC-I the NK cells play a more dominant role, adding an additional deleterious effect upon tumour growth.

In addition to exponential decay we have also considered a sigmoidal decay by defining

$$\gamma(t) = \frac{1}{1 + \left(\frac{t}{\tau_\gamma}\right)^g}, \tag{2.73}$$

which is sigmoidal for $g > 1$ where g is the shape parameter. Furthermore, the function approaches a step function as $g \gg 1$. In the left panel of Figure 2.6 we plot the tumour concentration against time for different tumour replication rate r and functional form of MHC-I expression $\gamma(t)$. In the right panel of Figure 2.6 we plot $\gamma(t)$ for the corresponding curves in the left panel. In particular, we compare sigmoidal and exponential decay of MHC-I. Figure 2.6 shows that in the case where the tumour is initially growing at a rate faster than T-cell mediated death the behaviour changes significantly with the functional form of $\gamma(t)$. In the case of exponential MHC-I decay, the tumour cell concentration exponentially increases towards saturation. However, with a sigmoidal $\gamma(t)$, the tumour concentration increases and reaches a plateau then rapidly grows to saturation. No such difference is observed when the tumour is initially removed by the T-cells. We note that when the rate of T-cell mediated death is initially faster than the rate of replication, Figure 2.6 exhibits the "three Es" of cancer immunoediting first discussed by (194):

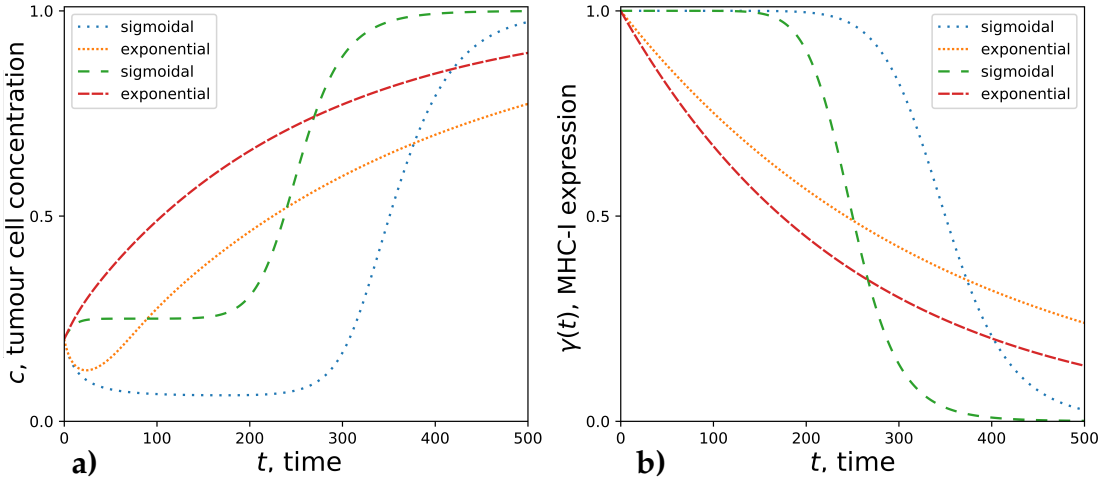

Figure 2.6: Time evolution of tumour cell concentration from numerical solution of equation (2.65) (**a**) subject to exponential and sigmoidal MHC-I decay profiles (**b**). We show results for two parameterisations: tumour replication rate $r = 0.4$, timescale of MHC-I expression decay $\tau_\gamma = 350$ (dotted lines); $r = 0.5$ and $\tau_\gamma = 200$ (dashed lines). In all cases the initial tumour cell concentration is $c_0 = 20$, $\bar{A} = 0.375$, and carrying capacity concentration $\rho_c = 100$. The shape parameter for the sigmoidal decay function is $g = 10$. The tumour cell concentration has been normalised with the carrying capacity ρ_c.

the tumour is initially eliminated, reaches a period of equilibrium, and then escapes. This qualitative behaviour was also observed in a previous model of helper/cytotoxic T-cell interactions in the anti-tumour immune response (64). Our model suggests that the profile of $\gamma(t)$ has a dominant effect on the duration of the elimination, equilibrium and escape phases of tumour progression. Experimental data revealing the longitudinal change in MHC-I expression in tumours may explain the extent that MHC-I plays in tumour equilibrium and escape.

2.3.6 Sobol Sensitivity Analysis

One may ask how sensitive our results are to the specific choice of parameters of our model. In our model the tumour cell concentration is a non-linear

function of 12 parameters. As a consequence of this it is difficult to understand the impact each parameter has on the tumour cell concentration. To better understand the sensitivity of our findings to choices of parameters, we perform a global stability analysis. In doing so, we shall vary several parameters concurrently, and deduce the impact that individual parameters, and the interaction between parameters, has on the output of our model. In particular we will perform a Sobol sensitivity analysis (195, 196, 197).

A Sobol sensitivity analysis assumes that the output of some model may be expressed as $Y = f(x_1, \ldots, x_p)$ where Y is some scalar output of the model that we are interested in, and $x_1, \ldots x_p$ are the p parameters of the model. The variance in the model output is defined as,

$$V(Y) = \int_P f^2(x_1, \ldots, x_p) \mathrm{d}x_1, \ldots, \mathrm{d}x_p - \int_P f(x_1, \ldots, x_p) \mathrm{d}x_1, \ldots, \mathrm{d}x_p \quad (2.74)$$

where P is the parameter space that defines the values that each of the parameters may take. In Sobol analysis, the function is decomposed into functions of different combinations of parameters,

$$f(x_1, \ldots, x_p) = f_0 + \sum_{i=1}^{p} f_i(x_i) + \sum_{i=1}^{p} \sum_{j=i+1}^{p} f_{ij}(x_i, x_j) + \cdots + f_{1,\ldots,p}(x_1, \ldots, x_p). \quad (2.75)$$

As a result of this, it is possible to represent the variance in the model output as a summation of variances associated with changes in individual parameters, and combinations of different parameters. We may define the contribu-

tion to the model variance from a set of parameters $\{x_{i_1}, \ldots, x_{i_n}\}$ as,

$$V_{i_1,\ldots,i_n} = \int_{P_n} f^2_{i_1,\ldots,i_n}(x_{i_1}, \ldots, x_{i_n}) \mathrm{d}x_{i_i} \ldots \mathrm{d}x_{i_n}, \tag{2.76}$$

where P_n is the parameter space that defines the range of values parameters $\{x_{i_1}, \ldots, x_{i_n}\}$ may take. The total variance is then given by,

$$V(Y) = \sum_{i=1}^{p} V_i(Y) + \sum_{i=1}^{p} \sum_{j=i+1}^{p} V_{i,j} + \cdots + V_{1,\ldots,p}. \tag{2.77}$$

To measure the contribution of a parameter, or a set of parameters, to the variance in the model output, one may compute the the Sobol indices. The first order Sobol indices are given by,

$$S_i = \frac{V_i}{V(Y)} \tag{2.78}$$

which is a measure of the contribution of an individual parameter x_i to the overall variance in the model output. Similarly, second order Sobol indices are defined,

$$S_{ij} = \frac{V_{ij}}{V(Y)} \tag{2.79}$$

which tells us how the interaction between parameters x_i and x_j contribute to the overall variance in Y. In general, the n^{th} Sobol index is given by,

$$S_{i_1,\ldots i_n} = \frac{V_{i_1,\ldots,i_n}}{V(Y)}. \tag{2.80}$$

The total Sobol index of parameter x_i is defined as the sum of all Sobol indices involving parameter x_i,

$$ST_i = S_i + \sum_{j \neq i} S_{ij} + \ldots S_{1,\ldots,p}. \tag{2.81}$$

Carrying out a Sobol sensitivity analysis requires computing the multiple integrals in equation (2.76) over the parameter space we wish to assess the model output variance. For complex models, this is typically intractable analytically, and one must resort to numerical methods. Practically, this can be computationally expensive, especially for models with many parameters that may take a wide range of values. In our case we used the Python package SALib to compute the Sobol indices in our sensitivity analysis (198). This package solves these integrals using Monte Carlo methods, where the integrand is approximated as the sum of the integrand evaluated at random points in the parameter space considered. The accuracy of such methods will increase with the number of Monte Carlo samples, and typically high-dimensional integrands require many samples for accurate approximations.

To perform the sensitivity analysis, we must first pick the output of our model, the variance of which we will measure with respect to the model parameters. We choose the stable tumour cell concentration in the long time limit as our model output, as it has been the focus of the preceding sections, such that the sensitivity analysis will tell us how robust the results in the preceding section are to uncertainty in the parameter values. In Figure 2.7 we show the first order and total Sobol indices for each of the parameters in our

model. In this analysis we kept the carrying capacity $\rho_c = 1000$, as this will set the scale of the stable tumour cell concentration we are considering, and will keep different parameterisations comparable. Of the 11 parameters we vary there are 5 with relatively high first order Sobol indices; namely, the tumour replication rate, r, the expression of MHC-I, γ, the fraction of helper/cytotoxic T-cells, ϵ, the specificity of T-cells, A, and the density of T-cells, ρ. The tumour replication rate, r, contributes to over 50% of the variance in the tumour cell concentration. Additionally, we see that for each of these parameters, the total Sobol index is higher than the first order, an indication that higher order interactions between parameters may be important. However, higher order Sobol indices were found to be small relative to their first order counterparts. Hence, it is the direct influence of individual parameters, and not their interactions, that plays the greatest role in the variance of the stable tumour cell concentration. From this we identify the set of parameters $(r, \gamma, \epsilon, A, \rho)$ as the most influential on the stable tumour cell concentration, and uncertainty in the other parameters of our model will not affect the qualitative results of the preceding section.

However, to further evaluate which set of parameters is the most influential on the variance in the stable tumour cell concentration, we performed a test that evaluates our model across 3 independent sets of parameter values sampled via the Sobol sequence as proposed in (199). From the Sobol analysis above, we rank the parameters according to their total Sobol index. We then draw 3 sets of samples of parameters. In the first set, Set 1, we draw 1000 samples of each of the 11 parameters. In the second set, Set 2, we draw 1000 parameters, but set the n parameters with highest total Sobol index in

our original analysis, to be equal to the values drawn in Set 1. In Set 3, we draw 1000 parameters and set the $11 - n$ parameters with lowest total Sobol index to be equal to their values in Set 1. We then assess the correlation between the stable tumour cell concentration that is generated by these 3 sets of parameter groups, for different values of n. In principle, if $n = 11$, then the correlation between Set 1 and Set 2 should be 1, and Set 1 and Set 3 exactly 0. The correlations between Set 1, Set 2 and Set 3, for different values of n, are shown in Table 2.1. We see that as we increase the number of parameters of influence, n, the correlation between Set 1 and Set 2 increases, but the difference is negligible between $n = 5$ and $n = 6$. Furthermore, the correlation between Set 1 and Set 3 decreases with increasing n, and the change is also negligible between $n = 5$ and $n = 6$. This suggests that according to the Sobol analysis of our model, the uncertainty in the tumour cell concentration is well described by a set of $n = 5$ influential parameters; namely, r, γ, A, ϵ and ρ. This gives us greater confidence in the results of the previous sections. In particular, it suggests our choice to set $\phi = 0$ will not significantly alter the qualitative nature of our results.

2.4 Discussion

The complexities of tumour immunology require a systemic approach to better understand cancer and inform treatment. Quantitative tools are being used to a greater extent, due to the vast data produced by next generation experimental technology; mathematical modelling being among them. Mathematical modelling can suffer from two extremes: models that include detail

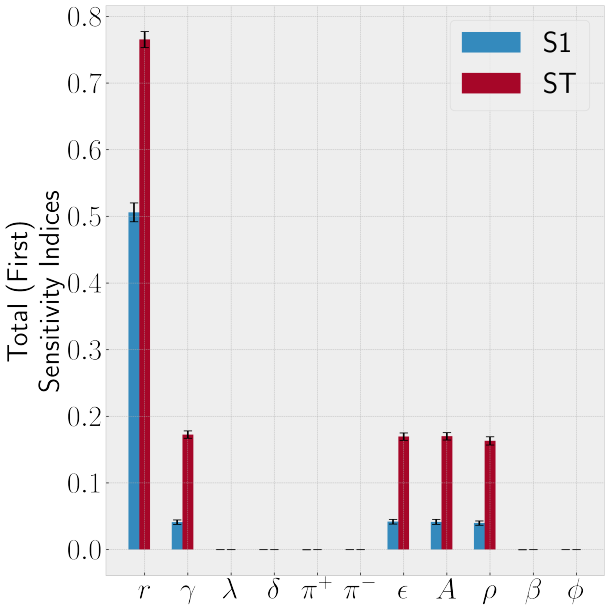

Figure 2.7: Total and first Sobol indices for each parameter in a global sensitivity analysis. Model output is the tumour cell concentration at the fixed point of the system of equations (2.26), and the Sobol indices describe the first order and total contribution to the variance in the model output. 10^5 random samples of parameters were taken, uniformly, from the following range of parameters: $r \in [0.01, 2]$, $\pi^{\pm} \in [0.01, 1]$, $\lambda \in [0.01, 2]$, $\delta \in [0.01, 2]$, $A \in [0, 1]$, $\epsilon \in [0, 1]$, $\rho \in [0.01, 1]$, $\beta \in [10^{-3}, 10^2]$, $\phi \in [-1, 1]$. Carrying capacity for the tumour cell concentration was fixed to $\rho_c = 1000$ in order to keep the model with different parameterisations comparable.

Table 2.1: Pearson correlation coefficient between the stable tumour cell concentration for different sets of parameters. In Set 1, all parameters are sampled uniformly from a range of parameters specified in the caption of Figure 2.7. Set 2 is a new set of parameters independently drawn from the same range of parameter values, but the n parameters with highest total variance in the Sobol analysis conducted to produce Figure 2.7 are set identical to that in Set 1. Set 3, is another independent set of parameters, but the lowest $11 - n$ parameters are set to be equal to Set 1.

n	Set 1 vs Set 2	Set 1 vs Set 3
2	0.628	0.306
3	0.662	0.333
4	0.774	0.330
5	1.000	0.147
6	1.000	0.147

at the molecular level tend to focus on a small set of processes to achieve analytical results at the expense of a systemic view; on the other hand, macroscopic models which achieve greater systemic resolution, tend to have a large number of parameters, which makes statistical validation impractical, especially in absence of large data sets. In our work we used statistical mechanics and dynamical systems approaches to analyse the anti-tumour response of a simplified model of the adaptive immune system, comprising antigen presenting cells, helper T-cells and cytotoxic T-cells. The end result is a system of five ODEs that highlights the role in tumour growth of different parameters linked to key cellular processes.

Previously, it has been shown empirically that the prognostic value of the $CD4^+/CD8^+$ ratio, and the expression of MHC-I, are improved when considered in combination (136). Our work provides a simple model for the mechanistic interplay between these two parameters during the anti-tumour immune response, from which apparent contradictions in the literature can be rationalised. In particular, our model suggests that, when using the $CD4^+/CD8^+$ ratio as a prognostic marker, the expression of MHC-I must also be taken into account, due to its interplay with the helper/cytotoxic T-cell ratio, otherwise this may risk incorrect prognosis. A good prognosis of clinical outcome has been associated with different $CD4^+/CD8^+$ ratios across different cancers, and this model suggests that this is due to variations in MHC-I expression. If proved correct this could help to potentially unify efforts across different cancers, something that can rarely be achieved. Our model also highlights that the infiltration of specific T-cells is an important parameter, that will also affect the growth of a tumour and could potentially obfuscate the prognos-

tic value of $CD4^+/CD8^+$ and MHC-I. Recent work has shown that the TCR repertoire of tumour infiltrating T-cells has low tumour reactivity (134). Our model highlights the dramatic effect such a small pool of specific T-cells can have on the prognostic value of $CD4^+/CD8^+$ and MHC-I. Encouragingly, the model shows that the adaptive immune response is robust to changes in the helper/cytotoxic ratio, as one would hope.

Our work has focused on modelling the immune response where MHC-I expression is assumed to be constant to highlight its interplay with the helper/cytotoxic ratio R. However, we have shown the role that MHC-I decay can play in the evolution of tumours. The eradication of tumours will depend on the minimum expression of MHC-I - if this is too low the T-cell response will fail and other cells, most likely NK, are required for eradication, otherwise the tumour will escape. In addition to this, our work highlights the role that the profile of MHC-I decay can have on the growth of tumours. To the best of our knowledge, there is no data measuring the time evolution of MHC-I expression in tumours to be able to estimate this profile. However, availability of such data could confirm whether the variation in MHC-I expression leads to periods of equilibrium in tumour growth.

One issue with mathematical models is that they often focus on the dynamics of immune cells, for which experimental data is rare. Although our model is based on dynamics, we have provided results which focus on non-temporal quantities that could be verified with standard measurements in immunology. We hope our model can serve as a motivation for experimental investigation into the combined effect of $CD4^+/CD8^+$ and MHC-I, and provide a useful theoretical framework to interpret results.

The work presented here is a theoretical minimal model of the adaptive immune system, and as such has limitations. For example, the model only considers the adaptive immune response and does not explicitly take into account innate immunity such as the natural killer cells and macrophages, both of which play an important role in the anti-tumour immune response. The benefit of our approach is the rigorous mathematics which can be analysed to understand qualitative behaviour, something which is often lost when considering too many parameters.

A generally applicable feature of our work is the use of non-equilibrium statistical mechanics to include an additional level of microscopic detail into the modelling of cell concentrations with ODEs. Here our model has considered the activation and sub-type of T-cells, but this framework could also be used to study other biological systems where constituent cells fluctuate stochastically between different states, while interacting with other cell concentrations in the environment. For example, there is a long history of modelling neurons as stochastic entities that fluctuate stochastically between two states, quiescent or firing an electrical signal, (for examples see (200, 201, 202, 203)). On the other hand, neurons are known to be embedded in different tissues, including muscles and the gut, where they conceivably interact with other cells, whose concentrations may follow (approximately) deterministic dynamics.

There are two potential extensions of our work we consider to be of particular interest. Firstly, as we have discussed, our work has neglected spatial heterogeneity by modelling a small macroscopic area of a tumour which can be regarded as uniform. Spatial heterogeneity plays an important role

in the anti-tumour immune response, and the extension of the techniques from non-equilibrium statistical mechanics to systems of PDEs could provide important new results although at expense of increased model complexity. Secondly, although we consider phenotypic heterogeneity implicitly when we allow MHC-I to vary with time, we have not explicitly modelled competition between tumour cell phenotypes. This model could be extended to account for several tumour phenotypes, evolving with different rates, with heterogeneity in the T-cell response to each phenotype. Although this framework is well adapted to such a scenario, analytical progress with multiple phenotypes may provide an interesting avenue of investigation, elucidating the evolutionary game between phenotypes. Another extension would be to adapt this model to understand how tumours begin in the first place, including the healthy tissue cells from which the tumour cells derive. Tumour immunology is rich with complexity and bringing refined tools from statistical mechanics may shed light on this complex system of processes.

Appendices

2.A Kramers-Moyal expansion of the master equation

In this section, we derive a master equation for the probability $\mathrm{P}_t(\boldsymbol{\sigma})$ to observe a T-cell configuration $\boldsymbol{\sigma} \in \{0,1\}^N$ at time t, from the stochastic update rule (2.14) and we will use it to derive equations for the time evolution of the macroscopic variables $a(\boldsymbol{\sigma})$ and $m(\boldsymbol{\sigma})$. Denoting by $\mathcal{P}(x) = \int_{-\infty}^{x} dz\, \mathrm{P}(z)$ the cumulative distribution function of the noise distribution $\mathrm{P}(z)$, the likelihood to observe configuration σ_i at time $t + \Delta$, given the T-cell configuration $\boldsymbol{\sigma}'$ at the earlier time step t, is, for any symmetric distribution $\mathrm{P}(z) = \mathrm{P}(-z)$,

$$\mathrm{P}(\sigma_i, t+\Delta|\boldsymbol{\sigma}', t) = \mathcal{P}(z \leq (2\sigma_i - 1)\beta \left(\eta_i \xi_i p(t) + (1-\eta_i)\xi_i c(t) m(\boldsymbol{\sigma}') - \phi(t)\right). \tag{2.82}$$

For the Glauber choice $\mathcal{P}(x) = \frac{1}{2}(1 + \tanh\frac{x}{2})$, the probability that T-cell i changes, in a single time step, its state at time t is

$$W_i^t(\sigma) = \mathrm{P}_t(F_i\sigma|\sigma) = \frac{1}{2}\left(1 + (2\sigma_i - 1)\tanh\left(\frac{\beta h_i(t,\sigma)}{2}\right)\right) \tag{2.83}$$

where we have defined the 'flip' operator F_i such that $F_i\sigma = (\sigma_1, ..., 1 - \sigma_i, ..., \sigma_N)$ and $h_i(t,\sigma) = \eta_i\xi_i p(t) + (1 - \eta_i)\xi_i c(t)m(\sigma) - \phi(t)$. Assuming that the update of T-cells is sequential, i.e. at each time step one T-cell i, drawn at random, is updated with likelihood $W_i^t(\sigma)$, one obtains, for $\Delta = 1/N$ and N large, the following master equation

$$\partial_t \mathrm{P}_t(\sigma) = \sum_i \left[\mathrm{P}_t(F_i\sigma)W_i^t(F_i\sigma) - \mathrm{P}_t(\sigma)W_i^t(\sigma)\right]. \tag{2.84}$$

From the master equation, the time evolution of the macroscopic variables can be retrieved using the Kramers-Moyal (KM) expansion. To perform this expansion we note that we can define the time-dependent probability distribution of the macroscopic variables as

$$\mathrm{P}_t(a,m) = \sum_\sigma \mathrm{P}_t(\sigma)\delta(a - a(\sigma))\delta(m - m(\sigma)) \tag{2.85}$$

from which the master equation tells us,

$$\partial_t \mathrm{P}_t(a,m) = \sum_\sigma \delta(a - a(\sigma))\delta(m - m(\sigma))\left[\mathrm{P}_t(F_i\sigma)W_i^t(F_i\sigma) - \mathrm{P}_t(\sigma)W_i^t(\sigma)\right]. \tag{2.86}$$

Defining $\mathbf{\Omega}(\sigma) = (m(\sigma), a(\sigma))$ and relabelling the first term in our sum with $F_i\sigma \to \sigma$ we have

$$\partial_t \mathrm{P}(\mathbf{\Omega}) = \sum_{\sigma} \mathrm{P}_t(\sigma) W_i^t(\sigma) \left[\delta(\mathbf{\Omega} - \mathbf{\Omega}(F_i\sigma)) - \delta(\mathbf{\Omega} - \mathbf{\Omega}(\sigma))\right]. \tag{2.87}$$

We now define the change in the macroscopic parameter $\Omega_\mu(\sigma)$ (where $\Omega_0(\sigma) = m(\sigma)$ and $\Omega_1(\sigma) = a(\sigma)$) caused by a flip in a single T-cell i as $\Delta_{i\mu}(\sigma) = \Omega_\mu(F_i\sigma) - \Omega_\mu(\sigma)$ such that $\Delta_{i0}(\sigma) = m(F_i\sigma) - m(\sigma) = \frac{1}{V}(1 - 2\sigma_i)\eta_i\xi_i$ and $\Delta_{i1}(\sigma) = a(F_i\sigma) - a(\sigma) = \frac{1}{V}(1 - 2\sigma_i)\xi_i$. The KM expansion can then be carried out in powers of $\Delta_{i\mu}(\sigma)$,

$$\partial_t \mathrm{P}(\mathbf{\Omega}) = \sum_i \sum_{\sigma} W_i^t(\sigma)\mathrm{P}_t(\sigma)\Big[-\sum_{\mu} \frac{\partial^2}{\partial\Omega_\mu} \delta\left[\mathbf{\Omega} - \mathbf{\Omega}(\sigma)\right] \Delta_{i\mu}(\sigma) + \frac{1}{2}\sum_{\mu\nu} \frac{\partial^2}{\partial\Omega_\mu\partial\Omega_\nu} \delta\left[\mathbf{\Omega} - \mathbf{\Omega}(\sigma)\right] \Delta_{i\mu}(\sigma)\Delta_{i\nu}(\sigma) + ...\Big]. \tag{2.88}$$

A special case where the dynamical equations close is found when $\sum_i W_i^t(\sigma)\Delta_{i\mu}(\sigma) = F_\mu^t(\mathbf{\Omega}(\sigma), ...)$, where F_μ^t is some function that depends on the microscopic variable σ, through the macroscopic variables only, $\mathbf{\Omega}(\sigma)$. To

this end we evaluate $\sum_i W_i^t(\boldsymbol{\sigma})\Delta_{i\mu}(\boldsymbol{\sigma})$ for the cases $\mu = 0, 1$,

$$\sum_i W_i^t(\boldsymbol{\sigma})\Delta_{i0}(\boldsymbol{\sigma}) = \sum_i \frac{1}{2}\left(1 + (1-2\sigma_i)\tanh\left(\frac{\beta h_i(t,\boldsymbol{\sigma})}{2}\right)\right)\frac{1}{V}(1-2\sigma_i)\eta_i\xi_i \tag{2.89}$$

$$= -m(\boldsymbol{\sigma}) + \frac{1}{2V}\sum_i \eta_i\xi_i \tag{2.90}$$

$$+ \frac{1}{2V}\sum_i \eta_i\xi_i \tanh\left(\frac{\beta}{2}\left(\eta_i\xi_i p(t) + (1-\eta_i)\xi_i c(t) m(\boldsymbol{\sigma}) - \phi(t)\right)\right) \tag{2.91}$$

$$= F_0^t(\boldsymbol{\Omega}(\boldsymbol{\sigma}), \boldsymbol{c}) \tag{2.92}$$

and similarly,

$$\sum_i W_i^t(\boldsymbol{\sigma})\Delta_{i1}(\boldsymbol{\sigma}) = \sum_i \frac{1}{2}\left(1 + (1-2\sigma_i)\tanh\left(\frac{\beta h_i}{2}\right)\right)\frac{1}{V}(1-2\sigma_i)\xi_i \tag{2.93}$$

$$= -a(\boldsymbol{\sigma}) + \frac{1}{2V}\sum_i \xi_i \tag{2.94}$$

$$+ \frac{1}{2V}\sum_i \xi_i \tanh\left(\frac{\beta}{2}\left(\eta_i\xi_i p(t) + (1-\eta_i)\xi_i c(t) m(\boldsymbol{\sigma}) - \phi(t)\right)\right) \tag{2.95}$$

$$= F_1^t(\boldsymbol{\Omega}(\boldsymbol{\sigma}), \boldsymbol{c}) \tag{2.96}$$

where we have denoted $\boldsymbol{c} = (c, b, p)$ and note that from equations (2.15)-(2.17), $\boldsymbol{c}$ only depends on $\boldsymbol{\sigma}$ through $\boldsymbol{\Omega}(\boldsymbol{\sigma})$. Indeed, it is the case that

$$\sum_i W_i^t(\boldsymbol{\sigma})\Delta_{i\mu}(\boldsymbol{\sigma}) = F_\mu^t(\boldsymbol{\Omega}(\boldsymbol{\sigma}), \boldsymbol{c}) \tag{2.97}$$

with no explicit dependence on $\boldsymbol{\sigma}$. By substituting equation (2.97) into (2.88)

the sum over σ can be taken; this constrains the macroscopic variable to its average $\Omega_\mu(\sigma) = \sum_\sigma \mathrm{P}_t(\sigma)\Omega_\mu(\sigma) = \Omega_\mu(t)$ and yields,

$$\partial_t \mathrm{P}_t(\mathbf{\Omega}) = -\sum_{\mu=0}^{1} \frac{\partial}{\partial \Omega_\mu} \left[\mathrm{P}(\mathbf{\Omega}) F_\mu^t(\mathbf{\Omega}, \boldsymbol{c})\right] + ... \tag{2.98}$$

Higher order terms in the KM expansion are shown to be proportional to V^{-d}, where $d \geq 1$, and are therefore negligible in the limit that V is large. Equation (2.98) in this limit reduces to the Liouville equation

$$\frac{\mathrm{d}\mathbf{\Omega}}{\mathrm{d}t} = \mathbf{F}^t(\mathbf{\Omega}, \boldsymbol{c}) \tag{2.99}$$

which is otherwise written,

$$\frac{\mathrm{d}m}{\mathrm{d}t} = -m + \frac{1}{2V}\sum_i \eta_i \xi_i \left(1 + \tanh\left(\frac{\beta}{2}\left(\eta_i \xi_i p + (1-\eta_i)\xi_i c m - \phi(t)\right)\right)\right) \tag{2.100}$$

$$\frac{\mathrm{d}a}{\mathrm{d}t} = -a + \frac{1}{2V}\sum_i \xi_i \left[1 + \tanh\left(\frac{\beta}{2}\left(\eta_i \xi_i p + (1-\eta_i)\xi_i c m - \phi(t)\right)\right)\right]. \tag{2.101}$$

To simplify these equations further, we make use of the empirical joint distribution of η and ξ,

$$\mathrm{P}(\eta, \xi) \hat{=} \frac{1}{N}\sum_j \delta_{\eta,\eta_j}\delta_{\xi,\xi_j} \tag{2.102}$$

with averages over this distribution then defined as

$$\langle ... \rangle_{\eta,\xi} = \sum_{\eta,\xi} ... \mathrm{P}(\eta, \xi). \tag{2.103}$$

The macroscopic dynamics are then summarised by the following ODEs,

$$\frac{\mathrm{d}m}{\mathrm{d}t} = -m + \frac{\rho}{2}\left\langle \eta\xi\left[1+\tanh\left(\frac{\beta}{2}\left(\eta\xi p + (1-\eta)\xi c m - \phi(t)\right)\right)\right]\right\rangle_{\eta,\xi} \quad (2.104)$$

$$\frac{\mathrm{d}a}{\mathrm{d}t} = -a + \frac{\rho}{2}\left\langle \xi\left[1+\tanh\left(\frac{\beta}{2}\left(\eta\xi p + (1-\eta)\xi c m - \phi(t)\right)\right)\right]\right\rangle_{\eta,\xi}. \quad (2.105)$$

This corresponds to a mean-field description of the evolution of the stochastic variables $\Omega_\mu(\sigma)$. For large but finite values of V, $\Omega_\mu(\sigma)$ will fluctuate about its mean value $\Omega_\mu = \left\langle \Omega_\mu(\sigma)\right\rangle_\sigma$ with fluctuations of order $\sqrt{\Delta_{i\mu}} = \mathcal{O}(V^{-\frac{1}{2}})$.

2.B Fixed points under the assumption of slow T-cell activation

In section 2.3.2 we evaluated the system of equations (2.26) under the assumption that $\tau_c \gg \tau_p$, deriving equations (2.41)-(2.43), and then studied this reduced system of equations under the assumption that $\frac{1}{\tau_c} \to 0$, such that in our model tumour cell concentration evolves at a slower rate than T-cell activation. In doing so, we derive expressions for the fixed points of a reduced system of equations. Here we show that the fixed points of the system are identical if we assume that $\tau_c \to 0$, such that tumour cell concentration evolves much faster than T-cell activation.

We can, again, study the solution to this system of equations (2.41)-(2.43) under the assumption that $\tau_c \to 0$ via singular perturbation theory. Note that now τ_c is our small parameter, as oppose to $\frac{1}{\tau_c}$ which we considered in section 2.3.2. The "outer" solution in this case assumes that $t = \mathcal{O}(1)$ and is found

by sending $\tau_c \to 0$, such that from equation (2.41) $\tau_c \frac{\mathrm{d}c}{\mathrm{d}t} = 0$ and we have that the tumour cell concentration will reach one of its nullclines,

$$c = 0 \tag{2.106}$$

$$c = \rho_c \left[1 - \frac{\gamma}{r}(a - m)\right] \tag{2.107}$$

and the system of equations is reduced to,

$$\frac{\mathrm{d}m}{\mathrm{d}t} = -m + \frac{\epsilon A \rho}{2}\left[1 + \tanh\left(\frac{\beta}{2}p\right)\right] \tag{2.108}$$

$$\frac{\mathrm{d}a}{\mathrm{d}t} = -a + \frac{A\rho}{2}\left[1 + \epsilon \tanh\left(\frac{\beta}{2}p\right) + (1-\epsilon)\tanh\left(\frac{\beta}{2}cm\right)\right]. \tag{2.109}$$

with $p = \frac{\pi^+ \lambda m c}{\pi^- \delta}$.

The inner solution is found by rescaling time such that $t = \tau\tau_c$, assuming $\tau = \mathcal{O}(1)$ (i.e. $t = \mathcal{O}(\frac{1}{\tau_c})$), and sending $\tau_c \to 0$. After rescaling time, equations (2.41)-(2.43) become,

$$\frac{\mathrm{d}c}{\mathrm{d}\tau} = \left[\tilde{r} - \tilde{\gamma}(a - m) - \frac{\tilde{r}c}{\rho_c}\right] c \tag{2.110}$$

$$\frac{\mathrm{d}m}{\mathrm{d}\tau} = \tau_c \left(-m + \frac{\epsilon A \rho}{2}\left[1 + \tanh\left(\frac{\beta}{2}p\right)\right]\right) \tag{2.111}$$

$$\frac{\mathrm{d}a}{\mathrm{d}\tau} = \tau_c \left(-a + \frac{A\rho}{2}\left[1 + \epsilon \tanh\left(\frac{\beta}{2}p\right) + (1-\epsilon)\tanh\left(\frac{\beta}{2}cm\right)\right]\right). \tag{2.112}$$

We find that by sending $\tau_c \to 0$, m and a are set to their initial conditions,

$$\frac{\mathrm{d}m}{\mathrm{d}\tau} = 0 \implies m = m(\tau = 0) = m_0 \tag{2.113}$$

$$\frac{\mathrm{d}a}{\mathrm{d}\tau} = 0 \implies a = a(\tau = 0) = a_0. \tag{2.114}$$

Hence, by substituting m_0 and a_0 into equation (2.110) we find that the inner solution is given by

$$\frac{\mathrm{d}c}{\mathrm{d}\tau} = \left[\tilde{r} - \tilde{\gamma}(a_0 - m_0) - \frac{\tilde{r}c}{\rho_c}\right] c. \tag{2.115}$$

If we send $t \to 0$ in the outer solution and $\tau \to \infty$ in the inner solution, we find in both cases that,

$$m = m_0 \tag{2.116}$$

$$a = a_0 \tag{2.117}$$

and

$$c\left[\tilde{r} - \tilde{\gamma}(a_0 - m_0) - \frac{\tilde{r}c}{\rho_c}\right] = 0. \tag{2.118}$$

Hence, the outer and inner solutions match in the expected limits.

As we are interested in the long-time dynamics of our system, we consider the outer solution in the limit $t \to \infty$. In this limit m and a approach the fixed point of equations (2.108) and (2.109) given by equations (2.52) and (2.51), respectively. What remains is to determine which of the two nullclines of c, equations (2.106) and (2.107), is stable. To do so, we assume that m and a have reached the fixed points, given by equations (2.52) and (2.51), and substitute

them into equation (2.41),

$$\frac{\mathrm{d}c}{\mathrm{d}\tau} = \left[\tilde{r} - \frac{\tilde{\gamma}A\rho}{2}(1-\epsilon)\left[1+\tanh\left(\beta c F^{-1}(c)/2\right)\right] - \frac{\tilde{r}c}{\rho_c}\right]c, \tag{2.119}$$

where we have used $t = \tau\tau_c$, such that we are considering the fast evolution of c when a and m are approaching the fixed point. This equation is identical to equation (2.54), the evolution of tumour cell concentration when we considered $\tau_c \gg 1$. This implies that for both $\tau_c \gg 1$ and $\tau_c \ll 1$, the fixed points of the system are the same, and share the same stability criteria. The transient behaviour, however, will differ as shown by the differences in the inner solution when considering either $\tau_c \to 0$ or $\frac{1}{\tau_c} \to 0$.

2.C Solution for time-dependent MHC-I expression

The solution to the equation for tumour cell concentration in the "best-case scenario" (2.65) can be found using symbolic computational software. In particular we used Mathematica, using the following line of code,

```
DSolve[{c'[t] == (r - A \[Gamma][t] - (r c[t])/rho )* c[t],
  c[0] == c0}, c[t], t]
```

which yields equation (2.67) as a solution. To verify that this is the solution, we compared the solution from Mathematica to the solution of equation (2.65) using numerical integration. In the left of Figure 2.C.1 the trajectories of $c(t)$, computed by the numerical solution of equation (2.65), and from equation (2.67), are overlapping. The right of Figure 2.C.1 shows that there is small difference between the numerical solution of equation (2.65) and equation

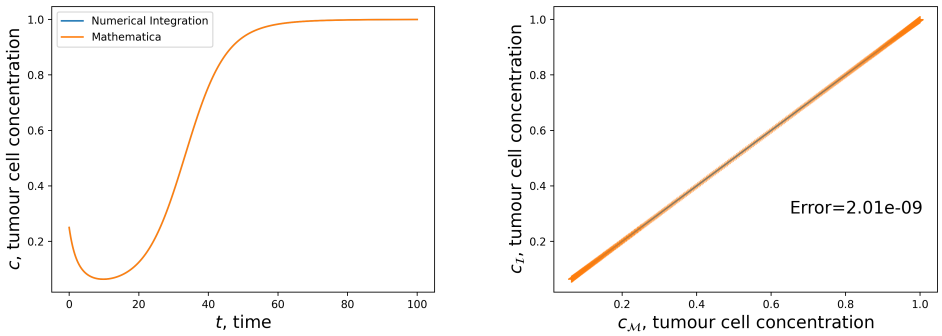

Figure 2.C.1: Left: Tumour cell concentration against time. Results are shown from the numerical solution to equation (2.65), and the symbolic solution from Mathematica (2.67). Right: For values of $t \in [0, 100]$ we plot $c(t)$ from the numerical solution of equation (2.65), $c_{\mathcal{I}}$, against the solution from Mathematica (2.67), $c_{\mathcal{M}}$. Annotation indicates mean square error. In left and right figures, parameter values are: $r = 0.2$, $\bar{A} = 0.5$, $\rho_c = 100$. MHC-I decayed according to $\gamma(t) = \mathrm{e}^{-\frac{t}{\tau_\gamma}}$ with $\tau_\gamma = 10$.

(2.67). The error between them is of the same order of magnitude as the precision of the numerical integrator used to generate this plot. This suggests that the solution provided by Mathematica is correct.

3

Herd immunity in social contact networks with heterogeneous transmission probabilities

3.1 Introduction

In the previous chapter we have shown how heterogeneity in the immune response of individuals (i.e differences in the $CD4^+/CD8^+$ T-cell ratio etc) affects tumour progression. In this chapter we study how heterogeneities in the immune response of individuals affect the collective, or *herd*, immunity of populations to infectious diseases.

The study of compartmental models, where a population is split into, for example, 'Susceptible', 'Infected' and 'Recovered' compartments in the SIR model, have formed an important theoretical and computational basis for the study of epidemics and design of vaccination campaigns. An increased understanding of contact networks, which detail physical contacts of a sustained duration between individuals in a population (see e.g. (204)), has been complemented by mathematical results for compartmental epidemic models on networks. One such contribution is the prediction of an epidemic threshold

dependent upon the rates of infection and recovery, as well as the contact network topology (66, 205, 206). Many important results concerning the SIR model on networks have been derived by message-passing approaches, also known as the cavity method, including the size and risk of epidemics on networks with arbitrary degree distributions (207) and degree correlations (208, 209). The cavity method originated in statistical physics to solve models of spin glasses (210). In brief, it is an iterative method, that considers the influence of the neighbours of a node on the state of that node. Similarly, the state of the neighbours can be analysed through the influence of its own neighbours. This reasoning can be applied iteratively, such that the cavity method derives a set of iterative equations which describe the properties of each node in the network as a function of the properties of their neighbours. A broader introduction to the cavity method can be found in Appendix A. Recently, these methods have been employed to model epidemic mitigation via contact tracing apps (80) and competing strains of infectious diseases (75, 76, 77). In addition to analytical results, the cavity method provides a set of equations that allows for an efficient *parallel* numerical implementation, as opposed to direct simulations of the SIR model, which are usually *sequential* and typically marred by long computation times, scaling with the size and connectivity of the network and the infection rate relative to the recovery rate.

One of the key problems that mathematical epidemiology has addressed is the optimisation of vaccination strategies, i.e given a finite supply of vaccines, who should be vaccinated to mitigate an epidemic. Previous work has studied vaccination strategies based upon network topology. Vaccination which prioritises nodes of higher degree, i.e. people with a high number of social

contacts, is known to lead to better outcomes in comparison with a random vaccination campaign (211). Furthermore, it has been shown that vaccination using information beyond the degree can improve upon degree-based strategies (69, 70). Recently, it has been shown that the condition for an epidemic in the SIR model is described by the eigenvalues of the Hashimoto non-backtracking matrix (212, 213, 214). For a network with M edges, this is a $M \times M$ matrix with $B_{j\to i,m\to \ell} = \delta_{j\ell}(1-\delta_{im})$ where δ_{ij} is the Kronecker delta function, such that $B_{j\to i,m\to \ell}$ is non-zero when $j = \ell$ and $m \neq i$. In other words, $B_{j\to i,m\to \ell}$ is non-zero when the edges $j \to i, m \to \ell$ describe a path that goes from m to ℓ but does not then return to m. The eigenvalues of this matrix have been used to rank nodes for prioritisation of vaccination (71). The efficacy of strategies initially explored on static networks, have also been studied on temporal networks, which account for the time-varying nature of social contacts (215). The benefit of modelling such strategies is that they provide principles upon which vaccination campaigns can be based with only partial knowledge of the contact network. For example, it can provide theoretical insight into prioritising vaccination for parts of the population with higher than average social connectivity. More generally, finding an optimal vaccination strategy is difficult, but has been studied in the context of ODE epidemic models using methods from control theory (216, 217).

Vaccination is usually modelled by placing an individual into a separate vaccinated compartment, such that vaccinated nodes block incoming infections, so that if enough people are vaccinated the infection can no longer spread through the population, a phenomena referred to as herd immunity. This assumes that a vaccine provides full protection against transmission of an

infectious disease for any individual. In general, it may be desirable to relax this assumption. For example, although the efficacy of a vaccine in preventing symptoms is ascertained before approval for public use, it is more difficult to determine how a given vaccine prevents transmission until data is collected during or after vaccine roll-out. In this case, it may be desirable to assume that vaccination reduces the transmissibility of an individual to a small but finite value. Furthermore, it is also important to recognise that vaccines are usually given to priority groups first, such as people with underlying health conditions, medical staff, or people above a certain age. Due to the correlated nature of social contacts (218, 219), prioritising vaccinations may lead to correlations between the vaccinated status of a node and its topological properties. Indeed recent work has explored vaccination strategies with an age-structured variant of the SIR model, with a separate S/I/R compartment for each (discrete) age group, with different rates of transmission from one age group to another to account for different levels of social mixing between them (220). Variation in the transmissibility of *individuals* has been explored in previous works (66, 81, 221, 222), however, analytical results have been restricted to the average risk or size of the epidemic. It has previously been shown that there is high variability in the risk of individual nodes, due to differences in the node environment (214, 223), which is neglected when only considering the average risk. In our work, we show that this variability is more prominent when transmissibility varies between individuals and focus on how this impacts the distribution of risk.

After reviewing the cavity approach to vaccination that eliminates transmission, we focus our study on vaccination with partial transmission by ex-

tending the cavity approach to allow for *heterogeneity* in the transmission between individuals. At first we consider transmissibility and degree to be uncorrelated, and we derive the herd immunity threshold in this scenario, showing that vaccination with partial transmission will always require a greater proportion of the population vaccinated to achieve herd immunity. We then relax the assumption that transmissibility and degree are uncorrelated to show how these correlations affect epidemic risk. Using this framework, we then study the impact of social distancing between groups of different transmissibility, by deriving equations for the risk of an epidemic under link percolation, where we consider the effect of removing links from the network at random. In particular, we consider link percolation that targets either links between nodes of high transmissibility, or nodes of high degree. To go beyond the average risk of an epidemic, we follow techniques that were recently developed to analyse the distribution of node properties in large networks using the cavity method (223). In particular, we extend these methods to investigate the distribution of risk in networks with strong degree correlations and heterogeneous transmissibility of individuals. Our analysis reveals a highly non-trivial distribution of risk, even amongst nodes of the same degree and transmissability. Finally, we extend the cavity approach for the distributional equations of risk to account for node and link deletion. We comment that this provides a succinct procedure to explore the impact of targeted vaccination and social distancing strategies on the distribution of risk.

The remaining sections of this chapter are organised as follows. In Sec. 3.2 we review the cavity approach to the study of the steady state reached in the SIR model on networks with arbitrary degree distributions and degree corre-

lations. In Sec. 3.3 we extend the cavity method to account for a network with nodes assigned to sub-types of different transmissibility, and provide a closed set of equations for the average risk a node poses to the network. We consider the cases where node transmissibility is and is not correlated with social contact, separately. In Sec. 3.4 we derive equations for the average risk under link percolation, and show how the choice of the links which are deleted affects the risk. Sec. 3.5 demonstrates how the cavity method may be used to derive the distributional equations of risk and how to solve these equations via a population dynamics procedure. We conclude with a discussion of the theoretical value of our results and potential avenues for future work. Technical details are described in the appendices at the end of the chapter.

3.2 Impact of vaccination on the epidemic risk in contact networks

One of the main interests in the study of the risk of epidemics spreading on contact networks is the exploration of vaccination strategies. A question that arises, when assessing vaccination strategies, is what fraction of the population needs to be vaccinated to achieve herd immunity. In this section we consider the SIR epidemic model on contact networks and we show that this question can be answered by studying a simple node percolation problem.

3.2.1 Herd immunity with perfect vaccination in the SIR model on structured networks

We consider the SIR model on an undirected network with N nodes and adjacency matrix $\mathbf{A}$. The elements $A_{ij} = A_{ji} \in \{0, 1\}\ \forall\ i, j$ denote presence ($A_{ij} = 1$) or absence ($A_{ij} = 0$) of link for each pair of nodes (i, j) and $A_{ii} = 0\ \forall\ i$. Following the formulation in (214), we assume that an infected node may pass an infection to a neighbouring node in a short time interval dt with probability βdt and an infected node recovers from an infection at a time drawn from an 'infectious time' distribution, $\gamma(t)$, normalised such that $\int_0^\infty \mathrm{d}t\gamma(t) = 1$, to ensure that an infected node eventually recovers. In order to quantify the fraction of the population that needs to be vaccinated to achieve herd immunity, we note that if a vaccine provides perfect immunity, its action on an individual is functionally equivalent to deleting a node in the network, as this prevents the spread of infection through that node and its links. In order to incorporate the effect of node deletion we define a binary variable $\sigma_i \in \{0, 1\}$ which describes whether a node has been vaccinated ($\sigma_i = 0$) or not ($\sigma_i = 1$). The probability $r_i(\mathbf{A})$ that an infection starting from a single node i causes an outbreak across the bulk of the network, also called the *risk* of node i, can be determined, via the cavity method.

The cavity method first assumes that the network we consider is a tree, where between any two nodes there is a single path only. In such networks, there are no cycles, a set of links which starts and ends at the same node. We sketch a subsection of a tree in the left panel of Figure 3.1 where we show node i and its neighbours j, k and ℓ, which are linked to further nodes in the

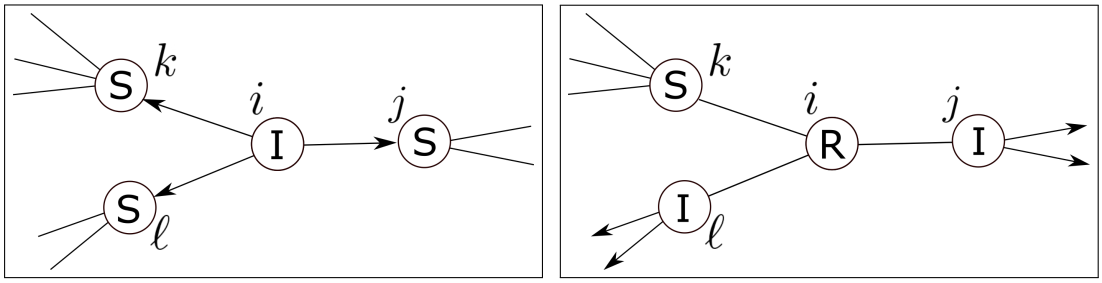

Figure 3.1: A sketch of a portion of a network that is a tree. We show four nodes, i at the centre, with three neighbours j, k and ℓ. Nodes j, k and ℓ are shown to have links to other nodes in the network (not sketched). Links with arrows indicate the path that an infection can currently take. In the left panel, we show the initial state of the network, a single node, in this case node i, is infected. It can infect any of its neighbours j,k and ℓ. In the right panel, we show the network after node i has infected nodes j and ℓ, and node i has recovered. The infection can now spread to any of the nodes in the sub-tree rooted at node j or node ℓ. The infection may not pass back to node i, as node i has recovered and can not become susceptible to infection again. This means that node k, its neighbours, and all other nodes in the sub-tree rooted at node k will not become infected in the future, as the tree nature of the network means that there is no path from node j or ℓ to nodes in the sub-tree rooted at k that does not pass through node i. We indicate the sub-trees rooted at node j in the left panel.

network (not sketched). It is important to note that if we removed node i and its links from this sketch, nodes j, k and ℓ would become disconnected, there would be no path between them. Indeed, when node i is removed from the network, the network separates into three distinct trees, rooted at nodes j, k and ℓ. We refer to these as the sub-trees rooted at nodes j, k and ℓ.

In the cavity approach to the SIR model we then consider that the network starts with a single infected node. In the left panel of Figure 3.1, node i is initially infected and its neighbours (and nodes in the network not included in the sketch) are all susceptible to infection. Node i may pass this infection on to any of its neighbours. If it does so, the infected neighbour may in turn spread the infection to one of its other neighbours. In the right panel of Figure

3.1 we sketch the scenario where node i has spread the infection to two of its neighbours, and indicate the paths that the infection may now pass along, noting that this does not include paths back to node i. The latter is due to the *unidirectional* nature of the SIR model, the infection can not be passed back to node i, since node i will either already be infected or will have recovered and *cannot* become susceptible to infection again. If we now consider node j in the right panel of Figure 3.1 after being infected by node i, we see that the only way a node in the sub-tree rooted at node j may become infected is if j first passes the infection to one of its neighbours. This is a consequence of the network being a tree, there are no paths connecting the nodes in the sub-trees rooted at node k and ℓ, to the nodes in the sub-tree rooted at j. Hence, if any node in the sub-tree rooted at j is to become infected, the infection must first spread from node j to its neighbours.

The cavity argument is to then say that the risk of node i will depend upon the risk of its neighbours in a copy of the network where node i and its links are removed, which is referred to as the i-cavity graph, which we denote as $\mathbf{A}_{\setminus i}$. We refer to the risk of a node j in the i-cavity graph, as the cavity risk $r_j^{(i)}(\mathbf{A})$. The risk of node i is the probability that while node i is infectious, it infects at least one of the nodes in its neighbourhood which then cause an epidemic in the remaining network. The remaining network after node i is infected is equivalent to the i-cavity graph. Under the assumption that the network is a tree, the cavity risks are independent of each other, since when node i is removed, the i-cavity graph is formed of several sub-trees rooted at each of the neighbours of node i, as can be seen if one considers removing node i and its links from the left panel of Figure 3.1.

This allows us to write that the probability that node i, in the time that it is infectious, does not infect at least one of its neighbours which then cause an epidemic, is given by, $\int_0^\infty \mathrm{d}t\, \gamma(t) \prod_{j\in\partial_i^{\mathbf{A}}} \left(1 - \left(1 - \mathrm{e}^{-\beta t}\right) r_j^{(i)}(\mathbf{A})\right)$, where the product over the neighbourhood $\partial_i^{\mathbf{A}}$ indicates that each cavity risk is independent of each other. Note that, given the (random) time $t \in [0, \infty)$, the term $(1 - \mathrm{e}^{-\beta t})\, r_j^{(i)}(\mathbf{A})$ is the probability that node j, infected with probability $(1 - \mathrm{e}^{-\beta t})$, causes an outbreak in the cavity graph $\mathbf{A}_{\setminus i}$. In other words, $\int_0^\infty \mathrm{d}t\, \gamma(t) \prod_{j\in\partial_i^{\mathbf{A}}} \left(1 - \left(1 - \mathrm{e}^{-\beta t}\right) r_j^{(i)}(\mathbf{A})\right)$ is the time-averaged probability that neighbourhood $\partial_i^{\mathbf{A}}$ is *not* a source of outbreak in $\mathbf{A}_{\setminus i}$. Finally, we note that for i to cause an epidemic it must not be vaccinated, i.e $\sigma_i = 1$, such that the risk of node i is given by,

$$r_i(\mathbf{A}) \;=\; \sigma_i \left[1 - \int_0^\infty \mathrm{d}t\, \gamma(t) \prod_{j\in\partial_i^{\mathbf{A}}} \left(1 - \left(1 - \mathrm{e}^{-\beta t}\right) r_j^{(i)}(\mathbf{A})\right)\right]. \qquad (3.1)$$

In summary, equation (3.1) then states that the risk of node i, $r_i(\mathbf{A})$, is exactly zero when i has been vaccinated, i.e. $\sigma_i = 0$, and otherwise equal to one minus the probability that its neighbourhood $\partial_i^{\mathbf{A}}$ is not a source of outbreak in the cavity graph $\mathbf{A}_{\setminus i}$. It is then argued that a similar equation is derived for $r_j^{(i)}(\mathbf{A})$. Due to the assumption that the network is a tree, the cavity risk $r_j^{(i)}(\mathbf{A})$ is unaffected by the nodes in the other trees rooted at the other neighbours of i. Hence, to write an expression for $r_j^{(i)}(\mathbf{A})$ we consider the risk of a node in the sub-tree rooted at node j. In this case, we can apply exactly the same reasoning as above, to the sub-tree rooted at j, such that the cavity risk

$r_j^{(i)}(\mathbf{A})$ is given the above equation with node i removed,

$$r_j^{(i)}(\mathbf{A}) \;=\; \sigma_j \left[1 - \int_0^\infty \mathrm{d}t\, \gamma(t) \prod_{\ell \in \partial_j^{\mathbf{A}} \setminus i} \left(1 - \left(1 - \mathrm{e}^{-\beta t} \right) r_\ell^{(j)}(\mathbf{A}) \right) \right]. \quad (3.2)$$

In writing these equations we have assumed that the network is a tree, and in this case they are exact. However, for large random graphs the length of a cycle typically grows logarithmically with the number of nodes in the network (224). Such networks are referred to as *locally tree-like*, as if one looked at a small fraction of connected nodes, it would be improbable to find a closed cycle. Hence, for large random graphs which are locally tree-like, it has been shown that these equations are a good approximation, and are exact in the limit $N \to \infty$. For a given contact network, one can solve the cavity equations (3.1) and (3.2) numerically. Alternatively, in absence of true knowledge of the contact network one can assume that it is *random* and use equations (3.1) and (3.2) to derive equations for the global risk $g(\mathbf{A}) = \frac{1}{N} \sum_{i=1}^N r_i(\mathbf{A})$, which is expected to be *self-averaging* (210) when $N \to \infty$ and thus independent of its microscopic details. Averaging (3.1) over all sites as shown in 3.A, one obtains, for a single graph instance $\mathbf{A}$

$$\begin{aligned} g(\mathbf{A}) \;&=\; \sum_\sigma \sigma \left[\mathrm{P}(\sigma|\mathbf{A}) - \sum_k \mathrm{P}(k,\sigma|\mathbf{A}) \int_0^\infty \mathrm{d}t\, \gamma(t)\, (1 - \alpha(t) \hat{g}_k(\mathbf{A}))^k \right] \quad (3.3) \\ \hat{g}_k(\mathbf{A}) \;&=\; \sum_{\sigma'} \sigma' \left[\mathrm{P}(\sigma'|\mathbf{A}) - \sum_{k' \geq 1} \frac{\mathrm{W}(k;k',\sigma'|\mathbf{A})}{\mathrm{W}(k|\mathbf{A})} \int_0^\infty \mathrm{d}t\, \gamma(t)\, (1 - \alpha(t) \hat{g}_{k'}(\mathbf{A}))^{k'-1} \right] \end{aligned}$$

where we have denoted for brevity $1 - \mathrm{e}^{-\beta t} = \alpha(t)$. We have defined the likelihood to draw at random a node with degree k and label σ for the graph in-

stance $\mathbf{A}$ as $\mathrm{P}(k,\sigma|\mathbf{A}) = N^{-1}\sum_i \delta_{\sigma,\sigma_i(\mathbf{A})}\delta_{k,k_i(\mathbf{A})}$, with $k_i(\mathbf{A}) = |\partial_i^{\mathbf{A}}|$ denoting the degree of node i and $\mathrm{P}(\sigma|\mathbf{A}) = \sum_k \mathrm{P}(k,\sigma|\mathbf{A})$ the marginal distribution. Furthermore, we have defined $\mathrm{W}(k;k',\sigma'|\mathbf{A}) = \sum_{ij} A_{ij}\delta_{k,k_i(\mathbf{A})}\delta_{k',k_j(\mathbf{A})}\delta_{\sigma',\sigma_j(\mathbf{A})}/N\bar{k}(\mathbf{A})$ as the likelihood that by drawing a link at random we choose a link with a node of degree k at one end and a node with degree k' and label σ' at the other. We denote by $\bar{k}(\mathbf{A}) = N^{-1}\sum_i k_i(\mathbf{A})$ the mean degree. The distribution $\mathrm{W}(k;k'|\mathbf{A}) = \sum_\sigma \mathrm{W}(k;k',\sigma|\mathbf{A})$ is known as the degree correlations, and $\mathrm{W}(k|\mathbf{A}) = \sum_{k'} \mathrm{W}(k;k'|\mathbf{A})$ is its marginal distribution. Here and below we adopt the convention to denote a joint probability distribution of node quantities across connected node pairs with $\mathrm{W}(\dots;\dots)$. We will consider vaccination strategies based upon the degree of nodes, such that $\mathrm{P}(k,\sigma|\mathbf{A}) = \mathrm{P}(k|\mathbf{A})\mathrm{P}(\sigma|k)$ and $\mathrm{W}(k;k',\sigma'|\mathbf{A}) = \mathrm{W}(k;k'|\mathbf{A})\mathrm{P}(\sigma'|k')$, where $\mathrm{P}(\sigma|k)$ models the degree-dependent vaccination strategy.

In the limit of large networks, $N \to \infty$, we expect fluctuations of intensive network observables to vanish and their value on a single graph realisation to coincide with their ensemble averaged value. Assuming that the degree distribution and degree correlations display such self-averaging behavior in the limit of large N, we average the cavity equations over a suitably defined random graph ensemble, obtaining

$$g = \sum_\sigma \sigma \left[\mathrm{P}(\sigma) - \sum_k \mathrm{P}(k,\sigma) \int_0^\infty \mathrm{d}t\, \gamma(t)\, (1-\alpha(t)\hat{g}_k)^k \right] \tag{3.4}$$

$$\hat{g}_k = \sum_{k'\geq 1}\sum_{\sigma'} \mathrm{W}(k'|k)\mathrm{P}(\sigma'|k')\sigma' \left[1 - \int_0^\infty \mathrm{d}t\, \gamma(t)\, (1-\alpha(t)\hat{g}_{k'})^{k'-1} \right] \tag{3.5}$$

where we have introduced the ensemble averages $\mathrm{P}(\sigma) = \langle \mathrm{P}(\sigma|\mathbf{A})\rangle_{\mathbf{A}}$, $\mathrm{P}(k,\sigma) =$

$\langle \mathrm{P}(k,\sigma|\mathbf{A})\rangle_{\mathbf{A}}$, $\mathrm{W}(k'|k') = \langle \mathrm{W}(k'|k,\mathbf{A})\rangle_{\mathbf{A}}$ and $\langle k\rangle = \langle \bar{k}(\mathbf{A})\rangle_{\mathbf{A}}$, with $\langle\,\cdot\,\rangle_{\mathbf{A}} = \sum_{\mathbf{A}} \cdot \mathrm{P}(\mathbf{A})$ and $\mathrm{P}(\mathbf{A})$ the probability over the set of symmetric adjacency matrices $\mathbf{A} \in \{0,1\}^{N(N-1)/2}$, which defines the random graph ensemble.

The set of equations (3.5) may be solved numerically. It is easy to check that they always have a trivial solution $\hat{g}_k = 0 \,\forall\, k$, corresponding to the absence of an epidemic outbreak, i.e. $g = 0$. The stability of this solution depends upon the Jacobian, of the system of equations (3.5),

$$M_{k,k'} = \frac{\partial \hat{g}_k}{\partial k'}\Big|_{\hat{g}_k=0\forall k} = (k'-1)\mathrm{W}(k'|k)\sum_{\sigma'}\sigma'\mathrm{P}(\sigma'|k')T, \tag{3.6}$$

where $T = \int_0^\infty \mathrm{d}t\,\gamma(t)\alpha(t)$ is known as the transmissability of the nodes (207). An epidemic will occur if the largest eigenvalue of the Jacobian, λ_1^M, satisfies the condition $|\lambda_1^M| > 1$. The above result was first derived in (208), in absence of node deletion. For uncorrelated networks, $\mathrm{W}(k'|k) = \mathrm{W}(k')$ and one has $\hat{g}_k = \hat{g}\ \forall\ k \geq 1$ with

$$\hat{g} = \sum_{\sigma}\sigma\left[\mathrm{P}(\sigma) - \sum_{k\geq 1}\mathrm{P}(\sigma|k)\frac{k\mathrm{P}(k)}{\langle k\rangle}\int_0^\infty \mathrm{d}t\,\gamma(t)\,(1-\alpha(t)\hat{g})^{k-1}\right] \equiv f(\hat{g}). \tag{3.7}$$

We can find a condition for an epidemic to occur if we consider a graphical argument for the solution to equation (3.7). Looking at the first derivative of $f(\hat{g})$,

$$f'(\hat{g}) = \sum_{\sigma,k\geq 1}\frac{\sigma\mathrm{P}(\sigma|k)k(k-1)\mathrm{P}(k)}{\langle k\rangle}\int_0^\infty \mathrm{d}t\,\gamma(t)\,(1-\alpha(t)\hat{g})^{k-2} \geq 0 \tag{3.8}$$

we find that $f(\hat{g})$ is monotonically increasing. Additionally, by taking the

second derivative,

$$f''(\hat{g}) = -\sum_{\sigma,k\geq 1} \frac{\sigma \mathrm{P}(\sigma|k)k(k-1)(k-2)\mathrm{P}(k)}{\langle k\rangle} \int_0^\infty \mathrm{d}t\, \gamma(t)\,(1-\alpha(t)\hat{g})^{k-2} \leq 0 \tag{3.9}$$

we find that $f(\hat{g})$ is convex. The graphical solution (which is reviewed in Appendix A) then follows: if we sketch $y = f(\hat{g})$ and $y = \hat{g}$, solutions to (3.7) are found at the intersections of these two curves. There is a trivial solution $\hat{g} = 0$, but there is potentially a second solution. Due to the monotonic and convex nature of $f(\hat{g})$, if $y = f(\hat{g} = 0)$ passes above the diagonal $y = \hat{g}$, eventually $f(\hat{g})$ will cross through the diagonal for some non-zero value of $\hat{g}$ (a sketch illustrating this argument, Figure A.1.2, can be found in Appendix A). The condition for this to occur is given by $f'(0) > 1$. By evaluating the first derivative at $\hat{g} = 0$,

$$f'(0) = \sum_{\sigma,k\geq 1} \frac{\sigma \mathrm{P}(\sigma|k)k(k-1)\mathrm{P}(k)}{\langle k\rangle}, \tag{3.10}$$

we can express the condition for an epidemic, $f'(0) > 1$ as,

$$T > \frac{\langle k\rangle}{\sum_{k,\sigma} \sigma \mathrm{P}(\sigma|k)k(k-1)\mathrm{P}(k)}. \tag{3.11}$$

. Focusing on the simplest case of a random vaccination campaign, where the variables $\{\sigma_i\}_{i=1}^N$ do not depend on the network degrees and are random i.i.d. with distribution

$$\mathrm{P}(\sigma) = p\delta_{\sigma,1} + (1-p)\delta_{\sigma,0}, \tag{3.12}$$

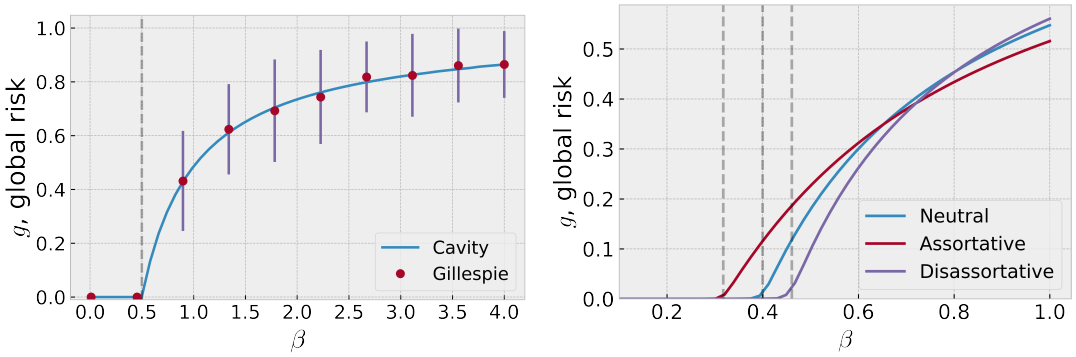

Figure 3.2: Global risk as a function of the infection rate β, for nodes with exponential infectious time distribution $\gamma(t) = \xi e^{-\xi t}$ where ξ is the rate of node recovery. Left: Results shown for an Erdös-Rényi (ER) graph with average connectivity $\langle k \rangle = 5$ and nodes with mean infectious time $\xi^{-1} = 1/2$. Solid lines indicate theoretical predictions from the cavity equations (3.5) while symbols show results from simulations on an ER graph of size $N = 3000$, averaged over 100 initial sites of infection, and 20 runs starting from each site. The dashed line indicating the epidemic threshold is computed from equation (3.13), which simplifies to $p_c = 1/T\langle k \rangle$ for ER graphs. Error bars show the standard deviation of the risk across different initial sites of infection. Right: Theoretical predictions from equation (3.5) are shown for graphs with Poissonian degree distribution with $\langle k \rangle = 3$ and nodes with mean infectious time $\xi^{-1} = 1.25$. Results are shown for graphs with neutral, assortative and disassortative degree correlations. Dashed lines indicate the predicted epidemic threshold from the largest eigenvalue of (3.6).

where $(1 - p) \in [0, 1]$ describes the fraction of nodes that are vaccinated, one finds a critical value of p below which epidemics are prevented,

$$p < p_c = \frac{\langle k \rangle}{T\langle k(k-1) \rangle}. \tag{3.13}$$

This is the herd immunity threshold, a rearranged form of the percolation threshold in the configuration model (225).

In Figure 3.2 (left panel) the global risk predicted from the cavity equation (3.4) is plotted for an Erdös-Rényi (ER) graph with mean degree $\langle k \rangle = 5$ and shown to be in excellent agreement with results from simulations

(226, 227, 228) of the stochastic SIR model on networks with $N = 3000$ nodes. In particular, the cavity method captures the correct qualitative change in the global risk with the rate of infection. Moreover, the error in the prediction of g between the cavity method and simulations is $\mathcal{O}(N^{-\frac{1}{2}})$, suggesting that the cavity equations are correct up to finite size corrections. Details of how simulations were performed can be found in 3.B. We note that the wide error bars, showing the standard deviation of the risk across different initial sites of infection, indicate that there is large variation in the risk of individual nodes in a given ER network. The impact of degree correlations is shown on the right panel of Figure 3.2, where results from the cavity equations are shown for networks with the same average connectivity and Poissonian degree distribution, but for two different types of degree correlations; where nodes preferentially link with nodes of similar degree, known as assortative degree mixing, or where nodes preferentially link with nodes of dissimilar degree, known as disassortative degree mixing. To compute the degree correlation function $W(k, k')$ for assortative and disassortative Poissonian graphs we followed the methods described in (229). Our results are consistent with earlier work which studied the size of the giant connected component (formally, a set of connected nodes whose size is a finite fraction of N in the limit $N \to \infty$) in random graphs with degree correlations (65). In Figure 3.3 we plot the global risk as a function of the fraction $1 - p$ of vaccinated population in ER graphs with average connectivity $\langle k \rangle = 5$. In the left panel we see that predictions from the cavity equations (3.5) are in agreement with results from simulations on networks of size $N = 1000$. The right panel shows that the herd immunity threshold in Poissonian graphs is lowest with disassortative

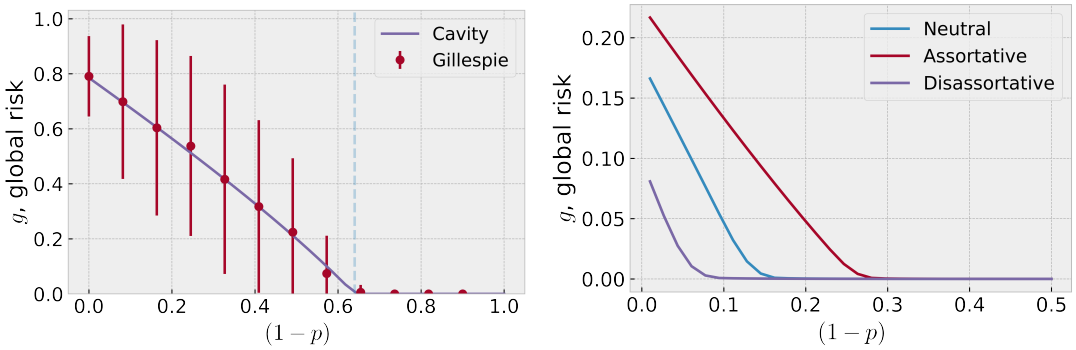

Figure 3.3: Global risk plotted as a function of the fraction $1 - p$ of vaccinated nodes with infection rate $\beta = 0.5$ and exponential distribution of infectious times $\gamma(t) = \xi e^{-\xi t}$ with recovery rate $\xi = 0.4$. Left: For an ER graph with $\langle k \rangle = 5$ we show predictions (solid line) from the cavity equations (3.5) and results of simulations (circles) on graphs with size $N = 1000$, where nodes were selected with probability $1 - p$ to be vaccinated, averaged over 10 configurations of vaccinated nodes, 25 initial sites of infection, and 25 runs. The dashed line indicates the herd immunity as computed from equation (3.13). Right: Theoretical results from the cavity equations (3.5) are shown for graphs with Poissonian degree distribution, mean degree $\langle k \rangle = 3$, for neutral, assortative and disassortative degree correlations.

correlations, and highest with assortative correlations.

3.3 Impact of vaccination with partial transmission

In the previous section we have considered an idealised vaccine that prevented all infection passing through paths containing vaccinated nodes. In general, vaccinations may not prevent all transmission, and individuals may respond to vaccines differently, leading to heterogeneities in individual infectious potential. It is not possible to know *a priori* how an individual will respond to a vaccine, however it is feasible to gather data on the impact of vaccination on transmissibility within a population and estimate differences in transmission between different demographics. It is therefore of interest to

understand how variations in coverage and infectious potential of individuals can affect vaccination strategies. In order to do so, we extend the cavity approach to the SIR model to account for heterogeneity in the transmissibility of individuals. We then go on to show how this affects the herd immunity threshold.

3.3.1 Epidemic risk with heterogeneous transmissibility

In order to account for heterogeneity in the transmissibility of individuals, we assume that individuals remain infectious for different times. Without loss of generality we assume that the infectious time distribution of each individual has the same functional form but its scale varies between individuals of different sub-type. Therefore, we introduce M node sub-types, identified by labels $\xi \in \{\xi^1, ..., \xi^M\}$, and assign each node a label, $\{\xi_i\}_{i=1}^N$, according to some probability distribution $\mathrm{P}(\xi)$. The labels $\{\xi^1, ..., \xi^M\}$ take values in $(0, \infty)$, such that ξ parameterises the infectious time distribution $\gamma(t|\xi)$ of nodes with label ξ. For the remainder of this chapter we choose $\gamma(t|\xi) = \xi \mathrm{e}^{-\xi t}$ such that $\frac{1}{\xi}$ represents the *mean infectious time* of individuals with label ξ. This particular choice for the recovery time distribution is known as Markovian recovery, however, our approach also holds for non-Markovian recovery times, which could be implemented by e.g. a Weibull distribution (230).

In this case, the risk of node i depends on the label of node i, and all labels downstream of node i. We denote the set of labels downstream of node i, including node i, by $\boldsymbol{\xi}_i$. The equations for the local risk for a given instance of a contact network $\mathbf{A}$ with prescribed labels $\boldsymbol{\xi} = (\xi_1, \ldots, \xi_N)$ are derived

by exactly the same reasoning as equations (3.1) and (3.2). However, the risk of a node, i, will now be a function of its individual mean infectious time ξ_i^{-1}, and the mean infectious times of its neighbours (the risk of which will in turn depend on the mean infectious time of their neighbours etc.). As a consequence of this, the risk of node i will depend explicitly on both the network $\mathbf{A}$ and the labels $\boldsymbol{\xi}$ as follows,

$$r_i(\mathbf{A}, \boldsymbol{\xi}_i) = 1 - \int_0^\infty \mathrm{d}t\, \gamma(t|\xi_i) \prod_{j \in \partial_i^{\mathbf{A}}} \left(1 - \alpha(t) r_j^{(i)}(\mathbf{A}, \boldsymbol{\xi}_j)\right) \tag{3.14}$$

$$r_j^{(i)}(\mathbf{A}, \boldsymbol{\xi}_j) = 1 - \int_0^\infty \mathrm{d}t\, \gamma(t|\xi_j) \prod_{\ell \in \partial_j^{\mathbf{A}} \setminus i} \left(1 - \alpha(t) r_\ell^{(j)}(\mathbf{A}, \boldsymbol{\xi}_\ell)\right). \tag{3.15}$$

Averaging over the nodes, we find the equation for the global risk, which depends on the whole label sequence $\boldsymbol{\xi}$ and the network $\mathbf{A}$

$$g(\mathbf{A}, \boldsymbol{\xi}) = \frac{1}{N} \sum_{i=1}^{N} r_i(\mathbf{A}, \boldsymbol{\xi}). \tag{3.16}$$

In 3.C we show, under the assumption that the random network that describes the population is locally tree-like, that one can derive a closed expression for the global risk in the $N \to \infty$ limit, that once averaged over the graph and label ensemble, reads as

$$g = 1 - \sum_{k,\xi} \mathrm{P}(k, \xi) \int_0^\infty \mathrm{d}t \gamma(t|\xi) \left(1 - \alpha(t) \hat{g}_{k,\xi}\right)^k \tag{3.17}$$

$$\hat{g}_{k,\xi} = \sum_{k',\xi'} \mathrm{W}(k', \xi'|k, \xi) \left[1 - \int_0^\infty \mathrm{d}t \gamma(t|\xi') \left(1 - \alpha(t) \hat{g}_{k',\xi'}\right)^{k'-1}\right] \tag{3.18}$$

where $\mathrm{P}(k, \xi)$ and $\mathrm{W}(k', \xi'|k, \xi)$ are the ensemble-averaged values of $\mathrm{P}(k, \xi|\mathbf{A}, \boldsymbol{\xi}) =$

$\frac{1}{N}\sum_i \delta_{k,k_i(\mathbf{A})}\delta_{\xi,\xi_i}$ and $\mathrm{W}(k',\xi'|k,\xi,\mathbf{A},\boldsymbol{\xi}) = \mathrm{W}(k,\xi;k',\xi'|\mathbf{A},\boldsymbol{\xi})/\mathrm{W}(k,\xi|\mathbf{A},\boldsymbol{\xi})$, respectively, where $\mathrm{W}(k,\xi;k',\xi'|\mathbf{A},\boldsymbol{\xi}) = \frac{1}{N\bar{k}(\mathbf{A})}\sum_{ij} A_{ij}\delta_{k,k_i(\mathbf{A})}\delta_{k',k_j(\mathbf{A})}\delta_{\xi,\xi_i}\delta_{\xi',\xi_j}$. For a given kernel $\mathrm{W}(k',\xi'|k,\xi)$ of a network with maximum degree $k_{\max}$ one may solve the system of $M \times k_{\max}$ equations (3.18) numerically and substitute the result into (3.17) to find the global risk.

Alternatively, one may be able to simplify these equations for specific choices of $\mathrm{W}(k,\xi;k',\xi')$. For example, if we assume the transmissibility of an individual is uncorrelated with its degree, the degree of its neighbours and the transmissibility of its neighbour, in this case $\mathrm{W}(k,\xi;k',\xi') = \mathrm{W}(k;k')\mathrm{P}(\xi)\mathrm{P}(\xi')$, and upon substitution of this kernel into the RHS of (3.18) we see that $\hat{g}_{k,\xi} = \hat{g}_k \forall \xi$, and the system of equations (3.18) reduce to,

$$\hat{g}_k = \sum_{k'} \mathrm{W}(k'|k)\left[1 - \int_0^\infty \mathrm{d}t\, \langle \gamma(t|\xi)\rangle_\xi \left(1-\alpha(t)\hat{g}_{k'}\right)^{k'-1}\right] \tag{3.19}$$

where $\langle ...\rangle_\xi = \sum_\xi ...\mathrm{P}(\xi)$. We see that equation (3.19) takes the same form as (3.5) but now depends upon the 'average' infectious time distribution $\langle \gamma(t|\xi)\rangle_\xi$. The stability criteria is therefore identical to that of (3.5) but now depends upon the average transmissibility, such that an epidemic will occur if

$$|\lambda_1^{(\mathbf{J})}| > 1 \tag{3.20}$$

where $\lambda_1^{(\mathbf{J})}$ is the largest eigenvalue of the Jacobian of (3.19) with entries $J_{k,k'} = \langle T(\xi)\rangle_\xi (k'-1)\mathrm{W}(k'|k)$ and $T(\xi) = \int_0^\infty \mathrm{d}t \gamma(t|\xi)\alpha(t)$. A further simplification can be made if we assume the degrees are uncorrelated, in which

case equations (3.19) reduces to a single equation,

$$\hat{g} = 1 - \sum_k \frac{k\mathrm{P}(k)}{\langle k \rangle} \int_0^\infty \mathrm{d}t \, \langle \gamma(t|\xi) \rangle_\xi \, (1 - \alpha(t)\hat{g})^{k-1} \tag{3.21}$$

which can be solved by a graphical solution, similarly to equation (3.7). From this we find that equation (3.21) has a non-zero solution when the epidemic threshold exceeds a value dependent on the average transmissibility,

$$\frac{\langle k^2 \rangle - \langle k \rangle}{\langle k \rangle} \geq \frac{1}{\langle T(\xi) \rangle_\xi}. \tag{3.22}$$

Another case where the cavity equations simplify is where we choose $\mathrm{W}(k, \xi; k', \xi')$ of the form,

$$\mathrm{W}(k, \xi; k', \xi') = \mathrm{W}(\xi, \xi')\mathrm{W}(k|\xi)\mathrm{W}(k'|\xi'). \tag{3.23}$$

This choice of degree correlations describes networks where degree correlations are driven by differences in the degree of nodes with different transmissibility i.e the probability for a node to have degree k may differ between nodes of transmissibility ξ and ξ', but nodes with the same transmissibility show no preference for linking with nodes of a particular degree. Hence, degree correlations are controlled by $\mathrm{W}(\xi, \xi')$ the probability to observe a link between nodes with labels ξ and ξ'. Indeed, by Bayes theorem we may show that $\mathrm{W}(k; k'|\xi, \xi') = \mathrm{W}(k|\xi)\mathrm{W}(k'|\xi')$ such that the degree of two nodes, k and k' are conditionally uncorrelated given their labels ξ and ξ'.

For this choice of $W(k,\xi;k',\xi')$ we find that

$$W(k',\xi'|k,\xi) = \frac{W(k,\xi;k',\xi')}{W(k,\xi)} \tag{3.24}$$

$$= \frac{W(\xi;\xi')W(k|\xi)W(k'|\xi')}{W(k|\xi)W(\xi)} \tag{3.25}$$

$$= \frac{W(\xi;\xi')W(k'|\xi')}{W(\xi)} \tag{3.26}$$

and as a result of this, the cavity equations (3.18) simplify such that $\hat{g}_{k,\xi} = \hat{g}_{\xi}\ \forall\ k$ where,

$$\hat{g}_{\xi} = 1 - \sum_{k',\xi'} W(\xi'|\xi)W(k'|\xi') \int_0^\infty \mathrm{d}t\gamma(t|\xi') \left(1 - \alpha(t)\hat{g}_{\xi'}\right)^{k'-1}. \tag{3.27}$$

By using this form of $W(k,\xi;k',\xi')$ we have reduced (3.18) from a system of $k_{\max} \times M$ equations to just M equations. This is a significant reduction, particularly for networks with large maximum degree $k_{\max}$. By analysis of the Jacobian of the system of equations (3.27), we find that an epidemic will occur if $|\lambda_1^{(J_{\xi,\xi'})}| > 1$ where $\lambda_1^{(J_{\xi,\xi'})}$ is the largest eigenvalue of $J_{\xi,\xi'} = \sum_{k'} W(\xi'|\xi)(k'-1)W(k'|\xi')T(\xi')$.

3.3.2 Herd immunity for vaccines with partial transmission

Having extended the cavity approach to account for heterogeneity in individual transmissibility, we can now consider vaccination with partial transmission. In this case, vaccinated individuals can still catch and transmit the disease, but we assume their transmissability is reduced, such that an individual i who is vaccinated will have a lower mean infectious time $1/\xi_i$ than an

unvaccinated individual. To analyse this scenario, we split a population into two clusters: an unvaccinated population with low infectious time decay rate ξ^ℓ and a vaccinated population with high decay rate $\xi^h > \xi^\ell$. The fraction of the population that is vaccinated is given by $\mathrm{P}(\xi^h) = 1 - \mathrm{P}(\xi^\ell)$. To keep the analysis simple, we focus on random vaccinations, where one can assume that the labels ξ are not correlated with the network degrees, and we will assume that degrees are uncorrelated. The critical fraction $P_c(\xi^h)$ of the population that needs to be vaccinated to prevent epidemics, assuming vaccination with partial transmission, can be found from (3.22) by writing

$$\begin{aligned} \langle T(\xi)\rangle_\xi &= \mathrm{P}(\xi^h)T(\xi^h) + [1 - \mathrm{P}(\xi^h)]T(\xi^\ell) \\ &= T(\xi^\ell) - \mathrm{P}(\xi^h)\Delta \end{aligned} \tag{3.28}$$

with $\Delta = T(\xi^\ell) - T(\xi^h) > 0$, which, substituted in (3.22), gives

$$\mathrm{P}(\xi^h) > \frac{T(\xi^\ell)}{T(\xi^\ell) - T(\xi^h)} \left[1 - \frac{\langle k\rangle}{T(\xi^\ell)\,\langle k(k-1)\rangle}\right] \equiv P_c(\xi^h) \tag{3.29}$$

Clearly, the fraction of the population that has to be vaccinated to achieve herd immunity must be greater when the vaccination leads to partial transmission, as opposed to no transmission. The herd immunity threshold under vaccination without transmission is given by $1 - p_c$ from (3.13), where T is the transmissibility of the unvaccinated population i.e $T = T(\xi^\ell)$. One can express the herd immunity threshold under vaccination with partial trans-

mission, $P_c(\xi^h)$, in terms of $1 - p_c$,

$$P_c(\xi^h) = \frac{T(\xi^\ell)}{T(\xi^\ell) - T(\xi^h)}(1 - p_c). \tag{3.30}$$

Since $T(\xi^\ell) > T(\xi^\ell) - T(\xi^h)$, it is clear that vaccination with partial transmission requires a greater number of people to be vaccinated when compared with vaccination with no transmission i.e $P_c(\xi^h) > 1 - p_c$.

3.3.3 Networks with correlated structure and transmissibility

In general, social contacts will be correlated with the transmissibility of individuals. For example, vaccinations are often prioritised for at risk groups, and for people above a certain age. Furthermore, vaccine distribution is dependent upon supply chains, and this can lead to higher levels of vaccination in one geographic area to another. Aside from vaccinations, transmissibility may correlate with social contacts, for example differences in transmissibility between children and adults have been noted for some infectious diseases, and hence if a social interaction network shows correlation with age, this may affect the spread of epidemics.

To understand how this affects the epidemic risk and vaccination we need to specify an ensemble of networks where links between individuals are based upon their respective transmissibility. For simplicity we do not specify any hard constraints on the degree sequence and instead define an ensemble of networks with average degree $\langle k \rangle$ where links are drawn in a way that allows for preferential attachment between nodes with specific transmissibilities, on the basis of an arbitrary function $W(\xi; \xi')$ of the labels of the two nodes con-

cerned. More specifically, we assume that a random network with adjacency matrix $\mathbf{A}$ is drawn with probability

$$\mathrm{P}(\mathbf{A}) = \prod_{i<j} \left[\frac{\langle k \rangle}{N} \frac{\mathrm{W}(\xi_i;\xi_j)}{\mathrm{P}(\xi_i)\mathrm{P}(\xi_j)} \delta_{A_{ij},1} + \left(1 - \frac{\langle k \rangle}{N} \frac{\mathrm{W}(\xi_i;\xi_j)}{\mathrm{P}(\xi_i)\mathrm{P}(\xi_j)}\right) \delta_{A_{ij},0} \right]. \tag{3.31}$$

Here, $\mathrm{W}(\xi;\xi')$ can be interpreted as the probability to draw a link with node labels ξ and ξ' at either end, hence it must be non-negative and normalised to one $\sum_{\xi,\xi'} \mathrm{W}(\xi;\xi') = 1$. Due to the undirected nature of the links, we also have $\mathrm{W}(\xi;\xi') = \mathrm{W}(\xi';\xi)$. We will refer to nodes with the same label, ξ, as a *cluster*, hence W controls the links between clusters. This choice of random graph ensemble allows us to model populations that are split into groups of different transmissibility, making minimum assumptions about the population, namely, the average degree of an individual, $\langle k \rangle$, and the likelihood of two nodes of transmissibilities ξ and ξ' to be connected $\mathrm{W}(\xi,\xi')$. In 3.D we show that the degree distribution of a graph drawn from this ensemble is given by

$$\mathrm{P}(k) = \sum_{\xi} \mathrm{P}(\xi)\mathrm{P}(k|\xi) = \sum_{\xi} \mathrm{P}(\xi) \mathrm{e}^{-\bar{k}(\xi)} \frac{(\bar{k}(\xi))^k}{k!} \tag{3.32}$$

where the average degree is $\langle k \rangle = \sum_{\xi} \mathrm{P}(\xi)\bar{k}(\xi)$. This is such that each cluster of nodes in this ensemble has a Poissonian degree distribution $\mathrm{P}(k|\xi)$ with mean degree $\bar{k}(\xi)$, where ξ is the cluster label. Furthermore, we find that the degree correlations are of the special form (3.23), where $\mathrm{W}(k|\xi) = k\mathrm{P}(k|\xi)/\bar{k}(\xi)$, which allows us to use the reduced form of the cavity equations (3.27) to study the risk on graphs from this ensemble. Finally, we note that the marginal of $\mathrm{W}(\xi;\xi')$ is $\mathrm{W}(\xi) = \sum_{\xi'} \mathrm{W}(\xi;\xi') = \mathrm{P}(\xi)\bar{k}(\xi)/\langle k \rangle$.

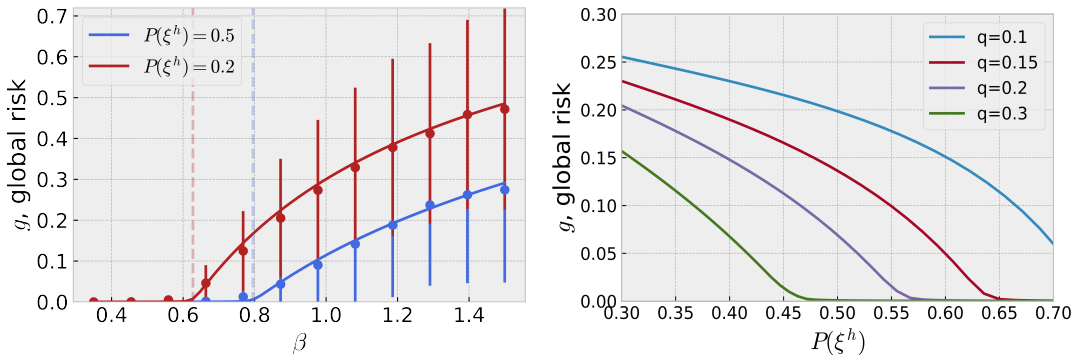

Figure 3.4: Left: Global risk plotted against infection rate β for a population where nodes have an infectious time distribution $\gamma(t|\xi) = \xi e^{-\xi t}$ and are separated into two sub-types with $\xi \in \{\xi^\ell, \xi^h\} = \{1.0, 5.0\}$. The network is drawn from the ensemble (3.31) with $\langle k \rangle = 3$ and the kernel W defined in (3.34) with $q = 0.15$ and $\bar{k}(\xi^\ell) = \langle k \rangle$ (and $\bar{k}(\xi^h) = \langle k \rangle$, via (3.33)). Results from cavity equations (lines) and simulations (symbols) are shown. Simulations were performed on networks of size $N = 2000$, averaged over 500 different sites of initial infection and 100 repetitions. Dashed lines indicate epidemic threshold predicted by the Jacobian of (3.27). Right: For the same population, we plot the global risk against the fraction of fast recovery nodes $P(\xi^h)$. We set the infection rate to $\beta = 1$. Results from the cavity equations (3.27) are shown for different inter-connectivity $q = \{0.1, 0.15, 0.2, 0.3\}$ (curves from top to bottom).

We now consider networks with two clusters, labelled by ξ^h and $\xi^\ell < \xi^h$, so that the transmissability kernel $W(\xi; \xi')$ is a 2×2 matrix, $P(\xi^h) = 1 - P(\xi^\ell)$ and the average connectivity is related to the intra-cluster connectivities by

$$\begin{aligned} \langle k \rangle &= \bar{k}(\xi^\ell) + P(\xi^h)(\bar{k}(\xi^h) - \bar{k}(\xi^\ell)) \\ &= \bar{k}(\xi^h) + P(\xi^\ell)(\bar{k}(\xi^\ell) - \bar{k}(\xi^h)). \end{aligned} \tag{3.33}$$

Given the properties of symmetry, marginalization and normalization of W, we can parameterise $W(\xi, \xi')$ in terms of two control parameters, the intra-cluster connectivity $\bar{k}(\xi^\ell)$ and a parameter, q, that controls the inter-cluster

connectivity, via the matrix,

$$\mathrm{W} = \begin{pmatrix} \frac{\bar{k}(\xi^\ell)\mathrm{P}(\xi^\ell)}{\langle k\rangle} - q & q \\ q & 1 - \frac{\bar{k}(\xi^\ell)\mathrm{P}(\xi^\ell)}{\langle k\rangle} - q \end{pmatrix}. \tag{3.34}$$

Since the elements of W are probabilities, they must take values in $[0, 1]$, hence the free parameters can take values in the range

$$\frac{q\langle k\rangle}{\mathrm{P}(\xi^\ell)} < \bar{k}(\xi^\ell) < \frac{(1-q)\langle k\rangle}{\mathrm{P}(\xi^\ell)} \tag{3.35}$$

with $q \in [0, 1/2]$.

In Figure 3.4 (left panel) the global risk, as predicted from the cavity equations, is plotted for a population with fast and slow recovery nodes, as a function of the infection rate β, for different values of the fast recovery population density, $\mathrm{P}(\xi^h)$. The difference in the global risk predicted by the cavity equations and computed from simulations is found to be $\mathcal{O}(N^{-\frac{1}{2}})$, suggesting that the cavity equations are in agreement with simulations up to finite size effects. Figure 3.4 (right panel) shows that as the proportion of nodes of fast recovery increases, herd immunity is eventually reached. Interestingly, as the inter-connectivity q is increased, the global risk decreases, as does the herd immunity threshold. This can intuitively be explained by first considering the scenario where $q = 0$ and the network is split into two disconnected sets of nodes, one where an epidemic is unlikely to be caused by any node, the other where nodes have a non-zero probability of causing an epidemic. As q is increased, the number of links between these sets of nodes increases, with the fast recovery nodes acting as a blockade to the path of infection, lowering

the global risk and herd immunity threshold. We note that in Figure 3.4 we choose $\bar{k}(\xi^{\ell}) = \bar{k}(\xi^{h}) = \langle k \rangle$ such that changes in $P(\xi^{h})$ do not affect the average degree of the nodes of fast and slow recovery. This ensures that changes in risk in the figure are due to the proportion of the vaccinated nodes, $P(\xi^{h})$, and the inter-connectivity, q, between the vaccinated and unvaccinated, as oppose to changes in the degree of these nodes that are a result of changes in $P(\xi^{h})$ and q. This does, however, mean that, by equation (3.35), the value of $\mathrm{P}(\xi^{h})$ is restricted to $q < \mathrm{P}(\xi^{h}) < 1 - q$, such that for larger values of q we can evaluate the risk over a smaller range of $\mathrm{P}(\xi^{h})$. Hence, in Figure 3.4 we show the global risk against $P(\xi^{h})$ for several values of q, where $P(\xi^{h})$ can still be varied over a broad range of values.

The graph ensembles (3.31) we used to generate networks with degree correlations (3.23), belongs to a general class of network ensembles with structure controlled by hidden variables (95). In our case, the hidden variables are the node labels ξ. We note that although we have chosen ξ to label nodes of different transmissibility, we could choose $\gamma(t|\xi) = \gamma(t)$ and allow ξ to label some other node property (e.g age). Equations (3.27) would therefore provide a quick numerical implementation to find epidemic risk in networks where degree correlations are generated by a node property, ξ, according to (3.23). Through suitable choice of $\mathrm{P}(\xi)$ and $\mathrm{W}(\xi;\xi')$ this random graph ensemble can be used to generate many types of networks including networks with modular structure, scale-free networks and random geometric graphs (95, 231). To demonstrate this and provide additional verification of our results, we generate networks with degree distribution as shown in the left panel of Figure 3.5. This degree distribution is noteworthy since it is multi-modal, and there-

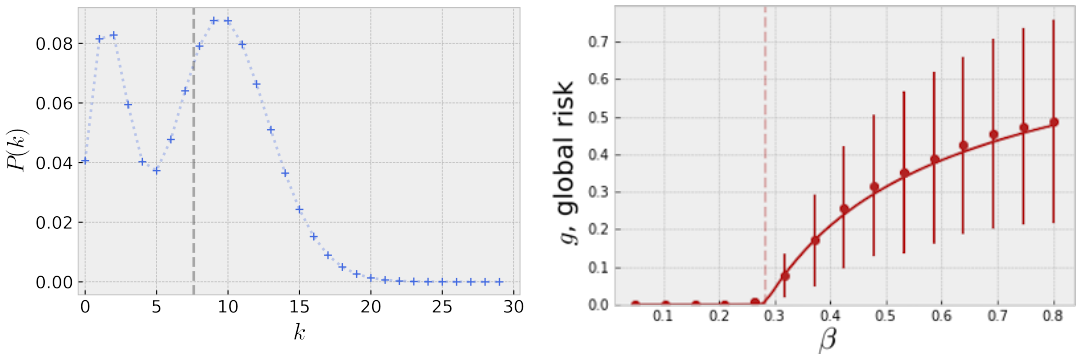

Figure 3.5: Left: Degree distribution of the network simulated in right panel. Symbols indicate degree distribution and dotted lines provide visual aid. Dashed vertical line indicates mean degree, $\langle k \rangle$. Right: Global risk, g, plotted against infection rate, β, for a network drawn from ensemble (3.31) with kernel given by (3.34). Nodes belong to two clusters, which share the same recovery rate $\xi = \{\xi^1, \xi^2\} = \{2.5, 2.5\}$, but differ in mean degree $\bar{k}(\xi^1) = 2$, $\bar{k}(\xi^2) = 10$. The fraction of nodes in each cluster is given by $\mathrm{P}(\xi^1) = (1 - \mathrm{P}(\xi^2)) = 0.3$, and inter-connectivity is equal to $q = 0.015$. Solid line show solution to the cavity equations (3.17) and (3.18), while symbols indicate simulations on networks of size $N = 2000$, with error bars indicating standard deviation over simulations started on 1000 different nodes with 100 runs from each node.

fore not well described by the mean degree alone. Despite this, the right panel of this figure shows that the solution to the cavity equations (3.17) and (3.18) qualitatively captures the change in the global risk g with the infection rate β as observed in MC simulations. Quantitatively, the difference in the global risk predicted by the cavity equations and computed from simulations is found, again, to be $\mathcal{O}(N^{-\frac{1}{2}})$. Hence, the cavity equations are in agreement up to finite size effects.

3.4 Social distancing in populations with heterogeneous transmissibility

We now show how social distancing affects epidemic risk in a population with heterogeneous transmissibility. We model social distancing as a bond percolation (also known as link percolation) process in which we assess how removing a random fraction of links from the network affects the risk of an epidemic. We introduce the random binary variables $\tau_{ij} \in \{0, 1\}$ which indicates whether a link between two individuals is broken due to social distancing ($\tau_{ij} = 0$) or not ($\tau_{ij} = 1$). These are drawn from the distribution,

$$\mathrm{Q}(\boldsymbol{\tau}|\mathbf{y}) = \prod_{i<j} \left[(1 - y_{ij})\delta_{\tau_{ij},0} + y_{ij}\delta_{\tau_{ij},1} \right] \tag{3.36}$$

where $1 - y_{ij}$ is the probability that a link between i and j is broken. To derive equations for the local risk for networks subject to bond percolation, one only needs to consider the effect of deleting a link between node i and j on equation (3.14). If $\tau_{ij} = 0$ the link between node i and j has been removed and so the node j should not contribute to the risk of node i. Hence, under bond percolation equations (3.14) and (3.15) are modified as follows,

$$r_i(\mathbf{A}, \boldsymbol{\xi}) = 1 - \int_0^\infty \mathrm{d}t\, \gamma(t|\xi_i) \prod_{j \in \partial_i^{\mathbf{A}}} \left(1 - \tau_{ij}\alpha(t) r_j^{(i)}(\mathbf{A}, \boldsymbol{\xi}) \right) \tag{3.37}$$

$$r_j^{(i)}(\mathbf{A}, \boldsymbol{\xi}) = 1 - \int_0^\infty \mathrm{d}t\, \gamma(t|\xi_j) \prod_{\ell \in \partial_j^{\mathbf{A}} \setminus i} \left(1 - \tau_{jl}\alpha(t) r_\ell^{(j)}(\mathbf{A}, \boldsymbol{\xi}) \right). \tag{3.38}$$

We consider three different types of bond percolation: random percolation

$y_{ij} = y \; \forall \; i, j$, degree-based percolation $y_{ij} = y(k_i, k_j)$, and sub-type percolation $y_{ij} = y(\xi_i, \xi_j)$. Following steps in 3.C, one can find the closed expressions for the global risk

$$g = 1 - \sum_{k\xi} \mathrm{P}(k, \xi) \int \mathrm{d}t \gamma(t|\xi) \left(1 - \alpha(t) \tilde{g}_{k,\xi}\right)^k \tag{3.39}$$

$$\tilde{g}_{k,\xi} = \sum_{k'\xi'} y(k, \xi, k', \xi') \mathrm{W}(k', \xi'|k, \xi) \left[1 - \int \mathrm{d}t \gamma(t|\xi') \left(1 - \alpha(t) \tilde{g}_{k',\xi'}\right)^{k'-1}\right] \tag{3.40}$$

where $y(k, \xi, k', \xi') = y$ for random bond percolation, $y(k, \xi, k', \xi') = y(k, k')$ for degree-dependent bond percolation and $y(k, \xi, k', \xi') = y(\xi, \xi')$ for sub-type dependent bond percolation. In Figure 3.6 (left panel) we consider an ER network, with individuals randomly assigned one of two sub-types, high and low transmissibility, $\xi \in \{\xi^\ell, \xi^h\}$ with $\xi^\ell < \xi^h$, such that degree and node sub-type are uncorrelated. We then compare the global risk following random, degree-based, and sub-type bond percolation for the same fraction of links removed. For degree-based percolation we choose $y(k, k') = \alpha \left(1 - \frac{kk'}{k^2_{\max}}\right)$ to preferentially remove links attached to nodes of high degree. For sub-type percolation, we consider the scenario where nodes of low transmissibility (i.e. fast recovery $\xi = \xi^h$) do not reduce their social contact, i.e. $y(\xi^h, \xi^h) = 1$, and we set $y(\xi^\ell, \xi^h) = y(\xi^\ell, \xi^\ell)$, such that $y(\xi^\ell, \xi^\ell)$ is the only free parameter which controls the overall fraction of links removed. We see that link percolation based upon degree and node-type yields lower global risk relative to random link percolation. Furthermore, for this parameterisation we see that percolation based upon node-type is preferable to degree-based percolation. This is because, for a fixed fraction of links that are removed from the net-

work, $1 - y$, the degree-based strategy removes a higher proportion of links between nodes of low transmissibility, which typically have less impact on the risk of an epidemic, in comparison with the strategy that removes links based on node-type. In Figure 3.6 (right panel) we show the global risk for different levels of vaccination with partial transmission and random link percolation. As is to be expected, the risk is lowest for high vaccine coverage (high $\mathrm{P}(\xi^h)$), and high social distancing (low y). There is greater variation in the global risk with y than $\mathrm{P}(\xi^h)$ suggesting that for given parameterisations, social distancing may be more effective than vaccination with partial transmission. If we compared the global risk when p% of nodes are deleted, with the risk when p% of links are deleted, (we show this explicitly later, in Figure 3.13) the risk would be lower under node deletion, showing that vaccination which blocks all transmission is more effective than social distancing. The result shown in Figure 3.6 is thus noteworthy in showing that for vaccines that allow partial transmission, the opposite is true for certain values of the model parameters, i.e. link deletion can be more effective than vaccination with partial transmission.

For the same population considered in the right panel of Figure 3.6 we computed the the global risk for different levels of vaccination with partial transmission and link percolation with either a degree-based strategy, or a strategy based upon node-type. In left panel of Figure 3.7 we find that for a degree-based strategy, the behaviour of the global risk with changes in $\mathrm{P}(\xi^h)$ and y is markedly similar to when link percolation occurs randomly. However, we show that there is a difference in the right panel of Figure 3.7, where we plot $\Delta_g = g_{\text{random}} - g_{\text{degree}}$ (where g_{random} and g_{degree} are the global risk

under random and degree-based link percolation, respectively). From this figure we find that in a population subject to a degree-based strategy, a smaller fraction of links, $1-y$, are required to be removed for the herd immunity threshold to be reached, hence, degree-based strategies are favorable in this population over random link percolation.

When the population is subject to link percolation based on node type, the behaviour of the global risk g with changes in $\mathrm{P}(\xi^h)$ and y is notably different, as shown in Figure 3.8. In particular, g is a non-monotonic function of both y and $\mathrm{P}(\xi^h)$. This behaviour can be explained by considering the effect of link percolation, with our strategy based on node-type, for different values of $\mathrm{P}(\xi^h)$. As we previously stated, we consider link percolation where nodes of low transmissibility do not reduce their social contact, i.e. $y(\xi^h,\xi^h)=1$, and we set $y(\xi^\ell,\xi^h)=y(\xi^\ell,\xi^\ell)$, such that $y(\xi^\ell,\xi^\ell)$ is the only free parameter which controls the overall fraction of links removed, $1-y$. In the top left of Figure 3.8, $\mathrm{P}(\xi^h)$ is high, such that we have many nodes of low transmissibility. Since we do not remove links between nodes of low transmissibility, there is a high density of links in the network, despite y being low, and therefore the global risk is relatively high. For high $\mathrm{P}(\xi^h)$, as we increase y, we increase the number of links between nodes of low and high transmissibility, as well as links between nodes which both have high transmissibility. However, since for high $\mathrm{P}(\xi^h)$ there are few nodes of high transmissibility, and we do not remove links between nodes of low transmissibility, the global risk is relatively high for all values of y. If we consider the bottom right, where y is high and $\mathrm{P}(\xi^h)$ is low, the population has many nodes of high transmissibility with many links, and the global risk is high. As we decrease y, we remove links

connected to nodes of high transmissibility. Since $P(\xi^h)$ is low, the majority of links are connected to nodes of high transmissibility, and so the impact of decreasing y is more pronounced; eventually a sufficient fraction of links is removed to pass the herd immunity threshold. For intermediate values of $P(\xi^h)$, for example when $P(\xi^h) = 0.65$, the global risk is a non-monotonic function of y. Due to the large fraction of nodes with low transmissibility, at low values of y there is sufficient density of links to keep the population above the herd immunity threshold. As y is increased, there is a greater proportion of links between nodes of low and high transmissibility, such that nodes of low transmissibility shield nodes of high transmissibility, and the population attains herd immunity. However, as y is increased further, the density of links is sufficiently high that shielding becomes ineffective, and the global risk increases.

3.5 Beyond the mean: distribution of risk in the SIR model

3.5.1 Distribution of risk in networks with degree correlations

In the previous sections we have used the cavity method to obtain a closed set of equations for the average risk of epidemics in a network where nodes have heterogeneous infectious time. Previous work has shown that epidemic risk varies considerably from node to node, even with homogeneous transmission probabilities, due to variations in the local environment (214). The presence of

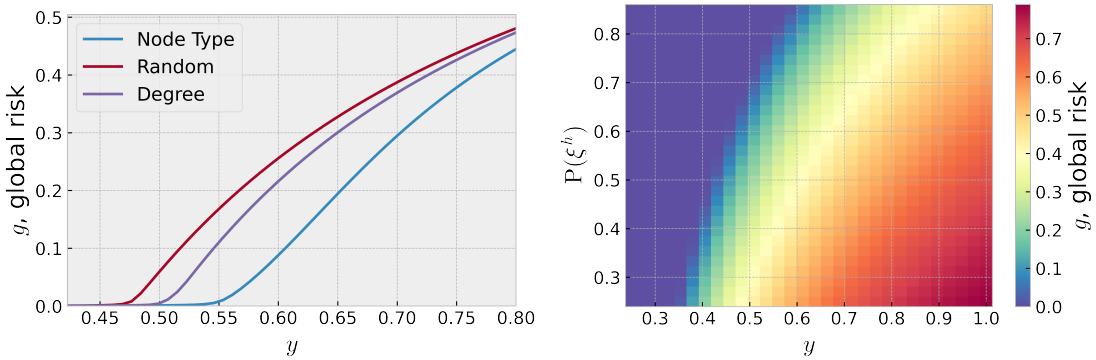

Figure 3.6: We consider an ER graph with mean degree $\langle k \rangle = 5$. Nodes have infectious time distribution $\gamma(t|\xi) = \xi e^{-\xi t}$ and are assigned to one of two sub-types of slow and fast recovery, $\xi \in \{\xi^\ell, \xi^h\} = \{1, 5\}$. The infection rate is set to $\beta = 2$. Left: Global risk plotted as a function of the fraction of links not removed, y. The fraction of nodes of each sub-type is $P(\xi^h) = 1 - P(\xi^\ell) = 0.65$. Results are shown for the cases where links are removed i) at random ii) with preference for links connecting nodes of high degree $y = \sum_{k,k'} W(k,k')\alpha \left(1 - \frac{kk'}{k_{\max}}\right)$, such that α set the value of y, and iii) with preference for nodes with slow recovery $y = \sum_{\xi,\xi'} W(\xi;\xi')y(\xi,\xi')$ where we set $y(\xi^h,\xi^h) = 1$ and $y(\xi^\ell,\xi^h) = y(\xi^\ell,\xi^\ell)$ such that $y(\xi^\ell,\xi^\ell)$ is the free parameter that controls y. Right: Global risk plotted as a function of both $P(\xi^h)$ and y with links removed at random. Results in both figures are from solutions to the cavity equations (3.39) and (3.40).

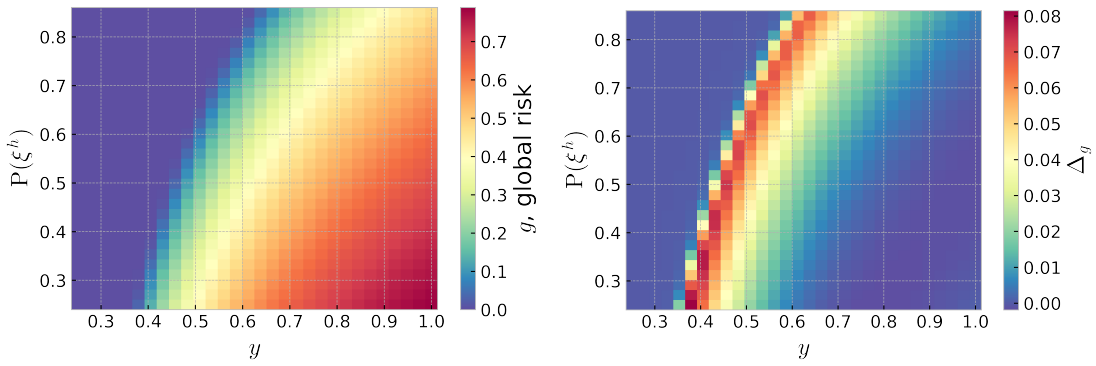

Figure 3.7: We consider an ER graph with mean degree $\langle k \rangle = 5$. Nodes have infectious time distribution $\gamma(t|\xi) = \xi e^{-\xi t}$ and are assigned to one of two subtypes of slow and fast recovery, $\xi \in \{\xi^\ell, \xi^h\} = \{1, 5\}$. The infection rate is set to $\beta = 2$. Left: Global risk plotted as a function of both $\mathrm{P}(\xi^h)$ and y with links removed with preference for links connecting nodes of high degree $y = \sum_{k,k'} \mathrm{W}(k,k')\alpha \left(1 - \frac{kk'}{k_{\max}}\right)$, such that α set the value of y. Right: Difference in the global risk subject to random and degree-based link percolation Δ_g plotted as a function of $\mathrm{P}(\xi^h)$ and y. Results in both figures are from solutions to the cavity equations (3.39) and (3.40. .

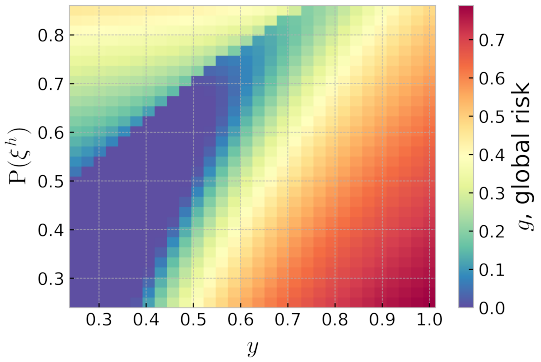

Figure 3.8: We consider an ER graph with mean degree $\langle k \rangle = 5$. Nodes have infectious time distribution $\gamma(t|\xi) = \xi e^{-\xi t}$ and are assigned to one of two subtypes of slow and fast recovery, $\xi \in \{\xi^\ell, \xi^h\} = \{1, 5\}$. The infection rate is set to $\beta = 2$. Global risk is plotted as a function of both $\mathrm{P}(\xi^h)$ and y with links removed with preference for nodes with slow recovery $y = \sum_{\xi,\xi'} \mathrm{W}(\xi;\xi')y(\xi,\xi')$ where we set $y(\xi^h,\xi^h) = 1$ and $y(\xi^\ell,\xi^h) = y(\xi^\ell,\xi^\ell)$ such that $y(\xi^\ell,\xi^\ell)$ is the free parameter that controls y. Global risk is computed by the solution to the cavity equations (3.39) and (3.40.

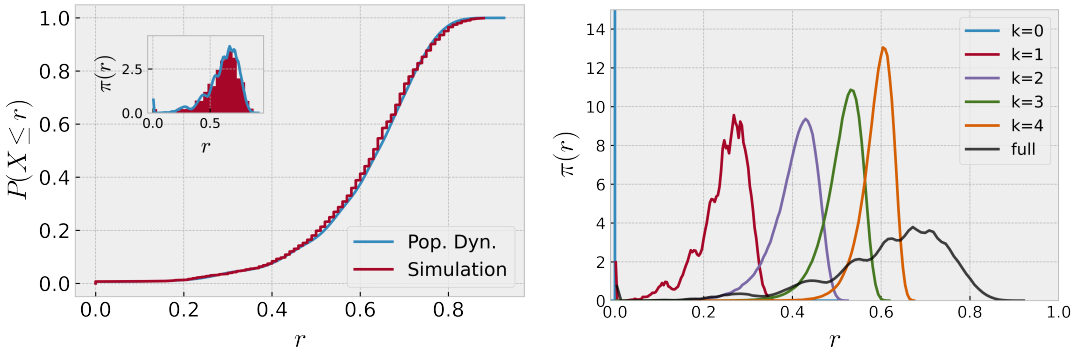

Figure 3.9: Results from population dynamics, with population size $S = 2 \times 10^5$ and 2×10^6 samples to form the histogram, for an ER network with mean degree $\langle k \rangle = 5$, infection rate $\beta = 0.5$ and homogeneous transmission. Left: Cumulative distribution function of the risk, $\mathrm{P}(X \leq r)$, for inverse mean infectious time $\xi = 0.75$. Results from population dynamics and simulations on a network of size $N = 2000$ are shown. Inset shows same information for the risk distribution $\pi(r)$, with simulations plotted as a histogram and population dynamics plotted as a solid line. Right: Distribution of the risk distribution $\pi(r)$ (black line) and degree conditional risk distributions $\pi_k(r)$, for $k \in \{0, 1, 2, 3, 4\}$ (peaks from left to right) for inverse mean infectious time $\xi = 0.6$.

heterogeneities in node infectious times is expected to add an extra source of fluctuations, therefore studying the distribution of the node risks is expected to provide important information that is not captured by the mean risk.

Recently, the cavity method has been used to assess the heterogeneous behaviour of individual nodes in the context of percolation in sparse networks (214, 223). Here we extend this approach to account for degree correlations and heterogeneities in the node transmissability and calculate the functional form of the distribution of node risks. The latter is defined as

$$\pi(r|\mathbf{A}) = \frac{1}{N} \sum_{i=1}^{N} \delta \left(r - r_i(\mathbf{A}) \right) \tag{3.41}$$

and a closed set of equation can be derived for it by substituting the RHS of

equation (3.1) into equation (3.41) and following a similar procedure as in 3.A for the global risk, which leads, after averaging over the graph ensemble, to an equation for the risk distribution $\pi(r)$

$$\pi(r) = \sum_{k\geq 0} \mathrm{P}(k) \left\{ \prod_{j=1}^{k} \int \mathrm{d}\hat{r}_j \hat{\pi}_k(\hat{r}_j) \right\} \delta\left(r - \phi(k, \hat{\boldsymbol{r}})\right) \tag{3.42}$$

where we have defined the degree-dependent 'cavity' risk distribution, $\hat{\pi}_k(\hat{r})$, which is the probability for a node with degree k to have a neighbour with cavity risk $\hat{r}$. We have also defined the function,

$$\phi(k, \hat{\boldsymbol{r}}) = 1 - \int_0^\infty \mathrm{d}t \gamma(t) \prod_{j=1}^{k} \left(1 - \alpha(t)\hat{r}_j\right) \tag{3.43}$$

and denoted $\hat{\boldsymbol{r}} = \{\hat{r}_1, ..., \hat{r}_k\}$ the cavity risk of each of the k neighbours of the node with risk r. The degree-dependent cavity risk distribution is given by,

$$\hat{\pi}_k(\hat{r}) = \sum_{k'\geq 1} \mathrm{W}(k'|k) \left\{ \prod_{j=1}^{k'-1} \int \mathrm{d}\hat{r}'_j \hat{\pi}_{k'}(\hat{r}'_j) \right\} \delta\left(\hat{r} - \phi(k'-1, \hat{\boldsymbol{r}}')\right) \tag{3.44}$$

where we have denoted $\hat{\boldsymbol{r}}' = \{\hat{r}_1, ..., \hat{r}_{k'-1}\}$ the cavity risk of each of the $k'-1$ neighbours of the node with cavity risk $\hat{r}$. The set of equations (3.44) for the degree-dependent 'cavity' risk distributions $\hat{\pi}_k(\hat{r})$ must be solved first to then solve equation (3.42) for the distribution of risk $\pi(r)$. This can be accomplished numerically by using a population dynamics algorithm (232). This consists of approximating each $\hat{\pi}_k(\hat{r})$ by the empirical cavity risk frequencies computed from a large number (i.e. a population) of cavity risks, which are updated at each iteration of the algorithm following a stochastic map. We start by initializing $k_{\max}$ populations of cavity risks, each of size S, by draw-

ing $k_{\max} \times S$ random variables $\hat{r}_i^{(k)}$, $i = 1, \ldots, S$ in the $[0, 1]$ interval. Their empirical distribution represents the zero-step approximation $\hat{\pi}_k^0(\hat{r})$ of $\hat{\pi}_k$. A single iteration of the algorithm consists of the following steps,

1. Set $k = 1$.
2. Draw degree k' with probability $\mathrm{W}(k'|k)$.
3. Randomly select $k' - 1$ risks from the k'-th population of risks.
4. Compute the function $\phi(k' - 1, \hat{\boldsymbol{r}})$ using the $k' - 1$ values of risk.
5. Select a random risk from the k-th population and set its value to $\phi(k' - 1, \hat{\boldsymbol{r}})$.
6. Set $k = k + 1$ and go back to step (2).

Upon reaching step 6, the empirical distribution of the cavity risks is one-step approximation $\hat{\pi}_k^1(\hat{r})$ of $\hat{\pi}_k$. Steps steps 2 to 6 define a Markov chain that we expect to reach a unique fixed point after many iterations (233). Hence, by following steps 2 to 6 repeatedly, we expect the n-step approximation $\hat{\pi}_k^n(\hat{r})$ to converge to $\hat{\pi}_k(\hat{r})$. Practically, we say that convergence has been reached when the average cavity risk in each population $\psi^{n,(k)} = \frac{1}{S}\sum_i \hat{r}_i^{n,(k)}$, stabilises such that fluctuations in $\psi^{n,(k)}$ are of order $\mathcal{O}(S^{-\frac{1}{2}})$ and can be thought of as finite size effects (233). Once the populations have converged the distribution of risk $\pi(r)$ can be computed in a similar manner by taking samples from the population and computing the histogram of $\phi(k, \hat{\boldsymbol{r}})$.

In Figure 3.9 (left panel) we show results from the population dynamics algorithm for an ER graph with average connectivity $\langle k \rangle = 5$. Results are

in very good agreement with simulations, carried out on networks of size $N = 2000$. As previously shown in (223), the distribution of risk can be conditioned upon the degree of a node, leading to the degree-conditional risk distributions

$$\pi_k(r) = \left\{ \prod_{j=1}^{k} \int \mathrm{d}\hat{r}_j \hat{\pi}_k(\hat{r}_j) \right\} \delta\left(r - \phi(k, \hat{\boldsymbol{r}})\right). \tag{3.45}$$

These are plotted in Figure 3.9 (right panel) and show that the peaks and troughs apparent in $\pi(r)$ are caused by nodes of different degree, with the peak at $r = 0$ arising from disconnected nodes. From this figure we see that the mean risk increases with degree, showing the benefit of degree-based vaccination strategies. However, the skew in the degree-conditional risk distributions means that degrees which have a high *mean* risk, also contain nodes of relatively low risk, and vaccinating these nodes would reduce the overall risk and epidemic size by little, highlighting the limitations of a degree-based strategy. It can be checked analytically and verified numerically that the risk distribution for random regular graphs are delta-peaked, with the peak corresponding to the solution to equation (3.5) for the global risk, which suggests that the random nature of the degree of the neighbours of a node in graphs with heterogeneous structure are the source of variability in the risk of nodes with the same degree.

Figure 3.10 (left panel) shows the cumulative distribution of risk for networks with Poissonian degree distribution and assortative and disassortative degree correlations, respectively. Results from the cavity method are found in good agreement with simulations on networks with size $N = 2000$. Degree

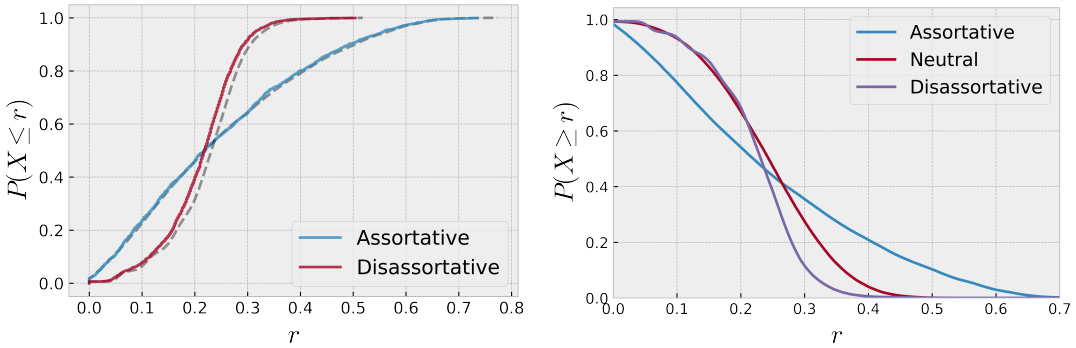

Figure 3.10: Results from population dynamics, with population size $S = 1 \times 10^4$ and 1×10^5 samples to form the histogram, for a network with Poissonian degree distribution, mean degree $\langle k \rangle = 5$, infection rate $\beta = 0.25$ and homogeneous recovery rate $\xi = 0.75$. Left: cumulative distribution function of the risk, $\mathrm{P}(X \leq r)$, computed from the cavity method (dashed line) compared with simulations (solid line) on a network of size $N = 2000$, for assortative and disassortative degree correlations. Right: same information from the cavity method shown for the survival function, $\mathrm{P}(X \geq r)$, with the curve for a neutral graph added for comparison.

correlations are seen to have a significant impact on the risk distribution. This is further shown on the right panel, where the survival function $\mathrm{P}(X \geq r)$ of assortative graphs is seen to have larger tails than disassortative or neutral graphs, due to a higher proportion of high risk nodes.

3.5.2 Distribution of risk in networks with heterogeneous transmission

The equations for the distribution of risk can be immediately generalised to the case of heterogeneous transmission, giving

$$\pi(r) = \sum_{k\geq 0,\xi} \mathrm{P}(k,\xi) \left\{ \prod_{j=1}^{k} \int \mathrm{d}\hat{r}_j \hat{\pi}_{k,\xi}(\hat{r}_j) \right\} \delta\left(r - \phi(k,\xi,\hat{\boldsymbol{r}})\right) \tag{3.46}$$

$$\hat{\pi}_{k,\xi}(\hat{r}) = \sum_{k'\geq 1,\xi'} \mathrm{W}(k',\xi'|k,\xi) \left\{ \prod_{j=1}^{k'-1} \int \mathrm{d}\hat{r}'_j \hat{\pi}_{k',\xi'}(\hat{r}'_j) \right\} \delta\left(\hat{r} - \phi(k'-1,\xi',\hat{\boldsymbol{r}}')\right) \tag{3.47}$$

$$\phi(k,\xi,\hat{\boldsymbol{r}}) = 1 - \int_0^\infty \mathrm{d}t \gamma(t|\xi) \prod_{j=1}^{k} \left(1 - \alpha(t)\hat{r}_j\right). \tag{3.48}$$

These equations can be solved using a generalisation of the population dynamics algorithm above with $M \times k_{\max}$ populations. The risk distribution $\pi(r)$ can be de-convoluted either in terms of degree, or node label ξ or both. To illustrate this, we first consider a random regular graph with degree $\langle k \rangle = 5$, where each node is independently assigned a random label $\xi \in \{\xi^\ell, \xi^h\}$. Figure 3.11 (left panel) shows that the risk distribution neatly splits into the distribution of risk for each cluster. The risk distribution for nodes of a given label ξ, is seen to have several peaks, corresponding to the different neighbourhoods a node may have: in a regular graph of degree c, with two clusters, there are $c+1$ different labelling configurations for the neighbourhood of a node. The height of the peaks in this distribution are therefore related to the multiplicity of these possible labelling configurations. It is important to note, that these peaks are not delta-peaked, but are broader,

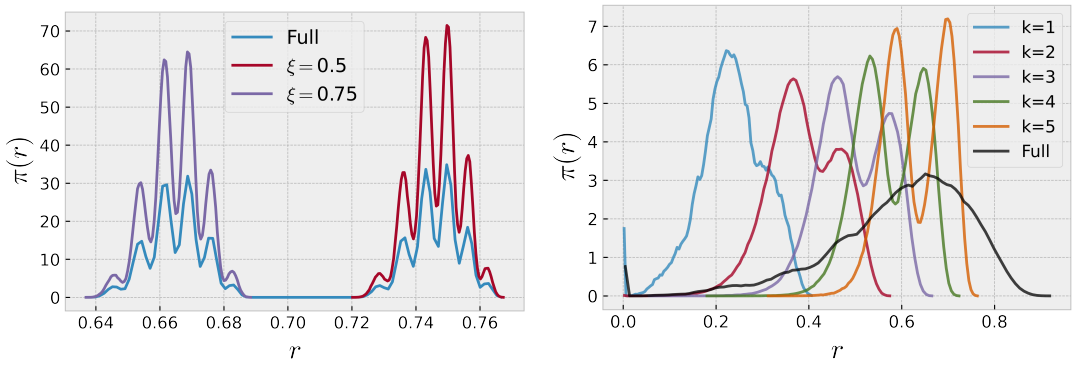

Figure 3.11: Left: Risk distribution $\pi(r)$ of regular graph with connectivity $\langle k \rangle = 5$, rate of infection $\beta = 0.5$, and two recovery rates $\xi \in \{0.5, 0.75\}$ with probability $\mathrm{P}(\xi) = 0.5$ for all ξ. The curves with larger peaks correspond to the risk distribution conditioned upon ξ. Right: risk distribution $\pi(r)$ for a network from the ensemble (3.31) with mean degree $\langle k \rangle = 5$, rate of infection $\beta = 0.5$, and two recovery rates $\xi \in \{0.6, 1.0\}$ with probability $\mathrm{P}(\xi = 1.0) = 0.5$. The transmissability kernel is defined in (3.34) with $\bar{k}(\xi = 0.6) = \bar{k}(\xi = 1.0) = \langle k \rangle$. Larger peaks correspond to the risk distribution conditioned upon k. In both plots the population size is $S = 10^5$ and 10^6 samples are taken from the converged cavity distribution to form $\pi(r)$.

and overlap, due to the risk being dependent not only upon the neighbourhood of a node, but on the neighbours of neighbours as explored in (234). Figure 3.11 (right panel) shows the risk distribution and the degree conditional risk distributions for the ensemble defined in (3.31), with average connectivity $\langle k \rangle = 5$. When compared to Figure 3.9 we see a greater amount of heterogeneity for nodes of a given degree. This highlights the importance of understanding differences in transmissability in individuals and its interplay with the network structure: the efficacy of sub-type based or degree based vaccination depends on the level of links between each cluster and their relative transmissability.

3.5.3 Risk distribution in the limit of large connectivity

An exact expression for the risk distribution may be derived in the limit of large connectivity, for graphs with homogeneous transmissibility, using methods demonstrated in (223). To extend these methods to graphs with heterogeneous transmissibility we use the *ansatz* that as $\langle k \rangle \to \infty$ the cavity field distributions will become delta-peaked i.e. $\hat{\pi}_{k,\xi}(\hat{r}) = \delta(\hat{r} - \hat{r}^*_{k,\xi})$. Inserting this into equation (3.47), multiplying by $\hat{r}$ and integrating both sides over $\hat{r}$, we find

$$\hat{r}^*_{k,\xi} = \sum_{k',\xi'} \mathrm{W}(k',\xi'|k,\xi) \left[1 - \int_0^\infty \mathrm{d}t \gamma(t|\xi') \left(1 - \alpha(t)\hat{r}^*_{k',\xi'} \right)^{k'-1} \right]. \tag{3.49}$$

Similarly, we insert $\hat{\pi}_{k,\xi}(\hat{r}) = \delta(\hat{r} - \hat{r}^*_{k,\xi})$ into equation (3.46) which yields,

$$\pi(r) = \sum_{k,\xi} \mathrm{P}(k,\xi) \delta \left(r - \left[1 - \int_0^\infty \mathrm{d}t \gamma(t|\xi) \left(1 - \alpha(t)\hat{r}^*_{k,\xi} \right)^{k} \right] \right). \tag{3.50}$$

Given that $\pi(r) = \sum_{k,\xi} \pi(r|k,\xi)\mathrm{P}(k,\xi)$ we find the conditional risk distribution to be delta-peaked under this ansatz,

$$\pi(r|k,\xi) \;\; = \;\; \delta \left(r - f_\xi(k) \right) \tag{3.51}$$

where

$$f_\xi(k) \;\; = \;\; 1 - \int_0^\infty \mathrm{d}t \gamma(t|\xi) \left(1 - \alpha(t)\hat{r}^*_{k,\xi} \right)^{k}. \tag{3.52}$$

We can simplify the above by choosing $\gamma(t|\xi) = \delta\left(t + \frac{1}{\beta}\ln\left(1 - T(\xi)\right)\right)$ such that,

$$f_\xi(k) \;=\; 1 - \left(1 - T(\xi)\hat{r}^*_{k,\xi}\right)^k. \tag{3.53}$$

In order to retrieve a non-trivial distribution of risk in the limit $\bar{k} \to \infty$, we assume that $T(\xi) \ll 1 \;\forall\; \xi$ (at finite transmissibility, every node will be near-certain of causing an epidemic in the large connectivity limit). This allows us to write $f_\xi(k) = 1 - \mathrm{e}^{-kT(\xi)\hat{r}^*_{k,\xi}}$. To proceed we assume that degree correlations are of the form $W(k', \xi'|k, \xi) = W(\xi'|\xi)W(k'|\xi')$, which by equation (3.49) yields $r^*_{k,\xi} = r^*_\xi \;\forall\; k$. To find the risk distribution of nodes of a given label $\pi_\xi(r) = \sum_k \pi(r|k, \xi)\mathrm{P}(k|\xi)$, we then use (3.51) and properties of the Dirac delta-function to write,

$$\pi_\xi(r) = \sum_k \mathrm{P}(k|\xi)\frac{\delta\left(k - f^{-1}_\xi(r)\right)}{|f'_\xi(f^{-1}_\xi(r))|} = \frac{1}{T(\xi)\hat{r}^*_\xi(1-r)}\sum_k \mathrm{P}(k|\xi)\delta\left(k + \frac{\ln(1-r)}{T(\xi)\hat{r}^*_\xi}\right). \tag{3.54}$$

To proceed further we must specify the degree distribution, and so we consider the distribution of risk in graphs drawn from the graph ensemble defined by (3.31) and assume that as $\langle k\rangle \to \infty$ the conditional mean degree $\bar{k}(\xi) \to \infty \;\forall\; \xi$. Noting that the degrees in this ensemble are distributed according to $\mathrm{P}(k|\xi) = \mathrm{e}^{-\bar{k}(\xi)}\bar{k}^k(\xi)/k!$, which in the limit of $\bar{k}(\xi) \to \infty$ is well

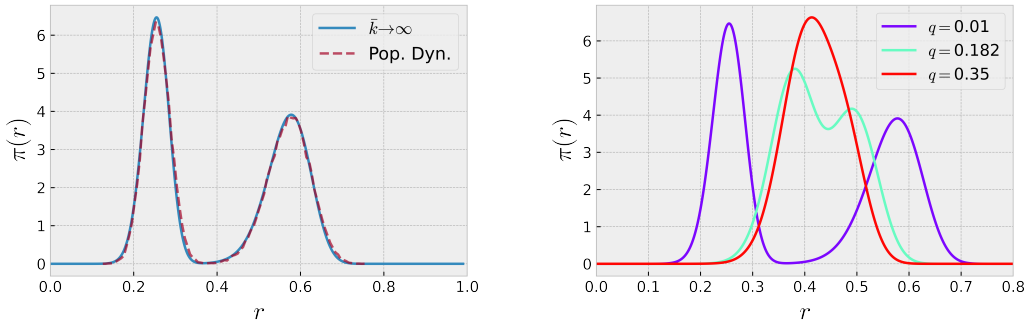

Figure 3.12: Risk distribution $\pi(r)$, for a network in the ensemble (3.31) with $\langle k\rangle = 50$ and two clusters, with recovery time distribution $\gamma(t|\xi) = \delta(t + \frac{1}{\beta}\ln(1-T(\xi)))$, parameterised by $T(\xi) \in \{0.0225, 0.03\}$ with $\mathrm{P}(\xi) = 0.5$ and inter-connectivity q. Left: The dashed lines show the solutions to equations (3.46) and (3.47) via population dynamics, with population size $S = 10^5$ and 10^6 samples forming the final distribution. The solid curve shows the large mean limit approximation (3.55). The inter-connectivity is set to $q = 0.01$. Right: Large mean limit approximation for different values of q, as shown in the legend.

approximated by $\mathrm{P}(k|\xi) \sim \mathcal{N}(\bar{k}(\xi), \bar{k}(\xi))$, we find,

$$\pi_\xi(r) = \frac{1}{T(\xi)r^*_\xi}\sqrt{\frac{1}{2\pi\bar{k}(\xi)}}\exp\left[-\frac{\bar{k}(\xi)}{2}\left(1+\frac{\ln(1-r)}{T(\xi)r^*_\xi\bar{k}(\xi)}\right)^2 - \ln(1-r)\right]. \quad (3.55)$$

The unconditional risk distribution is then given by $\pi(r) = \sum_\xi \mathrm{P}(\xi)\pi_\xi(r)$. We can compare this expression with the results of population dynamics for a system with two clusters with transmissability $T(\xi) = \{0.0225, 0.03\}$ of equal size $\mathrm{P}(\xi) = 0.5$. We see in Figure 3.12 that for the case where $\langle k\rangle = 50$ there is excellent agreement with the expression (3.55). In Figure 3.12 we also see the impact of changing the inter-connectivity in this ensemble: for low q we see two distinct peaks, corresponding to the risk of nodes of different transmissability, but as q increases the two peaks begin to overlap, until the distribution becomes unimodal for high q.

3.5.4 Distributional equations of risk with node and link percolation

Finally, we use the cavity method to investigate the effect of node and link percolation on the distribution of risk in the SIR model. Node deletion models perfect vaccination, as before, and link percolation models the loss of a social contact between two individuals, due to, for example, social-distancing measures. To do so we introduce a binary variable τ_{ij} which indicates whether a link in a contact network has been deleted ($\tau_{ij} = 0$) or not ($\tau_{ij} = 1$). The local risk subject to node and link percolation is then written,

$$r_i(\mathbf{A}) = \sigma_i \left[1 - \int_0^\infty \mathrm{d}t\, \gamma(t) \prod_{j \in \partial_i^{\mathbf{A}}} \left(1 - \tau_{ij} \alpha(t) r_j^{(i)}(\mathbf{A}) \right) \right] \tag{3.56}$$

$$r_j^{(i)}(\mathbf{A}) = \sigma_j \left[1 - \int_0^\infty \mathrm{d}t\, \gamma(t) \prod_{\ell \in \partial_j^{\mathbf{A}} \setminus i} \left(1 - \tau_{j\ell} \alpha(t) r_\ell^{(j)}(\mathbf{A}) \right) \right]. \tag{3.57}$$

We consider the case where node and links are randomly and independently deleted with probability dependent on their degree, so that

$$\mathrm{P}(\boldsymbol{\sigma}|\mathbf{k}) = \prod_i \left[(1 - x(k_i)) \delta_{\sigma_i,0} + x(k_i) \delta_{\sigma_i,1} \right] \tag{3.58}$$

$$\mathrm{Q}(\boldsymbol{\tau}|\mathbf{k}) = \prod_{i<j} \left[(1 - y(k_i, k_j)) \delta_{\tau_{ij},0} + y(k_i, k_j) \delta_{\tau_{ij},1} \right]. \tag{3.59}$$

By proceeding as in 3.A, and averaging over the graph ensemble, we find that the distribution of risk is given by,

$$\begin{aligned}
\pi(r) &= \sum_k \mathrm{P}(k) \sum_\sigma P(\sigma|k) \\
&\quad \times \left\{ \prod_{j=1}^{k} \sum_{k'_j} \mathrm{W}(k'_j|k) \sum_{\hat{\tau}_j} \mathrm{Q}(\hat{\tau}_j|k,k'_j) \int \mathrm{d}\hat{r}_j \hat{\pi}_{k'_j}(\hat{r}_j) \right\} \\
&\quad \times \delta\left(r - \phi(k,\sigma,\hat{\boldsymbol{\tau}},\hat{\boldsymbol{r}})\right) \\
\hat{\pi}_k(\hat{r}) &= \sum_\sigma \mathrm{P}(\sigma|k) \left\{ \prod_{\ell=1}^{k-1} \sum_{k_\ell} \mathrm{W}(k'_\ell|k) \sum_{\hat{\tau}'_\ell} \mathrm{Q}(\hat{\tau}'_\ell|k,k'_\ell) \int \mathrm{d}\hat{r}'_\ell \hat{\pi}_{k'_\ell}(\hat{r}'_\ell) \right\} \\
&\quad \times \delta\left(\hat{r} - \phi(k-1,\sigma,\hat{\boldsymbol{\tau}}',\hat{\boldsymbol{r}}')\right)
\end{aligned} \tag{3.60}$$

with $\hat{\boldsymbol{\tau}} = \{\hat{\tau}_1, ..., \hat{\tau}_k\}$, $\hat{\boldsymbol{\tau}}' = (\hat{\tau}'_1, \ldots, \hat{\tau}'_{k'-1})$ and

$$\phi(k,\sigma,\hat{\boldsymbol{\tau}},\hat{\boldsymbol{r}}) = \sigma\left[1 - \int_0^\infty \mathrm{d}t\gamma(t) \prod_{j=1}^{k} \left(1 - \alpha(t)\hat{\tau}_j\hat{r}_j\right)\right]. \tag{3.61}$$

Equation (3.60) can be solved by a generalisation of the populations dynamics algorithm above. To evaluate the cavity distribution $\hat{\pi}(\hat{r})$:

1. Set $k = 1$.
2. Draw σ with probability $\mathrm{P}(\sigma|k)$
3. Draw k' degree from the distribution $\mathrm{W}(k'|k)$.
4. Select a risk from the k'-th population of risks.
5. Select $\hat{\tau}'$ with probability $\mathrm{Q}(\hat{\tau}'|k,k')$.
6. Repeat steps (3-5) $k-1$ times, and store each τ, and individual to form

the vectors $\hat{\boldsymbol{\tau}}'$ and $\hat{\boldsymbol{r}}'$.

7. Select a random risk from the k-th population and set its value to $\phi(k-1, \sigma, \hat{\boldsymbol{\tau}}', \hat{\boldsymbol{r}}')$.

8. Set $k = k+1$ and go back to step (2).

9. Repeat all steps until all populations have converged.

As discussed in section 3.5.1 the convergence of $\hat{\pi}_k(\hat{r})$ can be checked by monitoring $\psi^{n,(k)} = \frac{1}{S}\sum_i \hat{r}_i^{n,(k)}$, where $\hat{r}_i^{n,(k)}$ is the value of risk i in the n^{th} iteration of the above steps. One can then compute the risk distribution $\pi(r)$ by taking samples from the population and computing the histogram of $\phi(k, \sigma, \hat{\boldsymbol{\tau}}, \hat{\boldsymbol{r}})$. We note that, by equations (3.60), the risk distribution $\pi(r)$ can be deconvoluted in terms of k and σ. By conditioning upon $\sigma = 1$ it is possible to retrieve the risk distribution of unvaccinated nodes, therefore providing a method to see how vaccination strategies affect risk in the network of unvaccinated nodes.

In Figure 3.13 we show the effects of node and link deletion, representing perfect vaccination and social distancing respectively. We consider two cases: random and degree-based strategies. For random vaccination we have $x(k) = x \ \forall \ k$ and $y(k,k') = y \ \forall \ k,k'$. For degree based strategies we set $x(k) = 1 - \alpha\frac{k}{k_{\max}}$ and $y(k,k') = 1 - \alpha\frac{kk'}{k_{\max}^2}$ such that nodes of high degree and links connecting nodes of high degree are more likely to be deleted. We show the case where 15% of nodes/links are deleted in an ER graph. We see that for the same fraction of nodes/links deleted, the overall risk of the population is lower under random node deletion than random link deletion. Furthermore,

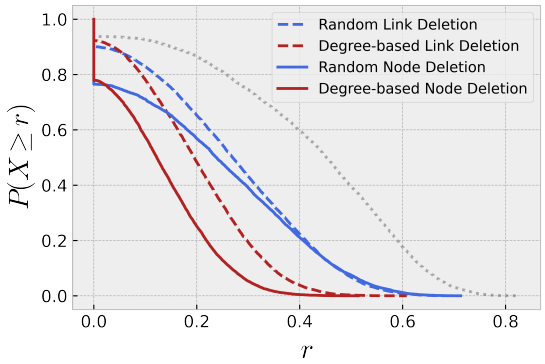

Figure 3.13: Survival function for the risk of nodes in an ER graph with mean degree $\langle k \rangle = 3$. Infection rate is $\beta = 0.7$ and nodes have exponential infectious time distribution $\gamma(t) = \xi e^{-\xi t}$ with mean infectious time $\xi = 0.75$. The dotted line indicates case where no node or link deletion has occurred. In all other cases 15% nodes/links are deleted, subject to either random (blue curves) or degree-based (red curves) deletion where high degree nodes/links are preferentially selected for deletion. For degree based node deletion we have nodes deleted according to (3.58) with $x(k) = 1 - \alpha \frac{k}{k_{\max}}$, and for degree based link deletion we delete nodes according to (3.59) with $y(k, k') = 1 - \alpha \frac{kk'}{k^2_{\max}}$.

risk under degree-based node deletion is lower than degree-based link deletion. This is consistent with the idea that social distancing measures, which assume an imperfect break in the chain of social contacts, are a less effective method of epidemic prevention than vaccination. It is however, interesting to compare the effect of degree-based link deletion, to random node deletion: in this case link deletion has the greater reduction of risk in the population. This highlights the importance of strategy in vaccination, although deleting a node blocks all paths of infection through that node, a targeted strategy of link deletion can lead to greater reductions in risk than random node deletion.

3.6 Discussion and conclusion

Predicting the effect of vaccination in epidemic models on networks continues to be a source of interesting inquiry. In our work we have relaxed the common assumption that vaccination blocks all transmission and instead assumed that vaccinated individuals have reduced transmissibility. From a modelling perspective this is useful when assessing the risk of epidemics and there is a lack of data for the impact of a given vaccine on transmission. To explore this, we have extended the cavity method to account for heterogeneity in the transmissibility of groups of individuals. These groups could represent differences in age, pre-existing medical conditions, or any other known correlates with transmissibility. Here however we have focused on a population of vaccinated and unvaccinated individuals, distinguished from each other by their transmissibility. Our results reveal that herd immunity is still attained from vaccination with partial transmission, if vaccination reduces transmissibility to a sufficiently low level that depends on both the infection rate of the disease and contact network topology. We have shown that vaccination with partial transmission requires a greater proportion of the population to be vaccinated to achieve herd immunity, as intuitively expected. This highlights the importance of estimating the transmissibility of an infectious disease, and the impact that vaccination has upon individual transmissibility. However, it also highlights the robustness of vaccination as a strategy for the mitigation of epidemics, as even a partial reduction of transmission can achieve the desired herd immunity effect.

The benefit of the cavity approach to the SIR model on networks is that it

allows one to evaluate the epidemic risk without simulation. Our equations for the global risk provide a quick method to calculate epidemic risk in populations with groups of different transmissibility. By solving the distributional equations of epidemic risk we have revealed the stark impact of heterogeneity in transmissibility. For graphs with homogeneous degree structure, the distribution of risk is delta-peaked when transmissibility of each individual is the same, but non-trivial when nodes take one of two values of transmissibility. This reveals that it is a strong assumption to make that the transmissibility of individuals is homogeneous, and that to ignore such heterogeneity can potentially dampen epidemic mitigation strategies that focus on network topology alone. Indeed our equations show that by introducing groups of different transmissibility, the epidemic risk will depend upon the size and transmissibility of each group, as well as the assortativity of links between nodes in different groups.

While vaccination is an important part of epidemic mitigation, we have also shown that the cavity method can model social distancing via bond percolation. Our framework allows us to compare random bond percolation with percolation that targets either links connecting nodes of high degree, or nodes of a particular sub-type. This may be useful when studying variations in the social distancing of different demographics and their impact on epidemic risk. One example could be studying the effect of relaxed social distancing amongst the vaccinated population who are perhaps less risk averse. Our work also shows that in some cases social distancing may be more effective than vaccination with partial transmission.

When studying populations with groups of different transmissibility we

have provided a method to reduce the complexity of the cavity equations for the global risk by suitable choice of random graph ensemble. Specifically, we chose a graph ensemble where degrees are correlated by some hidden variables, in this case the transmissibility of an individual. While we have used our choice of graph ensemble to study the effect of heterogeneity in transmissibility, we have proved the validity of our approach in general for this graph ensemble which can be used in many scenarios. For example, we may choose that the transmissibility of each group is the same, such that the groups of nodes now only vary in their mean degree and assortativity between different groups. Therefore, this ensemble would provide a low complexity method to study the effect of degree correlations on epidemic risk, where correlations are driven by some hidden variable, perhaps reflecting differences in demographic. Furthermore, this graph ensemble can generate many different types of networks, including networks with modular structure, power-law degree distribution and geometric random graphs, and as such our methods can also be applied to networks of this type.

The distributional equations of risk give insight into the impact of different vaccination strategies and social distancing behaviours beyond their effect on the global risk. This is particularly interesting with respect to the tails of these distributions, corresponding to the probability of high risk nodes. We have shown that assortative graphs have fat tailed distributions, and a further avenue of work may be to elucidate more information about the tail of the risk distribution in graphs with strong degree correlations from the cavity method. Interestingly, the distributional equations allow one to study the risk distribution in the sub-network of unvaccinated nodes with no further

technicalities.

There are several limitations of our work. Firstly, the equations we provide only describe the steady state of the SIR model, but dynamics are an important consideration in the modelling of epidemics, for example the timing of peak infections is of particular interest. An interesting avenue of further work could be to extend our investigations to the dynamics of the SIR model using the dynamical cavity method, exploring how differences in transmission and assortativity affect the peak of infections. Additionally, our modelling approach is restricted to static networks, whereas realistically contact networks vary with time, as discussed in (235, 236). For simplicity, we have restricted our numerical results to populations with exponential infectious time distributions, where heterogeneity in the transmissibility of individuals is parameterised by differences in the average recovery time. It would however be interesting to apply our methods to populations split into clusters with different infectious time distributions, i.e a population where each individual either has exponentially distributed infectious times, or infectious times drawn from a Weibull distribution. Lastly, it is important to note that the SIR model does not allow for reinfection of individuals, making it unsuitable for the modelling of some infectious diseases where reinfection is a common occurrence. Despite these limitations our work shows that the cavity approach to the epidemic risk in the SIR model reveals rich behaviour governed by the heterogeneity in the transmissibility of individuals.

Appendices

3.A Risk with homogeneous transmission and node and link deletion

Here we show how to derive a closed set of equations for the average, or 'global', risk that a node causes an epidemic across a network that is subject to node and link deletion, when nodes are homogeneous in transmissibility. We introduce a binary random variable $\sigma_i \in \{0,1\} \ \forall \ i$ to indicate if a node i is deleted (σ_i=0) or not ($\sigma_i = 1$) and $\tau_{ij} \in \{0,1\} \ \forall \ i,j$ to indicate if the link between i and j is deleted ($\tau_{ij} = 0$) or not ($\tau_{ij} = 1$). We consider the case where node and links are randomly and independently deleted with probability dependent on their degree, according to,

$$\mathrm{P}(\sigma_i|k_i) = (1 - x(k_i))\,\delta_{\sigma_i,0} + x(k_i)\delta_{\sigma_i,1} \tag{3.62}$$

$$\mathrm{Q}(\tau_{ij}|k_i,k_j) = \big(1 - y(k_i,k_j)\big)\,\delta_{\tau_{ij},0} + y(k_i,k_j)\delta_{\tau_{ij},1}. \tag{3.63}$$

For a graph with adjacency matrix $\mathbf{A}$ the risk that node i causes an epidemic is given by,

$$r_i(\mathbf{A}) = \sigma_i \left[1 - \int_0^\infty \mathrm{d}t\, \gamma(t) \prod_{j \in \partial_i^{\mathbf{A}}} (1 - \alpha(t)\tau_{ij} r_j^{(i)}(\mathbf{A})) \right] \tag{3.64}$$

$$r_j^{(i)}(\mathbf{A}) = \sigma_j \left[1 - \int_0^\infty \mathrm{d}t\, \gamma(t) \prod_{\ell \in \partial_j^{\mathbf{A}} \setminus i} \left(1 - \alpha(t)\tau_{j\ell} r_\ell^{(j)}(\mathbf{A}) \right) \right]. \tag{3.65}$$

Summing (3.64) over i, dividing by N and inserting unity in the form

$$1 = \sum_\sigma \delta_{\sigma,\sigma_i} \sum_{k \geq 0} \delta_{k,|\partial_i^{\mathbf{A}}|} \prod_{j \in \partial_i^{\mathbf{A}}} \int \mathrm{d}\hat{r}_j\, \delta(\hat{r}_j - r_j^{(i)}(\mathbf{A})) \sum_{\hat{\tau}_j} \delta_{\hat{\tau}_j,\tau_{ij}} \tag{3.66}$$

we obtain

$$\begin{aligned} g(\mathbf{A}) &= \frac{1}{N} \sum_\sigma \sum_{i=1}^N \delta_{\sigma,\sigma_i} \sigma \Bigg\{ 1 - \sum_{k \geq 0} \delta_{k,k_i(\mathbf{A})} \left[\prod_{j \in \partial_i^{\mathbf{A}}} \int \mathrm{d}\hat{r}_j\, \delta(\hat{r}_j - r_j^{(i)}(\mathbf{A})) \sum_{\hat{\tau}_j} \delta_{\hat{\tau}_j,\tau_{ij}} \right] \\ &\quad \times \int_0^\infty \mathrm{d}t \gamma(t) \prod_{j \in \partial_i^{\mathbf{A}}} (1 - \alpha(t)\hat{\tau}_j \hat{r}_j) \Bigg\} \\ &= \sum_\sigma \sigma \Bigg[\mathrm{P}(\sigma) - \sum_{k \geq 0} \sum_{\hat{\boldsymbol{\tau}}} \int \mathrm{d}\hat{\boldsymbol{r}}\, \mathrm{W}_c(k, \sigma; \hat{\boldsymbol{\tau}}, \hat{\boldsymbol{r}} | \mathbf{A}) \\ &\qquad \times \int_0^\infty \mathrm{d}t \gamma(t) \prod_{j \in \partial_i^{\mathbf{A}}} \left(1 - \alpha(t)\hat{\tau}_j \hat{r}_j \right) \Bigg] \end{aligned} \tag{3.67}$$

where we have defined $k_i(\mathbf{A}) = |\partial_i^{\mathbf{A}}|$ the degree of node i in network $\mathbf{A}$, $\hat{\boldsymbol{r}} = (\hat{r}_1, \ldots, \hat{r}_k)$ the cavity fields of the neighbours of a site with degree k, $\hat{\boldsymbol{\tau}} = (\hat{\tau}_1, \ldots, \hat{\tau}_k)$ the labels that describe which links of a site with degree k have been deleted, $\mathrm{P}(\sigma) = N^{-1} \sum_i \delta_{\sigma,\sigma_i}$ the probability that a node has label σ,

and

$$\mathrm{W}_c(k,\sigma;\hat{\boldsymbol{\tau}},\hat{\boldsymbol{r}}|\mathbf{A}) = \frac{1}{N}\sum_{i=1}^{N}\delta_{k,k_i(\mathbf{A})}\delta_{\sigma,\sigma_i}\prod_{j\in\partial_i^{\mathbf{A}}}\delta(\hat{r}_j - r_j^{(i)}(\mathbf{A}))\delta_{\hat{\tau}_j,\tau_{ij}} \tag{3.68}$$

the likelihood that a site drawn at random in network $\mathbf{A}$ has degree k, label σ, and neighbours with cavity fields, $\hat{\boldsymbol{r}}$, with the links to these neighbours deleted according to $\hat{\boldsymbol{\tau}}$. We denote probability distributions of variables that are linked by an edge with $\mathrm{W}(\ ;\ )$. We have also denoted distributions which depend upon the cavity fields $\hat{\boldsymbol{r}}$ with a subscript c and refer to them as 'cavity distributions'. We note that integrating a cavity distribution W_c over its cavity fields leads to a normal (i.e. not cavity) distribution W. Furthermore, we note that integrating (3.68) over $\hat{\boldsymbol{\tau}}$ and $\hat{\boldsymbol{r}}$ leads to a distribution of single site variables, that we denote with P. For later reference, we will denote with Q distributions of single link quantities, in accordance with (3.63).

Using Bayes relation, we then have $\mathrm{W}_c(k,\sigma;\hat{\boldsymbol{\tau}},\hat{\boldsymbol{r}}|\mathbf{A}) = \mathrm{P}(k,\sigma|\mathbf{A})\mathrm{W}_c(\hat{\boldsymbol{\tau}},\hat{\boldsymbol{r}}|k,\mathbf{A})$ where we have used that, in the absence of correlations between node labels, and between node labels and link labels, the distribution $\mathrm{W}_c(\hat{\boldsymbol{\tau}},\hat{\boldsymbol{r}}|k,\mathbf{A})$ in the cavity graph where node i has been removed is independent of the label σ of node i. We proceed by writing $\mathrm{W}_c(\hat{\boldsymbol{\tau}},\hat{\boldsymbol{r}}|k,\mathbf{A}) = \sum_{\mathbf{q}}\mathrm{W}_c(\boldsymbol{q},\hat{\boldsymbol{\tau}},\hat{\boldsymbol{r}}|k,\mathbf{A})$ where $\mathbf{q} = (q_1,...,q_k)$ are the degrees of the neighbours of a node with degree k. Using Bayes relations, we can write $\mathrm{W}_c(\boldsymbol{q},\hat{\boldsymbol{\tau}},\hat{\boldsymbol{r}}|k,\mathbf{A}) = \mathrm{W}(\mathbf{q}|k,\mathbf{A})\mathrm{Q}(\hat{\boldsymbol{\tau}}|k,\mathbf{q})\mathrm{W}_c(\hat{\boldsymbol{r}}|\mathbf{A},k,\mathbf{q})$ where we have used the conditional independence of $\hat{\boldsymbol{r}}$ (when conditioned on the degrees k and $\mathbf{q}$), on $\hat{\boldsymbol{\tau}}$, in the cavity graph where node i and all its links have been removed. Here $\mathrm{Q}(\hat{\boldsymbol{\tau}}|k,\mathbf{q})$ is the joint distribution of deleting k links according to $\hat{\boldsymbol{\tau}}$. Here $\mathrm{W}_c(\hat{\boldsymbol{r}}|\mathbf{A},k,\mathbf{q})$ is the joint distribution of

the cavity fields $\hat{\boldsymbol{r}}$ given that the node removed from the cavity graph has degree k with neighbours with degrees $\mathbf{q}$. By equation (3.63) we have that $\mathrm{Q}(\hat{\boldsymbol{\tau}}|k,\mathbf{q}) = \prod_{j=1}^{k}\mathrm{Q}(\hat{\tau}_j|k,q_j)$. Furthermore, in the limit $N\to\infty$, by virtue of a locally tree-like assumption, $\mathrm{W}_c(\hat{\boldsymbol{r}}|\mathbf{A},k,\mathbf{q})$ also factorises $\mathrm{W}_c(\hat{\boldsymbol{r}}|\mathbf{A},k,\mathbf{q}) = \prod_{j=1}^{k}\mathrm{W}_c(\hat{r}_j|\mathbf{A},k,q_j)$, for any $k>0$. For $k=0$, we can set $\mathrm{W}_c(\hat{\boldsymbol{r}}|\mathbf{A},0,\mathbf{q}) = \delta(\hat{\boldsymbol{r}})$ as the product in (3.64) is empty and evaluates to one, regardless of $\hat{\boldsymbol{r}}$. When we insert this into (3.67) we find,

$$\begin{aligned} g(\mathbf{A}) = \sum_{\sigma,k\geq 0,\mathbf{q}} &\sigma \mathrm{P}(k,\sigma|\mathbf{A})\mathrm{W}(\mathbf{q}|k,\mathbf{A}) \\ &\times\left[1-\int_0^\infty \mathrm{d}t\,\gamma(t)\prod_{j=1}^{k}\Big(1-\alpha(t)y(k,q_j)\hat{g}_{k,q_j}(\mathbf{A})\Big)\right] \end{aligned} \tag{3.69}$$

where $\hat{g}_{k,q}(\mathbf{A}) = \int \mathrm{d}\hat{r}\mathrm{W}_c(\hat{r}|\mathbf{A},k,q)\,\hat{r}$ is the average contribution to the cavity field of a random node with degree k from a random neighbour with degree q. We now assume that the degrees of the neighbours of a random site with degree k are independent when conditioned upon k such that $\mathrm{W}(\mathbf{q}|k,\mathbf{A}) = \prod_{j=1}^{k}\mathrm{W}(q_j|k,\mathbf{A})$. While this assumption is only true for particular graph ensembles, it will act as a useful approximation for ensembles where it is not true, as it leads to a closed set of equations. Inserting this into (3.69) yields,

$$g(\mathbf{A}) = \sum_{k\geq 0}\mathrm{P}(k|\mathbf{A})x(k)\left[1-\int_0^\infty \mathrm{d}t\,\gamma(t)\prod_{j=1}^{k}(1-\alpha(t)\tilde{g}_k(\mathbf{A}))\right] \tag{3.70}$$

where

$$\tilde{g}_k(\mathbf{A}) = \sum_q \mathrm{W}(q|k,\mathbf{A}) y(k,q) \hat{g}_{k,q}. \tag{3.71}$$

To make progress, we need an equation for $\tilde{g}_k(\mathbf{A})$,

$$\begin{aligned}
\tilde{g}_k(\mathbf{A}) &= \sum_q \mathrm{W}(q|k,\mathbf{A}) y(k,q) \int \mathrm{d}\hat{r}\ \mathrm{W}_c(\hat{r}|k,q,\mathbf{A})\hat{r} && (3.72)\\
&= \sum_q \mathrm{W}(q|k,\mathbf{A}) y(k,q) \int \mathrm{d}\hat{\boldsymbol{r}} \frac{\mathrm{W}_c(k;\hat{\boldsymbol{r}},q|\mathbf{A})}{\mathrm{P}(k|\mathbf{A})\mathrm{W}(q|k,\mathbf{A})} \frac{1}{k}\sum_{j=1}^{k}\hat{r}_j && (3.73)\\
&= \sum_q \mathrm{W}(q|k,\mathbf{A}) y(k,q) \sum_{\mathbf{q}} \int \mathrm{d}\hat{\boldsymbol{r}} \frac{\mathrm{W}_c(k;\hat{\boldsymbol{r}},\mathbf{q}|\mathbf{A})}{\mathrm{P}(k|\mathbf{A})\mathrm{W}(q|k,\mathbf{A})} \frac{1}{k}\sum_{j=1}^{k}\hat{r}_j\delta_{q,q_j} && (3.74)\\
&= \sum_q \frac{y(k,q)}{k\mathrm{P}(k|\mathbf{A})} \sum_{j=1}^{k}\sum_{\mathbf{q}} \int \mathrm{d}\hat{\boldsymbol{r}} \frac{1}{N}\sum_i^N \delta_{k,k_i(\mathbf{A})}[\prod_{l\in\partial_i^{\mathbf{A}}}\delta_{q_l,k_l(\mathbf{A})}\delta(\hat{r}_l - r_l^{(i)}(\mathbf{A}))]\hat{r}_j\delta_{q,q_j} && \\
&= \sum_q \frac{y(k,q)}{k\mathrm{P}(k|\mathbf{A})} \sum_{j=1}^{k} \int \mathrm{d}\hat{\boldsymbol{r}} \frac{1}{N}\sum_i^N \delta_{k,k_i(\mathbf{A})}[\prod_{l\in\partial_i^{\mathbf{A}}}\delta(\hat{r}_l - r_l^{(i)}(\mathbf{A}))]\hat{r}_j\delta_{q,k_j} && \\
&= \sum_q \frac{y(k,q)}{k\mathrm{P}(k|\mathbf{A})} \frac{1}{N}\sum_{j=1}^{k}\sum_i^N A_{ij}\delta_{k,k_i(\mathbf{A})}\delta_{q,k_j(\mathbf{A})}\hat{r}_j^{(i)}(\mathbf{A}) && (3.75)
\end{aligned}$$

where we have used Bayes relations and the definition

$$\mathrm{W}_c(k;\mathbf{q},\hat{\boldsymbol{r}}|\mathbf{A}) = \frac{1}{N}\sum_i^N \delta_{k,k_i(\mathbf{A})}[\prod_{j\in\partial_i^{\mathbf{A}}}\delta_{q_j,k_j(\mathbf{A})}\delta(\hat{r}_j - r_j^{(i)}(\mathbf{A}))]$$

Hence, using the cavity equation (3.65) we find an expression for $\tilde{g}_k$ as follows,

$$\begin{aligned}
\tilde{g}_k(\mathbf{A}) &= \sum_q \frac{y(k,q)}{Nk\mathrm{P}(k|\mathbf{A})} \sum_{i,j=1}^{N} A_{ij}\delta_{k,k_i(\mathbf{A})}\delta_{q,k_j(\mathbf{A})}\sigma_j \\
&\quad \times \left[1 - \int_0^\infty \mathrm{d}t\gamma(t) \prod_{\ell\in\partial_j^{\mathbf{A}}\setminus i} \left(1-\alpha(t)\tau_{j\ell}r_\ell^{(j)}\right)\right] \\
&= \sum_q \frac{y(k,q)}{Nk\mathrm{P}(k|\mathbf{A})} \left[\prod_{\ell\in\partial_j^{\mathbf{A}}\setminus i} \int \mathrm{d}\hat{r}'_\ell \delta(\hat{r}'_\ell - r_\ell^{(j)}) \sum_{\hat{\tau}'_\ell} \delta_{\hat{\tau}'_\ell,\tau_{j\ell}}\right] \\
&\quad \times \sum_\sigma \sum_{i,j=1}^{N} A_{ij}\delta_{k,k_i(\mathbf{A})}\delta_{q,k_j(\mathbf{A})}\delta_{\sigma,\sigma_j}\sigma \left[1 - \int_0^\infty \mathrm{d}t\,\gamma(t) \prod_{\ell=1}^{q-1} \left(1-\alpha(t)\hat{\tau}'_\ell\hat{r}'_\ell\right)\right] \\
&= \sum_q \frac{y(k,q)\bar{k}(\mathbf{A})}{k\mathrm{P}(k|\mathbf{A})} \int \mathrm{d}\hat{\boldsymbol{r}}' \sum_{\hat{\boldsymbol{\tau}}'} \sum_\sigma \mathrm{W}_c(k;q,\sigma;\hat{\boldsymbol{\tau}}',\hat{\boldsymbol{r}}'|\mathbf{A})\sigma \\
&\quad \times \left[1 - \int_0^\infty \mathrm{d}t\,\gamma(t) \prod_{\ell=1}^{q-1} \left(1-\alpha(t)\hat{\tau}'_\ell\hat{r}'_\ell\right)\right]
\end{aligned} \tag{3.76}$$

where

$$\mathrm{W}_c(k;q,\sigma;\hat{\boldsymbol{\tau}}',\hat{\boldsymbol{r}}'|\mathbf{A}) = \frac{\sum_{ij} A_{ij}\delta_{k,k_i(\mathbf{A})}\delta_{\sigma,\sigma_j}\,\delta_{q,k_j(\mathbf{A})}[\prod_{\ell\in\partial_j^{\mathbf{A}}\setminus i}\delta(\hat{r}'_\ell - r_\ell^{(j)}(\mathbf{A}))\delta_{\hat{\tau}'_\ell,\tau_{j\ell}}]}{N\bar{k}(\mathbf{A})} \tag{3.77}$$

is the likelihood that a randomly drawn link connects a node i with degree k to a node j with degree q, label σ and neighbours (i excluded) with cavity fields $\hat{\boldsymbol{r}}' = (\hat{r}'_1,\ldots,\hat{r}'_{q-1})$ and links deleted according to $\hat{\boldsymbol{\tau}}' = (\hat{\tau}'_1,\ldots,\hat{\tau}'_{q-1})$. We next use Bayes and the independence of $\hat{\boldsymbol{\tau}}'$ and $\hat{\boldsymbol{r}}'$ on σ when conditioned on q to write $\mathrm{W}_c(k;q,\sigma;\hat{\boldsymbol{\tau}}',\hat{\boldsymbol{r}}'|\mathbf{A}) = \mathrm{W}(k;q,\sigma|\mathbf{A})\mathrm{W}_c(\hat{\boldsymbol{\tau}}',\hat{\boldsymbol{r}}'|k,q,\mathbf{A})$ and write $\mathrm{W}_c(\hat{\boldsymbol{\tau}}',\hat{\boldsymbol{r}}'|k,q,\mathbf{A}) = \sum_{\mathbf{q}'}\mathrm{W}_c(\hat{\boldsymbol{\tau}}',\hat{\boldsymbol{r}}',\mathbf{q}'|k,q,\mathbf{A})$ where $\mathbf{q}' = (q'_1,\ldots,q'_{q-1})$ are the degrees of the neighbours of a node with degree q, excluding the neighbour

with degree k. Using again the independence of $\hat{\boldsymbol{r}}'$ and $\hat{\boldsymbol{\tau}}'$ when conditioned on the degrees q and $\mathbf{q}'$, we have $\mathrm{W}_c(\hat{\boldsymbol{\tau}}', \hat{\boldsymbol{r}}', \mathbf{q}'|k, q, \mathbf{A}) = \mathrm{W}(\mathbf{q}'|q, \mathbf{A})\mathrm{Q}(\hat{\boldsymbol{\tau}}'|q, \mathbf{q}')$ $\mathrm{W}_c(\hat{\boldsymbol{r}}'|q', \mathbf{q}', \mathbf{A})$ where we also note that $\mathbf{q}'$, $\hat{\boldsymbol{r}}'$ and $\hat{\boldsymbol{\tau}}'$ are independent of k when conditioned on q. By equation (3.63) the $\hat{\boldsymbol{\tau}}'$ factorise, in addition to the $\hat{\boldsymbol{r}}'$ which factorise under the tree-like assumption, and we again assume that $\mathbf{q}'$ factorise when conditioned on q, hence we have

$$\mathrm{W}_c(\mathbf{q}'|q, \mathbf{A})\mathrm{Q}(\hat{\boldsymbol{\tau}}'|q, \mathbf{q}')\mathrm{W}_c(\hat{\boldsymbol{r}}'|q, \mathbf{q}', \mathbf{A}) = \prod_{\ell=1}^{q-1} \mathrm{W}(q'_\ell|q, \mathbf{A})\mathrm{Q}(\hat{\tau}'_\ell|q, q'_\ell)\mathrm{W}_c(\hat{r}'_\ell|q, q'_\ell, \mathbf{A}). \tag{3.78}$$

Inserting this into (3.76) leads to the system of equations,

$$\begin{aligned}\tilde{g}_k(\mathbf{A}) = &\sum_{q\geq 1}\sum_{\sigma} y(k,q)\frac{\mathrm{W}(k;q,\sigma|\mathbf{A})}{\mathrm{W}(k|\mathbf{A})}\sigma \\ &\times\left[1-\int_0^\infty \mathrm{d}t\,\gamma(t)\left(1-\alpha(t)\sum_{q'}\mathrm{W}(q'|q,\mathbf{A})y(q,q')\hat{g}_{q,q'}(\mathbf{A})\right)^{q-1}\right]\end{aligned} \tag{3.79}$$

where $\mathrm{W}(k|\mathbf{A}) = \sum_q \mathrm{W}(k;q|\mathbf{A}) = k\mathrm{P}(k|\mathbf{A})/\bar{k}(\mathbf{A})$ and the sum over q has been restricted to $q \geq 1$, as $\mathrm{W}(k;q|\mathbf{A})$ vanishes for $q = 0$. Finally, by using (3.71) we have the following set of equations

$$g(\mathbf{A}) = \sum_{k\geq 0}\mathrm{P}(k|\mathbf{A})x(k)\left[1-\int_0^\infty \mathrm{d}t\,\gamma(t)(1-\alpha(t)\tilde{g}_k(\mathbf{A}))^k\right] \tag{3.80}$$

$$\tilde{g}_k(\mathbf{A}) = \sum_{q\geq 1} y(k,q)\mathrm{W}(q|k,\mathbf{A})x(q)\left[1-\int_0^\infty \mathrm{d}t\,\gamma(t)\left(1-\alpha(t)\tilde{g}_q(\mathbf{A})\right)^{q-1}\right] \tag{3.81}$$

where we have used (3.62) and denoted $\mathrm{W}(q|k,\mathbf{A}) = \mathrm{W}(k;q|\mathbf{A})/\mathrm{W}(k|\mathbf{A})$. These show that the global risk $g(\mathbf{A})$ has the same self-averaging properties

of $P(k|\mathbf{A})$ and $W(k;q|\mathbf{A})$. If the set of equations (3.81) is solved numerically, the solution can be substituted into equation (3.80) to find the global risk.

3.B Stochastic simulations of the SIR model on networks

All simulations used for comparison with the results of the cavity equations were performed using the Python package "Epidemics on Networks" (228). This package contains an extensive number of functions for the analysis of different compartmental models of epidemics on networks. For the simulation of the SIR model, one can use one of two functions `Gillespie_SIR`, which uses the Gillespie algorithm (226), and `fast_SIR` which provides a faster method to simulate the SIR model when nodes have exponential recovery and infection rate (227). Figures 3.2 and 3.3 were created using `Gillespie_SIR` whereas all other figures that compare simulations to the cavity equations made use of `fast_SIR`. The choice of which of the two functions we used did not affect our results, but `fast_SIR` was found to be significantly quicker and hence was used for the majority of figures. Below, we provide an example of Python code to compute the risk of each node in an ER network.

```
import numpy as np
import numpy.random as rn
import networkx as nx
import EoN as eon
```

```
N = 2500 #Number of nodes in network
mean_degree = 5 #Mean degree of network
p = mean_degree/N #Probability that a pair of nodes are linked
G = nx.erdos_renyi_graph(N, p) #draw ER graph
Ninits = 100 #Number of initialisations
Nseeds = 100 #Number of repetitions starting
             #from the same intial infected node
beta = 0.5 #rate of infection
xi = 2 #rate of recovery
number_infected = np.zeros((Ninits,Nseeds))
for i in range(Ninits):
    #Choose a node at random to be infected
    initial_node = rn.choice(np.arange(0,N,1))
    for j in range(Nseeds):
        #Run SIR simulation
        t,S,I,R = eon.fast_SIR(G, beta, xi,
                               initial_infecteds = initial_node)
        #Store total number of individuals who became infected
        number_infected[i,j] = R[-1]


risk = np.zeros(Ninits)
threshold = 0.01*N #small threshold to determine if an epidemic occured
for i in range(Ninits):
    #The risk of a node is computed as the fraction of simulations starting
    #with that node infected that lead to a significant
```

```
#number of nodes infected
risk[i] = np.sum(number_infected[i,:] > threshold)/Nseeds
```

3.C Risk with heterogeneous transmission and link deletion

In this section we find closed equations for the global risk when nodes have heterogeneous transmissibility. For brevity we do not consider node deletion in this section. We consider link deletion but now based upon the label and degree of nodes, such that,

$$\mathrm{Q}(\tau_{ij}) = \big(1 - y(k_i, \xi_i, k_j, \xi_j)\big)\, \delta_{\tau_{ij},0} + y(k_i, \xi_i, k_j, \xi_j)\delta_{\tau_{ij},1} \tag{3.82}$$

where $1 - y(k, \xi, k', \xi')$ is the probability of deleting a link with a node with degree k and label ξ at one end and a node with degree k' and label ξ' at the other. Summing (3.37) over i, dividing by N and inserting unity in the form

$$1 = \sum_{\xi} \delta_{\xi,\xi_i} \sum_{k\geq 0} \delta_{k,|\partial_i^{\mathbf{A}}|} \prod_{j\in\partial_i^{\mathbf{A}}} \int \mathrm{d}\hat{r}_j\, \delta(\hat{r}_j - r_j^{(i)}(\mathbf{A})) \sum_{\hat{\tau}_j} \delta_{\hat{\tau}_j,\tau_{ij}} \tag{3.83}$$

we obtain

$$\begin{aligned} g(\mathbf{A},\boldsymbol{\xi}) &= 1-\frac{1}{N}\sum_{i=1}^{N}\sum_{k\geq 0}\delta_{k,k_i(\mathbf{A})}\sum_{\xi}\delta_{\xi,\xi_i}\left[\prod_{j\in\partial_i^{\mathbf{A}}}\int \mathrm{d}\hat{r}_j\,\delta(\hat{r}_j-r_j^{(i)}(\mathbf{A},\boldsymbol{\xi}))\sum_{\hat{\tau}_j}\delta_{\hat{\tau}_j,\tau_{ij}}\right] \\ &\quad\times\int_0^{\infty}\mathrm{d}t\gamma(t|\xi)\prod_{j\in\partial_i^{\mathbf{A}}}(1-\alpha(t)\hat{\tau}_j\hat{r}_j) \\ &= 1-\sum_{k\geq 0,\xi,\hat{\boldsymbol{\tau}}}\int \mathrm{d}\hat{\boldsymbol{r}}\,\mathrm{W}_c(k,\xi;\hat{\boldsymbol{r}},\hat{\boldsymbol{\tau}}|\mathbf{A},\boldsymbol{\xi})\int_0^{\infty}\mathrm{d}t\,\gamma(t|\xi)\prod_{j\in\partial_i^{\mathbf{A}}}\left(1-\alpha(t)\hat{\tau}_j\hat{r}_j\right) \end{aligned} \tag{3.84}$$

where we have defined $\hat{\boldsymbol{r}}=(\hat{r}_1,\ldots,\hat{r}_k)$ and

$$\mathrm{W}_c(k,\xi;\hat{\boldsymbol{r}},\hat{\boldsymbol{\tau}}|\mathbf{A},\boldsymbol{\xi})=\frac{1}{N}\sum_{i=1}^{N}\delta_{k,k_i(\mathbf{A})}\delta_{\xi,\xi_i}\prod_{j\in\partial_i^{\mathbf{A}}}\delta(\hat{r}_j-r_j^{(i)}(\mathbf{A},\boldsymbol{\xi}))\delta_{\hat{\tau}_j,\tau_{ij}} \tag{3.85}$$

the likelihood that a site drawn at random in network $\mathbf{A}$ has degree k, label ξ and neighbours with cavity fields $\hat{\boldsymbol{r}}=(\hat{r}_1,\ldots,\hat{r}_k)$, and links deleted according to $\hat{\boldsymbol{\tau}}=(\hat{\tau}_1,\ldots,\hat{\tau}_k)$. Similarly to before, we use Bayes relation to write $\mathrm{W}_c(k,\xi;\hat{\boldsymbol{r}},\hat{\boldsymbol{\tau}}|\mathbf{A},\boldsymbol{\xi})=\mathrm{P}(k,\xi|\mathbf{A},\boldsymbol{\xi})\mathrm{W}_c(\hat{\boldsymbol{r}},\hat{\boldsymbol{\tau}}|k,\xi,\mathbf{A},\boldsymbol{\xi})$ and we then write $\mathrm{W}_c(\hat{\boldsymbol{r}},\hat{\boldsymbol{\tau}}|k,\xi,\mathbf{A},\boldsymbol{\xi})=\sum_{\boldsymbol{\zeta},\mathbf{q}}\mathrm{W}_c(\hat{\boldsymbol{r}},\hat{\boldsymbol{\tau}},\boldsymbol{\zeta},\mathbf{q}|k,\xi,\mathbf{A},\boldsymbol{\xi})$, where $\boldsymbol{\zeta}=(\zeta_1,\ldots,\zeta_k)$ and $\mathbf{q}=(q_1,\ldots,q_k)$ are the labels and degrees of the neighbours of a random site with degree k and label ξ. Using Bayes theorem this becomes $\mathrm{W}_c(\hat{\boldsymbol{r}},\hat{\boldsymbol{\tau}},\boldsymbol{\zeta},\mathbf{q}|k,\xi,\mathbf{A},\boldsymbol{\xi})=\mathrm{W}(\boldsymbol{\zeta},\mathbf{q}|k,\xi,\mathbf{A},\boldsymbol{\xi})\mathrm{Q}(\hat{\boldsymbol{\tau}}|k,\xi,\boldsymbol{\zeta},\mathbf{q})\mathrm{W}_c(\hat{\boldsymbol{r}}|k,\xi,\boldsymbol{\zeta},\mathbf{q},\mathbf{A},\boldsymbol{\xi})$ where we have also used the independence of $\hat{\boldsymbol{\tau}}$ and $\hat{\boldsymbol{r}}$ when conditioned on $\boldsymbol{\zeta}$ and $\mathbf{q}$. For $k=0$ we can set $\mathrm{W}_c(\hat{\boldsymbol{r}}|0,\xi,\boldsymbol{\zeta},\mathbf{q},\mathbf{A},\boldsymbol{\xi})=\delta(\hat{\boldsymbol{r}})$ as the products in (3.84) evaluate to one. In the limit $N\to\infty$, by virtue of a locally tree-like assumption, the joint distribution of the cavity fields $\hat{\boldsymbol{r}}$ factorises $\mathrm{W}_c(\hat{\boldsymbol{r}}|k,\xi,\boldsymbol{\zeta},\mathbf{q},\mathbf{A},\boldsymbol{\xi})=\prod_{j=1}^{k}\mathrm{W}_c(\hat{r}_j|k,\xi,q_j,\zeta_j,\mathbf{A},\boldsymbol{\xi})$, as does $\mathrm{Q}(\hat{\boldsymbol{\tau}}|k,\xi,\boldsymbol{\zeta},\mathbf{q})=$

$\prod_{j=1}^{k} \mathrm{Q}(\hat{\tau}_j|k,\xi,q_j,\zeta_j)$ by equation (3.82). Again, we assume the degrees and labels of the neighbours of a random site with degree k and label ξ, are independent, when conditioned on the degree k and label ξ, such that $\mathrm{W}(\boldsymbol{\zeta},\mathbf{q}|k,\xi,\mathbf{A},\boldsymbol{\xi}) = \prod_{j=1}^{k} \mathrm{W}(\zeta_j,q_j|k,\xi,\mathbf{A},\boldsymbol{\xi})$. As noted above, although this is only true for particular graph ensembles, it acts as a useful approximation for ensembles where it is not true, as it leads to a closed set of equations. When this is inserted into (3.84) we find,

$$g(\mathbf{A},\boldsymbol{\xi}) = 1 - \sum_{k,\xi} \mathrm{P}(k,\xi|\mathbf{A},\boldsymbol{\xi}) \int_0^\infty \mathrm{d}t\, \gamma(t|\xi) \left(1-\alpha(t)\tilde{g}_{k,\xi}(\mathbf{A},\boldsymbol{\xi})\right)^k \tag{3.86}$$

where $\tilde{g}_{k,\xi}(\mathbf{A},\boldsymbol{\xi}) = \sum_{q,\xi'} \mathrm{W}(q,\zeta|k,\xi,\mathbf{A},\boldsymbol{\xi}) y(k,\xi,q,\zeta) \int \mathrm{d}\hat{r} \mathrm{W}_c(\hat{r}'|k,\xi,q,\zeta,\mathbf{A},\boldsymbol{\xi})\,\hat{r}$ is the average cavity field of a random neighbour of a random node with degree k and label ξ. To make progress, we need an equation for $\tilde{g}_{k,\xi}(\mathbf{A},\boldsymbol{\xi})$. To this end we can write $\tilde{g}_{k,\xi}(\mathbf{A},\boldsymbol{\xi})$ as

$$\begin{aligned}
\hat{g}_{k,\xi}(\mathbf{A},\boldsymbol{\xi}) &= \sum_{q,\zeta} \mathrm{W}(q,\zeta|k,\xi,\mathbf{A},\boldsymbol{\xi}) y(k,\xi,q,\zeta) \int \mathrm{d}\hat{r} \mathrm{W}_c(\hat{r}|k,\xi,q,\zeta,\mathbf{A},\boldsymbol{\xi})\,\hat{r} \\
&= \sum_{q,\zeta} y(k,\xi,q,\zeta) \int \mathrm{d}\hat{\boldsymbol{r}}\, \frac{\mathrm{W}_c(k,\xi;q,\zeta,\hat{\boldsymbol{r}}|\mathbf{A},\boldsymbol{\xi})}{\mathrm{P}(k,\xi|\mathbf{A},\boldsymbol{\xi})} \frac{1}{k} \sum_{j=1}^{k} \hat{r}_j \\
&= \sum_{q,\zeta} y(k,\xi,q,\zeta) \sum_{\mathbf{q},\boldsymbol{\zeta}} \int \mathrm{d}\hat{\boldsymbol{r}}\, \frac{\mathrm{W}_c(k,\xi;\mathbf{q},\boldsymbol{\zeta},\hat{\boldsymbol{r}}|\mathbf{A},\boldsymbol{\xi})}{\mathrm{P}(k,\xi|\mathbf{A},\boldsymbol{\xi})} \frac{1}{k} \sum_{j=1}^{k} \hat{r}_j \delta_{q,q_j} \delta_{\zeta,\zeta_j} \\
&= \sum_{q,\zeta} \frac{y(k,\xi,q,\zeta)}{k\mathrm{P}(k,\xi|\mathbf{A},\boldsymbol{\xi})} \sum_{j=1}^{k} \sum_{\mathbf{q},\boldsymbol{\zeta}} \int \mathrm{d}\hat{\boldsymbol{r}}\, \frac{1}{N} \sum_i \delta_{k,k_i(\mathbf{A})} \delta_{\xi,\xi_i} \\
&\quad \times \left[\prod_{l \in \partial_i^{\mathbf{A}}} \delta(\hat{r}_l - r_l^{(i)}(\mathbf{A},\boldsymbol{\xi})) \delta_{q_l,k_l(\mathbf{A})} \delta_{\zeta_l,\xi_l} \right] \hat{r}_j \delta_{q,q_j} \delta_{\zeta,\zeta_j} \\
&= \sum_{q,\zeta} \frac{y(k,\xi,q,\zeta)}{Nk\mathrm{P}(k,\xi|\mathbf{A},\boldsymbol{\xi})} \sum_{i,j=1}^{N} A_{ij} \delta_{k,k_i(\mathbf{A})} \delta_{\xi,\xi_i} \delta_{q,k_j(\mathbf{A})} \delta_{\zeta,\xi_j} r_j^{(i)}(\mathbf{A},\boldsymbol{\xi})
\end{aligned} \tag{3.87}$$

Hence, using the cavity equation (3.38) we find an expression for $\tilde{g}_{k,\xi}$ as follows,

$$\begin{aligned}
\tilde{g}_{k,\xi}(\mathbf{A},\boldsymbol{\xi}) &= \sum_{q,\zeta} \frac{y(k,\xi,q,\zeta)}{Nk\mathrm{P}(k,\xi|\mathbf{A},\boldsymbol{\xi})} \sum_{i,j=1}^{N} A_{ij}\delta_{k,k_i(\mathbf{A})}\delta_{\xi,\xi_i}\delta_{q,k_j(\mathbf{A})}\delta_{\zeta,\xi_j} r_j^{(i)}(\mathbf{A},\boldsymbol{\xi}) \\
&= \sum_{q,\zeta} \frac{y(k,\xi,q,\zeta)}{Nk\mathrm{P}(k,\xi|\mathbf{A},\boldsymbol{\xi})} \sum_{i,j=1}^{N} A_{ij}\delta_{k,k_i(\mathbf{A})}\delta_{\xi,\xi_i}\delta_{q,k_j(\mathbf{A})}\delta_{\zeta,\xi_j} \\
&\quad \times \left\{ \prod_{\ell\in\partial_j^{\mathbf{A}}\setminus i} \int \mathrm{d}\hat{r}'_\ell\, \delta(\hat{r}'_\ell - r_\ell^{(j)}(\mathbf{A},\boldsymbol{\xi})) \sum_{\hat{\tau}'_\ell} \delta_{\hat{\tau}'_\ell,\tau_{j\ell}} \right\} \\
&\quad \times \left[1 - \int_0^\infty \mathrm{d}t\, \gamma(t|\zeta) \prod_{\ell\in\partial_j^{\mathbf{A}}\setminus i} \left(1-\alpha(t)\hat{\tau}'_\ell\hat{r}'_\ell\right) \right] \\
&= \sum_{q,\zeta} \frac{y(k,\xi,q,\zeta)}{k\mathrm{P}(k,\xi|\mathbf{A},\boldsymbol{\xi})} \sum_{\hat{\boldsymbol{\tau}}'} \int \mathrm{d}\hat{\boldsymbol{r}}' \mathrm{W}_c(k,\xi;q,\zeta;\hat{\boldsymbol{\tau}}',\hat{\boldsymbol{r}}'|\mathbf{A},\boldsymbol{\xi}) \\
&\quad \times \left[1 - \int_0^\infty \mathrm{d}t\, \gamma(t|\zeta) \prod_{\ell=1}^{q-1} \left(1-\alpha(t)\hat{\tau}'_\ell\hat{r}'_\ell\right) \right]
\end{aligned} \tag{3.88}$$

where

$$\begin{aligned}
\mathrm{W}_c(k,\xi;q,\zeta;\hat{\boldsymbol{\tau}}',\hat{\boldsymbol{r}}'|\mathbf{A},\boldsymbol{\xi}) = \frac{1}{N\bar{k}(\mathbf{A})} \sum_{ij} A_{ij}\delta_{k,k_i(\mathbf{A})}\,\delta_{q,k_j(\mathbf{A})}\delta_{\xi,\xi_i}\delta_{\zeta,\xi_j} \\
\times \prod_{\ell\in\partial_j^{\mathbf{A}}\setminus i} \delta(\hat{r}'_\ell - r_\ell^{(j)}(\mathbf{A},\boldsymbol{\xi}))\delta_{\hat{\tau}'_\ell,\tau_{j\ell}}
\end{aligned} \tag{3.89}$$

is the likelihood that a randomly drawn link connects a node i with degree k and label ξ to a node j with degree q, label ζ and neighbours (excluded i) with cavity fields $\hat{\boldsymbol{r}}' = (\hat{r}'_1,\ldots,\hat{r}'_{q-1})$ with links deleted according to $\hat{\boldsymbol{\tau}}' = (\hat{\tau}'_1,\ldots,\hat{\tau}'_{q-1})$. By Bayes theorem $\mathrm{W}_c(k,\xi;q,\zeta;\hat{\boldsymbol{\tau}}',\hat{\boldsymbol{r}}'|\mathbf{A},\boldsymbol{\xi}) = \mathrm{W}(k,\xi;q,\zeta|\mathbf{A},\boldsymbol{\xi})$

$W_c(\hat{\boldsymbol{\tau}}', \hat{\boldsymbol{r}}'|k, \xi, q, \zeta, \mathbf{A}, \boldsymbol{\xi})$ and we my then write $W_c(\hat{\boldsymbol{\tau}}', \hat{\boldsymbol{r}}'|k, \xi, q, \zeta, \mathbf{A}, \boldsymbol{\xi}) = \sum_{\mathbf{q}', \zeta'} W_c(\mathbf{q}', \boldsymbol{\zeta}', \hat{\boldsymbol{\tau}}', \hat{\boldsymbol{r}}'|k, \xi, q, \zeta, \mathbf{A}, \boldsymbol{\xi})$ where $\mathbf{q}' = (q'_1, \ldots, q'_{q-1})$ and $\boldsymbol{\zeta}' = (\zeta'_1, \ldots, \zeta'_{q-1})$ are the degrees and labels of the neighbours of a site with degree q and label ζ which is itself connected to a site with degree k and label ξ. By Bayes theorem we may write, $W_c(\mathbf{q}', \boldsymbol{\zeta}', \hat{\boldsymbol{\tau}}', \hat{\boldsymbol{r}}'|k, \xi, q, \zeta, \mathbf{A}, \boldsymbol{\xi}) = W(\mathbf{q}', \boldsymbol{\zeta}'|q, \xi, \mathbf{A}, \boldsymbol{\xi}) \times Q(\hat{\boldsymbol{\tau}}', \hat{\boldsymbol{r}}'|q, \xi, \mathbf{q}', \boldsymbol{\zeta}') W_c(\hat{\boldsymbol{r}}'|q, \xi, \mathbf{q}', \boldsymbol{\zeta}', \mathbf{A}, \boldsymbol{\xi})$, and noted that $\hat{\boldsymbol{\tau}}'$ and $\hat{\boldsymbol{r}}'$ are independent when conditioned on the labels and degrees. We have also noted that $\mathbf{q}'$, $\boldsymbol{\zeta}'$, $\hat{\boldsymbol{\tau}}'$ and $\hat{\boldsymbol{r}}'$ are independent of k and ξ. By equation (3.82) we have $Q(\hat{\boldsymbol{\tau}}'|q, \xi, \mathbf{q}', \boldsymbol{\zeta}') = \prod_{l=1}^{q-1} Q(\hat{\tau}'_\ell|q, \xi, q'_\ell, \zeta'_\ell)$ and by the tree-like assumption $W_c(\hat{\boldsymbol{r}}'|q, \xi, \mathbf{q}', \boldsymbol{\zeta}', \mathbf{A}, \boldsymbol{\xi}) = \prod_{\ell=1}^{q-1} W_c(\hat{r}'_\ell|q, \xi, q'_\ell, \zeta'_\ell, \mathbf{A}, \boldsymbol{\xi})$. Furthermore, we again assume that degrees and labels of neighbours factorise when conditioned upon the degree and labels of their neighbours i.e. $W(\mathbf{q}', \boldsymbol{\zeta}'|q, \xi, \mathbf{A}, \boldsymbol{\xi}) = \prod_{\ell=1}^{q-1} W(q'_\ell, \zeta'_\ell|q, \xi, \mathbf{A}, \boldsymbol{\xi})$. Inserting this into (3.88) leads to a closed set of equations for $\tilde{g}_{k,\xi}(\mathbf{A}, \boldsymbol{\xi})$,

$$\begin{aligned} \tilde{g}_{k,\xi}(\mathbf{A}, \boldsymbol{\xi}) &= \sum_{q,\zeta} y(k, \xi, q, \zeta) W(q, \zeta|k, \xi, \mathbf{A}, \boldsymbol{\xi}) \\ &\quad \times \left[1 - \int_0^\infty \mathrm{d}t\, \gamma(t|\zeta) \left(1 - \alpha(t)\, \tilde{g}_{q,\zeta}(\mathbf{A}, \boldsymbol{\xi}) \right)^{q-1} \right]. \end{aligned} \tag{3.90}$$

Assuming that $P(k, \xi|\mathbf{A}, \boldsymbol{\xi})$ and $W(q, \zeta|k, \xi, \mathbf{A}, \boldsymbol{\xi})$ are self-averaging over the graph ensemble and the node label distribution, we finally average equations (3.86) and (3.90) over the distribution $P(\mathbf{A}, \boldsymbol{\xi})$ of graphs and node labels, ob-

taining

$$g = 1 - \sum_{k,\xi} \mathrm{P}(k,\xi) \int_0^\infty \mathrm{d}t\, \gamma(t|\xi) \left(1 - \alpha(t)\, \tilde{g}_{k,\xi}\right)^k \tag{3.91}$$

$$\tilde{g}_{k,\xi} = \sum_{q,\zeta} y(k,\xi,q,\zeta) \mathrm{W}(q,\zeta|k,\xi) \left[1 - \int_0^\infty \mathrm{d}t\, \gamma(t|\zeta) \left(1 - \alpha(t)\, \tilde{g}_{q,\zeta}\right)^{q-1}\right] \tag{3.92}$$

where $\mathrm{P}(k,\xi) = \langle \mathrm{P}(k,\xi|\mathbf{A},\boldsymbol{\xi}) \rangle_{\mathbf{A},\boldsymbol{\xi}}$ and $\mathrm{W}(q,\zeta|k,\xi) = \langle \mathrm{W}(q,\zeta|k,\xi,\mathbf{A},\boldsymbol{\xi}) \rangle_{\mathbf{A},\boldsymbol{\xi}}$ with $\langle \cdot \rangle_{\mathbf{A},\boldsymbol{\xi}} = \sum_{\mathbf{A},\boldsymbol{\xi}} \cdot \mathrm{P}(\mathbf{A},\boldsymbol{\xi})$.

3.D An ensemble of networks linking nodes of similar or dissimilar transmissability

In this section we derive relations for the average degree distribution $\mathrm{P}(k|\boldsymbol{\xi})$ and average degree correlations $\mathrm{W}(k,\xi;k',\xi'|\boldsymbol{\xi})$ for networks drawn from the ensemble

$$\mathrm{P}(\boldsymbol{A}|\boldsymbol{\xi}) = \prod_{i<j} \left[\frac{\langle k \rangle}{N} \frac{\mathrm{W}(\xi_i;\xi_j)}{\mathrm{P}(\xi_i)\mathrm{P}(\xi_j)} \delta_{A_{ij},1} + \left(1 - \frac{\langle k \rangle}{N} \frac{\mathrm{W}(\xi_i;\xi_j)}{\mathrm{P}(\xi_i)\mathrm{P}(\xi_j)}\right) \delta_{A_{ij},0} \right] \tag{3.93}$$

considered in (3.31), in the limit of large network size $N \to \infty$. We start by computing $\mathrm{P}(k|\boldsymbol{\xi})$, the probability of a node to have degree k in a network with node labels $\boldsymbol{\xi} = (\xi_1, \ldots, \xi_N)$, which is written as the ensemble average,

$$\mathrm{P}(k|\boldsymbol{\xi}) = \sum_{\boldsymbol{A}} \mathrm{P}(\boldsymbol{A}|\boldsymbol{\xi}) \mathrm{P}(k|\boldsymbol{A}) \tag{3.94}$$

of the degree distribution for the single network instance

$$\mathrm{P}(k|\boldsymbol{A},\boldsymbol{\xi}) \;=\; \frac{1}{N}\sum_{i=1}^{N}\delta_{k,\sum_{j(\neq i)}A_{ij}}. \tag{3.95}$$

Inserting (3.95) and (3.93) into (3.94), writing $\mathrm{P}(\mathbf{A}|\boldsymbol{\xi}) = \prod_{i<j}\mathrm{P}(A_{ij}|\boldsymbol{\xi})$ and using Fourier representations of Kronecker delta-functions, as well as the symmetric property of the adjacency matrix $A_{ij} = A_{ji}$, we get

$$\begin{aligned}
\mathrm{P}(k|\boldsymbol{\xi}) &= \frac{1}{N}\sum_{i}\sum_{\boldsymbol{A}}\int\frac{\mathrm{d}\omega}{2\pi}\mathrm{e}^{\mathrm{i}\omega k-\mathrm{i}\omega\sum_{j(\neq i)}A_{ij}}\prod_{k<j}\mathrm{P}(A_{kj}|\boldsymbol{\xi})\\
&= \frac{1}{N}\sum_{i}\sum_{\boldsymbol{A}}\int\frac{\mathrm{d}\omega}{2\pi}\mathrm{e}^{\mathrm{i}\omega k-\mathrm{i}\omega\sum_{k\neq j}A_{kj}\delta_{ki}}\prod_{k<j}\mathrm{P}(A_{kj}|\boldsymbol{\xi})\\
&= \frac{1}{N}\sum_{i}\sum_{\boldsymbol{A}}\int\frac{\mathrm{d}\omega}{2\pi}\mathrm{e}^{i\omega k-i\omega\sum_{k<j}A_{kj}(\delta_{ki}+\delta_{ji})}\prod_{k<j}\mathrm{P}(A_{kj}|\boldsymbol{\xi})\\
&= \frac{1}{N}\sum_{i}\int\frac{d\omega}{2\pi}\mathrm{e}^{i\omega k}\prod_{k<j}\sum_{A_{kj}}\mathrm{P}(A_{kj}|\boldsymbol{\xi})\,\mathrm{e}^{-i\omega A_{kj}(\delta_{ki}+\delta_{ji})}.
\end{aligned} \tag{3.96}$$

Taking the sum over A_{kj} and employing the (asymptotic) identity $1 + x/N = \mathrm{e}^{x/N+O(1/N^2)}$, we have

$$\begin{aligned}
\mathrm{P}(k|\boldsymbol{\xi}) &= \frac{1}{N}\sum_{i}\int\frac{\mathrm{d}\omega}{2\pi}\mathrm{e}^{\mathrm{i}\omega k}\prod_{k<j}\mathrm{e}^{\frac{\langle k\rangle}{N}\frac{\mathrm{W}(\xi_k,\xi_j)}{\mathrm{P}(\xi_k)\mathrm{P}(\xi_j)}\left(\mathrm{e}^{-\mathrm{i}\omega(\delta_{ki}+\delta_{ji})}-1\right)}\\
&= \frac{1}{N}\sum_{i}\int\frac{\mathrm{d}\omega}{2\pi}\mathrm{e}^{\mathrm{i}\omega k}\prod_{k<j}\mathrm{e}^{\frac{\langle k\rangle}{N}\frac{\mathrm{W}(\xi_k,\xi_j)}{\mathrm{P}(\xi_k)\mathrm{P}(\xi_j)}\left((\mathrm{e}^{-\mathrm{i}\omega}-1)(\delta_{ki}+\delta_{ji})\right)}\\
&= \frac{1}{N}\sum_{i}\int\frac{\mathrm{d}\omega}{2\pi}\mathrm{e}^{\mathrm{i}\omega k}\mathrm{e}^{\frac{\langle k\rangle}{2N}\sum_{k\neq j}\frac{\mathrm{W}(\xi_k,\xi_j)}{\mathrm{P}(\xi_k)\mathrm{P}(\xi_j)}\left((\mathrm{e}^{-\mathrm{i}\omega}-1)(\delta_{ki}+\delta_{ji})\right)}\\
&= \frac{1}{N}\sum_{i}\int\frac{\mathrm{d}\omega}{2\pi}\mathrm{e}^{\mathrm{i}\omega k}\mathrm{e}^{(\mathrm{e}^{-\mathrm{i}\omega}-1)\frac{\langle k\rangle}{N}\sum_{k(\neq i)}\frac{\mathrm{W}(\xi_k,\xi_i)}{\mathrm{P}(\xi_k)\mathrm{P}(\xi_i)}}.
\end{aligned} \tag{3.97}$$

At this point we make use of properties of the kernel $W(\xi;\xi')$ as follows,

$$\begin{aligned}\frac{\langle k\rangle}{N}\sum_{k(\neq i)}\frac{W(\xi_k;\xi_i)}{P(\xi_k)P(\xi_i)} &= \frac{\langle k\rangle}{N}\sum_{k(\neq i)}\sum_{\xi}\delta_{\xi,\xi_k}\frac{W(\xi;\xi_i)}{P(\xi)P(\xi_i)}\\ &= \langle k\rangle\sum_{\xi}P(\xi)\frac{W(\xi;\xi_i)}{P(\xi)P(\xi_i)} = \langle k\rangle\frac{W(\xi_i)}{P(\xi_i)}\end{aligned} \tag{3.98}$$

where we have used the law of large numbers $P(\xi) = \lim_{N\to\infty}\frac{1}{N}\sum_{i=1}^{N}\delta_{\xi,\xi_i}$ and neglected $\mathcal{O}(N^{-1})$ terms. This allows us to derive the following result

$$\begin{aligned}P(k|\boldsymbol{\xi}) &= \frac{1}{N}\sum_i\int\frac{d\omega}{2\pi}e^{i\omega k}e^{(e^{-i\omega}-1)\langle k\rangle\frac{W(\xi_i)}{P(\xi_i)}}\\ &= \frac{1}{N}\sum_i\sum_{\xi}\delta_{\xi,\xi_i}\int\frac{d\omega}{2\pi}e^{i\omega k}e^{(e^{-i\omega}-1)\langle k\rangle\frac{W(\xi)}{P(\xi)}}\\ &= \sum_{\xi}P(\xi)\,e^{-\langle k\rangle\frac{W(\xi)}{P(\xi)}}\int\frac{d\omega}{2\pi}e^{i\omega k}\,e^{e^{-i\omega}\langle k\rangle\frac{W(\xi)}{P(\xi)}}\\ &= \sum_{\xi}P(\xi)\,e^{-\langle k\rangle\frac{W(\xi)}{P(\xi)}}\int\frac{d\omega}{2\pi}e^{i\omega k}\sum_{\ell\geq 0}\frac{(\langle k\rangle\frac{W(\xi)}{P(\xi)})^{\ell}}{\ell!}e^{-i\omega\ell}\\ &= \sum_{\xi}P(\xi)\,e^{-\langle k\rangle\frac{W(\xi)}{P(\xi)}}\frac{(\langle k\rangle\frac{W(\xi)}{P(\xi)})^{k}}{k!}.\end{aligned} \tag{3.99}$$

The above can be simplified further. Starting from the definition of the kernel $W(\xi;\xi') = \frac{\sum_{i\neq j}A_{ij}\delta_{\xi,\xi_i}\delta_{\xi',\xi_j}}{\sum_{i\neq j}A_{ij}}$ we can write an expression for the marginal distri-

bution $W(\xi)$,

$$\begin{aligned} W(\xi) &= \sum_{\xi'} \frac{\sum_{i\neq j} A_{ij}\delta_{\xi,\xi_i}\delta_{\xi',\xi_j}}{\sum_{i\neq j} A_{ij}} = \frac{\sum_{i\neq j} A_{ij}\delta_{\xi,\xi_i}}{\sum_{i\neq j} A_{ij}} = \frac{\sum_i k_i \delta_{\xi,\xi_i}}{N\langle k\rangle} \\ &= \frac{1}{N\langle k\rangle}\sum_k \sum_i k\delta_{\xi,\xi_i}\delta_{k,k_i} = \frac{1}{\langle k\rangle}\sum_k kP(\xi,k) \\ &= \frac{1}{\langle k\rangle}P(\xi)\sum_k kP(k|\xi) = \frac{\bar{k}(\xi)}{\langle k\rangle}P(\xi) \end{aligned} \tag{3.100}$$

where we have defined $\bar{k}(\xi) = \sum_k P(k|\xi)k$, where $P(k|\xi)$ is the probability for a node to have degree k given that it has label ξ, (not to be confused with $P(k|\boldsymbol{\xi})$ which is conditioned on the labels of all nodes in the network $\boldsymbol{\xi} = (\xi_1,\ldots,\xi_N)$). We can now substitute this back into our previous expression to find,

$$P(k|\boldsymbol{\xi}) \;=\; \sum_{\xi} P(\xi)e^{-\bar{k}(\xi)}\frac{(\bar{k}(\xi))^k}{k!}. \tag{3.101}$$

We note that the dependence on the specific realisation of $\boldsymbol{\xi}$ is lost and only the distribution $P(\xi)$ enters the expression, hence we will write $P(k|\boldsymbol{\xi}) = P(k)$. We note that by writing the degree distribution as,

$$P(k) = \sum_{\xi} P(\xi)P(k|\xi) \tag{3.102}$$

comparison with (3.101) reveals the degree distribution of nodes with the same label is the Poissonian distribution

$$P(k|\xi) = e^{-\bar{k}(\xi)}\frac{(\bar{k}(\xi))^k}{k!}, \tag{3.103}$$

with mean degree $\bar{k}(\xi)$. We also note that the joint distribution $\mathrm{P}(k,\xi)$, which is required to solve (3.17), is obtained multiplying the above times $\mathrm{P}(\xi)$

$$\mathrm{P}(k,\xi) = \mathrm{P}(\xi)\mathrm{e}^{-\bar{k}(\xi)}\frac{(\bar{k}(\xi))^k}{k!}. \tag{3.104}$$

We can follow a similar procedure to find the average value of degree correlations in the ensemble (3.93)

$$\mathrm{W}(k,\xi;k',\xi'|\boldsymbol{\xi}) \;=\; \sum_{\mathbf{A}}\mathrm{P}(\mathbf{A}|\boldsymbol{\xi})\frac{1}{N\langle k\rangle}\sum_{ij}A_{ij}\delta_{k,k_i(\mathbf{A})}\delta_{k',k_j(\mathbf{A})}\delta_{\xi,\xi_i}\delta_{\xi',\xi_j}. \tag{3.105}$$

By using Fourier representations of the Kronecker delta-function and taking the sum over $\mathbf{A}$ we find, in the large N limit,

$$\mathrm{W}(k,\xi;k',\xi'|\boldsymbol{\xi}) \;=\; \mathrm{W}(\xi;\xi')\mathrm{W}(k|\xi)\mathrm{W}(k'|\xi') \tag{3.106}$$

with $\mathrm{W}(k|\xi) = k\mathrm{P}(k|\xi)/\bar{k}(\xi)$. This again reveals that the degree correlations, when averaged over the graph ensemble, no longer depend on the specific configuration $\boldsymbol{\xi}$, so we will write $\mathrm{W}(k,\xi;k',\xi'|\boldsymbol{\xi}) = \mathrm{W}(k,\xi;k',\xi')$.

3. HERD IMMUNITY IN SOCIAL CONTACT NETWORKS WITH HETEROGENEOUS TRANSMISSION PROBABILITIES

4 Dynamics of gene regulatory networks with self-regulation

4.1 Introduction

As we have discussed in previous chapters, the immune system is comprised of many different cell types (T-cells, B-cells, etc) which perform a wide array of functions that contribute to immunity. Within a single organism, different cell types have the same genetic make-up but differ in the set of genes which are expressed, such that one can determine cell type from gene expression profiles. The expression of one gene can influence the expression of another such that the interaction between genes creates a large, sparse, directed network known as a gene regulatory network (GRN). In this chapter, we study a model of GRNs, with the aim of understanding the conditions under which sparse, directed, randomly connected networks can support a diverse set of stable gene expression profiles, corresponding to different cell types, necessary for multi-cellular life. Since the early work of Kauffman (82, 83), systemic features of GRNs have been studied using Boolean networks. In these models

each node of the network represents a gene that is assumed to be in one of two states (expressed/not expressed). The state of a node, described by a Boolean variable (1 or 0), evolves in discrete time steps and at a given point in time is updated according to some function of the state of its neighbouring nodes at the *previous* time point. In these models it is typically chosen that all nodes are updated together in a single time step, a modelling choice referred to as *synchronous* (or *parallel*) dynamics. While it is unrealistic that genes update in this fashion, the simplicity of synchronous Boolean networks has made them popular choice for modelling the behaviour of GRNs and have been shown to complement limited experimental data (237). Since their introduction, Boolean networks have also been popular choices to model the operation of a broad range of complex systems, ranging from credit contagion (238, 239, 240) to epidemic spreading (241) and opinion dynamics (242, 243).

It is well known that gene expression is biologically regulated by transcription factors (TFs). These are single (or small complexes of) proteins, synthesised by genes, which can bind to certain portions of DNA, and selectively promote or inhibit the expression of genes. Recently, *bipartite* Boolean networks have been introduced to incorporate the role of TFs in the dynamics of gene expression (98, 244, 245). In these models, genes and TFs are modelled by two sets of Boolean variables which interact with each other via directed links. A directed link from a gene to a TF indicates that the gene codes for a protein that constitutes the TF. Conversely, a directed link from a TF to a gene indicates that the TF regulates the expression of that gene. In these models, links were assumed to be sparse, directed and drawn randomly and independently from given distributions, so that links were typically unidirectional, i.e.

the probability to have a bidirectional link vanished in the thermodynamic limit, where the number of nodes in the network is infinitely large, due to sparsity and directionality. Unidirectional interactions meant that genes did not contribute to the synthesis of TFs that would regulate them, a process we refer to as self-regulation. It is known that self-regulation is a common feature of GRNs, and feedback loops, where a gene is directly or indirectly involved in the regulation of its own expression, are important. It is the objective of this work to relax the assumptions made in earlier works, and allow interactions to be correlated, such that we can study the effect of self-regulation on the dynamics of GRNs. In particular, we focus on attractors of Boolean networks; a sequence of states, where if the network evolves to any state in that sequence, it shall then cycle through that sequence of states in perpetuity.

Past models of GRNs have been shown to support only a single attractor and this was hypothesised to be due to the lack of bidirectional links in the networks that were studied (98, 244, 245). This is consistent with recent numerical work which suggests that sparse, fully asymmetric networks, in which there are no pair of nodes that both have a direct interaction with each other, tend toward supporting a single attractor as dilution is increased (246). A study of sparsely connected, *partially* symmetric networks, to the best of our knowledge, is absent from the literature. In this work we show that partially symmetric networks can support multiple attractors, as observed in multi-cellular life, at low, but finite, temperature. In order to do so we apply the dynamical cavity method to the study of bipartite systems, with two distinct sets of variables that evolve according to different sets of linear threshold functions. By suitable parameterisation of such systems one can

study models of gene expression, with pairwise and multi-node interactions, previously studied in (98, 244, 245). By mapping these models to suitably defined bipartite systems, we find that we can solve for the dynamics of systems with two-body, arbitrarily asymmetric interactions, even in the presence of *self-interactions*. This represents a major technical advance, as self-interactions are well known to introduce long-time correlations which would normally make direct application of the dynamical cavity method (or equivalent methods based on generating functionals) cumbersome. By a similar mapping to bipartite networks, we are also able to investigate the dynamics of systems with multi-node (arbitrarily asymmetric) interactions. Such systems are similar to mixed p-spin models, where nodes may not only interact in a pairwise manner, but may have higher order interactions with an arbitrary number of nodes (247). However, previous investigations into mixed p-spin models have considered nodes to be described by Ising spins which take value either -1 or 1, whereas in our case we consider nodes to be described by Boolean variables, which take value 0 or 1. We find that networks with arbitrarily symmetric pairwise or multi-node interactions support, at low temperature, a multiplicity of (cyclic) attractors, as soon as a degree of bidirectionality is introduced in the links. Interestingly, multi-node interactions increase the diversity of attractors.

The remainder of this chapter is split into several sections. In the following section we define our model of GRNs, and include two different models of the dynamics of gene expression with pairwise and multi-node interactions, leading to linear and nonlinear dynamics, respectively. We show that both models are described by a bipartite Boolean system, and provide a general

model from which the linear or nonlinear model can be recovered by suitable choice of parameters. In Sec. 4.3 we describe how the dynamical cavity method may be extended to bipartite spin systems, and present a closed set of equations which may be solved numerically within a one time approximation (OTA) scheme, originally developed for monopartite systems (87, 96, 97, 248). In Sec. 4.4 we solve for the dynamics of the linear model of gene expression with self-interactions. Additionally, we analyse this model in equilibrium and show that is in agreement with the dynamical cavity in the steady-state. In Sec. 4.5 we study the nonlinear model of gene expression. We provide an assessment of the OTA scheme in the presence of nonlinear dynamics and then go on to demonstrate the existence of multiple attractors caused by bidirectional links and the impact of multi-node interactions on their diversity. In Sec. 4.6 we demonstrate how the dynamical cavity method may derive an efficient set of equations to solve for the dynamics of systems in the thermodynamic limit. We end with a discussion of our results, and posit further ideas for the study of multiple attractors in GRNs from a statistical mechanics perspective. Technical details are contained in the appendices at the end of the chapter.

4.2 Model definitions

We consider a bipartite model of GRNs, recently introduced in (244), which comprises N genes and $M = \alpha N$ TFs, with directed interactions described by two matrices, $\boldsymbol{\eta}$ and $\boldsymbol{\xi}$, giving unweighted links from genes to TFs and weighted links from TFs to genes, respectively. Entry $\eta_i^\mu \in \{0, 1\}$ denotes

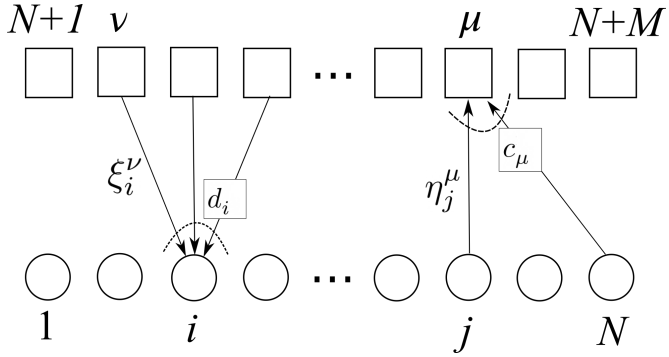

Figure 4.1: A sketch of the bipartite gene-TF network. Circles indicate genes, and squares indicate TFs.

whether (1) or not (0) gene i contributes to the synthesis of TF μ, whereas entry $\xi_i^\mu \in \mathbb{R}$ describes the regulatory effect of TF μ on gene i, which can be excitatory ($\xi_i^\mu > 0$), inhibitory ($\xi_i^\mu < 0$) or null ($\xi_i^\mu = 0$). We will denote with $\partial_i = \{\mu : \xi_i^\mu \neq 0\}$ and $\partial_\mu = \{i : \eta_i^\mu = 1\}$ the in-neighbourhoods of gene i and TF μ, respectively, and with $d_i = |\partial_i|$ and $c_\mu = |\partial_\mu|$ their in-degrees, respectively, as sketched in Figure 4.1. Interactions are assumed sparse, as in real GRNs, i.e. the average values of the local degrees $\langle d \rangle = N^{-1} \sum_i d_i$, $\langle c \rangle = (\alpha N)^{-1} \sum_\mu c_\mu$ are $\mathcal{O}(N^0)$. The parameters $\langle c \rangle$ and $\langle d \rangle$ are free parameters of our model, that control the fraction of genes that regulate TFs and vice versa.

Earlier analysis of this model (98, 244, 245) regarded $\boldsymbol{\xi}$ and $\boldsymbol{\eta}$ as quenched random variables, drawn independently from given probability distributions $P(\boldsymbol{\xi})$ and $P(\boldsymbol{\eta})$, respectively. For this choice, the probability to observe a bidirectional link $\xi_i^\mu \eta_i^\mu \neq 0$ is $\mathcal{O}(N^{-1})$, due to the sparsity of the links, and thus vanishes in the thermodynamic limit $N \to \infty$. This assumption is however not justified by biological observations, suggesting that TFs which regulate genes contributing to their own synthesis are commonplace. In this work, we will regard $\boldsymbol{\xi}$ and $\boldsymbol{\eta}$ as drawn from a joint probability distribution $\mathrm{P}(\boldsymbol{\xi}, \boldsymbol{\eta}) =$

$\mathrm{P}(\boldsymbol{\xi}|\boldsymbol{\eta})\mathrm{P}(\boldsymbol{\eta})$, such that there is a finite probability $P(\xi_i^\mu \neq 0|\eta_i^\mu = 1) = p$ to observe a bidirectional link between a TF μ and a gene i. Note, that we could easily have chosen $\mathrm{P}(\boldsymbol{\xi},\boldsymbol{\eta}) = \mathrm{P}(\boldsymbol{\eta}|\boldsymbol{\xi})\mathrm{P}(\boldsymbol{\xi})$ and defined $P(\eta_i^\mu = 1|\xi_i^\mu \neq 0) = p$. Which choice we make is arbitrary, as we can define the distributions to draw networks with the same degree statistics of genes and TFs, regardless of the choice made. By either specifying $\mathrm{P}(\boldsymbol{\eta}|\boldsymbol{\xi})$ or $\mathrm{P}(\boldsymbol{\xi}|\boldsymbol{\eta})$, we introduce a correlation in the links that allows us to explicitly control the number of bidirectional links and assess their impact on the attractors of Boolean networks.

Following earlier studies (98, 244, 245), we model the state of each gene, labelled by $i = 1, \ldots, N$, with a Boolean variable $s_i \in \{0, 1\}$, indicating whether gene i is expressed (1) or not (0). Each TF, labelled by $\mu = N+1, \ldots, N+M$, is associated with a variable $\tau_\mu \in [0, 1]$, which describes its concentration. Genes update their state at regular time intervals of duration Δ according to a linear threshold model,

$$s_i(t+\Delta) = \theta\left(\sum_\mu \xi_i^\mu \tau_\mu(t) + \vartheta_i - z_i(t)\right), \tag{4.1}$$

where $\theta(x)$ is the Heaviside step function, defined such that $\theta(x) = 1$ for $x > 0$ and $\theta(x) = 0$ for $x < 0$, ϑ_i can be thought of as a local external field or threshold and the $z_i(t)$'s are independent identically distributed zero-averaged random variables mimicking biological noise. We denote their cumulative distribution function (c.d.f.) with $\mathrm{Prob}[z_i(t) < x] = \phi_\beta(x)$, for all i, t, where $\beta^{-1} = T$ is a parameter that characterises the noise strength. We shall assume, throughout the paper, a "thermal" (or Glauber) noise distribution

with

$$\phi_\beta(x) = \frac{1}{2}[1 + \tanh\frac{\beta x}{2}]. \tag{4.2}$$

Two types of dynamics for the synthesis of TFs were considered in (98, 244, 245), following different logic operations, respectively

- 'OR' logic

$$\tau_\mu(t) = \frac{1}{c_\mu}\sum_j \eta_j^\mu s_j(t) \tag{4.3}$$

  where at least one gene in the in-neighbourhood of μ must be expressed for the synthesis of that TF to occur,

- 'AND' logic

$$\tau_\mu(t) = \prod_{j\in\partial_\mu} s_j(t) \tag{4.4}$$

  where all genes in the in-neighbourhood of μ must be expressed for TF μ to be synthesised (in this case τ_μ takes values in $\{0,1\}$ rather than $[0,1]$).

If we choose that TFs evolve according to an 'OR' logic, upon eliminating the TFs from the description, we obtain a system of genes with their evolution given by a linear threshold model

$$s_i(t+\Delta) = \theta\left(\sum_j J_{ij}s_j(t) + \vartheta_i - z_i(t)\right) \tag{4.5}$$

with effective two-body interactions $J_{ij} = \sum_\mu \frac{\xi_i^\mu \eta_j^\mu}{c_\mu}$. Conversely, if TFs perform an 'AND' logic, the evolution of genes is given by *nonlinear* threshold

dynamics

$$s_i(t+\Delta) = \theta\left(\sum_\mu \xi_i^\mu \prod_{j\in\partial_\mu} s_j(t) + \vartheta_i - z_i(t)\right), \tag{4.6}$$

with multi-body interactions between genes. For later convenience, it is useful to note that the 'AND' logic (4.4) can be expressed in terms of a linear threshold function with suitably chosen threshold

$$\tau_\mu(t) = \theta\left(\sum_j \eta_j^\mu s_j(t) - c_\mu + \epsilon\right) \tag{4.7}$$

where $0 < \epsilon \ll 1$ ensures that the argument of the step function is greater than zero when *all* of the c_μ genes contributing to TF μ are expressed and negative otherwise. Thus, an equivalent description of (4.6) is given by the system of equations (4.1) and (4.7). Out of mathematical convenience we will define a closely related model, where TFs are not updated instantaneously, but on the same timescale as the genes

$$\begin{aligned} s_i(t+\tilde{\Delta}) &= \theta\left(\sum_\mu \xi_i^\mu \tau_\mu(t) + \vartheta_i - z_i(t)\right) \\ \tau_\mu(t+\tilde{\Delta}) &= \theta\left(\sum_j \eta_j^\mu s_j(t) - c_\mu + \epsilon\right). \end{aligned} \tag{4.8}$$

Upon choosing $\tilde{\Delta} = \Delta/2$ and initial condition $\tau_\mu(0) = \theta\left(\sum_j \eta_j^\mu s_j(0) - c_\mu + \epsilon\right) \forall \mu$, the trajectory $s_i(t)$ resulting from (4.8) at times $t = n\Delta/2$, with $n \in \mathbb{N}$, is identical to the trajectory of (4.6) at times $t = n\Delta$. On the other hand, the trajectories of (4.8) and (4.6) at $t = n\Delta$ represent two independent thermal

histories of the same system, as noise is drawn at each time step from the same distribution. Hence, the two systems defined in (4.8) and (4.6) are fully equivalent at integer multiples of Δ. The advantage of using (4.8) is that it makes the application of the dynamical cavity method straightforward (see Sec. 4.3).

The dynamics of GRNs evolving according to (4.5) has previously been studied for random interactions J_{ij} with an arbitrary degree of symmetry, in the absence of self-interactions, i.e. $J_{ii} = 0$ (249). This corresponds, in the context of our bipartite network, to a lack of bidirectional links i.e. $\xi_i^\mu \eta_i^\mu = 0$. Similarly, the dynamics of GRNs evolving according to (4.6) has been studied under the assumption that $\mathrm{P}(\boldsymbol{\xi}, \boldsymbol{\eta}) = \mathrm{P}(\boldsymbol{\xi})\mathrm{P}(\boldsymbol{\eta})$, such that the probability of observing a bidirectional link is zero in the limit of large system size (98, 244, 245). It was shown in (244) that in the absence of bidirectional links this model has no multiplicity of attractors, i.e. of stable gene expression profiles, even in the absence of noise, $T = 0$. Thus, the fully asymmetric version of this model does not fulfill an important requirement for a GRN to sustain multiple cell types, as observed in multi-cellular life.

In this work we solve the dynamics (4.5) in the presence of self-interactions, i.e. $J_{ii} \neq 0$, and the dynamics (4.8) in the presence of bidirectional links, i.e. $P(\xi_i^\mu \neq 0 | \eta_i^\mu = 1) = \mathcal{O}(N^0)$. Previous work has shown that dynamical analysis of (4.5) via generating functionals is cumbersome in the presence of self-interactions due to the strong memory effects that they produce (250), which make the complexity of the analysis exponential in the time horizon considered. We show that, while the dynamical cavity method faces a similar time-complexity barrier, when applied to the system (4.5) with self-interactions,

it is possible, by a suitable mapping of (4.5) to a bipartite system $\hat{\eta}, \hat{\xi}$ with bidirectional links, to apply the dynamical cavity method and solve the equations explicitly under the so-called one-time approximation (OTA) scheme, that is effective in reducing the time-complexity of systems with bidirectional links (87, 96, 97, 248). This allows us to solve the dynamics of systems with self-interactions both at short and long times, accessing in particular the non-equilibrium steady-state. To best of our knowledge, this is the first work to do so. We will define in Sec. 4.4 the bipartite model $\hat{\eta}, \hat{\xi}$ that achieves the suitable mapping, here we limit to stress that this is different from the links ξ, η, appearing in (4.1) and (4.3), respectively, from which the interactions $\{J_{ij}\}$ were derived. Similarly, by mapping the nonlinear threshold model (4.6) to the bipartite model with two-body interactions (4.8), we are able to solve the dynamical cavity equations in the presence of bidirectional links, under the OTA scheme, thus relaxing the assumption of fully asymmetric links used in previous work (98, 244, 245). We will show that, upon introducing bidirectionality in the links, the nonlinear threshold model (4.6) is able to support a multiplicity of attractors at low noise level.

4.3 Dynamical cavity method for bipartite systems with parallel dynamics

As explained above, both the linear threshold model with self-interactions (4.5) and the nonlinear model with multi-node interactions (4.6) can be mapped to an equivalent bipartite system. In this section we solve the dynamics of a

general bipartite system, from which either the linear or nonlinear model can be recovered by suitable choice of parameters. In this generalised model, two sets of Boolean variables, that we shall refer to as genes and TFs, update their state at regular time intervals of duration $\tilde{\Delta}$ according to the following linear threshold functions

$$s_i(t+\tilde{\Delta}) = \theta\left(\sum_\mu \xi_i^\mu \tau_\mu(t) + \vartheta_i - z_i(t)\right) \qquad i = 1,\dots,N \tag{4.9}$$

$$\tau_\mu(t+\tilde{\Delta}) = \theta\left(\sum_j \eta_j^\mu s_j(t) + \vartheta_\mu - \hat{z}_\mu(t)\right) \qquad \mu = N+1,\dots,N+M. \tag{4.10}$$

Here, ϑ_i and ϑ_μ are the thresholds of gene i and TF μ, respectively, and $z_i(t)$ and $\hat{z}_\mu(t)$ are random i.i.d random variables with c.d.f. $\phi_\beta(x)$ and $\phi_{\hat{\beta}}(x)$, respectively. It is clear that (4.10) reduces to (4.8) for $\vartheta_\mu = -c_\mu + \epsilon$ and $\hat{T} = \hat{\beta}^{-1} = 0$, hence for this choice of parameters, the generalised model defined by (4.9) and (4.10) recovers model (4.6) with $\Delta = 2\tilde{\Delta}$ (thanks to its equivalence with (4.8), pointed out earlier). In Sec. 4.4 we will show that the system defined in (4.9) and (4.10) can also recover (4.5) for suitable choices of the links $\{\xi_i^\mu\}$ and $\{\eta_j^\mu\}$. For the remainder of this chapter, we shall set $\tilde{\Delta} = 1$.

In order to solve the dynamics of the generalised model (4.9) and (4.10) we use the dynamical cavity method previously used to study systems with sparse interactions. Earlier studies have successfully applied dynamical cavity to the study of monopartite systems of Ising (87, 96, 97, 248) and Boolean (98) variables with bidirectional links, and bipartite systems of binary variables with unidirectional interactions (98). Here we apply the method to the study of bipartite systems with (partially) bidirectional links, where each set

of variables is subject to different noise (the method would equally work for two sets of variables evolving via different dynamical rules).

We define the vectors $\mathbf{s}(t) = (s_1(t), \ldots, s_N(t))$ and $\boldsymbol{\tau}(t) = (\tau_{N+1}(t), \ldots, \tau_{N+M}(t))$, which denote the state of the genes and TFs at time t, respectively. The state of the network at some time t is therefore described by the vectors $(\mathbf{s}(t), \boldsymbol{\tau}(t))$ and a trajectory of the system from time $t = 0, \ldots, t_m$ is written $(\mathbf{s}(0), \boldsymbol{\tau}(0)) \to (\mathbf{s}(1), \boldsymbol{\tau}(1)) \to \cdots \to (\mathbf{s}(t_m), \boldsymbol{\tau}(t_m))$, which for brevity we denote $(\mathbf{s}^{0\ldots t_m}, \boldsymbol{\tau}^{0\ldots t_m})$. We wish to write an expression for the probability to observe a trajectory, $(\mathbf{s}^{0\ldots t_m}, \boldsymbol{\tau}^{0\ldots t_m})$, for the system defined in (4.9) and (4.10). To do so, we first consider the probability to observe a gene i in state s_i at time $t+1$. From equation (4.9) we see that it will depend on the state of the TFs at time t. According to this equation, the gene will activate if the random noise $z_i(t) < \sum_\mu \xi_i^\mu \tau_\mu(t) + \vartheta_i$ and will be inactive if $z_i(t) < -(\sum_\mu \xi_i^\mu \tau_\mu(t) + \vartheta_i)$. The probability that $z \leq \pm x$ is given by the c.d.f of z, and hence, the probability to observe a gene i in state s_i at time $t+1$, given the state of the TFs at time t, is given by,

$$\mathrm{P}(s_i(t+1)|\boldsymbol{\tau}(t)) = \phi_\beta \left((2s_i - 1) \sum_\mu \xi_i^\mu \tau_\mu(t) + \vartheta_i \right). \tag{4.11}$$

Since we are assuming the random noise follows a thermal noise distribution $\phi_\beta(x) = \frac{1}{2}\left[1 + \tanh\frac{\beta}{2}x\right]$ we may use the relation $\frac{1}{2}\left[1 + \tanh\frac{\beta}{2}x\right] = \frac{\mathrm{e}^{\frac{\beta}{2}x}}{2\cosh\frac{\beta}{2}x}$ to define the probability to observe a gene i in state s_i at time $t+1$ given the

local field $h_i(\boldsymbol{\tau}^t) = \sum_\mu \xi_i^\mu \tau_\mu^t + \vartheta_i$ that acts upon it,

$$\mathrm{W}(s_i^{t+1}|h_i(\boldsymbol{\tau}^t)) = \frac{\mathrm{e}^{\frac{\beta}{2}\left(2s_i^{t+1}-1\right)h_i(\boldsymbol{\tau}^t)}}{2\cosh\frac{\beta}{2}h_i(\boldsymbol{\tau}^t)}, \tag{4.12}$$

where we have adopted the shorthand notation $s_i(t) = s_i^t$ and $\tau_\mu(t) = \tau_\mu^t$. We notice that the local field $h_i(\boldsymbol{\tau}^t)$ depends only on the TFs in the neighbourhood of i, $\boldsymbol{\tau}_{\partial_i} = \{\tau_\mu : \xi_i^\mu \neq 0\}$, and hence we shall write $h_i(\boldsymbol{\tau}^t) = h_i(\boldsymbol{\tau}_{\partial_i}^t)$. By the same reasoning, we can deduce from equation (4.10) the probability to observe a TF μ in state τ_μ at time $t+1$ given the local field $h_\mu(\mathbf{s}_{\partial_\mu}^t) = \sum_j \eta_j^\mu s_j^t + \vartheta_\mu$ that acts upon it, is given by,

$$\widetilde{\mathrm{W}}\left(\tau_\mu^{t+1}|h_\mu(\mathbf{s}_{\partial_\mu}^t)\right) = \frac{\mathrm{e}^{\frac{\beta}{2}\left(2\tau_\mu^{t+1}-1\right)h_\mu(\mathbf{s}_{\partial_\mu}^t)}}{2\cosh\frac{\beta}{2}h_\mu(\mathbf{s}^t)}, \tag{4.13}$$

where $\mathbf{s}_{\partial_\mu} = \{s_j : \eta_j^\mu = 1\}$ are the genes that neighbour TF μ.

According to equations (4.9) and (4.10) in a single discrete time step, all genes and TFs are updated simultaneously. Indeed, given the state of the network at the previous time point, genes and TFs are updated independently of one another, such that we may write the probability for the network to evolve from $(\mathbf{s}^t, \boldsymbol{\tau}^t)$ to $(\mathbf{s}^{t+1}, \boldsymbol{\tau}^{t+1})$ as,

$$W\left(\mathbf{s}^{t+1}, \boldsymbol{\tau}^{t+1}|\mathbf{s}^t, \boldsymbol{\tau}^t\right) = \prod_{i=1}^{N}\prod_{\mu=N+1}^{N+M} \mathrm{W}(s_i^{t+1}|h_i(\boldsymbol{\tau}_{\partial_i}^t))\widetilde{\mathrm{W}}(\tau_\mu^{t+1}|h_\mu(\mathbf{s}_{\partial_\mu}^t)) \tag{4.14}$$

where it then follows that the probability to observe a trajectory of the system

is given by,

$$\mathrm{P}(\mathbf{s}^{0\dots t_m}, \boldsymbol{\tau}^{0\dots t_m}) = \mathrm{P}(\mathbf{s}^0, \boldsymbol{\tau}^0) \prod_{t=1}^{t_m} W(\mathbf{s}^t, \boldsymbol{\tau}^t | \mathbf{s}^{t-1}, \boldsymbol{\tau}^{t-1}). \tag{4.15}$$

As we detail in 4.A,by marginalising equation (4.15) over $\mathbf{s}^{0\dots t_m} \setminus s_i^{0\dots t_m}$ and $\boldsymbol{\tau}^{0\dots t_m}$, the dynamical cavity method allows us to derive an expression for the probability to observe the trajectory $s_i^{0\dots t_m}$ for the single gene i, in the cavity graph where TF ν has been removed, subject to a time dependent external field with trajectory $\zeta_i^{(\nu),1\dots t_m} = \xi_i^\nu \tau_\nu^{0\dots t_m-1}$,

$$\begin{aligned}\mathrm{P}_i^{(\nu)}(s_i^{0\dots t_m} | \zeta_i^{(\nu),1\dots t_m}) = \mathrm{P}(s_i^0) \sum_{\boldsymbol{\tau}_{\partial_i\setminus\nu}^{0\dots t_m-1}} \left[\prod_{t=1}^{t_m} \mathrm{W}(s_i^t | h_i(\boldsymbol{\tau}_{\partial_i}^{t-1})) \right] \\ \times \prod_{\mu\in\partial_i\setminus\nu} \mathrm{P}_\mu^{(i)}(\tau_\mu^{0\dots t_m-1} | \zeta_\mu^{(i),1\dots t_m-1})\end{aligned} \tag{4.16}$$

and similarly for the trajectory of a single TF μ in the cavity graph where gene ℓ has been removed, subject to a time dependent external field $\zeta_\mu^{(\ell),1\dots t_m} = \eta_\ell^\mu s_\ell^{0\dots t_m-1}$,

$$\begin{aligned}\mathrm{P}_\mu^{(\ell)}(\tau_\mu^{0\dots t_m} | \zeta_\mu^{(\ell),1\dots t_m}) = \mathrm{P}(\tau_\mu^0) \sum_{\mathbf{s}_{\partial_\mu\setminus\ell}^{0\dots t_m-1}} \left[\prod_{t=1}^{t_m} \widetilde{\mathrm{W}}(\tau_\mu^t | h_\mu(\mathbf{s}_{\partial_\mu}^{t-1})) \right] \\ \times \prod_{j\in\partial_\mu\setminus\ell} \mathrm{P}_j^{(\mu)}(s_j^{0\dots t_m-1} | \zeta_j^{(\mu),1\dots t_m-1}).\end{aligned} \tag{4.17}$$

These expressions are exact when the bipartite network is a tree, and are expected to be a good approximation for sparse (bipartite) networks, where in the limit $N \to \infty$ the length of loops grows as $\log N$. In principle, they may

be solved recursively for the probability of a trajectory up to a given time t_m. However, in expression (4.16) this requires a sum over $|\boldsymbol{\tau}_{\partial_i \setminus \nu}^{0,\dots,t_m-1}| = (2^{d_i-1})^{t_m}$ variables, which grows exponentially with time, and similarly, expression (4.17) requires a sum over $|\mathbf{s}_{\partial_\mu \setminus \ell}^{0,\dots,t_m-1}| = (2^{c_\mu-1})^{t_m}$ variables. In practice, this means that these equations can only be solved for very short times, making them unsuitable for the study of long time dynamics and stationary states. The exception is for systems with unidirectional interactions, where these equations drastically simplify (see 4.A for details), as reported in the literature for monopartite systems (96).

When bidirectional interactions are present, an approximation scheme, known as the One Time Approximation (OTA), has been proposed to reduce the computational complexity of the dynamical cavity method (87, 96, 97, 98, 248). This approximation neglects correlations in time, such that the state of a node in the network will depend upon the state of its neighbours at the previous time step only. This is of course not generally true, one can imagine a short cycle of nodes of length l in which case the state of each node in the cycle will depend upon its own state l time steps ago. This approximation is, however, necessary in order to deal with the computational complexity of the dynamical cavity equations, which increases exponentially in time. To neglect correlations in time, we assume

$$\mathrm{P}_\mu^{(\ell)}(\tau_\mu^{0\dots t_m}|\zeta_\mu^{(\ell),1\dots,t_m}) = \mathrm{P}_\mu(\tau_\mu^0)\prod_{t=1}^{t_m}\mathrm{P}_\mu^{(\ell)}(\tau_\mu^t|\zeta_\mu^{(\ell),t}) \tag{4.18}$$

and

$$\mathrm{P}_i^{(\nu)}(s_i^{0\dots t_m}|\zeta_i^{(\nu),1\dots t_m}) = \mathrm{P}_i(s_i^0)\prod_{t=1}^{t_m}\mathrm{P}_i^{(\nu)}(s_i^t|\zeta_i^{(\nu),t}). \tag{4.19}$$

As we detail in 4.A, equations (4.19) and (4.18) can be used in conjunction with (4.16) and (4.17) to derive an equation for the probability to observe a gene i in a given state $s_i^{t_m}$, at time t_m, in the cavity graph where TF ν has been removed, *given* the external field induced by its state at the earlier time step $\zeta_i^{(\nu),t_m} = \xi_i^\nu \tau_\nu^{t_m-1}$,

$$\begin{aligned}\mathrm{P}_i^{(\nu)}(s_i^{t_m}|\zeta_i^{(\nu),t_m}) &= \sum_{s_i^{t_m-2}}\sum_{\boldsymbol{\tau}_{\partial_i\setminus\nu}^{t_m-1}} \mathrm{W}(s_i^{t_m}|h_i^{(\nu)}(\boldsymbol{\tau}_{\partial_i}^{t_m-1}) + \zeta_i^{(\nu),t_m}) \\ &\qquad \times\left[\prod_{\mu\in\partial_i\setminus\nu}\mathrm{P}_\mu^{(i)}(\tau_\mu^{t_m-1}|\zeta_\mu^{(i),t_m-1})\right]\mathrm{P}_i(s_i^{t_m-2}).\end{aligned} \tag{4.20}$$

This depends on the probability to observe the TF μ in a given state $\tau_\mu^{t_m-1}$, at time t_m-1, in the cavity graph where gene i has been removed, *given* the state of i at the earlier time step $\zeta_\mu^{(i),t_m-1} = \eta_i^\mu s_i^{t_m-2}$,

$$\begin{aligned}\mathrm{P}_\mu^{(\ell)}(\tau_\mu^{t_m}|\zeta_\mu^{(\ell),t_m}) &= \sum_{\tau_\mu^{t_m-2}}\sum_{\mathbf{s}_{\partial_\mu\setminus\ell}^{t_m-1}} \widetilde{\mathrm{W}}(\tau_\mu^{t_m}|h_\mu^{(\ell)}(\mathbf{s}_{\partial_\mu}^{t_m-1}) + \zeta_\mu^{(\ell),t_m}) \\ &\qquad \times\left[\prod_{j\in\partial_\mu\setminus\ell}\mathrm{P}_j^{(\mu)}(s_j^{t_m-1}|\zeta_j^{(\mu),t_m-1})\right]\mathrm{P}_\mu(\tau_\mu^{t_m-2}).\end{aligned} \tag{4.21}$$

As we detail in 4.A, and as observed earlier in the literature (see (96, 98, 248)),

the assumption of time factorisation is not enough to find a closed set of equations and one must make additional assumptions. In writing equations (4.20) and (4.21) we assume that the cavity distributions, with external field from the removed site, may be approximated by their non-cavity counterparts i.e

$$\mathrm{P}_i^{(\nu)}(s_i^{t_m-2}|\zeta_i^{(\nu),t_m-2}) \approx \mathrm{P}_i(s_i^{t_m-2}) \tag{4.22}$$

and

$$\mathrm{P}_\mu^{(\ell)}(\tau_\mu^{t_m-2}|\zeta_\mu^{(\ell),t_m-2}) \approx \mathrm{P}_\mu(\tau_\mu^{t_m-2}), \tag{4.23}$$

following the approach of (248). This has recently been shown to accurately predict single-site marginals in non-equilibrium steady-states (98). Equations (4.20) and (4.21) then depend upon the marginal probability to observe gene i at time t_m, $\mathrm{P}_i(s_i^{t_m})$, and TF μ at time t_m, $\mathrm{P}_\mu(\tau_\mu^{t_m})$, which evolve according to,

$$\begin{aligned}\mathrm{P}_i(s_i^{t_m}) &= \sum_{s_i^{t_m-2}} \mathrm{P}_i(s_i^{t_m-2}) \sum_{\boldsymbol{\tau}_{\partial_i}^{t_m-1}} \mathrm{W}(s_i^{t_m}|h_i(\boldsymbol{\tau}_{\partial_i}^{t_m-1})) \\ &\quad \times \left[\prod_{\mu\in\partial_i} \mathrm{P}_\mu^{(i)}(\tau_\mu^{t_m-1}|\zeta_\mu^{(i),t_m-1})\right]\end{aligned} \tag{4.24}$$

and

$$\mathrm{P}_\mu(\tau_\mu^{t_m}) = \sum_{\tau_\mu^{t_m-2}} \mathrm{P}_\mu(\tau_\mu^{t_m-2}) \sum_{\mathbf{s}_{\partial\mu}^{t_m-1}} \widetilde{\mathrm{W}}(\tau_\mu^{t_m}|h_\mu(\mathbf{s}_{\partial\mu}^{t_m-1})) \times \left[\prod_{j\in\partial_\mu} \mathrm{P}_j^{(\mu)}(s_j^{t_m-1}|\zeta_j^{(\mu),t_m-1})\right]. \tag{4.25}$$

For a given bipartite network $(\boldsymbol{\eta}, \boldsymbol{\xi})$ and initial condition $\mathrm{P}_i(s_i^0)\ \forall i$ and $\mathrm{P}_\mu(\tau_\mu^0)\ \forall\ \mu$, one can solve these equations by simple iteration. By neglecting long-time correlations, the dynamical cavity equations under the OTA scheme, (4.20), (4.21), (4.24), and (4.25), no longer contain a sum over a set of variables the size of which is exponential in the number of time steps t_m. Hence, these equations provide an efficient numerical scheme to solve for the transient and long-time dynamics of bipartite systems for networks with arbitrary bidirectionality. Furthermore, to compute the same quantities using Monte Carlo (MC) simulations requires simulating many trajectories and to then compute the statistics of the state of each node at each point in time. Equations (4.20), (4.21), (4.24), and (4.25) are an alternative to computing the probability of the state of each node without the need for simulating many trajectories.

4.4 Linear threshold model with self-interactions

4.4.1 Equilibrium analysis of monopartite systems with self-interactions

In this section we analyse the equilibrium behaviour of the linear threshold model with symmetric interactions $J_{ij} = J_{ji}$, evolving via parallel dynamics (4.5) in the presence of self-interactions J_{ii}. It is well-known that for symmetric interactions $J_{ij} = J_{ji}$, linear threshold models evolving via parallel dynamics converge, both in the presence and the absence of self-interactions, to an equilibrium state described by a probability distribution known as the Peretto distribution, $p_{\text{eq}}(\mathbf{s}) = Z^{-1}\mathrm{e}^{-\beta H_\beta(\mathbf{s})}$ where $Z = \sum_{\mathbf{s}} \mathrm{e}^{-\beta H_\beta(\mathbf{s})}$ is the partition function of the system. This distribution has the functional form of the Gibbs-Boltzmann distribution, but with an exponent characterised by a function, $H_\beta(\mathbf{s})$, which is dependent on the noise level $T = \beta^{-1}$ (251). If we ignored the dependence on β, $H_\beta(\mathbf{s})$ would be the Hamiltonian of our system. However, for systems with symmetric interactions the noise level T is notionally the temperature of the system, and therefore $H_\beta(\mathbf{s})$ is *temperature dependent* and can not be interpreted as the Hamiltonian of our system. It is for this reason referred to as a pseudo-Hamiltonian. Writing the Peretto distribution in the same functional form as the Gibbs-Boltzmann distribution allows us to apply techniques used to study systems obeying the Gibbs-Boltzmann distribution to systems obeying the Peretto distribution. Equilibrium analysis of such systems has been carried out for Ising variables via transfer matrices (252, 253) and the replica method (254, 255). An equilibrium analysis of sparse

Boolean networks, however, is absent from the literature. Here we fill this gap by using the cavity method, originally formulated for the Gibbs-Boltzmann distribution, reached by systems evolving via sequential dynamics in the absence of self-interactions. We use this method to study the equilibrium of the linear threshold model (4.5) with symmetric interactions, evolving by parallel dynamics, in the presence of self-interactions. As we show in 4.B this is described by the Peretto distribution with the *pseudo*-Hamiltonian,

$$H_\beta(\mathbf{s}) = -\frac{1}{\beta}\sum_i \ln 2\cosh\frac{\beta}{2}h_i(\mathbf{s}_{\partial_i}, s_i) - \frac{1}{2}\sum_i h_i(\mathbf{s}_{\partial_i}, s_i) - \sum_i \vartheta_i s_i \tag{4.26}$$

where $h_i(\mathbf{s}_{\partial_i}, s_i) = \sum_{j\in\partial_i} J_{ij}s_j + J_{ii}s_i + \vartheta_i$. In 4.B we show that one can use the relation $2\cosh(x) = \sum_{\tau\in\{0,1\}} e^{(2\tau-1)x}$ to simplify the first term in $H_\beta(\mathbf{s})$, as it was similarly used in (254, 255) for models of Ising spins. We introduce a set of variables $\tau_i \in \{0,1\} \forall i = 1\dots N$, one for each contribution to the sum in the first term in $H_\beta(\mathbf{s})$. By doing so, we can write the equilibrium distribution in the following form,

$$p_{\text{eq}}(\mathbf{s}) = \sum_{\boldsymbol{\tau}} p(\mathbf{s}, \boldsymbol{\tau}) \tag{4.27}$$

$$p(\mathbf{s}, \boldsymbol{\tau}) = \frac{1}{Z}\mathrm{e}^{-\beta\mathcal{H}(\mathbf{s},\boldsymbol{\tau})} \tag{4.28}$$

with $\mathcal{H}(\mathbf{s}, \boldsymbol{\tau}) = -\sum_{\ell,j} s_\ell J_{\ell j}\tau_j - \sum_\ell s_\ell J_{\ell\ell}\tau_\ell - \sum_\ell \vartheta_\ell(s_\ell + \tau_\ell)$ and where we have redefined $Z = \sum_{\mathbf{s},\boldsymbol{\tau}} \mathrm{e}^{-\beta\mathcal{H}(\mathbf{s},\boldsymbol{\tau})}$. The equilibrium distribution has been shown to be equivalent to the marginal of the joint distribution $p(\mathbf{s}, \boldsymbol{\tau})$ which takes the form of an equilibrium distribution for a network with $2N$ nodes $s_i, \tau_i \ \forall \ i = 1, \dots, N$, and hence the $\boldsymbol{\tau} = (\tau_1, \dots, \tau_N)$ can be thought of as *fictitious* vari-

ables; they have no physical meaning, but they allow us to write an equilibrium distribution, $p(\mathbf{s}, \boldsymbol{\tau})$, from which we can use the cavity method to find equations for the single site marginals,

$$p_i(s_i, \tau_i) = \frac{1}{Z_i} \mathrm{e}^{\beta(s_i J_{ii} \tau_i + \vartheta_i(s_i + \tau_i))} \prod_{j \in \partial_i} \sum_{s_j} \sum_{\tau_j} \mathrm{e}^{\beta\left(s_i J_{ij} \tau_j + \tau_i J_{ij} s_j\right)} p_j^{(i)}(s_j, \tau_j) \tag{4.29}$$

$$p_i^{(\ell)}(s_i, \tau_i) = \frac{1}{Z_i^{(\ell)}} \mathrm{e}^{\beta(s_i J_{ii} \tau_i + \vartheta_i(s_i + \tau_i))} \prod_{j \in \partial_i \setminus \ell} \sum_{s_j} \sum_{\tau_j} \mathrm{e}^{\beta\left(s_i J_{ij} \tau_j + \tau_i J_{ij} s_j\right)} p_j^{(i)}(s_j, \tau_j) \tag{4.30}$$

which can be solved by simple iteration (see 4.B for details). These equations are exact when the interaction matrix is a tree, and give a good approximation for sparse graphs where the length of loops grows logarithmically with the system size. From the solution of these equations we can compute the average activation probability of a site $\langle s_i \rangle = \sum_{s_i, \tau_i} s_i p_i(s_i, \tau_i)$.

To assess the accuracy of the cavity equations, we compare their solution with MC simulations (the computational details of which are described in 4.C). To do so, we consider a system with interactions drawn according to the following probability distributions

$$\mathrm{P}(J_{ij}) = \left(1 - \frac{c}{N}\right) \delta_{J_{ij},0} + \frac{c}{N} \left[\frac{1+\kappa}{2} \delta_{J_{ij},1} + \frac{1-\kappa}{2} \delta_{J_{ij},-1}\right] \qquad \forall i \neq j \tag{4.31}$$

$$\mathrm{P}(J_{ii}) = (1-p)\, \delta_{J_{ii},0} + p \left[\frac{1+b}{2}\, \delta_{J_{ii},1} + \frac{1-b}{2} \delta_{J_{ii},-1}\right] \qquad \forall i \tag{4.32}$$

such that c and p control the density of links, and $\kappa, b \in [-1, 1]$ control the sign of the interactions. By choosing interactions J_{ij} to be drawn from (4.31) and (4.32) we can ensure that the network we consider is sparse, where the average degree of a node is finite $\mathcal{O}(N^0)$. It is in this regime that the network is locally

tree-like and hence the cavity equations are expected to be accurate. We can show that the network is sparse if we consider that the average in-degree of node i, d_i, is given by $d_i = \left\langle \sum_{j=1}^{N} |J_{ij}| \right\rangle_{J_{i1},\dots J_{iN}} + \langle |J_{ii}| \rangle_{J_{ii}}$, where angled brackets denote an average $\langle \dots \rangle_X = \sum_X \dots \mathrm{P}(X)$. We can then show that,

$$d_i = \left\langle \sum_{j=1}^{N} |J_{ij}| \right\rangle_{J_{i1},\dots J_{iN}} + \langle |J_{ii}| \rangle_{J_{ii}} \tag{4.33}$$

$$= \sum_{J_{i1}\in\{0,\pm1\}} \cdots \sum_{J_{iN}\in\{0,\pm1\}} \mathrm{P}(J_{i1},\dots,J_{iN}) \sum_{j=1}^{N} |J_{ij}| + \sum_{J_{ii}\in\{0,\pm1\}} |J_{ii}| \mathrm{P}(J_{ii}) \tag{4.34}$$

$$= \sum_{J_{i1}\in\{0,\pm1\}} |J_{i1}| \mathrm{P}(J_{i1}) + \cdots + \sum_{J_{iN}\in\{0,\pm1\}} |J_{iN}| \mathrm{P}(J_{iN}) + p \tag{4.35}$$

$$= \sum_{j=1}^{N} \frac{c}{N} + p \tag{4.36}$$

$$= c + p \tag{4.37}$$

where we reveal that the average in-degree of a node i is $d_i = c + p$, such that if we choose $c = \mathcal{O}(N^0)$ the average in-degree of a node will be finite, since $p \in [0, 1]$ is also finite. Hence, by choosing interactions drawn from (4.31) and (4.32) we can ensure that our network is sparse, in which case the cavity method is applicable.

Predictions from the cavity method are compared with results from MC simulations via

$$\langle s_i \rangle_{\mathrm{MC}} = \frac{1}{t_l} \sum_{t=t_{eq}}^{t_l+t_{eq}} s_i^t \tag{4.38}$$

where t_{eq} is a large time where the system has reached equilibrium and t_l is a long time that we average the state of the site i over.

In the left panel of Figure 4.2, we show results for the average activation probability $a = N^{-1}\sum_i \langle s_i \rangle$, as a function of the noise level, whereas in the right panel of Figure 4.2, we show a scatter plot of the equilibrium activation probabilities of individual sites, at a given noise level, as predicted by the cavity method and computed from MC simulations, finding excellent agreement. Additionally, the left panel of Figure 4.2 shows that the average activation is higher if there is a bias towards positive self-interactions $b > 0$, and lower if there is a bias towards negative self-interactions $b < 0$.

It is well known that finitely connected systems of Ising spins undergo a phase transition at low noise and enter a *spin glass phase*. The properties of such phases are exotic, in particular due to the breaking of *ergodicity*: whereas one would typically expect a system to move through all the configurations of the system with the same free energy randomly and with equal probability, this is not the case in the spin glass phase. Crucially, for our purposes, it is important to note that the cavity equations are not exact for systems in the spin glass phase and we would expect their solution to become inaccurate (256). However, results in the left panel of Fig. 4.2 show that in the system of sparsely connected *Boolean* variables under study, the cavity equations converge to the correct solution down to low levels of noise. Since a system of Boolean variables can be mapped to an equivalent Ising spin system by adding a quenched random external field $\vartheta_i \to \vartheta_i + \sum_j J_{ij}$ and the presence of an external field is known to change the noise level at which a finitely connected system will enter a spin glass phase (257, 258, 259, 260, 261), this may explain the relatively low noise level at which the cavity equations successfully converge . We may expect, however, that by further lowering the temper-

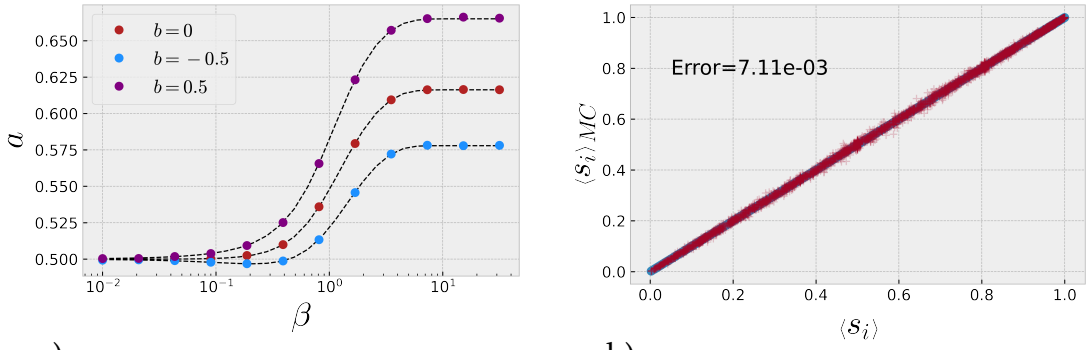

a) b)

Figure 4.2: (a) Average activation probability of genes $a = \frac{1}{N}\sum_i \langle s_i \rangle$ against inverse noise level β. Symbols indicate the site activation probability from MC simulations computed via (4.38) averaged over all sites whereas the dotted line indicates the solution from cavity equations (4.29)-(4.30). (b) Scatter plot of site activation probabilities $\langle s_i \rangle$ computed from static cavity method and MC simulations at noise level $\beta = 2$. Activation probability from MC simulations is computed by (4.38) with $t_l = 1000$ in (a) and $t_l = 5000$ in (b). In (a) and (b), genes evolve according to the linear threshold model defined in (4.5) with interactions drawn according to equations (4.31)-(4.32). Interaction networks were drawn with size $N = 5000$, average connectivity $c = 2$, density of self-interactions $p = 0.5$ and biases $\kappa = 0$. The external field is $\vartheta_i = 0 \; \forall \; i$. In (a) we show results for different biases in the self-interactions $b = 0, 0.5, -0.5$ and in (b) $b = 0$. Annotation in (b) indicates the root mean square error.

ature our system may undergo ergodicity breaking, as our (non-equilibrium) analysis at zero temperature will reveal for the case of partially symmetric interactions (see Sec. 4.5).

In Figure 4.3 we compute the site activation probabilities for each node in a network, by solving the cavity equations (4.29)-(4.30), and then plot the distribution $\mathrm{P}(\langle s_i \rangle)$, a histogram of the site activation probabilities, at different temperatures, for unbiased interactions i.e. $\kappa = 0$. In the absence of self-interactions (left panels), a bias in the fraction of sites that are activated in the steady state, emerges at low temperature. This is consistent with results obtained in (98) via dynamical cavity approaches (iterated until convergence),

in the absence of self-interactions. Right panels of Figure 4.3 show the distribution $P(\langle s_i \rangle)$, in the presence of self-interactions, where direct application of the dynamical cavity method would be cumbersome (see 4.D). By choosing that all self-interactions, where present, are negative, we see that the bias in the fraction of sites which are active at low temperature is modified. For example, at relatively high temperature, we see that, in addition to the expected peak at $a_i = 1/2$ (corresponding to fluctuating variables with zero field), there is an extra peak in the presence of self-interactions, due to sites associated with the single peak having their activation probability reduced by their self-interaction.

4.4.2 Dynamics of monopartite spin systems with self-interactions

Previously, the dynamics of the linear threshold model (4.5) have been studied using the dynamical cavity method in the absence of self-interactions (98). As we mentioned earlier, for networks with bidirectional links, the computational complexity of the cavity equations is exponential in time, due to memory effects, and the one time approximation (OTA) scheme has been proposed to reduce the computational complexity, so that the cavity equations can be solved at long and short times (87, 96, 97, 248). However, in 4.D we show that for systems with self-interactions the OTA scheme fails to provide a closed set of equations, and one is left with the computational complexity being exponential in time, which would prevent solving the equations at long times. To overcome this difficulty, we map our system to an equivalent bipartite system, which can be solved using the bipartite cavity equations under the

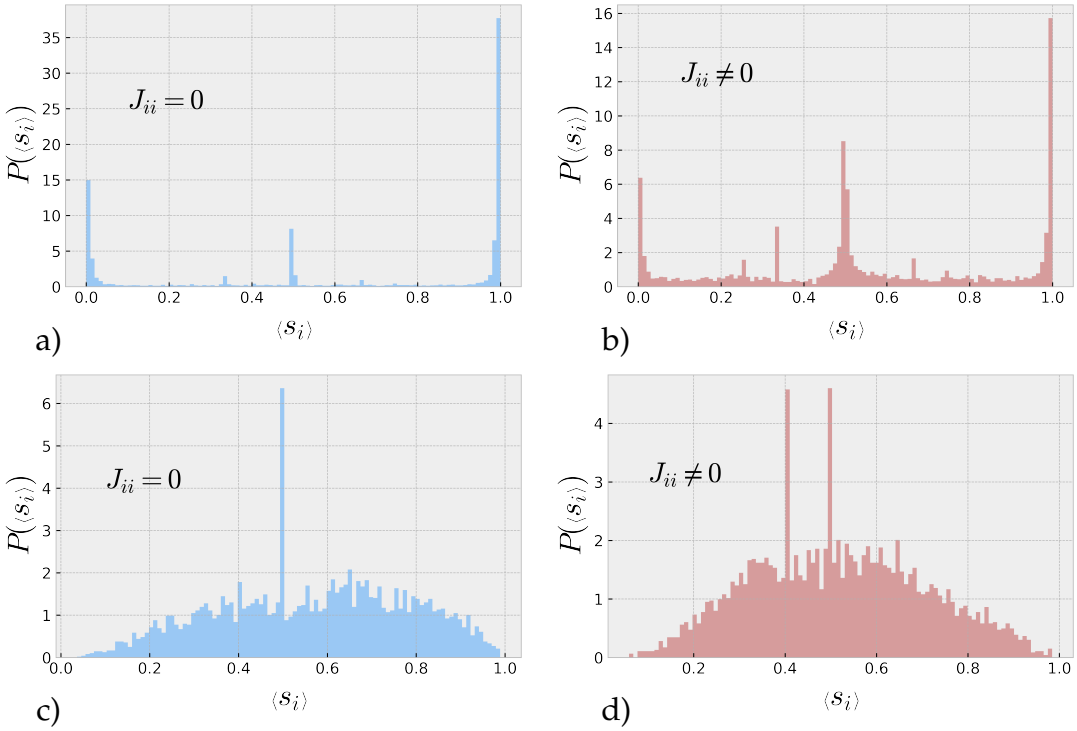

Figure 4.3: Probability density function for the activation probability of genes $P(\langle s_i \rangle)$ computed from the equilibrium cavity equations (4.29)-(4.30). Genes evolve according to the linear threshold model (4.5) with interactions drawn according to (4.31) and (4.32). Results in each panel are for the same network of size $N = 5000$, with connectivity $c = 3$, unbiased interactions $\kappa = 0$ and external field $\vartheta_i = 0 \ \forall \ i$. In (b) and (d), self-interactions are chosen with parameters $p = 0.5$ and $b = -1$ such that all self-interactions $J_{ii} = -1$. In (a) and (c), $J_{ii} = 0 \ \forall i$. In (a) and (b) inverse noise is set to $\beta = 5$, in (c) and (d) $\beta = 1$.

OTA scheme detailed in section 4.3.

To map our system of N variables with interactions J_{ij} to the model defined in (4.5), we create an additional set of N nodes, such that the system is now of size $2N$. This means that each site in the original system is given a partner site in the new set of variables, as shown in Figure 4.4. On the left side of this image we show a small network with three nodes, and on the right the equivalent network that is the result of our mapping. The original nodes are shown as circles, and new partner sites are shown as squares. All

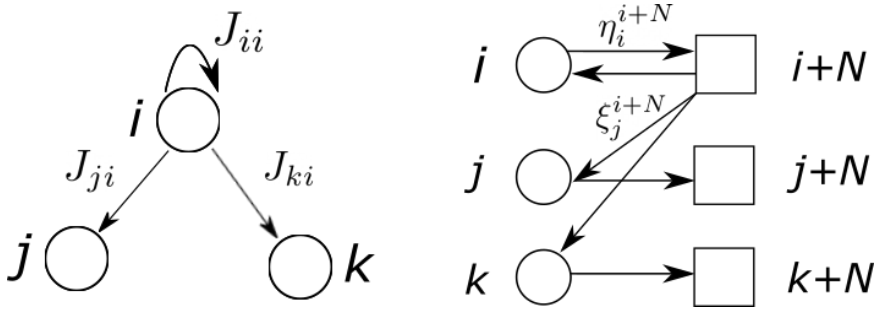

Figure 4.4: Sketch of how we map a monopartite system with self-interactions (left) to an equivalent bipartite spin system (right). Nodes in the original monopartite system are represented by circles, and new nodes in the bipartite system are represented by squares. In this mapping we have that the interaction site i has on site j is given by $J_{ji} = \xi_j^{i+N}$, and we have $\eta_i^\mu = \delta_{\mu,i+N}$.

original nodes have a directed link from themselves to their partner nodes. Self-interactions, J_{ii} in Figure 4.4, appear as bidirectional links between the node and its partner site. The interaction from one node to another in the original network is now represented by a path of length 2 in the new network i.e J_{ij} is represented in the new network by a link from node i to its partner site, and then a directed link from the partner site to node j. Formally, to achieve this we set $\eta_i^\mu = \delta_{\mu,i+N}$ in the bipartite model and $J_{ij} = \xi_i^{j+N}$. If we now set $\hat{T} = 0$ and $\vartheta_\mu = -\epsilon$ we have that (4.10) becomes,

$$\begin{aligned} \tau_\mu(t+\tilde{\Delta}) &= \theta\left(s_{\mu-N}(t) - \epsilon\right) \\ &= s_{\mu-N}(t) \end{aligned} \tag{4.39}$$

which when inserted into (4.9) we find,

$$s_i(t+\tilde{\Delta}) = \theta\left(\sum_{\mu=N}^{2N} \xi_i^\mu s_{\mu-N}(t-\tilde{\Delta}) + \vartheta_i - z_i(t)\right). \tag{4.40}$$

Hence,

$$s_i(t+\Delta) = \theta\left(\sum_{j=1}^{N} J_{ij}s_j(t) + \vartheta_i - z_i(t+\Delta/2)\right) \tag{4.41}$$

with $\Delta = 2\tilde{\Delta}$. We now see that equation (4.41) is of the same form as the linear threshold model with self-interactions (4.5). If we impose the initial conditions $\tau_{i+N}(0) = s_i(0)\ \forall\ i$, and assume that $z_i(t)$ are drawn from the same distribution (4.2) at each time, these two models are equivalent, up to some random noise, at every 2Δ time points. With this mapping the procedure is now as follows

1. Draw interaction matrix J_{ij}
2. Construct bipartite system with $\xi_i^{j+N} = J_{ij}$ and $\eta_i^{\mu} = \delta_{\mu,i+N}$
3. Solve the bipartite dynamical cavity equations up to some time t_m, with $\tilde{\Delta} = 1$
4. Compare with MC simulations of the monopartite system (4.5) at $t = 0, 2, 4, \ldots, t_m$.

Assuming interactions are drawn according to equations (4.31) and (4.32), we follow this procedure and compute the activation probability of each site obtained via dynamical cavity applied to the bipartite system and via MC simulations of the equivalent monopartite system. Figure 4.5 (left panel) shows results for the transient behaviour where the dynamical cavity method accurately predicts the activation probability of each site. The right panel of Figure 4.5 shows the full time dependence of the average activation probability and

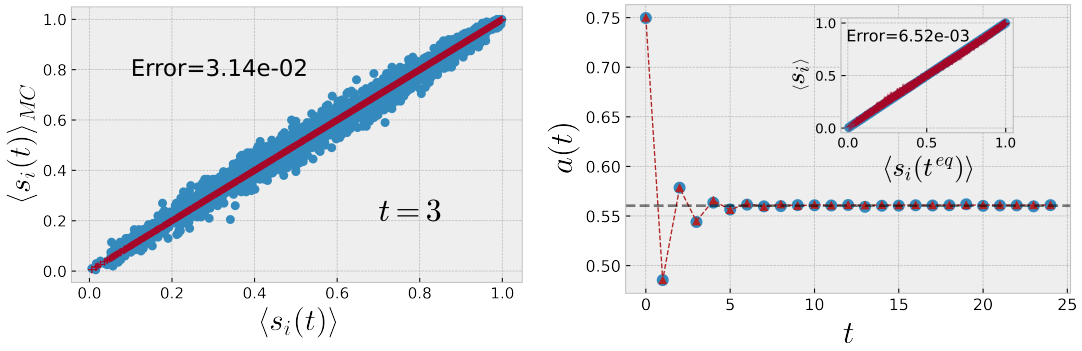

a) b)

Figure 4.5: (a) Scatter plot of gene activation probabilities $\langle s_i(t)\rangle$ computed via dynamical cavity and from MC simulations (average over 200 runs with different initial conditions drawn from the same distribution). (b) Average activation probabilities of genes, a, against time. Circles indicate MC simulations, triangles indicate the solution of the bipartite dynamical cavity equations (4.24) and (4.25) and are connected by red dashed lines for visual aid. Dashed horizontal line indicates the solution for average activation found from the cavity equations at equilibrium (4.29)-(4.30). Inset of (b) shows scatter plot of activation probability of each spin computed from equilibrium cavity and dynamical cavity method in the steady state. Annotation indicates the root mean square error. In (a) and (b), genes evolve according to the linear threshold model (4.5) with interactions drawn according to (4.31) and (4.32). Interaction networks are of size $N = 2500$ with connectivity $c = 2$, density of self-interactions $p = 0.25$, bias $\kappa = b = 0$, external field $\vartheta_i = 0\ \forall\ i$, noise level $\beta = 1.5$, and initial conditions $P(s_i^0) = P(\tau_\mu^0) = 0.75$.

agreement is excellent both during transient and in the steady state. Additionally, the inset of the right panel shows that the stationary state reached by the bipartite dynamical cavity method is in excellent agreement with the equilibrium state predicted by the static cavity equations. Therefore, by mapping a monopartite system with self-interactions to an equivalent bipartite system, we can now study their transient and long-time dynamics.

4.5 Nonlinear model with correlated, multi-node interactions

4.5.1 Dynamical analysis of systems with multi-node interactions

Previously, the dynamics of the nonlinear model (4.6) has been studied under the assumption that interactions are uncorrelated, $\mathrm{P}(\boldsymbol{\xi},\boldsymbol{\eta}) = \mathrm{P}(\boldsymbol{\xi})\mathrm{P}(\boldsymbol{\eta})$, and in the absence of noise in TF synthesis, $\hat{T} = 0$ (98, 244). Here we solve the dynamics of the system defined in (4.8), from which the dynamics of (4.6) can be recovered, with arbitrary noise $\hat{T}$ in TF synthesis and correlated interactions $\mathrm{P}(\boldsymbol{\xi},\boldsymbol{\eta}) = \mathrm{P}(\boldsymbol{\xi}|\boldsymbol{\eta})\mathrm{P}(\boldsymbol{\eta})$. We will assume $\mathrm{P}(\boldsymbol{\eta}) = \prod_{i,\mu}\mathrm{P}(\eta_i^\mu)$ with

$$\mathrm{P}(\eta_i^\mu) \;=\; \left(1-\frac{c}{N}\right)\delta_{\eta_i^\mu,0} + \frac{c}{N}\delta_{\eta_i^\mu,1} \tag{4.42}$$

and $\mathrm{P}(\boldsymbol{\xi}|\boldsymbol{\eta}) = \prod_{i,\mu}\mathrm{P}(\xi_i^\mu|\eta_i^\mu)$, with the choice

$$\mathrm{P}(\xi_i^\mu|\eta_i^\mu=0) \;=\; \left(1-\frac{d}{N}\right)\delta_{\xi_i^\mu,0} + \frac{d}{N}\left[\frac{1+\kappa}{2}\delta_{\xi_i^\mu,\frac{1}{d}} + \frac{1-\kappa}{2}\delta_{\xi_i^\mu,-\frac{1}{d}}\right] \tag{4.43}$$

$$\mathrm{P}(\xi_i^\mu|\eta_i^\mu=1) \;=\; (1-p)\,\delta_{\xi_i^\mu,0} + p\left[\frac{1+b}{2}\delta_{\xi_i^\mu,1} + \frac{1-b}{2}\delta_{\xi_i^\mu,-1}\right] \tag{4.44}$$

such that c is the average in-degree of a TF and $d + pc$ is the average out-degree of a TF, d being the average number of unidirectional links stemming from a TF and pc the average number of bidirectional links stemming from (and pointing to) a TF. In particular, $p \in [0,1]$ controls the density of bidirectional links, such that the network is unidirectional when $p = 0$, and when

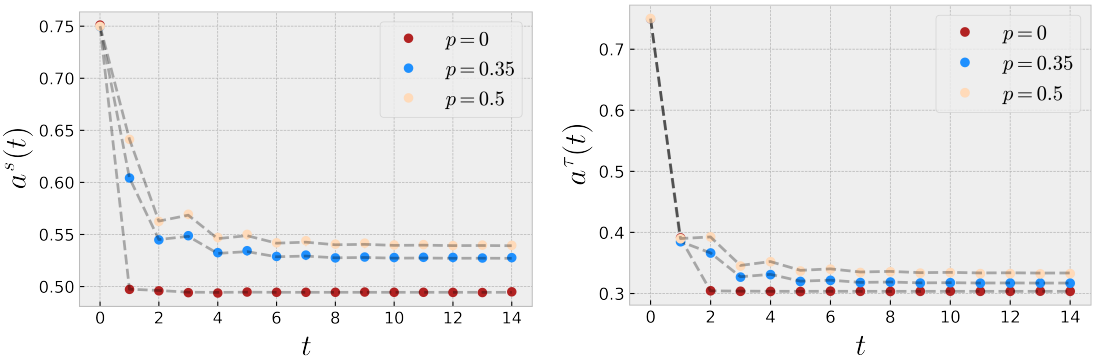

a) b)

Figure 4.6: Average activation of (a) genes $a^s(t) = N^{-1}\sum_i \langle s_i(t)\rangle$ and (b) TFs, $a^\tau(t) = (\alpha N)^{-1}\sum_\mu \langle \tau_\mu(t)\rangle$ against time. Genes and TFs evolve according to a bipartite linear threshold model (4.8) with interactions defined by equations (4.42)-(4.44). Markers indicate MC simulations on networks with size $N = 2500$ averaged over 100 runs with initial conditions drawn from $\mathrm{P}(s_i^0) = \mathrm{P}(\tau_\mu^0) = 0.75\ \forall\ i, \mu$. Dashed lines represent predictions from the dynamical cavity equations (4.24) and (4.25). Noise level is $\beta = \hat{\beta} = 10$, network parameters are $c = 1$, $d = 2$, $\kappa = 0$, $b = 1$. Results shown for different densities of self-interactions, p, as indicated in the legend.

$p = 1$ any gene that contributes to the synthesis of a TF will be regulated by that TF, in which case the number of bidirectional links in the network is maximal and equal to αcN. We note that when $p = 1$ the network is not fully bidirectional as $\eta_i^\mu = 0$ does not imply $\xi_i^\mu = 0$ and there are still αdN unidirectional links from TFs to genes. The bias in positive and negative regulatory couplings is controlled through the parameters $\kappa, b \in [-1, 1]$ such that all regulatory effects are excitatory ($\xi > 0$) if $\kappa, b = 1$ and all are inhibitory ($\xi < 0$) if $\kappa, b = -1$.

To assess the accuracy of the dynamical cavity method, we compute the time-dependent average activation probability of genes and TFs, given by $\langle s_i(t)\rangle = \sum_{s_i^t} s_i^t \mathrm{P}_i(s_i^t)$ and $\langle \tau_\mu(t)\rangle = \sum_{\tau_\mu^t} \tau_\mu^t \mathrm{P}_\mu(\tau_\mu^t)$, respectively. To compute this from MC simulations, we run many thermal realisations of a trajectory

and take the average over these thermal realisations,

$$\langle s_i(t)\rangle_{\mathrm{MC}} = \frac{1}{n}\sum_{\rho=1}^{n} s_i^{t,\rho} \tag{4.45}$$

$$\langle \tau_\mu(t)\rangle_{\mathrm{MC}} = \frac{1}{n}\sum_{\rho=1}^{n} \tau_\mu^{t,\rho} \tag{4.46}$$

where n is the number of thermal realisations of the trajectory we average over, and $s_i^{t,\rho}, \tau_\mu^{t\rho}$ denote the states of gene i and TF μ at time t in the ρ^{th} realisation of the trajectory, respectively. In Figure 4.6 we show the average activation probability of genes and TFs against time, and show that there is good agreement between the dynamical cavity method and MC simulations at all times, for different densities of bidirectional links and relatively low temperature. Additionally, the stationary values of the activation probabilities of individual sites are plotted in figure 4.7 for the same temperature and and are found in good agreement with MC simulations.

It is well known that the error in the predictions from the dynamical cavity method under the OTA scheme increases as the noise level is decreased. Previous work has demonstrated this looking at the error of macroscopic quantities in Ising spin models (87, 97) whereas for Boolean systems with pairwise interactions, such as the linear threshold model (4.5), predictions within a OTA scheme were found to remain accurate for microscopic quantities, even at relatively low temperatures. Here, we assess the accuracy of the OTA scheme in predicting microscopic quantities in Boolean systems with multi-node interactions, like the nonlinear threshold model defined in (4.6), and we find that the accuracy of OTA decreases when the temperature is

lowered, similarly to what was observed in Ising spin models. In the left panel of Figure 4.8 we show the mean square error in activation probabilities, $\delta_s(t) = N^{-1}\sum_i \left(\langle s_i(t)\rangle - \langle s_i(t)\rangle_{\rm MC}\right)^2$, at zero noise. For networks with an absence of bidirectional links, the OTA scheme is in perfect agreement with the MC simulations at long times, when the system has reached steady-state. The accuracy of the OTA scheme at zero noise, however, decreases as the density of bidirectional links increases. There are two potential sources of error. Firstly, the OTA scheme is based on two explicit assumptions, i.e. the Markovian factorization of cavity trajectories, (4.18) and (4.19), and the closure assumption, (4.22) and (4.23), which may break down at lower temperature due to stronger memory effects. Secondly, the dynamical cavity method implicitly assumes that there is no ergodicity breaking. Practically, the assumption that the system is ergodic in the cavity approach means that when we provide the dynamical cavity method with the initial conditions $\mathrm{P}_0(\mathbf{s}^0) = \prod_i \mathrm{P}_0(s_i^0)$ and $\mathrm{P}_0(\boldsymbol{\tau}^0) = \prod_\mu \mathrm{P}_0(\tau_\mu^0)$, it is implied that each configuration drawn from this distribution belongs to the same *ergodic sector*, and will hence reach the same attractor, which is untrue when ergodicity is broken. To deduce whether the loss of accuracy at zero temperature is due to the assumptions made in the OTA scheme, or by ergodicity breaking, we provide the dynamical cavity equations with a *specific configuration* $(\mathbf{s}^0, \boldsymbol{\tau}^0)$ as the initial condition, and then run zero temperature dynamics. In the right panel of Figure 4.8 we show that by initiaizing dynamical cavity in the same configuration (and thus in the same ergodic sector) as MC simulations, the OTA scheme predicts the trajectory without error. This suggests that the loss of accuracy observed in the left panel of Figure 4.8 is due to ergodicity breaking.

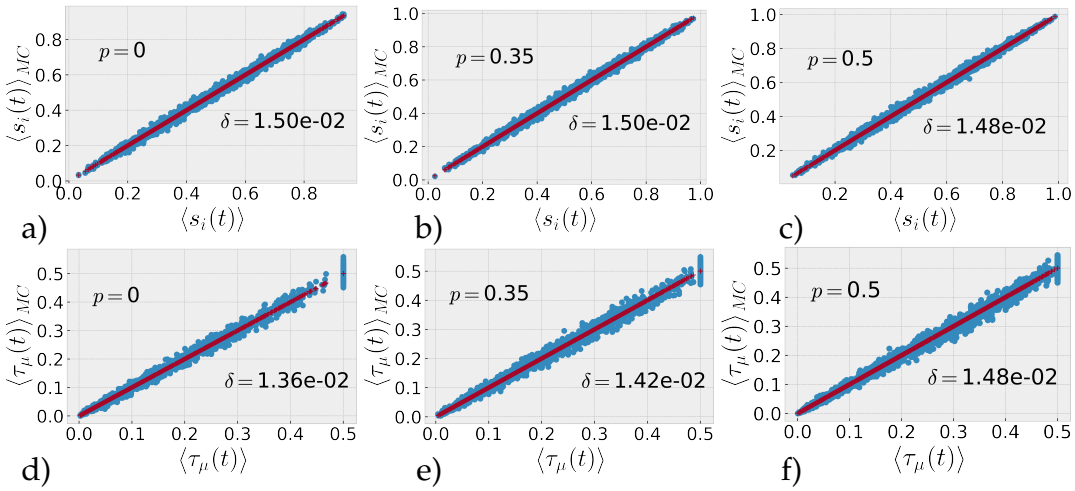

Figure 4.7: Scatter plot of the activation probability of genes $\langle s_i(t)\rangle$ (a)-(c) and TFs $\langle \tau_\mu(t)\rangle$ (d)-(f) computed from MC simulations and the dynamical cavity equations (4.24) and (4.25). MC simulations are averaged over 1000 thermal histories. Here we show the system at time $t = 15$ where the system has reached its steady-state. Genes and TFs evolve according to a bipartite linear threshold model (4.8) with interactions defined by equations (4.42)-(4.44). Parameters are: $N = 2500$, $c = 1$, $d = 2$, $\kappa = 0$, $b = 1$, $\beta = \hat{\beta} = 10$. The root mean square error, δ, and density of bidirectional links p is annotated in each plot.

4.5.2 Multiple attractors induced by self-regulation

The evidence of ergodicity breaking suggests that our system supports multiple attractors. To confirm this we show in Figure 4.9 the dynamics of genes and TFs starting from two different initial conditions for the same network. In the network we consider, a TF has an excitatory effect on every gene that is required for its own synthesis, $p = 1$ and $b = 1$, such that this network has a high density of bidirectional links. We again initialise the dynamical cavity method with the same initial configuration as the MC simulations, such that there is zero error in the dynamical cavity predictions. We see that the dynamics of the same network, starting from two different initial configurations, converges to two different 2-cycles, which shows that, at least at zero

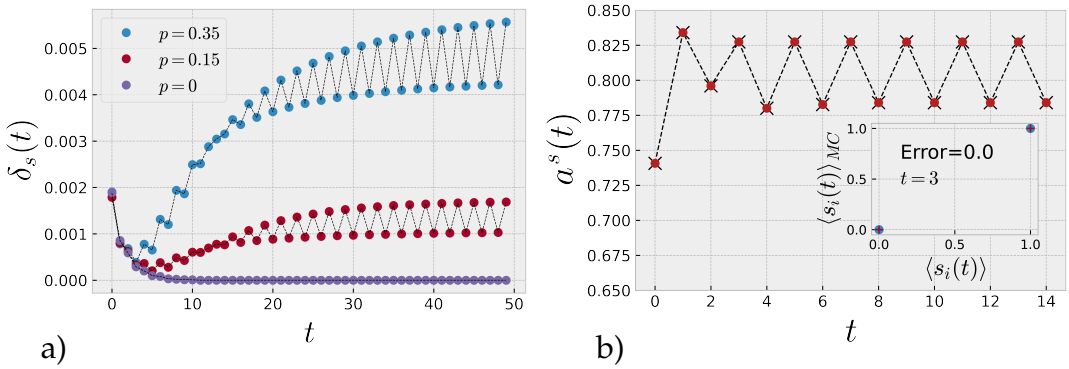

Figure 4.8: (a) Mean square error $\delta_s(t)$ between MC simulations (averages over 100 runs) and dynamical cavity equations (4.24) and (4.25), for the activation probabilities of genes, against time. Genes and TFs evolve according to a bipartite linear threshold model (4.8) with interactions defined by equations (4.42)-(4.44). Network size is $N = 2500$, connectivities are $c = 1$, $d = 2$, bias are $\kappa = 0$, $b = 1$, and initial conditions are set to $\mathrm{P}(s_i^0) = \mathrm{P}(\tau_\mu^0) = 0.75$. Legend indicates density of self-interactions, p. (b) Average activation probability of genes $a^s(t) = N^{-1}\sum_i \langle s_i(t)\rangle$ against time, computed by dynamical cavity (crosses) and MC simulations (circles). The dynamical cavity method is initialised with $\mathrm{P}_i(s_i^0) = \delta_{s_i^0, s_i^{MC}(0)}$ and $\mathrm{P}_\mu(\tau_\mu^0) = \delta_{\tau_\mu^0, \tau_\mu^{MC}(0)}$. Network parameters are: $N = 1500$, $c = 1$, $d = 3$, $\kappa = -1.5$, $b = 1$. Inset shows scatter plot of site activation probabilities of genes $\langle s_i(t)\rangle$, at time $t = 3$, computed by dynamical cavity and MC simulations. Annotation indicates root mean square error. In (a) and (b) external fields are set to $\vartheta_i = \epsilon$ and $\vartheta_\mu = -c_\mu + \epsilon$, with $\epsilon = 10^{-4}$, and the noise level is $\beta = \hat{\beta} = \infty$.

temperature, our model supports multiple attractors.

To better assess the type of attractors these systems exhibit, we look at the self-overlap, which we define as,

$$\Gamma^s(t,t') = \frac{1}{N}\sum_i (s_i^t - s_i^{t'})^2 \tag{4.47}$$

$$\Gamma^\tau(t,t') = \frac{1}{N}\sum_\mu (\tau_\mu^t - \tau_\mu^{t'})^2. \tag{4.48}$$

By running MC simulations at zero temperature for some long time t_w, and computing the self-overlap $\Gamma^s(t,t_w)$, with all other times $t \leq t_w$, we find, as

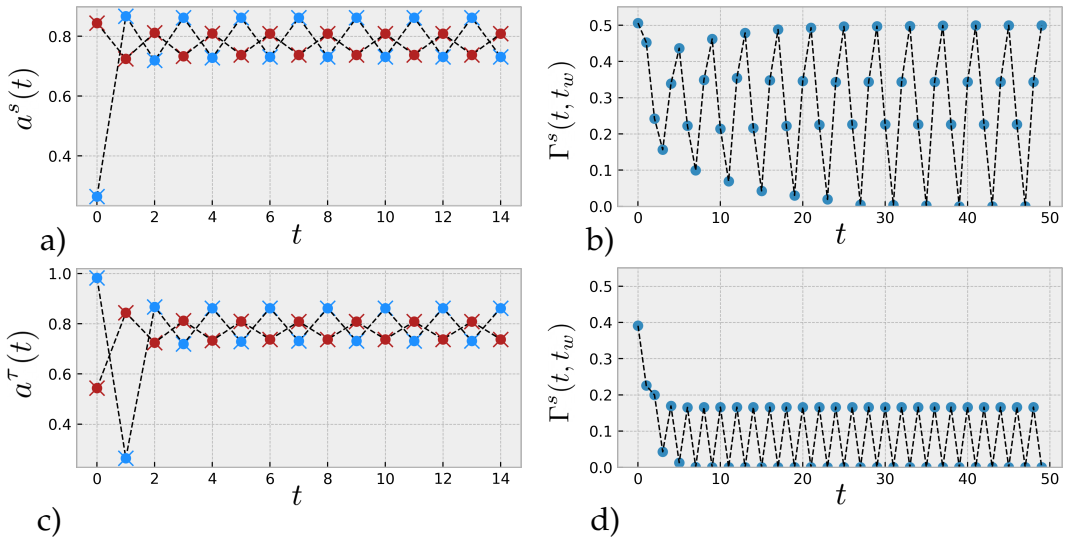

Figure 4.9: (a) and (c): Average activation of genes (a) and TFs (c) in the bipartite linear threshold model (4.8) with interactions defined by equations (4.42)-(4.44) and parameters: $N = 1500$, $c = 1$, $d = 3$, $\kappa = -1.5$, $b = 1$ (i.e. all self-interactions are positive) and $\beta = \hat{\beta} = \infty$. Results for two different initial conditions are shown. Circles indicate MC simulations, crosses indicate predictions from dynamical cavity equations (4.24) and (4.25). The dynamical cavity method is initialised with $\mathrm{P}_i(s_i^0) = \delta_{s_i^0, s_i^{MC}(0)}$ and $\mathrm{P}_\mu(\tau_\mu^0) = \delta_{\tau_\mu^0, \tau_\mu^{MC}(0)}$. (b) and (d): Self-overlap $\Gamma^s(t, t_w)$, defined in equation (4.47), against time t, with $t_w = 50$, for genes in the bipartite linear threshold model (4.8). Results are computed from MC simulations with $N = 2500$, $c = 1$, $d = 15$, $\kappa = 0$, for cases where (b) all self-interactions are inhibitory (i.e. $b = -1$) or (d) excitatory (i.e. $b = 1$). Similar plot can be obtained for the self-overlaps of the TFs, $\Gamma^\tau(t, t_w)$, but are not shown here.

shown in the right panels of Figure 4.9, that for systems with all positive self-regulatory effects the system will exhibits a 2-cycle, but the same network where the self-regulatory effects are negative will exhibit a 4-cycle. We find these results consistent for different realisations of the network, and for networks with different values of TF in-degree, $d + pc$. This suggests that the type of attractor that the dynamics converges to is determined by the type of self-regulatory effects present, alone.

To elucidate the effect that the density of bidirectional links has on the

attractors of our model, we study a dynamical variant of the overlap distribution. We exploit the fact that we are at zero temperature to run MC simulations until the system reaches its attractor, store them, and compare the attractors that are reached from different initial conditions. At zero temperature, the system is expected to reach a limit cycle, and so we compute the overlap between each point of the limit-cycles reached from two random initial conditions. The overlap for two replicas, $\mathbf{s}^{\rho}$ and $\mathbf{s}^{\nu}$, of the system starting from different random initial conditions is defined as

$$q^{s}_{\rho\nu} = \frac{1}{N}\sum_{i}\sum_{n=1}^{L}\left(2s_i^{n,\rho}-1\right)\left(2s_i^{n,\nu}-1\right) \tag{4.49}$$

where $s_i^{n,\rho}$ is the state of site i at the n^{th} point in the limit cycle of length L in replica ρ. We can similarly define the overlap for the TFs,

$$q^{\tau}_{\rho\nu} = \frac{1}{N}\sum_{\mu}\sum_{n=1}^{L}\left(2\tau_\mu^{n,\rho}-1\right)\left(2\tau_\mu^{n,\nu}-1\right). \tag{4.50}$$

The overlap takes values in $q \in [-1,1]$ such that $q = 1$ if the configurations are identical, and $q = -1$ if they are oppositely aligned i.e $s_i^{\rho} = 1 - s_i^{\nu}\ \forall\ i$. The above definition of the overlap is, however, dependent on the ordering of the points in the cycle. For example, it may be that two initial conditions lead to the same attractor, but enter the attractor at different points in the cycle, and so lead to an overlap $q \neq 1$. For this reason we compute the overlap between the attractors for different permutations of the points in the cycle and take the *maximum* value to be the true value of the overlap. By drawing many pairs of initial conditions and computing the overlap between the attractors according

the above, we compute the overlap distribution. Figure 4.10 shows that as the density of bidirectional links decreases, the width of the overlap distribution decreases and moves towards an overlap of $q_{12}^s, q_{12}^\tau = 1$, suggesting that the attractors become more similar as bidirectional links are removed, and that systems without bidirectional links will have just one attractor. Additionally, the external field acting on the TFs is shown to have a significant effect. When $\vartheta_\mu = -c_\mu + \epsilon$, such that TFs operate with AND logic, we see the existence of multiple attractors, with relatively low overlap (left panels). Conversely, for systems with external field $\vartheta_\mu = -\epsilon$, such that TFs operate with OR logic, we see that while these networks do support multiple attractors, the overlap is high, hence the attractors are very similar (right panels). Interpolating between these extreme cases, we set $\vartheta_\mu = -1 - \epsilon$, to add a little cooperativity to the OR logic, such that a TF requires at least two neighbouring genes to be active in order to be synthesised. In this case, we also see high overlap, even for systems with high densities of bidirectional links (middle panels).

Our work demonstrates the existence of multiple attractors in sparse, partially bidirectional networks. Previous analytical work has focused on the fully connected and fully asymmetric cases (201, 262, 263). More recently, numerical studies in small sparse networks showed that the number of attractors decreases to one as the dilution of the network is increased (246). Our results show that the presence of bidirectional links is crucial to have a multiplicity of attractors in sparse networks and that increasing the fraction of bidirectional interactions decreases the overlap between the attractors of the system. To the best of our knowledge, our work is the first to demonstrate that the existence of multiple attractors in sparse networks is conditional on the interactions

being at least partially bidirectional.

Additionally, we have seen that the overlap is lower in the nonlinear model, where TFs evolve according to AND logic, than in the linear model, where TFs evolve according to OR logic, suggesting that cooperativity in gene regulation promotes diversification of attractors. Our nonlinear model can be regarded as the Boolean equivalent of a mixed p-spin model, where the state of each site depends on a varying number of sites. The regular p-spin model has been shown in equilibrium to exhibit an ergodicity breaking phase at low noise levels, where multiple attractors are to be expected (264, 265, 266). Our numerical results show that ergodicity is also broken in our mixed p-Boolean model with asymmetric interactions, at low levels of noise, where the system exhibits a multiplicity of *cyclic* attractors. Interestingly, the overlap distribution is reminiscent of the one observed in equilibrium spin models exhibiting so-called "one step of replica symmetry breaking", a particular type of ergodicity breaking which is characterised by a delta-peaked distribution of overlaps (267). It can be shown that the width of the distributions in Figure 4.10 decreases with system size as $N^{-\frac{1}{2}}$, suggesting that this is a finite size effect and that for networks of infinite size these distributions are also delta-peaked at a single value.

While we have shown the existence of multiple attractors in the absence of noise, we expect that as noise is increased, the system will become ergodic, and the dynamics will converge to a single attractor. We can, however, show in Figure 4.11 that if TFs evolve without noise, but genes evolve with low but finite noise, the system still exhibits multiple attractors. Here, we have used a network with higher degree than in Figure 4.9 and see that there is a

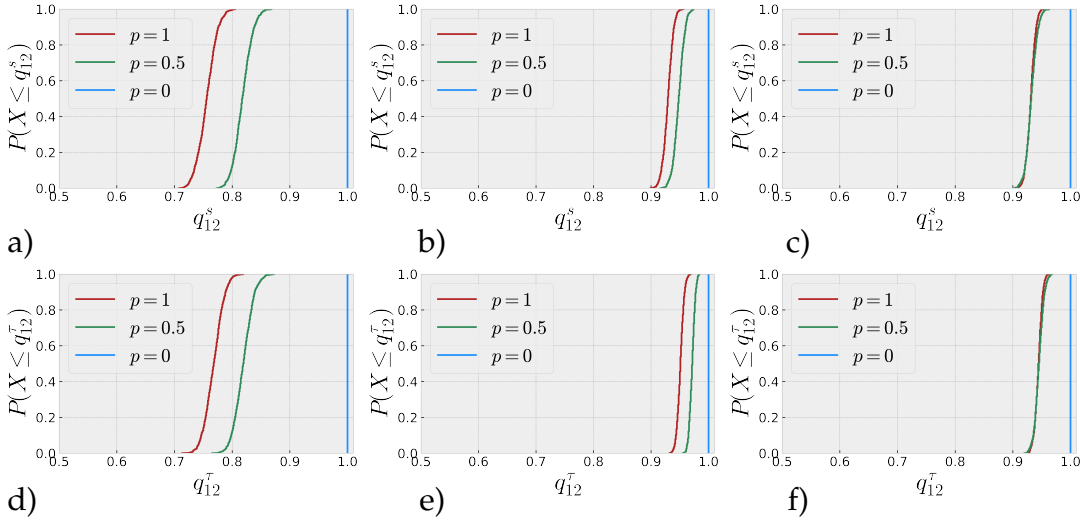

Figure 4.10: Cumulative distribution function of the overlap between attractors reached from different initial conditions in the bipartite linear threshold model (4.8). Panels (a)-(c) show results for genes, panels (d)-(e) show results for TFs. Network is drawn according to (4.42)-(4.44) with parameters: $N = 1000$, $c = 1$, $d = 3$, $\kappa = 0$, $b = 1$. Distributions are formed by comparing the attractors reached by 1000 random pairs of initial conditions. Results shown for different levels of bidirectional links, p, indicated by legend. Noise level is $\beta = \hat{\beta} = \infty$. Columns, from left to right, indicate cases where $\vartheta_\mu = -c_\mu + \epsilon$, $\vartheta_\mu = -1 - \epsilon$ and $\vartheta_\mu = -\epsilon$ with $\epsilon = 10^{-4}$. We also have $\vartheta_i = \epsilon$.

bigger difference in the average activation, suggesting that as the connectivity of the network is increased, the attractors become more dissimilar. Finally, we observe that any low but finite noise in the TFs dynamics leads to a single attractor, even when gene dynamics is noiseless.

4.6 OTA in the thermodynamic limit

In earlier sections we have derived expressions for activation probabilities of individual nodes in single graph instances. We can use these results to obtain expressions for typical (or average) activation probabilities by averaging over sites. For large networks, these expressions will depend on the distri-

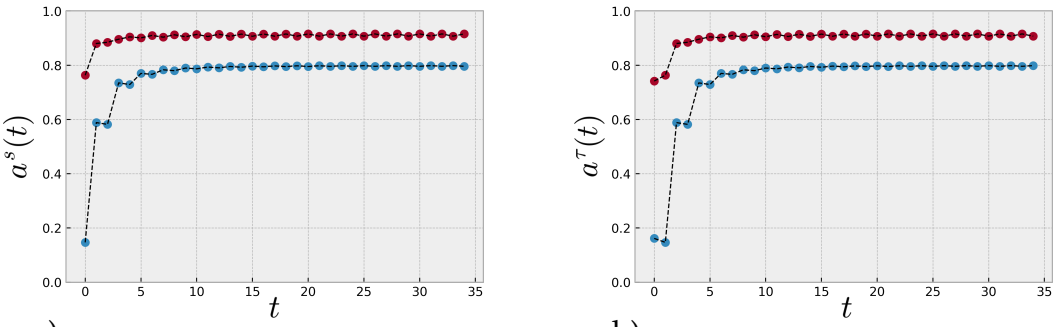

a) b)

Figure 4.11: Average activation of (a) genes $a^s(t) = N^{-1}\sum_i \langle s_i(t)\rangle$ and (b) TFs $a^\tau(t) = (\alpha N)^{-1}\sum_\mu \langle \tau_\mu(t)\rangle$ in the bipartite linear threshold model (4.8) against time. Symbols indicate result of MC simulations averaged over 100 thermal histories with dashed line for visual aid. Network is drawn according to equations (4.42)-(4.44) with parameters: $N = 1500$, $c = 1$, $d = 10$, $p = 1$, $\kappa = 0$ and $b = 1$. Noise level for TFs $\hat{\beta} = \infty$ and for genes $\beta = 100$.

bution $\mathrm{P}(\mathbf{J})$ (or $\mathrm{P}(\boldsymbol{\eta}, \boldsymbol{\xi})$) of the disorder and not on its realization $\mathbf{J}$ (or $\boldsymbol{\eta}, \boldsymbol{\xi}$), hence they give information on typical trajectories in the graph ensemble. Similar expressions can also be derived via generating functional analysis (GFA) (93, 94), however, no equivalent of the OTA scheme has been formulated within GFA, hence the resulting equations exhibit the aforementioned exponential time complexity. Taking averages of the dynamical cavity equations after application of the OTA scheme allows us to obtain equations for typical activation probabilities which do not exhibit such complexity and can therefore be solved explicitly at short and long times.

To demonstrate this we consider the linear threshold model (4.5) in the absence of self-interactions, such that $J_{ii} = 0$. In this case the probability of a site to have activation s_i^t at some time t, under the OTA scheme, is given by,

$$\mathrm{P}_i(s_i^t) = \sum_{s_i^{t-2}} \mathrm{P}_i(s_i^{t-2}) \sum_{\mathbf{s}_{\partial_i}^{t-1}} \mathrm{W}(s_i^t | h_i(\mathbf{s}_{\partial_i}^{t-1})) \left[\prod_{j\in\partial_i} \mathrm{P}_j^{(i)}(s_j^{t-1} | \zeta_j^{(i),t-1}) \right], \tag{4.51}$$

and the probability of a site to have activation s_i^t at time t, in the cavity graph where site ℓ is removed, subject to some external field $\zeta_i^{(\ell),t} = J_{i\ell} s_\ell^{t-1}$, is given by

$$\mathrm{P}_i^{(\ell)}(s_i^t|\zeta_i^{(\ell),t}) = \sum_{s_i^{t-2}} \mathrm{P}_i(s_i^{t-2}) \sum_{\mathbf{s}_{\partial_i\setminus\ell}^{t-1}} \mathrm{W}(s_i^t|h_i(\mathbf{s}_{\partial_i}^{t-1})) \left[\prod_{j\in\partial_i\setminus\ell} \mathrm{P}_j^{(i)}(s_j^{t-1}|\zeta_j^{(i),t-1})\right] \tag{4.52}$$

as shown in (248). From this we can define the distribution of site marginals as,

$$\pi(\{\mathrm{P}_t\}) = \frac{1}{N}\sum_i \prod_{s^t} \delta\left(\mathrm{P}_t(s^t) - \mathrm{P}_i(s^t)\right). \tag{4.53}$$

In 4.E we show that in the limit $N \to \infty$ the distribution of site marginals is found from the following closed set of equations,

$$\begin{aligned}\pi(\{\mathrm{P}_t\}) = \sum_k \mathrm{P}(k) \int \left[\prod_{j=1}^k \mathrm{d}J_j \mathrm{d}\hat{J}_j \{\mathrm{d}\hat{\mathrm{P}}_j\} \mathrm{P}(J_j)\mathrm{P}(\hat{J}_j|J_j)\right] \int \{\mathrm{d}\mathrm{P}_{t-2}\} \\ \times \pi_{t-2}\left[\{\mathrm{P}_{t-2}\}|k,\mathbf{J},\hat{\mathbf{J}}\right] \prod_{s^t} \delta\left(\mathrm{P}_t(s^t) - \phi(k,\{\mathrm{P}_{t-2}\},\mathbf{J},\hat{\mathbf{J}},\{\hat{\mathbf{P}}\})\right) \\ \times \prod_{j=1}^k \hat{\pi}_{t-1}\left[\{\hat{\mathrm{P}}_j\}|\hat{J}_j s^{t-2}\right]\end{aligned} \tag{4.54}$$

with

$$\phi(k,\{\mathrm{P}_{t-2}\},\mathbf{J},\hat{\mathbf{J}},\{\hat{\mathbf{P}}\}) = \sum_{s^{t-2}} \mathrm{P}_{t-2}(s^{t-2}) \sum_{s_1^{t-1},\ldots,s_k^{t-1}} \mathrm{W}(s^t|\sum_{j=1}^k J_j s_j^{t-1}) \prod_{j=1}^k \hat{\mathrm{P}}_j(s_j^{t-1}) \tag{4.55}$$

and

$$\hat{\pi}_t(\{\mathrm{P}_t\}|x) = \sum_k \frac{k\mathrm{P}(k)}{\langle k\rangle} \int \left[\prod_{j=1}^{k-1} \mathrm{d}J_j \mathrm{d}\hat{J}_j \{\mathrm{d}\hat{\mathrm{P}}_j\} \mathrm{P}(J_j)\mathrm{P}(\hat{J}_j|J_j)\right] \int \{\mathrm{d}\mathrm{P}_{t-2}\} \\ \times \pi_{t-2}\left[\{\mathrm{P}_{t-2}\}|k,\mathbf{J},\hat{\mathbf{J}}\right] \prod_{s^t} \delta\left(\mathrm{P}_t(s^t) - \widetilde{\phi}(k,\{\mathrm{P}_{t-2}\},\mathbf{J},\hat{\mathbf{J}},\{\hat{\mathbf{P}}\},x)\right) \\ \times \prod_{j=1}^{k-1} \hat{\pi}_{t-1}\left[\{\hat{\mathrm{P}}_j\}|\hat{J}_j s^{t-2}\right] \tag{4.56}$$

where we define,

$$\widetilde{\phi}(k,\{\mathrm{P}_{t-2}\},\mathbf{J},\hat{\mathbf{J}},\{\hat{\mathbf{P}}\},x) = \sum_{s^{t-2}} \mathrm{P}_{t-2}(s^{t-2}) \\ \times \sum_{s_1^{t-1},\ldots,s_k^{t-1}} W(s^t|\sum_{j=1}^{k} J_j s_j^{t-1} + x) \prod_{j=1}^{k} \hat{\mathrm{P}}_j(s_j^{t-1}). \tag{4.57}$$

Equations (4.54) and (4.56) can be solved by a population dynamics procedure (256, 268). In Figure 4.12 we show the cumulative distribution function of site activation probabilities $\mathrm{P}(\langle s(t)\rangle) = \pi(\mathrm{P}(s^t = 1))$ at different times, computed solving the above equations via population dynamics, for a random regular graph with fully symmetric interactions. We find reasonable agreement with MC simulations on a single instance of a network with size $N = 10^4$. We however, see small deviations due to the cavity equations in this instance being averaged over the disorder $\mathrm{P}(\mathbf{J})$. As expected from earlier analysis in Sec. 4.4 the time-dependent distribution of activation probabilities reaches a multi-modal steady-state.

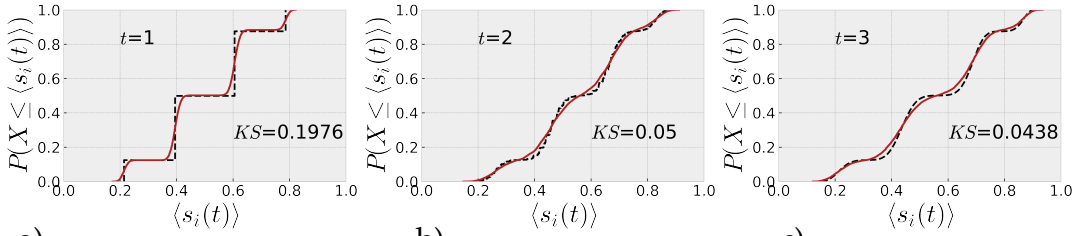

Figure 4.12: CDF of activation probabilities of genes in the linear threshold model defined in (4.5) at time $t = 1, 2, 3$ (from (a) to (c)). The network is a random regular graph with degree $c = 3$. Interactions are fully symmetric, i.e. $J_{ij} = J_{ji}$ and are drawn from the set $\{-1, 1\}$ with equal probability. The inverse temperature is $\beta = 1$ and initial conditions are set to $\mathrm{P}(s_i^t) = 0.5\ \forall i$. Dashed line indicates solution to equation (4.54) from population dynamics with sample size $S = 2.5 \times 10^5$. Solid line indicates results from MC simulations for a network of size $N = 10^4$. Annotations indicate the Kolmogorov–Smirnov (KS) statistic comparing the empirical distributions from the cavity method and MC simulations.

4.7 Discussion

In this chapter we have studied systems of sparsely connected Boolean variables with multi-node and self-interactions. Previous work has shown that self-interactions complicate the analysis of dynamics. However, by mapping to an equivalent bipartite system, we find that the dynamical cavity method, within a OTA scheme, provides an efficient numerical framework to study the dynamics of systems with arbitrary bidirectionality, multi-node and self-interactions. We have shown for such systems that the OTA scheme predicts the activation probability of each site in the transient and non-equilibrium steady-state, down to relatively low temperature, where the system is ergodic. As temperature is lowered further, ergodicity is eventually broken, and we have found that the error increases with the bidirectionality of the interactions. At zero temperature, however, if the dynamical cavity is given the same initial configuration as MC simulations, the OTA scheme is in excel-

lent agreement with simulations, showing that OTA accurately describes the dynamics within any given ergodic sector. We have also derived equations for the distribution (and mean) of site activations at a given time, in the thermodynamic limit, within a OTA scheme, which is numerically more efficient than previous approaches involving sums over the history of a trajectory (96). We comment that these equations, when compared to their analogue derived by generating functionals (93, 94) provide physical insight into the effect of truncating memory terms in the GFA. In principle, the dynamical cavity equations are also solveable for networks with strong degree correlations, as shown in previous work (268). By providing closed expressions for the distribution of site marginals, the dynamical cavity method can provide insight into the heterogeneity of site trajectories for a typical network drawn from some ensemble. This is unlike GFA which only provides information on the trajectory of a typical site.

From our work, it is clear that sparse networks with partially bidirectional interactions support multiple (cyclic) attractors, at low noise. Additionally, multi-node interactions are found to decrease the overlap between attractors, suggesting that cooperativity increases diversification of attractors. The existence of a multiplicity of attractors in partially bidirectional sparse systems is an important feature for models of GRNs to sustain multi-cellular life. It means that if a GRN is in an attractor, it can be pushed out of this attractor by some event, for example the sudden change in external field, and can move from one attractor to another. This could describe how cells move from one cell type to another. Both cooperative effects and gene self-regulation (i.e. a gene coding for a TF that regulates the gene itself) are commonly observed in

GRNs and our work suggests that it is these features in combination which allow GRNs to support a diverse set of stable gene expression profiles, corresponding to different cell types, with self-regulation playing an important role in determining the nature of attractors.

Our work poses interesting questions for future work. Our study suggests that there is an ergodicity breaking phase at low temperatures characterised by an overlap distribution which resembles one observed in equilibrium spin systems (with symmetric interactions and fixed-point attractors) . It would be an interesting pathway for future work to formally derive the critical line, in parameter space, where the transition to the ergodicity breaking phase takes place. In equilibrium, such transition takes place on the AT line, which has been derived for fully connected systems (269). For sparse systems, a formal derivation of the AT line is lacking in the literature. Instead, an alternative approach has been devised for sparse systems, where the transition to ergodicity breaking can be located as the critical line where the effective fields of two replicas of the system become sensitive to their boundary conditions, within a cavity approach (259). The formulation of dynamical versions of this approach would be welcome to locate such transitions in GRNs with asymmetric interactions. Similarly, devising methods to survey the ultrametric structure of stationary states in non-equilibrium settings would be useful to understand the observed shape of the overlap distribution. Of course, while we can deduce that a multiplicity of (cyclic) attractors exist, it remains an open question how the attractors relate to the specific realisation of the bipartite network and an analytical framework to deduce the number of attractors that are supported by a network remains likewise an open point of investi-

gation. Finally, an important focus for applications would be to study how a GRN may move from one attractor to another, either by the application of time-dependent external fields, or dynamic variations in the interaction network itself, which may shed light on the mechanisms through which cells differentiate. As discussed in the introduction, the immune system is an ideal system to study cell differentiation, since in some cases the molecular reaction that triggers differentiation is known. Our model has salient features of GRNs - sparsity, directed interactions, and multiple diverse attractors - and, hence, could provide a minimal model to elucidate the complex relationship between genotype and phenotype.

Appendices

4.A Dynamical cavity approach to bipartite systems

In the appendix to the thesis A.1, we provide an introduction to the cavity method and how it may be applied to dynamical processes on networks. In this section we show how the dynamical cavity method may be used to analyse the dynamics of the general bipartite system defined in (4.9) and (4.10), from which the linear model with self-interactions (4.5) and the nonlinear model with multi-node interactions (4.6) may be recovered by suitable choice of parameters. Starting with equation (4.15), we wish to derive a closed set of equations for single site quantities at a given time, like s_i^t and τ_μ^t. To do so, we first consider the trajectory of a single gene i,

$$\mathrm{P}_i(s_i^{0\ldots t_m}) = \sum_{\mathbf{s}^{0\ldots t_m}\setminus s_i^{0\ldots t_m},\boldsymbol{\tau}^{0\ldots t_m}} \mathrm{P}(\mathbf{s}^{0\ldots t_m}, \boldsymbol{\tau}^{0\ldots t_m}). \tag{4.58}$$

Inserting equation (4.15) into the above, we have,

$$\mathrm{P}_i(s_i^{0\ldots t_m}) = \sum_{\mathbf{s}^{0\ldots t_m}\setminus s_i^{0\ldots t_m},\boldsymbol{\tau}^{0\ldots t_m}} \mathrm{P}(\mathbf{s}^0,\boldsymbol{\tau}^0)\prod_{t=1}^{t_m}\prod_{i=1}^{N}\prod_{\mu=N+1}^{N+M}\mathrm{W}(s_i^{t+1}|h_i(\boldsymbol{\tau}_{\partial_i}^t))\widetilde{\mathrm{W}}(\tau_\mu^{t+1}|h_\mu(\mathbf{s}^t)) \tag{4.59}$$

As is typical of the cavity formalism, we assume that the bipartite network has the topological structure of a tree and that initial conditions factorise over the sites of the tree $\mathrm{P}(\mathbf{s}^0,\boldsymbol{\tau}^0) = \prod_{i\mu}\mathrm{P}(s_i^0,\tau_\mu^0)$. To proceed, we make use of the unique structural properties of a tree. To illustrate this, we sketch a fraction of the bipartite network we are considering in Figure 4.A.1, sketching gene i which is connected to TFs μ and ν which are themselves connected to further genes. We highlight that the bipartite network can be divided into different sub-trees. In Figure 4.A.1 we show T_i a tree rooted at the gene i. We also indicate the sub-tree $T_\mu \setminus i$ which is all the genes and TFs in the tree rooted at TF μ when i has been removed from the network. We may then consider reorganising the terms in the above equation, into products over nodes in

different sub-trees of the network,

$$\begin{aligned}
\mathrm{P}_i(s_i^{0\dots t_m}) = & \sum_{\mathbf{s}^{0\dots t_m}\setminus s_i^{0\dots t_m},\boldsymbol{\tau}^{0\dots t_m}} \mathrm{P}(\mathbf{s}^0,\boldsymbol{\tau}^0)\left[\prod_{t=1}^{t_m}\mathrm{W}(s_i^t|h_i(\boldsymbol{\tau}_{\partial_i}^{t-1}))\prod_{j\in T_i\setminus i}\mathrm{W}(s_j^t|h_j(\boldsymbol{\tau}_{\partial_j}^{t-1}))\right] \\
& \times\prod_{\mu\in\partial_i}\left[\prod_{t=1}^{t_m}\widetilde{\mathrm{W}}(\tau_\mu^t|h_\mu(\mathbf{s}_{\partial_\mu}^{t-1}))\prod_{\nu\in T_\mu\setminus\mu}\widetilde{\mathrm{W}}(\tau_\nu^t|h_\nu(\mathbf{s}_{\partial_\nu}^{t-1}))\right] \\
= & \sum_{\mathbf{s}^{0\dots t_m}\setminus s_i^{0\dots t_m},\boldsymbol{\tau}^{0\dots t_m}} \mathrm{P}(\mathbf{s}^0,\boldsymbol{\tau}^0)\left[\prod_{t=1}^{t_m}\mathrm{W}(s_i^t|h_i(\boldsymbol{\tau}_{\partial_i}^{t-1}))\right] \\
& \times\prod_{\mu\in\partial_i}\left[\prod_{t=1}^{t_m}\widetilde{\mathrm{W}}(\tau_\mu^t|h_\mu(\mathbf{s}_{\partial_\mu}^{t-1}))\prod_{\nu,j\in T_\mu\setminus\mu,i}\widetilde{\mathrm{W}}(\tau_\nu^t|h_\nu(\mathbf{s}_{\partial_\nu}^{t-1}))\mathrm{W}(s_j^t|h_j(\boldsymbol{\tau}_{\partial_j}^{t-1}))\right] \\
= & \,\mathrm{P}(s_i^0)\sum_{\boldsymbol{\tau}_{\partial_i}^{0\dots t_m}}\left[\prod_{t=1}^{t_m}\mathrm{W}(s_i^t|h_i(\boldsymbol{\tau}_{\partial_i}^{t-1}))\right]\prod_{\mu\in\partial_i}\left\{\sum_{\mathbf{s}_{T_\mu\setminus i}^{0\dots t_m},\boldsymbol{\tau}_{T_\mu\setminus\mu}^{0\dots t_m}}\mathrm{P}(\mathbf{s}_{T_\mu}^0\setminus s_i^0)\mathrm{P}(\boldsymbol{\tau}_{T_\mu}^0)\right. \\
& \left.\times\left[\prod_{t=1}^{t_m}\widetilde{\mathrm{W}}(\tau_\mu^t|h_\mu(\mathbf{s}_{\partial_\mu}^{t-1}))\prod_{\nu,j\in T_\mu\setminus\mu,i}\widetilde{\mathrm{W}}(\tau_\nu^t|h_\nu(\mathbf{s}_{\partial_\nu}^{t-1}))\mathrm{W}(s_j^t|h_j(\boldsymbol{\tau}_{\partial_j}^{t-1}))\right]\right\}
\end{aligned} \tag{4.60}$$

where we have defined $\mathbf{s}_{T_\mu} = \{s_i, i\in T_\mu\}$ and $\boldsymbol{\tau}_{T_\mu} = \{\tau_\nu, \nu\in T_\mu\}$ where T_μ and T_i are trees rooted at nodes μ and i.

We may then take the external sum over $\boldsymbol{\tau}_{\partial_i}^{t_m}$ and the internal sums over $\boldsymbol{\tau}_{T_\mu}^{t_m}$ and $\mathbf{s}_{T_\mu}^{t_m}$,

$$\begin{aligned}
\mathrm{P}_i(s_i^{0\dots t_m}) = & \,\mathrm{P}(s_i^0)\sum_{\boldsymbol{\tau}_{\partial_i}^{0\dots t_m-1}}\left[\prod_{t=1}^{t_m}\mathrm{W}(s_i^t|h_i(\boldsymbol{\tau}_{\partial_i}^{t-1}))\right]\prod_{\mu\in\partial_i}\left\{\sum_{\mathbf{s}_{T_\mu\setminus i}^{0\dots t_m-1},\boldsymbol{\tau}_{T_\mu\setminus\mu}^{0\dots t_m-1}}\mathrm{P}(\mathbf{s}_{T_\mu}^0\setminus s_i^0)\mathrm{P}(\boldsymbol{\tau}_{T_\mu}^0)\right. \\
& \left.\times\left[\prod_{t=1}^{t_m-1}\widetilde{\mathrm{W}}(\tau_\mu^t|h_\mu(\mathbf{s}_{\partial_\mu}^{t-1}))\prod_{\nu,j\in T_\mu\setminus\mu,i}\widetilde{\mathrm{W}}(\tau_\nu^t|h_\nu(\mathbf{s}_{\partial_\nu}^{t-1}))\mathrm{W}(s_j^t|h_j(\boldsymbol{\tau}_{\partial_j}^{t-1}))\right]\right\}.
\end{aligned} \tag{4.61}$$

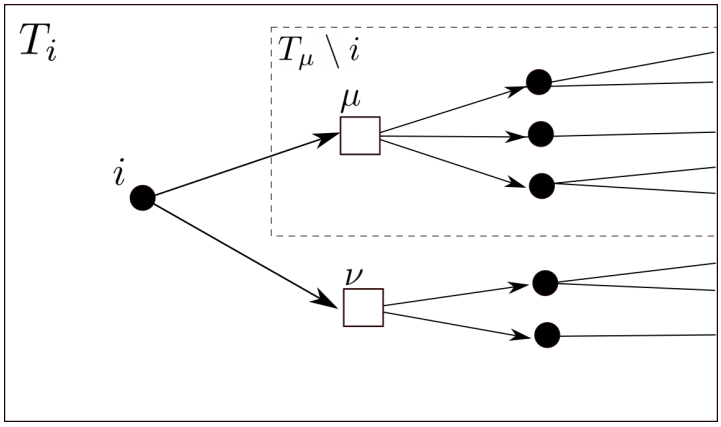

Figure 4.A.1: A sketch of a network which is a tree. Here the tree is rooted at gene i, which has neighbouring TFs μ and ν. The large black box contains the set of nodes T_i, which are all nodes in the tree rooted at node i. The dashed black box contains all the nodes belonging to the set $T_\mu \setminus i$, which are the nodes in the sub-tree rooted at TF μ.

We note that the local field that acts on TF μ can be written as,

$$h_\mu(\mathbf{s}_{\partial_\mu}^{t-1}) = \sum_{j \in \partial_\mu \setminus i} \eta_j^\mu s_j^{t-1} + \vartheta_\mu + \eta_i^\mu s_i^{t-1} = h_\mu^{(i)}(\mathbf{s}_{\partial_\mu}^{t-1}) + \zeta_\mu^{(i),t} \tag{4.62}$$

where we have defined the local field in a new copy of the network where site i is removed, referred to as the *cavity graph*, $h_\mu^{(i)}(\mathbf{s}_{\partial_\mu}^{t-1}) = \sum_{j \in \partial_\mu \setminus i} \eta_j^\mu s_j^{t-1} + \vartheta_\mu$, and the time dependent external field $\zeta_\mu^{(i),t} = \eta_i^\mu s_i^{t-1}$, which is the effect of the removed gene i on TF μ in the cavity graph. Similarly, we can write the local field that acts on gene i as,

$$h_i(\boldsymbol{\tau}_{\partial_i}^{t-1}) = \sum_{\mu \in \partial_i \setminus \nu} \xi_i^\mu \tau_\mu^{t-1} + \vartheta_i + \xi_i^\nu \tau_\nu^{t-1} = h_i^{(\nu)}(\boldsymbol{\tau}_{\partial_i}^{t-1}) + \zeta_i^{(\nu),t} \tag{4.63}$$

denoting the local field in the cavity graph where TF ν is removed, $h_i^{(\nu)}(\boldsymbol{\tau}_{\partial_i}^{t-1}) = \sum_{\mu \in \partial_i \setminus \nu} \xi_i^\mu \tau_\mu^{t-1} + \vartheta_i$, and external field $\zeta_i^{(\nu),t} = \eta_i^\mu s_i^{t-1}$.

At this stage we can inspect the the contents of the curly brackets in equation (4.61). We notice a sum over the variables $\sum_{\mathbf{s}_{T_\mu \setminus i}^{0\dots t_m-1}, \boldsymbol{\tau}_{T_\mu \setminus \mu}^{0\dots t_m-1}}$ that is taken over some joint distribution of the state of genes and nodes at different times. Once this sum has been taken, it would leave the joint distribution $\mathrm{P}_\mu^{(i)}(\tau_\mu^{0\dots t_m-1}|\zeta_\mu^{(i),1\dots t_m-1})$ which is interpreted as the probability to observe the trajectory $\tau_\mu^{0\dots t_m-1}$ in the cavity graph where gene i is removed, given that the time dependent external field, $\zeta_\mu^{(i),1,\dots,t_m-1}$, acts on TF μ. With this definition in place, equation (4.61) is now equivalent to

$$\mathrm{P}_i(s_i^{0\dots t_m}) = \mathrm{P}(s_i^0) \sum_{\boldsymbol{\tau}_{\partial_i}^{0\dots t_m-1}} \left[\prod_{t=1}^{t_m} \mathrm{W}(s_i^t|h_i(\boldsymbol{\tau}_{\partial_i}^{t-1}))\right] \prod_{\mu\in\partial_i} \mathrm{P}_\mu^{(i)}(\tau_\mu^{0\dots t_m-1}|\zeta_\mu^{(i),1\dots t_m-1}). \tag{4.64}$$

Following the same reasoning, we can derive an analogous expression for the trajectory of a single TF μ,

$$\mathrm{P}_\mu(\tau_\mu^{0\dots t_m}) = \mathrm{P}(\tau_\mu^0) \sum_{\mathbf{s}_{\partial_\mu}^{0\dots t_m-1}} \left[\prod_{t=1}^{t_m} \widetilde{\mathrm{W}}(\tau_\mu^t|h_\mu(\mathbf{s}_{\partial_\mu}^{t-1}))\right] \prod_{j\in\partial_\mu} \mathrm{P}_j^{(\mu)}(s_j^{0\dots t_m-1}|\zeta_j^{(\mu),1\dots t_m-1}) \tag{4.65}$$

where $\mathrm{P}_j^{(\mu)}(s_j^{0\dots t_m-1}|\zeta_j^{(\mu),1\dots t_m-1})$ is the probability to observe the trajectory $s_j^{0\dots t_m-1}$ in the cavity graph where site μ is removed, given that the time-dependent external field $\zeta_j^{(\mu),1\dots t_m-1} = \xi_j^\mu \tau_\mu^{1\dots t_m-1}$, acts on site j. Equations for the probability to observe the trajectory of a single gene i in the *cavity graph*

are found by considering the effect of removing TF ν from equation (4.64),

$$\mathrm{P}_i^{(\nu)}(s_i^{0\dots t_m}) = \mathrm{P}(s_i^0) \sum_{\boldsymbol{\tau}_{\partial_i\setminus\nu}^{0\dots t_m-1}} \left[\prod_{t=1}^{t_m} \mathrm{W}(s_i^t|h_i^{(\nu)}(\boldsymbol{\tau}_{\partial_i}^{t-1}))\right] \prod_{\mu\in\partial_i\setminus\nu} \mathrm{P}_\mu^{(i)}(\tau_\mu^{0\dots t_m-1}|\zeta_\mu^{(i),1\dots t_m-1}), \tag{4.66}$$

which depends upon the cavity field $h_i^{(\nu)}(\boldsymbol{\tau}_{\partial_i}^{t-1})$. Similarly, by removing gene ℓ from equation (4.65) we find,

$$\mathrm{P}_\mu^{(\ell)}(\tau_\mu^{0\dots t_m}) = \mathrm{P}(\tau_\mu^0) \sum_{\mathbf{s}_{\partial_\mu\setminus\ell}^{0\dots t_m-1}} \left[\prod_{t=1}^{t_m} \widetilde{\mathrm{W}}(\tau_\mu^t|h_\mu^{(\ell)}(\mathbf{s}_{\partial_\mu}^{t-1}))\right] \prod_{j\in\partial_\mu\setminus\ell} \mathrm{P}_j^{(\mu)}(s_j^{0\dots t_m-1}|\zeta_j^{(\mu),1\dots t_m-1}), \tag{4.67}$$

which depends upon the cavity field $h_\mu^{(\ell)}(\mathbf{s}_{\partial_\mu}^{t-1})$. If we now consider an external field $\zeta_i^{(\nu),1\dots t_m}$ acting on gene i in the cavity graph with TF ν removed, the cavity field in equation (4.66) will become $h_i^{(\nu)}(\boldsymbol{\tau}_{\partial_i}^{t-1}) + \zeta_i^{(\nu),t} = h_i(\boldsymbol{\tau}_{\partial_i}^{t-1})$, from which we deduce equation (4.16). Similarly, if an external field $\zeta_\mu^{(\ell),1\dots t_m}$ acts on TF μ in the cavity graph where gene ℓ is removed, from equation (4.66), we can deduce equation (4.17). We have derived a closed system of equations (4.64), (4.65), (4.16) and (4.17) which in principle can be solved recursively for the trajectory of the system. As noted in the main text, their computational complexity grows exponentially with the length of the trajectory.

If we assume that the system has unidirectional interactions, however, the cavity equations simplify. In this case, $\xi_i^\mu \neq 0$ implies $\eta_i^\mu = 0$, such that the external fields in equation (4.64) vanish, $\zeta_\mu^{(i),t} = 0$, and the RHS of equations (4.65) and (4.17) become identical, as $\ell \notin \partial_\mu$ when $\mu \in \partial_\ell$ and given (4.62) we

have $\mathrm{P}_\mu^{(i)}(\tau_\mu^{0\ldots t_m}|0) = \mathrm{P}_\mu(\tau_\mu^{0\ldots t_m})$. This simplifies equation (4.64) to

$$\mathrm{P}_i(s_i^{0\ldots t_m}) = \mathrm{P}(s_i^0) \sum_{\boldsymbol{\tau}_{\partial_i}^{0\ldots t_m-1}} \left[\prod_{t=1}^{t_m} \mathrm{W}(s_i^t|h_i(\boldsymbol{\tau}_{\partial_i}^{t-1}))\right] \prod_{\mu\in\partial_i} \mathrm{P}_\mu(\tau_\mu^{0\ldots t_m-1}) \tag{4.68}$$

and by the same argument one can also derive the trajectory for the TFs,

$$\mathrm{P}_\mu(\tau_\mu^{0\ldots t_m}) = \mathrm{P}(\tau_\mu^0) \sum_{\mathbf{s}_{\partial\mu}^{0\ldots t_m-1}} \left[\prod_{t=1}^{t_m} \widetilde{\mathrm{W}}(\tau_\mu^t|h_\mu(\mathbf{s}_{\partial_\mu}^{t-1}))\right] \prod_{j\in\partial_\mu} \mathrm{P}_j(s_j^{0\ldots t_m-1}). \tag{4.69}$$

We may now marginalise equation (4.68) over $s_i^{0,\ldots,t_m-1}$ and equation (4.69) over $\tau_\mu^{0,\ldots,t_m-1}$ and find,

$$\mathrm{P}_i(s_i^{t_m}) = \sum_{\boldsymbol{\tau}_{\partial_i}^{t_m-1}} \left[\mathrm{W}(s_i^{t_m}|h_i(\boldsymbol{\tau}_{\partial_i}^{t_m-1}))\right] \prod_{\mu\in\partial_i} \mathrm{P}_\mu(\tau_\mu^{t_m-1}) \tag{4.70}$$

$$\mathrm{P}_\mu(\tau_\mu^{t_m}) = \sum_{\mathbf{s}_{\partial\mu}^{t_m-1}} \left[\widetilde{\mathrm{W}}(\tau_\mu^{t_m}|h_\mu(\mathbf{s}_{\partial_\mu}^{t_m-1}))\right] \prod_{j\in\partial_\mu} \mathrm{P}_j(s_j^{t_m-1}). \tag{4.71}$$

Equations (4.70) and (4.71) are a closed set of equations which may be solved by simple iteration. They reveal that in systems with unidirectional interactions, $\mathrm{P}(\mathbf{s}_{\partial_\mu}^t) = \prod_{j\in\partial_\mu} \mathrm{P}_j(s_j^t)$.

As we note in Sec. 4.3, for systems with arbitrarily bidirectional interactions, we may use the OTA scheme to reduce the time complexity of the cavity equations, which in the case of our bipartite system means to assume (4.18) and (4.19). If we insert (4.19) into (4.16) and isolate the terms which contain $s_i^{t_m}$ and $\boldsymbol{\tau}_{\partial_i}^{t_m-1}$, we can rewrite the RHS in terms of the cavity distribution of

the s_i trajectory up until time $t_m - 1$,

$$\begin{aligned}
\mathrm{P}_i^{(\nu)}(s_i^{0\ldots t_m}|\zeta_i^{(\nu),1\ldots t_m}) &= \mathrm{P}(s_i^0) \sum_{\boldsymbol{\tau}_{\partial_i\setminus\nu}^{0\ldots t_m-1}} \left[\prod_{t=1}^{t_m} \mathrm{W}(s_i^t|h_i(\boldsymbol{\tau}_{\partial_i}^{t-1}))\right] \\
&\qquad \times \prod_{\mu\in\partial_i\setminus\nu} \mathrm{P}_\mu(\tau_\mu^0) \prod_{t=1}^{t_m-1} \mathrm{P}_\mu^{(i)}(\tau_\mu^t|\zeta_\mu^{(i),t}) \\
&= \sum_{\boldsymbol{\tau}_{\partial_i\setminus\nu}^{t_m-1}} \mathrm{W}(s_i^{t_m}|h_i(\boldsymbol{\tau}_{\partial_i}^{t_m-1})) \left[\prod_{\mu\in\partial_i\setminus\nu} \mathrm{P}_\mu^{(i)}(\tau_\mu^{t_m-1}|\zeta_\mu^{(i),t_m-1})\right] \\
&\quad \times \mathrm{P}(s_i^0) \sum_{\boldsymbol{\tau}_{\partial_i}^{0\ldots t_m-2}} \left[\prod_{t=1}^{t_m-1} \mathrm{W}(s_i^t|h_i(\boldsymbol{\tau}_{\partial_i}^{t-1}))\right] \\
&\quad \times \prod_{\mu\in\partial_i\setminus\nu} \mathrm{P}_\mu(\tau_\mu^0) \prod_{t=1}^{t_m-2} \mathrm{P}_\mu^{(i)}(\tau_\mu^t|\zeta_\mu^{(i),t}) \\
&= \sum_{\boldsymbol{\tau}_{\partial_i\setminus\nu}^{t_m-1}} \mathrm{W}(s_i^{t_m}|h_i(\boldsymbol{\tau}_{\partial_i}^{t_m-1})) \left[\prod_{\mu\in\partial_i\setminus\nu} \mathrm{P}_\mu^{(i)}(\tau_\mu^{t_m-1}|\zeta_\mu^{(i),t_m-1})\right] \\
&\quad \times \mathrm{P}_i^{(\nu)}(s_i^{0\ldots t_m-1}|\zeta_i^{(\nu),1\ldots t_m-1}). \qquad (4.72)
\end{aligned}$$

At this stage it is possible to marginalise the above over $s_i^{0,\dots,t_m-1}$,

$$\begin{aligned}
\mathrm{P}_i(s_i^{t_m}|\zeta_i^{(\nu),1\dots t_m}) &= \sum_{s_i^{0\dots t_m-1}} \sum_{\boldsymbol{\tau}_{\partial_i\setminus\nu}^{t_m-1}} \mathrm{W}(s_i^{t_m}|h_i(\boldsymbol{\tau}_{\partial_i}^{t_m-1})) \\
&\quad \times \left[\prod_{\mu\in\partial_i\setminus\nu} \mathrm{P}_\mu^{(i)}(\tau_\mu^{t_m-1}|\zeta_\mu^{(i),t_m-1})\right] \mathrm{P}_i^{(\nu)}(s_i^{0\dots t_m-1}|\zeta_i^{(\nu),1\dots t_m-1}) \\
&= \sum_{s_i^{0\dots t_m-1}} \sum_{\boldsymbol{\tau}_{\partial_i\setminus\nu}^{t_m-1}} \mathrm{W}(s_i^{t_m}|h_i(\boldsymbol{\tau}_{\partial_i}^{t_m-1})) \left[\prod_{\mu\in\partial_i\setminus\nu} \mathrm{P}_\mu^{(i)}(\tau_\mu^{t_m-1}|\zeta_\mu^{(i),t_m-1})\right] \\
&\quad \times \mathrm{P}_i(s_i^0) \prod_{t=1}^{t_m-1} \mathrm{P}_i^{(\nu)}(s_i^t|\zeta_i^{(\nu),t}) \\
&= \sum_{s_i^{t_m-2}} \sum_{\boldsymbol{\tau}_{\partial_i\setminus\nu}^{t_m-1}} \mathrm{W}(s_i^{t_m}|h_i^{(\nu)}(\boldsymbol{\tau}_{\partial_i}^{t_m-1}) + \zeta_i^{(\nu),t_m}) \\
&\quad \times \left[\prod_{\mu\in\partial_i\setminus\nu} \mathrm{P}_\mu^{(i)}(\tau_\mu^{t_m-1}|\zeta_\mu^{(i),t_m-1})\right] \mathrm{P}_i^{(\nu)}(s_i^{t_m-2}|\zeta_i^{(\nu),t_m-2}). \quad (4.73)
\end{aligned}$$

It is now apparent that the LHS only depends on $\zeta_i^{(\nu),t_m-2}$ and $\zeta_i^{(\nu),t_m}$ i.e $\mathrm{P}_i(s_i^{t_m}|\zeta_i^{(\nu),1\dots t_m}) = \mathrm{P}_i(s_i^{t_m}|\zeta_i^{(\nu),t_m-2,t_m})$, such that we can write

$$\begin{aligned}
\mathrm{P}_i^{(\nu)}(s_i^{t_m}|\zeta_i^{(\nu),t_m-2,t_m}) &= \sum_{s_i^{t_m-2}} \sum_{\boldsymbol{\tau}_{\partial_i\setminus\nu}^{t_m-1}} \mathrm{W}(s_i^{t_m}|h_i^{(\nu)}(\boldsymbol{\tau}_{\partial_i}^{t_m-1}) + \zeta_i^{(\nu),t_m}) \\
&\quad \times \left[\prod_{\mu\in\partial_i\setminus\nu} \mathrm{P}_\mu^{(i)}(\tau_\mu^{t_m-1}|\zeta_\mu^{(i),t_m-1})\right] \mathrm{P}_i^{(\nu)}(s_i^{t_m-2}|\zeta_i^{(\nu),t_m-2}).
\end{aligned} \quad (4.74)$$

In principle, this is in contradiction with the Markovian assumption made for the cavity distribution, which would require $\mathrm{P}_i^{(\nu)}(s_i^{t_m}|\zeta_i^{(\nu),t_m-2,t_m}) = \mathrm{P}_i^{(\nu)}(s_i^{t_m}|\zeta_i^{(\nu),t_m})$. Such inconsistency arises from treating a non-Markovian process as Marko-

vian. In order to get a closed set of equations for the one-time cavity marginal, further closure assumptions are thus required. As stated in Sec. 4.3, we assume that the cavity distribution, with external field from the removed site, may be approximated by its non-cavity counterpart i.e $\mathrm{P}_i^{(\nu)}(s_i^{t_m-2}|\zeta_i^{(\nu),t_m-2}) \approx \mathrm{P}_i(s_i^{t_m-2})$, following (248). Under this approximation, from (4.74) we retrieve equation (4.20), and by considering adding the removed TF ν back in and setting external fields to zero, we find, for the non-cavity distribution, the expression given in (4.24). By the same reasoning, we can derive analogous equations for the trajectory of a TF μ. In summary, the dynamics of the bipartite system are fully described, under the OTA scheme, by the closed, coupled set of equations (4.20),(4.21),(4.24), and (4.25), which can be solved by iteration given some initial conditions $\mathrm{P}_i(s_i^0)$ and $\mathrm{P}_\mu(\tau_\mu^0)$.

4.B Equilibrium analysis of (0,1) spins with parallel update and self-interactions

In this appendix we use the cavity method to calculate the equilibrium value of site marginals for the linear threshold model (4.5) with self-interactions. Assuming that $z_i(t)$ is a random variable with c.d.f. (4.2), we can write the evolution of the state probability as a Markov chain

$$\mathrm{P}_{t+1}(\mathbf{s}) = \sum_{\mathbf{s}'} W(\mathbf{s}|\mathbf{s}')\mathrm{P}_t(\mathbf{s}') \tag{4.75}$$

with transition probability

$$W(\mathbf{s}|\mathbf{s}') = \prod_{i=1}^{N} \mathrm{W}(s_i|h_i(\mathbf{s}'_{\partial_i}, s'_i)) = \prod_{i=1}^{N} \frac{e^{\frac{\beta}{2}(2s_i-1)h_i(\mathbf{s}'_{\partial_i}, s'_i)}}{2\cosh\frac{\beta}{2}h_i(\mathbf{s}'_{\partial_i}, s'_i)}, \tag{4.76}$$

where $h_i(\mathbf{s}_{\partial_i}, s_i) = \sum_{j\in\partial_i} J_{ij}s_j + J_{ii}s_i + \vartheta_i$. If the interactions are fully symmetric, $J_{ij} = J_{ji}$, the transition probabilities (4.76) satisfy detailed balance

$$p_{\mathrm{eq}}(\mathbf{s})W(\mathbf{s}'|\mathbf{s}) = p_{\mathrm{eq}}(\mathbf{s}')W(\mathbf{s}|\mathbf{s}') \tag{4.77}$$

with the equilibrium distribution

$$p_{\mathrm{eq}}(\mathbf{s}) = \frac{1}{Z}\mathrm{e}^{-\beta H_\beta(\mathbf{s})} \tag{4.78}$$

where $H_\beta(\mathbf{s}) = -\frac{1}{\beta}\sum_i \ln 2\cosh\frac{\beta}{2}h_i(\mathbf{s}_{\partial_i}, s_i) - \frac{1}{2}\sum_i h_i(\mathbf{s}_{\partial_i}, s_i) - \sum_i s_i\vartheta_i$. We can rewrite this distribution in a form more amenable to analysis if we consider a fictitious set of variables $\boldsymbol{\tau} = \{0,1\}^N$,

$$\begin{aligned} p_{\mathrm{eq}}(\mathbf{s}) &= \frac{1}{Z}\prod_{i=1}^{N} 2\cosh\frac{\beta}{2}h_i(\mathbf{s}_{\partial_i}, s_i)\mathrm{e}^{\frac{\beta}{2}h_i(\mathbf{s}_{\partial_i}, s_i)}\mathrm{e}^{\beta\vartheta_i s_i} \\ &= \frac{1}{Z}\prod_{i=1}^{N}\sum_{\tau_i}\mathrm{e}^{\frac{\beta}{2}(2\tau_i-1)h_i(\mathbf{s}_{\partial_i}, s_i)}\mathrm{e}^{\frac{\beta}{2}h_i(\mathbf{s}_{\partial_i}, s_i)}\mathrm{e}^{\beta\vartheta_i s_i} \end{aligned} \tag{4.79}$$

where we have used $2\cosh(x) = \sum_{\tau\in\{0,1\}} e^{(2\tau-1)x}$ as in (254, 255). The equilibrium distribution can then be written as

$$p_{\mathrm{eq}}(\mathbf{s}) = \frac{1}{Z}\sum_{\boldsymbol{\tau}}\mathrm{e}^{\beta\sum_{i\neq j}\tau_i J_{ij}s_j + \beta\sum_i \tau_i J_{ii}s_i + \beta\sum_i \vartheta_i(s_i+\tau_i)} \tag{4.80}$$

the marginalisation of the joint distribution of real and fictitious variables (4.28).

Now we use the cavity method to find a closed set of equations for single site quantities. To do so we marginalise (4.28) over all sites except i,

$$p_i(s_i, \tau_i) = \frac{1}{Z} \sum_{\mathbf{s}\setminus s_i} \sum_{\boldsymbol{\tau}\setminus\tau_i} \mathrm{e}^{-\beta\mathcal{H}(\mathbf{s},\boldsymbol{\tau})} \tag{4.81}$$

and note that the Hamiltonian can be written in the form $\mathcal{H}(\mathbf{s},\boldsymbol{\tau}) = -s_i h_i(\boldsymbol{\tau}_{\partial_i}) - \tau_i h_i(\mathbf{s}_{\partial_i}) - s_i J_{ii}\tau_i - \vartheta_i(\tau_i + s_i) + \mathcal{H}^{(i)}(\mathbf{s},\boldsymbol{\tau})$ where we have defined the Hamiltonian of the system where site i has been removed $\mathcal{H}^{(i)}(\mathbf{s},\boldsymbol{\tau}) = -\sum_{\ell\neq(i,j)} s_\ell J_{\ell j}\tau_j - \sum_{\ell\neq i} s_\ell J_\ell \tau_\ell - \sum_{\ell\neq i}\vartheta_\ell(s_\ell + \tau_\ell)$. With this definition the site marginal may be written in the following form,

$$p_i(s_i, \tau_i) = \frac{1}{Z_i} \sum_{\boldsymbol{\tau}_{\partial_i}} \mathrm{e}^{\beta\left(s_i h_i(\boldsymbol{\tau}_{\partial_i}) + \tau_i h_i(\mathbf{s}_{\partial_i}) + s_i J_{ii}\tau_i + \vartheta_i(s_i+\tau_i)\right)} p^{(i)}(\mathbf{s}_{\partial_i}, \boldsymbol{\tau}_{\partial_i}) \tag{4.82}$$

where $p^{(i)}(\mathbf{s}_{\partial_i}, \boldsymbol{\tau}_{\partial_i})$ is the equilibrium distribution of the neighbours of site i, in the cavity graph where i is removed, $Z^{(i)} = \sum_{\mathbf{s}\setminus s_i}\sum_{\boldsymbol{\tau}\setminus\tau_i} \mathrm{e}^{-\beta\mathcal{H}^{(i)}(\mathbf{s},\boldsymbol{\tau})}$ is its corresponding partition function and $Z_i = Z/Z^{(i)}$. The cavity approach assumes that cavity fields are independent of each other, such that $p^{(i)}(\mathbf{s}_{\partial_i}, \boldsymbol{\tau}_{\partial_i}) = \prod_{j\in\partial_i} p_j^{(i)}(s_j, \tau_j)$, which is exact on trees and sparse graphs which are locally tree-like in the limit $N \to \infty$. Under this assumption the site marginals and cavity site marginals can be found from the closed set of equations (4.29) and (4.30). In order to solve these equations, it is convenient to parameterise the

cavity marginals in terms of effective fields

$$p_i^{(\ell)}(s_i,\tau_i) \;=\; \frac{1}{Z_i^{(\ell)}} \mathrm{e}^{\frac{\beta}{2}\left((2s_i-1)h_{i\ell}^{s}+(2\tau_i-1)h_{i\ell}^{\tau}+(2s_i-1)(2\tau_i-1)h_{i\ell}^{s\tau}\right)} \tag{4.83}$$

and use (4.30) to obtain a closed set of equations for the cavity fields,

$$h_{i\ell}^{s} = \frac{1}{2\beta}\sum_{j\in\partial_i\setminus\ell}\ln\left(\frac{f_{ij}(1,1)f_{ij}(1,0)}{f_{ij}(0,1)f_{ij}(0,0)}\right)+\frac{1}{2}J_{ii}+\vartheta_i \tag{4.84}$$

$$h_{i\ell}^{\tau} = \frac{1}{2\beta}\sum_{j\in\partial_i\setminus\ell}\ln\left(\frac{f_{ij}(1,1)f_{ij}(0,1)}{f_{ij}(1,0)f_{ij}(0,0)}\right)+\frac{1}{2}J_{ii}+\vartheta_i \tag{4.85}$$

$$h_{i\ell}^{s\tau} = \frac{1}{2\beta}\sum_{j\in\partial_i\setminus\ell}\ln\left(\frac{f_{ij}(1,1)f_{ij}(0,0)}{f_{ij}(0,1)f_{ij}(1,0)}\right)+\frac{1}{2}J_{ii} \tag{4.86}$$

where we define,

$$f_{ij}(s_i,\tau_i) = \sum_{s_j}\sum_{\tau_j}\mathrm{e}^{\beta\left(s_iJ_{ij}\tau_j+\tau_iJ_{ij}s_j\right)}p_j^{(i)}(s_j,\tau_j). \tag{4.87}$$

These equations may be solved by simple iteration from some random initial condition. We can similarly parameterise the single site marginal as

$$p_i(s_i,\tau_i) \;=\; \frac{1}{Z_i}\mathrm{e}^{\frac{\beta}{2}\left((2s_i-1)h_i^{s}+(2\tau_i-1)h_i^{\tau}+(2s_i-1)(2\tau_i-1)h_i^{s\tau}\right)} \tag{4.88}$$

from which one finds,

$$h_i^s = \frac{1}{2\beta}\sum_{j\in\partial_i}\ln\left(\frac{f_{ij}(1,1)f_{ij}(1,0)}{f_{ij}(0,1)f_{ij}(0,0)}\right)+\frac{1}{2}J_{ii}+\vartheta_i \tag{4.89}$$

$$h_i^\tau = \frac{1}{2\beta}\sum_{j\in\partial_i}\ln\left(\frac{f_{ij}(1,1)f_{ij}(0,1)}{f_{ij}(1,0)f_{ij}(0,0)}\right)+\frac{1}{2}J_{ii}+\vartheta_i \tag{4.90}$$

$$h_i^{s\tau} = \frac{1}{2\beta}\sum_{j\in\partial_i}\ln\left(\frac{f_{ij}(1,1)f_{ij}(0,0)}{f_{ij}(0,1)f_{ij}(1,0)}\right)+\frac{1}{2}J_{ii}. \tag{4.91}$$

One must solve equations (4.84), (4.85) and (4.86) by iteration, and then substitute this solution into equations (4.89), (4.90) and (4.91) to find the fields h_i^s, h_i^τ and $h_i^{s\tau}$ from which one can find the average activation probability, $\langle s_i\rangle = \sum_{s_i,\tau_i} s_i p_i(s_i,\tau_i)$, from the following expression

$$\langle s_i\rangle = \frac{1}{Z_i}\mathrm{e}^{\frac{\beta}{2}h_i^s}\cosh\frac{\beta}{2}\left(h_i^\tau + h_i^{s\tau}\right), \tag{4.92}$$

where we have defined the normalisation constant

$$Z_i = \sum_{s_i,\tau_i}\mathrm{e}^{\frac{\beta}{2}\left((2s_i-1)h_i^s+(2\tau_i-1)h_i^\tau+(2s_i-1)(2\tau_i-1)h_i^{s\tau}\right)}. \tag{4.93}$$

4.C Monte Carlo Simulations

To assess the accuracy of the cavity equations, we compare their solution to MC simulations. To simulate a system which evolves with synchronous dynamics according to (4.75) we use the following procedure:

1. Specify the system size N, length of trajectory t_m, initialise the interaction matrix J_{ij} according to $\mathrm{P}(J_{ij})$, and specify the initial conditions

$\mathrm{P}_i(s_i^0)\ \forall\ i = 1, \ldots, N$. Set time variable $t = 0$.

2. Draw the initial configuration of the system $\mathbf{s}^0 = (s_1^0, \ldots, s_N^0)$ according to the initial conditions $\mathrm{P}_i(s_i^0)\ \forall\ i = 1, \ldots, N$.

3. Set $i = 1$.

4. Compute the probability

$$\mathrm{W}(s_i^{t+1} = 1 | h_i(\mathbf{s}_{\partial_i}^t, s_i^t)) = \frac{e^{\frac{\beta}{2} h_i(\mathbf{s}_{\partial_i}^t, s_i^t))}}{2 \cosh \frac{\beta}{2} h_i(\mathbf{s}_{\partial_i}^t, s_i^t)} \tag{4.94}$$

5. Draw a random number from the uniform distribution $X \sim U(0,1)$. If $X \leq \mathrm{W}(s_i^{t+1} = 1 | h_i(\mathbf{s}_{\partial_i}^t, s_i^t))$ set $s_i^{t+1} = 1$. Otherwise, set $s_i^{t+1} = 0$.

6. Set $i = i + 1$ and go back to step step 4 until $i = N$.

7. Set $t = t + 1$ and go back to step 3 until $t = t_m$.

The same procedure need only be modified slightly to simulate the bipartite spin system. In that case specify ξ_i^μ, η_i^μ instead of J_{ij}, according to $\mathrm{P}(\xi_i^\mu, \eta_i^\mu)$ and include additional initial conditions for the TFs $\mathrm{P}(\tau_\mu^0)$ as well as the number of TFs, M. After step 6, we then do the following

7. Set $\mu = 1 + N$.

8. Compute the probability

$$\mathrm{W}(\tau_\mu^{t+1} = 1 | h_\mu(\boldsymbol{\tau}_{\partial_\mu}^t, \tau_\mu^t)) = \frac{e^{\frac{\beta}{2} h_\mu(\boldsymbol{\tau}_{\partial_\mu}^t, \tau_\mu^t)}}{2 \cosh \frac{\beta}{2} h_\mu(\boldsymbol{\tau}_{\partial_\mu}^t, \tau_\mu^t)} \tag{4.95}$$

9. Draw a random number from the uniform distribution $X \sim U(0,1)$. If $X \leq \mathrm{W}(\tau_\mu^{t+1} = 1 | h_\mu(\boldsymbol{\tau}_{\partial_\mu}^t, \tau_\mu^t))$ set $\tau_\mu^{t+1} = 1$. Otherwise, set $\tau_\mu^{t+1} = 0$.

10. Set $\mu = \mu + 1$ and go back to step step 8 until $\mu = N + M$.

11. Set $t = t + 1$ and go back to step 7 until $t = t_m$.

By following steps 1-11, one can simulate a single trajectory of a bipartite network with interactions described by ξ_i^μ and η_i^μ, from time $t = 0, \ldots, t_m$.

4.D Dynamical cavity approach to systems with self-interactions

Here we detail the dynamical cavity approach for a system of N Boolean variables with pairwise as well as self-interactions, which evolves in time according to equation (4.75). As we shall show, it is possible to derive a closed set of equations for such systems but, even for systems with unidirectional interactions, these equations are exponential in complexity, and can not be simplified using OTA schemes. To begin, we consider the trajectory of the system from time $t = 0$ to $t = t_m$, $\mathbf{s}^0 \to \mathbf{s}^1 \to \cdots \to \mathbf{s}^{t_m}$, which we denote $\mathbf{s}^{0 \ldots t_m}$. From equation (4.75) the trajectory of the system follows,

$$\mathrm{P}(\mathbf{s}^{0 \ldots t_m}) = \mathrm{P}_0(\mathbf{s}^0) \prod_{t=1}^{t_m} W(\mathbf{s}^t | \mathbf{s}^{t-1}). \tag{4.96}$$

We now assume that the interactions, due to their sparsity, are represented by a network with the topology of a tree. By following steps in 4.A, now applied

to a monopartite system, we may write the probability to observe a single site trajectory as,

$$\begin{aligned} \mathrm{P}_i(s_i^{0\ldots t_m}) = \mathrm{P}_i(s_i^0) \sum_{\mathbf{s}_{\partial_i}^{0\ldots t_m-1}} \left[\prod_{t=1}^{t_m} \mathrm{W}(s_i^t | h_i(\mathbf{s}_{\partial_i}^{t-1}, s_i^{t-1})) \right] \\ \times \prod_{j\in\partial_i} \mathrm{P}_j^{(i)}(s_j^{0\ldots t_m-1} | \zeta_j^{(i),1\ldots t_m-1}) \end{aligned} \tag{4.97}$$

where $\mathrm{P}_j^{(i)}(s_j^{0\ldots t_m-1}|\zeta_j^{(i),1,\ldots t_m-1})$ is the probability to observe the trajectory $s_j^{0,\ldots t_m-1}$ in the cavity graph where site i has been removed, given that site j feels a time dependent external field $\zeta_j^{(i),t} = J_{ji} s_i^{t-1}$. Similarly, the probability of a trajectory in the cavity graph is found to be given by,

$$\begin{aligned} \mathrm{P}_i^{(\ell)}(s_i^{0\ldots t_m} | \zeta_i^{(\ell),1,\ldots,t_m}) = \mathrm{P}_i(s_i^0) \sum_{\mathbf{s}_{\partial_i\setminus\ell}^{0\ldots t_m-1}} \left[\prod_{t=1}^{t_m} \mathrm{W}(s_i^t | h_i(\mathbf{s}_{\partial_i}^{t-1}, s_i^{t-1}) \right] \\ \times \prod_{j\in\partial_i\setminus\ell} \mathrm{P}_j^{(i)}(s_j^{0\ldots t_m-1} | \zeta_j^{(i),1\ldots t_m-1}). \end{aligned} \tag{4.98}$$

We are interested in the site marginals at a given time, however, in the presence of self-interactions, we cannot perform the sum over $s_i^{0\ldots t_m-1}$ explicitly, even in the simplest scenario where interactions are unidirectional, as we will show explicitly below. As noted earlier, for unidirectional interactions, cavity and non-cavity distributions are equal, so we can write

$$\begin{aligned} \mathrm{P}_i(s_i^{0\ldots t_m}) = \mathrm{P}_i(s_i^0) \sum_{\mathbf{s}_{\partial_i}^{0\ldots t_m-1}} \left[\prod_{t=1}^{t_m} \mathrm{W}(s_i^t | h_i(\mathbf{s}_{\partial_i}^{t-1}, s_i^{t-1})) \right] \\ \times \prod_{j\in\partial_i} \mathrm{P}_j(s_j^{0\ldots t_m-1}) \end{aligned} \tag{4.99}$$

These equations cannot, however, be simplified by assuming suitably factorised forms of the trajectory distribution. Even if we were to assume a fully factorised distribution

$$\mathrm{P}_j(s_j^{0\ldots t_m-1}) = \prod_{t=0}^{t_m-1} \mathrm{P}_j(s_j^t)$$

we would be left with

$$\mathrm{P}_i(s_i^{t_m}) = \sum_{s_i^{0\ldots t_m-1}} \mathrm{P}_i(s_i^0) \prod_{t=1}^{t_m} \sum_{\mathbf{s}_{\partial_i}^{t-1}} \mathrm{W}(s_i^t|h_i(\mathbf{s}_{\partial_i}^{t-1}, s_i^{t-1})) \prod_{j\in\partial_i} \mathrm{P}_j(s_j^{t-1}) \tag{4.100}$$

which requires summing over a number $2^{t_m(1+|\partial_i|)}$ of variables which grows exponentially in time. We would thus need to face the full complexity of equations (4.97) and (4.98).

4.E One time approximation in the thermodynamic limit

We now show how the distribution of site marginals for monopartite systems without self-interactions, $\pi(\{\mathrm{P}_t\})$, defined in equation (4.53), may be computed from the cavity method in the limit $N \to \infty$. Starting from equation

(4.53) we insert unity of the form,

$$\begin{aligned}1 = \sum_k \delta_{k,|\partial_i|} \int \{\mathrm{dP}_{t-2}\} \prod_{s^{t-2}} \delta\left(\mathrm{P}_{t-2}(s^{t-2}) - \mathrm{P}_i(s^{t-2})\right) \\ \times \prod_{j\in\partial_i} \Bigg\{ \int \mathrm{d}J_j \mathrm{d}\hat{J}_j \delta\left(J_j - J_{ij}\right) \delta\left(\hat{J}_j - J_{ji}\right) \\ \times \int \{\mathrm{d}\hat{\mathrm{P}}_j\} \prod_{s_j^{t-1}} \delta\left(\hat{\mathrm{P}}_j(s_j^{t-1}) - \mathrm{P}_j^{(i)}(s_j^{t-1}|\hat{J}_j s^{t-2})\right) \Bigg\}\end{aligned} \tag{4.101}$$

which yields,

$$\begin{aligned}\pi(\{\mathrm{P}_t\}) = \sum_k \int \{\mathrm{dP}_{t-2}\} \int \left[\prod_{j=1}^{k} \mathrm{d}J_j \mathrm{d}\hat{J}_j \{\mathrm{d}\hat{\mathrm{P}}_j\}\right] \mathcal{P}\left[k, \{\mathrm{P}_{t-2}\}, \mathbf{J}, \hat{\mathbf{J}}, \{\hat{\mathbf{P}}\}\right] \\ \times \prod_{s^t} \delta\left(\mathrm{P}_t(s^t) - \phi(k, \{\mathrm{P}_{t-2}\}, \mathbf{J}, \hat{\mathbf{J}}, \{\hat{\mathbf{P}}\})\right)\end{aligned} \tag{4.102}$$

where we have defined,

$$\begin{aligned}&\mathcal{P}\left[k, \{\mathrm{P}_{t-2}\}, \mathbf{J}, \hat{\mathbf{J}}, \{\hat{\mathbf{P}}\}\right] \\ &= \frac{1}{N} \sum_i \delta_{k,|\partial_i|} \prod_{s^{t-2}} \delta\left(\mathrm{P}_{t-2}(s^{t-2}) - \mathrm{P}_i(s^{t-2})\right) \\ &\times \prod_{j\in\partial_i} \left\{ \delta\left(J_j - J_{ij}\right) \delta\left(\hat{J}_j - J_{ji}\right) \prod_{s_j^{t-1}} \delta\left(\hat{\mathrm{P}}_j(s_j^{t-1}) - \mathrm{P}_j^{(i)}(s_j^{t-1}|\hat{J}_j s^{t-2})\right) \right\}\end{aligned} \tag{4.103}$$

which is the probability that a site drawn at random has degree k, site marginal at two earlier time steps $\mathrm{P}(s^{t-2})$, where each of the k neighbours acts on the site with interactions $\mathbf{J} = (J_1, \ldots, J_k)$, and where the site acts on each neighbour with interactions $\hat{\boldsymbol{J}} = (\hat{J}_1, \ldots, \hat{J}_k)$, and where each neighbour in the cavity

graph with site i removed is described by the cavity site marginals at one earlier time step $\{\hat{\mathbf{P}}\} = (\hat{\mathrm{P}}(s_1^{t-1}), \ldots, \hat{\mathrm{P}}(s_k^{t-1}))$. The function $\phi(k, \{\mathrm{P}_{t-2}\}, \mathbf{J}, \hat{\mathbf{J}}, \{\hat{\mathbf{P}}\})$ is defined in equation (4.55). To proceed we assume that all interactions J_{ij} are drawn independently from some distribution $\mathrm{P}(J_{ij})$, and also assume that cavity fields are independent. Under these assumptions, we may use Bayes theorem to write,

$$\begin{aligned}\mathcal{P}\left[k, \{\mathrm{P}_{t-2}\}, \mathbf{J}, \hat{\mathbf{J}}, \{\hat{\mathbf{P}}\}\right] \\ = \mathrm{P}(k)\pi_{t-2}\left[\{\mathrm{P}_{t-2}\}|k, \mathbf{J}, \hat{\mathbf{J}}\right] \prod_{j=1}^{k} \mathrm{P}(J_j)\mathrm{P}(\hat{J}_j|J_j)\hat{\pi}_{t-1}\left[\{\hat{\mathrm{P}}_j\}|\hat{J}_j s^{t-2}\right]\end{aligned} \tag{4.104}$$

where we have defined $\hat{\pi}_{t-1}\left[\{\hat{\mathrm{P}}_j\}|x\right]$, the distribution of cavity site marginals, $\hat{\mathrm{P}}_j(s_j^{t-1})$, given that the site removed acts on the cavity graph with external field x. We note that by definition in absence of external field the cavity distribution is equal to its non-cavity counterpart, $\hat{\pi}_{t-1}\left[\{\hat{\mathrm{P}}_j\}|0\right] = \pi_{t-1}\left[\{\hat{\mathrm{P}}_j\}\right]$, since if there is no external field, this implies that the cavity distribution is uninfluenced by the removed site, such that $\hat{J} = 0$ i.e $\mathrm{P}_j^{(i)}(s_j^{t-1}|0) = \mathrm{P}_j(s_j^{t-1})$. We then insert (4.104) into (4.102) from which we find equation (4.54).

What remains is to find an expression for the distribution of cavity marginals $\hat{\pi}_{t-1}\left[\{\hat{\mathrm{P}}_j\}|x\right]$. By definition this object is, in the limit $N \to \infty$, equivalent to,

$$\hat{\pi}_t\left[\{\hat{\mathrm{P}}_i\}|x\right] = \frac{1}{N}\sum_{i\ell}\frac{A_{i\ell}}{k_i}\prod_{s_i^t}\delta\left(\hat{\mathrm{P}}_i(s_i^t) - \mathrm{P}_i^{(\ell)}(s_i^t|x)\right). \tag{4.105}$$

We insert into (4.105) unity of the form,

$$\begin{aligned}1 = \sum_k \delta_{k,|\partial_i|} \sum_{k'} \delta_{k',|\partial_\ell|} \int \{\mathrm{d}\mathrm{P}_{t-2}\} \prod_{s^{t-2}} \delta\left(\mathrm{P}_{t-2}(s^{t-2}) - \mathrm{P}_i(s^{t-2})\right) \\ \times \prod_{j\in\partial_i\setminus\ell} \left\{ \int \mathrm{d}J_j \mathrm{d}\hat{J}_j \delta\left(J_j - J_{ij}\right) \delta\left(\hat{J}_j - J_{ji}\right) \right. \\ \left. \times \int \{\mathrm{d}\hat{\mathrm{P}}_j\} \prod_{s_j^{t-1}} \delta\left(\hat{\mathrm{P}}_j(s_j^{t-1}) - \mathrm{P}_j^{(i)}(s_j^{t-1}|\hat{J}_j s^{t-2})\right) \right\}\end{aligned} \tag{4.106}$$

and define,

$$\begin{aligned}&\mathcal{W}\left[k,k',\{\mathrm{P}_{t-2}\},\mathbf{J},\hat{\mathbf{J}},\{\hat{\mathbf{P}}\}\right] \\ &= \frac{1}{N\langle k\rangle} \sum_{i\ell} A_{i\ell} \delta_{k,|\partial_i|} \delta_{k',|\partial_\ell|} \prod_{s^{t-2}} \delta\left(\mathrm{P}_{t-2}(s^{t-2}) - \mathrm{P}_i(s^{t-2})\right) \\ &\times \prod_{j\in\partial_i\setminus\ell} \left\{ \delta\left(J_j - J_{ij}\right) \delta\left(J_j - J_{ji}\right) \prod_{s_j^{t-1}} \delta\left(\hat{\mathrm{P}}_j(s_j^{t-1}) - \mathrm{P}_j^{(i)}(s_j^{t-1}|\hat{J}_j s^{t-2})\right) \right\}\end{aligned} \tag{4.107}$$

which, assuming that interactions are drawn independently, and that cavity fields are independent, can be written using Bayes theorem,

$$\begin{aligned}&\mathcal{W}\left[k,k',\{\mathrm{P}_{t-2}\},\mathbf{J},\hat{\mathbf{J}},\{\hat{\mathbf{P}}\}\right] \\ &\quad = W(k,k')\pi_{t-2}\left[\{\mathrm{P}_{t-2}\}|k,\mathbf{J},\hat{\mathbf{J}}\right] \prod_{j=1}^{k-1} \mathrm{P}(J_j)\mathrm{P}(\hat{J}_j|J_j)\hat{\pi}_{t-1}\left[\{\hat{\mathrm{P}}_j\}|\hat{J}_j s^{t-2}\right]\end{aligned} \tag{4.108}$$

where $\mathcal{W}\left[k,k',\{\mathrm{P}_{t-2}\},\mathbf{J},\hat{\mathbf{J}},\{\hat{\mathbf{P}}\}\right]$ is the probability to draw a link at random connecting site i with degree k' and site j with degree k, where j has neighbours (excluding i) which act on site j with interactions $\mathbf{J} = (J_1,\ldots,J_{k-1})$, and

where j acts on its neighbours with interactions $\hat{\boldsymbol{J}} = (\hat{J}_1, \ldots, \hat{J}_{k-1})$, and where the activation of each neighbour is described by the cavity site marginals $\{\hat{\mathbf{P}}\} = (\hat{\mathrm{P}}(s_1^{t-1}), \ldots, \hat{\mathrm{P}}(s_{k-1}^{t-1}))$. We have also defined the degree correlation function $W(k,k') = (N\langle k\rangle)^{-1}\sum_{ij} A_{ij}\delta_{k',|\partial_i|}\delta_{k,|\partial_j|}$ which is the probability to draw a link at random with a node of degree k at one end and k' at the other. By writing the cavity fields as independent, we have implicitly assumed that the network lacks strong degree correlations, and so we now explicitly assume that degrees are uncorrelated such that $W(k,k') = W(k)W(k')$ where $W(k) = \frac{k\mathrm{P}(k)}{\langle k\rangle}$ is the probability to draw a link at random that is attached to a node of degree k. Substituting this form of unity into the definition for the cavity marginal (4.105) we find equation (4.56). Equations (4.54) and (4.56) are a closed set of equations which may be solved via a population dynamics procedure. Note, this a dynamical variant of the population dynamics procedure, and can be used to compute the distribution of site marginals at each point in time.

From the distributional equations (4.54) and (4.56), one can also derive a closed set of equations for the *average* site marginal, which by definition is given by,

$$\overline{\mathrm{P}}_t(s^t) = \int \{\mathrm{dP}_t\}\pi(\{\mathrm{P}_t\})\{\mathrm{P}_t\}. \tag{4.109}$$

If we substitute equation (4.54) into (4.109) we find,

$$\begin{aligned}\overline{\mathrm{P}}_t(s^t) = \sum_k \mathrm{P}(k) \int \left[\prod_{j=1}^{k} \mathrm{d}J_j \mathrm{d}\hat{J}_j \{\mathrm{d}\hat{\mathrm{P}}_j\} \mathrm{P}(J_j)\mathrm{P}(\hat{J}_j|J_j)\right] \\ \times \sum_{s^{t-2}} \overline{\mathrm{P}}_{t-2}(s^{t-2}|k,\mathbf{J},\hat{\boldsymbol{J}}) \sum_{s_1^{t-1},\ldots,s_k^{t-1}} \mathrm{W}(s^t|\sum_{j=1}^{k} J_j s_j^{t-1}) \\ \times \prod_{j=1}^{k} \left[(1-\delta_{\hat{J}_j,0})\overline{Q}_{t-1}(s_j^{t-1}|\hat{J}_j s^{t-2}) + \delta_{\hat{J}_j,0}\overline{\mathrm{P}}_{t-1}(s_j^{t-1})\right]\end{aligned} \tag{4.110}$$

where we have defined,

$$\overline{Q}_t(s^t|x) = \int \{\mathrm{d}\hat{\mathrm{P}}\} \hat{\pi}(\{\hat{\mathrm{P}}_t\}|x)\{\hat{\mathrm{P}}_t\}. \tag{4.111}$$

If we then insert equation (4.56) into (4.111), we find,

$$\begin{aligned}\overline{Q}_t(s^t|x) = \sum_k \frac{k\mathrm{P}(k)}{\langle k\rangle} \int \left[\prod_{j=1}^{k-1} \mathrm{d}J_j \mathrm{d}\hat{J}_j \{\mathrm{d}\hat{\mathrm{P}}_j\} \mathrm{P}(J_j)\mathrm{P}(\hat{J}_j|J_j)\right] \\ \times \sum_{s^{t-2}} \overline{\mathrm{P}}_{t-2}(s^{t-2}|k,\mathbf{J},\hat{\boldsymbol{J}}) \sum_{s_1^{t-1},\ldots,s_{k-1}^{t-1}} \mathrm{W}(s^t|\sum_{j=1}^{k-1} J_j s_j^{t-1} + x) \\ \times \prod_{j=1}^{k-1} \left[(1-\delta_{\hat{J}_j,0})\overline{Q}_{t-1}(s_j^{t-1}|\hat{J}_j s^{t-2}) + \delta_{\hat{J}_j,0}\overline{\mathrm{P}}_{t-1}(s_j^{t-1})\right].\end{aligned} \tag{4.112}$$

Equations (4.110) and (4.112) are a closed set of equations that may be solved via iteration. Previously, generating functional analysis (94) has been used to derive the trajectory of an effective spin in a monopartite system without

self-interactions,

$$\begin{aligned} \mathrm{P}(s^0 \dots s^{t_m}) = \sum_k \mathrm{P}(k) \int \left[\prod_{j=1}^{k} \mathrm{d}J_j \mathrm{P}(J_j) \right] \\ \times \sum_{s_1^{0,\dots,t_m-1},\dots,s_k^{0,\dots,t_m-1}} \mathrm{P}(s^0) \prod_{t=0}^{t_m} \left[W(s^t | \sum_{j=1}^{k} J_j s_j^{t-1}) \right] \\ \times \prod_{j=1}^{k} \left[\epsilon Q(s_j^{0,\dots,t_m-1} | J_j s^{0,\dots,t_m-2}) + (1-\epsilon) \mathrm{P}(s_j^{0,\dots,t_m-1}) \right] \end{aligned} \quad (4.113)$$

with,

$$\begin{aligned} Q(s^{0,\dots,t_m} | \vartheta^{0,\dots,t_m}) = \sum_k \frac{k\mathrm{P}(k)}{\langle k \rangle} \int \left[\prod_{j=1}^{k-1} \mathrm{d}J_j \mathrm{P}(J_j) \right] \\ \times \sum_{s_1^{0,\dots,t_m-1},\dots,s_{k-1}^{0,\dots,t_m-1}} \mathrm{P}(s^0) \prod_{t=0}^{t_m} \left[W(s^t | \sum_{j=1}^{k-1} J_j s_j^{t-1} + \vartheta^t) \right] \\ \times \prod_{j=1}^{k-1} \left[\epsilon Q(s_j^{0,\dots,t_m-1} | J_j s^{0,\dots,t_m-2}) + (1-\epsilon) \mathrm{P}(s_j^{0,\dots,t_m-1}) \right]. \end{aligned} \quad (4.114)$$

Here $\epsilon \in [0,1]$ controls the symmetricity of the interactions and $\vartheta^{0,\dots,t_m}$ is a time dependent external field. For fully symmetric networks, $\epsilon = 1$, if one assumes that $Q(s_j^{0,\dots,t_m-1} | J_j s^{0,\dots,t_m-2}) = \prod_{t=0}^{t_m-1} Q(s_j^t | J_j s^{t-1})$, one can take the

sum over $s^{0,\dots,t_m-1}$, and find,

$$\begin{aligned}\mathrm{P}(s^{t_m}) = \sum_k \mathrm{P}(k) \int \left[\prod_{j=1}^{k} \mathrm{d}J_j \mathrm{P}(J_j)\right] \\ \times \sum_{s^{t_m-2}} \mathrm{P}(s^{t_m-2}|k,\mathbf{J}) \sum_{s_1^{t_m-1},\dots,s_k^{t_m-1}} W(s^t|\sum_{j=1}^{k} J_j s_j^{t-1}) \\ \times \prod_{j=1}^{k} Q(s_j^{t_m-1}|J_j s_j^{t-1}) \end{aligned} \tag{4.115}$$

and similarly,

$$\begin{aligned}Q(s^{t_m}|\vartheta^{t_m-1}) = \sum_k \frac{k\mathrm{P}(k)}{\langle k\rangle} \int \left[\prod_{j=1}^{k-1} \mathrm{d}J_j \mathrm{P}(J_j)\right] \\ \times \sum_{s^{t_m-2}} \mathrm{P}(s^{t_m-2}|k,\mathbf{J}) \sum_{s_1^{t_m-1},\dots,s_{k-1}^{t_m-1}} W(s^t|\sum_{j=1}^{k-1} J_j s_j^{t_m-1} + \vartheta^{t_m-1}) \\ \times \prod_{j=1}^{k-1} Q(s_j^{t_m-1}|J_j s^{t_m-2}). \end{aligned} \tag{4.116}$$

These equations are equivalent to (4.110) and (4.112) when we assume that interactions are fully symmetric. Hence, the GFA under the assumption of Markovian time factorisation is equivalent to the dynamical cavity method under OTA in the thermodynamic limit. If we assume time factorisation of $\mathrm{P}(s^0 \dots s^{t_m})$ one can also prove the equivalence of the GFA with dynamical cavity under OTA when $\epsilon = 0$. Curiously, for partially symmetric systems, where $0 < \epsilon < 1$, it would seem that GFA under time factorisation is *not* equivalent to dynamical cavity under OTA.

5 Summary & Outlooks

5.1 Summary

In this thesis we have applied and extended methods from statistical mechanics to study phenomena broadly related to immunity.

In Chapter 2, we proposed a model of the T-cell mediated anti-tumour immune response. Describing the adaptive immune response as a set of cellular interactions, this model retains a systemic view of anti-tumour immunity while being comprised of only 5 ODEs. The main result of this work is a relatively simple model which predicts a critical value of MHC-I above which the immune system will eliminate a tumour, and below which the tumour will escape the immune response. This critical value is dependent on the helper/cytotoxic T-cell ratio and shows that a high proportion of cytotoxic T-cells and high MHC-I expression are preferred conditions for tumour elimination and would suggest good prognosis. Additionally, this suggests that MHC-I and the $CD4^+/CD8^+$ T-cell ratio should be used as a marker of prognosis in combination, as their interplay will affect their efficacy as markers of

prognosis separately. This model also provides predictions of how the decay-profile of MHC-I expression will affect the dynamics of tumour growth. Data with temporal resolution sufficient to predict a functional form of MHC-I decay, to the best of our knowledge, has not been ascertained in the literature. However, we compared the predicted concentration of tumour cells under the assumption of either an exponential or sigmoidal decay of MHC-I expression. Strikingly, a sigmoidal decay lead to an elimination-equilibrium-escape profile of the tumour cell concentration, as has been theorised to be the case in reality. This begs the question is the loss of MHC-I the dominant factor in generating such profiles?

After modelling the individual anti-tumour immune response, in Chapter 3 we studied how individual immunity affects the *collective* immunity of populations. In particular, we studied the SIR model on networks, relaxing the commonly prescribed assumption that vaccinated individuals can not transmit an infection, and instead allowing vaccinated individuals to pass on an infection with lower probability. The key result of this work was the derivation of the cavity equations which compute the risk of nodes (the probability a node causes an outbreak if it is the initial infected node) in networks with node heterogeneity and strong degree correlations. In doing so, we assumed that the population could be split into subgroups, each with a different distribution from which the recovery time of an individual in that subgroup was drawn, and defined a graph ensemble which would link nodes between these subgroups with specified probabilities. We then derived the cavity equations for the average risk in a network drawn from this ensemble, which can be solved by gradient descent, and the distributional cavity equations, which

can be solved by population dynamics.

Using these equations we demonstrated how herd immunity can be attained via inoculation with vaccines that *reduce but do not prevent* transmission, provided that the vaccine reduces transmission sufficiently. Intuitively, we can show that the herd immunity threshold is higher when compared with the herd immunity threshold for a vaccine which prevents all transmission of an individual. In a population divided into vaccinated and unvaccinated subgroups, the threshold is shown to depend upon the density of links between these subgroups. Vaccines are often prioritised for those most at risk of serious ill health. These results provide a theoretical framework to reason whether vaccines should also be prioritised for groups in connection with those who are most at risk. These results also highlight the robustness of vaccination as a mitigation strategy for epidemics; a partial reduction of transmissibility of an individual is compounded at a population level, since each path of transmission from that individual is weakened and, with sufficient vaccine uptake, will lead to herd immunity.

The distributional equations of risk also demonstrate how the distribution of risk qualitatively changes as the density of links between unvaccinated and vaccinated subgroups increases, changing from a bimodal to a unimodal distribution. This demonstrates that in this simple model, as the density of links increases the risk of the unvaccinated tends to decrease, and the risk of the vaccinated tends to increase, since they can still catch and transmit the disease. The impact of strong degree correlations on the tail of the risk distribution was also demonstrated, and assortative networks were shown to be fat-tailed. Additionally, we have shown how to adapt the cavity equations

to compute the risk of nodes in networks subject to bond percolation. The deletion of a link was used as a simple model of measures which reduce social contact. It is clear that in some cases the selection of which links are deleted or which nodes are vaccinated will determine whether social contact reduction or vaccination is the preferred strategy given finite resource. The graph ensemble we defined can generate networks with modular structure, power-law degree distribution and geometric random graphs, and as such our methods can also be applied to networks of this type.

After using the cavity method to analyse the risk of nodes in the SIR model on networks, in Chapter 4 we used the *dynamical* cavity method to study the dynamics of sparse Boolean networks with self and multi-node interactions. In gene regulatory networks, one observes interactions between genes and TFs that in a Boolean network model of GRNs manifest as self and multi-node interactions. Solving the dynamics of such systems required extending the dynamical cavity formalism since direct application of the one-time approximation fails to provide a closed set of equations for systems with self-interactions. Instead we demonstrated that it is possible to map such systems to an equivalent bipartite system to which the OTA scheme can be directly applied, at the expense of doubling the size of the system of interest. Similarly, a bipartite Boolean network of genes and TFs was defined, which allowed TFs to operate with AND logic, where all genes that synthesise a TF must be expressed before it is synthesised. The dynamics of this model was also solved under the OTA scheme. We demonstrated that for both systems with self and multi-node interactions, the OTA can predict the activation probability of each site in the transient and non-equilibrium steady state, down to relatively low

temperature, where the system is ergodic. Evidence of ergodicity breaking at lower temperatures was also found in systems with bidirectional links. Interestingly, the dynamical cavity method under the OTA scheme was shown to be equivalent to MC simulations at zero temperature if they were both initialised in the same configuration. As well as providing the dynamical cavity equations for a given realisation of a network, we also derived equations for the distribution of activation probabilities in the thermodynamic limit, under the OTA scheme. These equations may be thought of as a dynamical variant of the distributional equations derived in Chapter 3. From these equations, expressions for the average site marginals were obtained and were found to be equivalent to expressions found via generating functional analysis with additional assumptions on the memory. Curiously, this equivalence can be shown for fully asymmetric and symmetric networks, but not partially symmetric. Finally, sparse Boolean networks were shown to support multiple (cyclic) attractors, at low temperatures. The diversity of attractors was shown to be significantly higher for networks with multi-node interactions. From this we posit that co-operation between genes in the formation of TFs may be a mechanism for the support of diverse stable gene expression profiles in GRNs. Since our bipartite model of GRNs supports multiple attractors, it may provide a theoretical framework to study cellular differentiation, the change from one stable gene expression profile to another.

5.2 Outlooks

One omission in our model of the anti-tumour immune response is the explicit heterogeneity of tumour cells. It would be of interest to generalise our model to have different tumour cell types, with tumour cells mutating from one type to another. Different tumour cells could have different expressions of MHC-I and different antigens, such that different T-cells mediate the immune response to different groups of tumour cells. To give an example we could modify the equation for tumour growth, as

$$\frac{\mathrm{d}c_\mu}{\mathrm{d}t} = \left[r - \frac{\gamma_\mu}{V} \sum_i \sigma_i \left(1 - \eta_i^\mu\right) \xi_i^\mu \right] c_\mu + \sum_{\nu=1}^{P} \left(A_{\mu\nu} c_\nu - A_{\nu\mu} c_\mu \right) \tag{5.1}$$

where we indicate the tumour clone with index $\mu = 1, \ldots, P$, such that the specificity of each T-cell is now indicated by ξ_i^μ, and its sub-type by η_i^μ such that the statistics of each clone's cognate T-cells may differ. We have also included a term $A_{\mu\nu}$ which describes the rate of mutation from tumour clone μ to ν. Another consideration would be to extend our model to include the innate immune response, which also plays an important role in tumour progression, in order to understand the interplay between the adaptive and innate immune responses in anti-tumour immunity.

Our work on the SIR model on networks is perhaps most readily extendable to the study of competitive and cooperative diseases. In the case of competitive diseases, two or more diseases spread through a population, but a host is only infected with one, such that the diseases compete for hosts. This is particularly relevant when understanding diseases that mutate from

host-to-host, such that new strains appear in the population. On the other hand, cooperative diseases may infect the same host together, and potentially prolong the immune response against them, such that hosts remain infected for longer. The question is whether our framework for analysing the distribution of node risk is amenable to the study of these processes. Our work has utilised the static cavity approach, focussing only on the steady state. Previous works have considered the static cavity approach to competitive and cooperative diseases (75, 76, 77). To take one example, in the work (76) they find the probability that a node is infected with a strain α of a disease is,

$$v_i^\alpha = 1 - \prod_{j \in \partial_i} h_{i \leftarrow j}^\alpha \tag{5.2}$$

$$h_{i \leftarrow j}^\alpha = 1 - \sum_\beta T^{\beta\alpha} \left[1 - \prod_{\ell \in \partial_j \setminus i} h_{j \leftarrow \ell}^\alpha \right] \tag{5.3}$$

where $T^{\beta\alpha}$ is the probability for a node infected with strain β to infect a node with strain α over the duration of its infectious period. Since it is well known that the node risk and vulnerabilities are heterogeneous, it would be interesting to see whether an analysis of the distribution of risk and vulnerabilities in the context of competitive and cooperative diseases reveals any new insights about these processes.

Studying GRNs as sparse Boolean networks has shown us that we can study the non-equilibrium dynamics and equilibrium behaviour of systems with self-interactions. For systems that reach an equilibrium state, the dynamical cavity method in the steady-state will agree with the equilibrium state, at both microscopic and macroscopic level. It remains an open point of inquiry

whether the equilibrium cavity equations can be derived from the dynamical cavity equations. A first point of investigation would be to consider a simple system, without self-interactions, for example, Ising spins along a chain. Additionally, we have also shown that for sparse systems with partially bidirectional interactions there is evidence of an ergodicity breaking transition at low temperatures. New tools are required to ascertain this formally. In equilibrium, the cavity method has been studied under the assumption of ergodicity breaking (see e.g (256, 270, 271)) but it remains an open question how one can reformulate the dynamical cavity under a similar assumption. It would also be of interest if our model could be used to infer the interactions which comprise the GRN from experimental data, by minimising the differences between predicted and observed gene expression profiles.

In this thesis we have used statistical mechanics to build mathematical models of processes related to immunity. These are phenomenological models, they are designed to capture specific behaviours at a macroscopic level (i.e tumour elimination, herd immunity, and multiple stable gene expression profiles) and highlight key microscopic interactions which govern them (i.e the helper/cytotoxic T-cell ratio, recovery rate of individuals, multi-node interactions). While outside the scope of this thesis, validating these models with observational data is a general point of outlook. The most readily amenable model to comparison with experimental data is contained within Chapter 2, due to it being comprised of ODEs describing cell concentration and activation, which can both be measured by experiment. Temporal data is often difficult to ascertain clinically due to the ethical considerations required when taking multiple samples from patients. However, this model can provide pre-

dictions without the need for direct comparison with the trajectory of cell concentrations. Dynamical data is more common in other areas of clinical science, such as pharmokinetic (PK) (i.e the change in concentration of drugs in the body with time) and pharmodynamic (PD) (i.e the change in effect of a drug on the body with its concentration) modelling which is often used in the regulatory approval process of commercial drugs (272, 273, 274). PK/PD modelling is particularly useful in the assessment of the recommended dose and schedule of a drug. To overcome the limited temporal resolution that is usually ascertained in clinical trials, so-called population models are created, where the limited observations from *many* patients are collated, and parameters of the model are estimated for the population as a whole. An analogous framework has recently been proposed for vaccine development, referred to as immunostimulation/immunodynamic modelling (275). The techniques used in Chapter 2 may be an interesting candidate for IS/ID modelling, due to it describing the change in the activation of T-cells over time, as oppose to their direct concentration. This reduces the model complexity (there are not separate compartments for activated and non-activated T-cells), and may be more amenable to population modelling of the kind used in PK/PD modelling.

A

The cavity method for processes on networks

In this section we provide an introduction to the cavity method, which we use to derive several results throughout the thesis. In the first section, we show how the cavity method may be used to deduce static properties of networks. In doing so, we will highlight the key assumptions and arguments that the cavity method rely on. In the second section, we show how these arguments may be extended to the analysis of dynamical processes on networks.

A.1 Static properties of networks

Consider a network that is comprised of N nodes. A pair of nodes may be connected by a link, and these links are described by an *adjacency matrix* $\boldsymbol{A} = \{0,1\}^{N^2}$ where,

$$A_{ij} = \begin{cases} 1, \text{ if there is a link between node } i \text{ and } j \\ 0, \text{otherwise.} \end{cases} \tag{A.1}$$

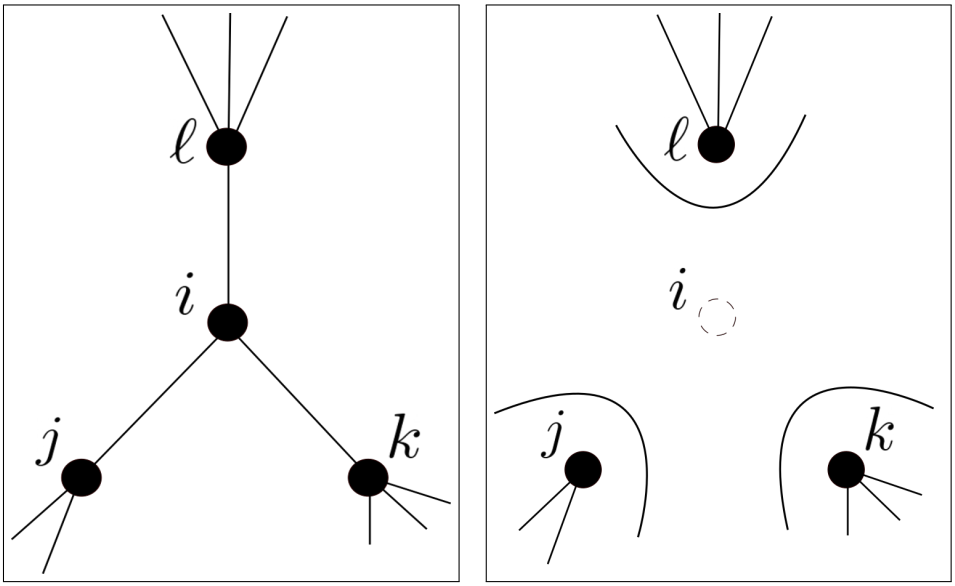

Figure A.1.1: Left: A sketch of a portion of a network which is a tree. Nodes are circles, and links are straight solid lines. Node i is shown to have three neighbours j, k and ℓ. Nodes j, k and ℓ also have links to other nodes in the network which are not sketched here. Right: The same network as in the left panel, with node i (indicated by the dashed circle) and its links removed. This is referred to as the i-cavity graph. The i-cavity graph is comprised of three subtrees, separated by the curved solid lines, rooted at nodes j, k and ℓ.

For simplicity we set $A_{ii} = 0 \; \forall \; i$ such that there are no self-loops, a link from node i to node i, in our network, (although, this will not affect the static cavity analysis that follows). We assume that $\boldsymbol{A}$ is drawn from some distribution $\mathrm{P}(\boldsymbol{A})$ such that it describes a *random graph*, a network where nodes are connected by some random process. We wish to know whether or not a network drawn from this distribution contains a *giant connected component* (GCC). This is a set of connected nodes whose number is a finite fraction of the network in the limit of infinite network size, $N \to \infty$.

We first define $c_i(\boldsymbol{A}) \in \{0, 1\}$ as an indicator variable that states whether node i is a member of the GCC ($c_i(\boldsymbol{A}) = 1$) or whether it is not ($c_i(\boldsymbol{A}) = 0$).

Note that we have written this explicitly as a function of the realisation of the network $\boldsymbol{A}$. The first step in the cavity method is to assume that the network is a *tree*, where there is a single path only between any two nodes. This is sketched in left hand side of Figure A.1.1. In this figure, we have sketched a portion of the network with just four nodes, the node in the centre of the sketch, i, and it's three neighbours j, k and ℓ, which are also shown to have links to other nodes in the network, which are left out of this sketch. From Figure A.1.1 it is clear that if any neighbour of node i is in a GCC, it follows that node i must also be in that GCC, since it shares a link with these nodes and must also be a member of the set of connected nodes. On the right of Figure A.1.1 we have sketched a copy of the network where node i and its links have been removed - we refer to this new network as the i-cavity graph. If one of the nodes j, k, ℓ are in a GCC in the i-cavity graph, adding node i and its links back into the network will not alter this. We denote whether or not node j belongs to a GCC in the network where i has been removed as $c_j^{(i)}(\boldsymbol{A}) \in \{0, 1\}$. These quantities are usually referred to as *cavity fields*. We also see, on the right of Figure A.1.1, that when node i has been removed the network has been divided into several smaller trees, which we refer to as sub-trees, rooted at each neighbour of node i. Since the original network is a tree, nodes belonging to different sub-trees in the i-cavity graph are *disconnected* from each other. Thus, $c_j^{(i)}(\boldsymbol{A})$, $c_k^{(i)}(\boldsymbol{A})$ and $c_\ell^{(i)}(\boldsymbol{A})$, the membership of each of these nodes to a GCC in the i-cavity graph, are *independent* of one another. The independence of the cavity fields is the second crucial assumption of the cavity method, and it is exact on networks which are trees.

By this reasoning, if *at least one* of the neighbours of i is in a GCC in the

i-cavity graph, it follows that i will be in the GCC in the original network. Mathematically, this statement is expressed as follows,

$$c_i(\boldsymbol{A}) = 1 - \prod_{j \in \partial_i^{\mathbf{A}}} (1 - c_j^{(i)}(\boldsymbol{A})) \tag{A.2}$$

where we have defined $\partial_i^{\mathbf{A}} = \{j : A_{ij} = 1\}$ as the set of nodes in the network $\mathbf{A}$ which are in the neighbourhood of node i. What remains is to write an expression for the cavity fields. Consider the sub-tree rooted at node j, sketched on the right of Figure A.1.1. This sub-tree is a tree like any other, and can be sketched as on the left of Figure A.1.1, with node j at its center, and its neighbours (excluding node i) connected it to it via a link. Hence, by exactly the same reasoning as we used before, we may say that node j is in a GCC in the i-cavity graph if at least one of the neighbours of node j (excluding node i) is in a GCC in the *j-cavity graph*. This is expressed mathematically by,

$$c_j^{(i)}(\boldsymbol{A}) = 1 - \prod_{\ell \in \partial_j^{\boldsymbol{A}} \setminus i} (1 - c_\ell^{(j)}(\boldsymbol{A})) \tag{A.3}$$

where the product is now over all nodes in the network $\mathbf{A}$ which are in the neighbourhood of node j with the exception of node i (which is absent from the cavity graph on which $c_j^{(i)}(\boldsymbol{A})$ is defined). Equations (A.2)-(A.3) may be solved by numerical iteration; one starts by initialising all $c_j^{(i)}(\boldsymbol{A}) \ \forall \ i, j = 1, \ldots, N$ with some arbitrary initial condition (usually setting all $c_j^{(i)}(\boldsymbol{A}) = 1$ is practically effective), and these equations are iteratively solved until they converge. Once they have converged their solution may be inserted into (A.2) to compute $c_i(\boldsymbol{A}) \ \forall \ i = 1, \ldots, N$ and reveal which nodes are in a GCC.

These expressions describe which nodes are in a GCC for a given instance of a network $\mathbf{A}$ drawn from the ensemble of random networks that $\mathrm{P}(\boldsymbol{A})$ defines. To find out whether or not a *typical* network drawn from this ensemble has a GCC we now consider the *fraction* of nodes which belong to the GCC, which is given by $m(\boldsymbol{A}) = \frac{1}{N}\sum_{i=1}^{N} c_i(\boldsymbol{A})$. By taking the sum over all nodes and dividing by N in (A.2) we may write,

$$m(\boldsymbol{A}) = 1 - \frac{1}{N}\sum_{i=1}^{N}\prod_{j\in\partial_i^{\boldsymbol{A}}}\left(1 - c_j^{(i)}(\boldsymbol{A})\right). \tag{A.4}$$

We can then denote the degree of a node, i.e the number of links attached to node i, as $k_i = \sum_j A_{ij}$ and insert $1 = \sum_k \delta_{k,k_i}$ into the above to find,

$$m(\boldsymbol{A}) = 1 - \frac{1}{N}\sum_{i=1}^{N}\sum_{k}\delta_{k,k_i}\prod_{j\in\partial_i^{\boldsymbol{A}}}\left(1 - c_j^{(i)}(\boldsymbol{A})\right). \tag{A.5}$$

We then insert $1 = \sum_{\hat{c}_j}\delta_{\hat{c}_j,c_j^{(i)}(\mathbf{A})}$ into the above, which yields,

$$m(\boldsymbol{A}) = 1 - \frac{1}{N}\sum_{i=1}^{N}\sum_{k}\delta_{k,k_i}\prod_{j\in\partial_i^{\boldsymbol{A}}}\left[\left(1 - c_j^{(i)}\right)\sum_{\hat{c}_j}\delta_{\hat{c}_j,c_j^{(i)}(\mathbf{A})}\right] \tag{A.6}$$

$$= 1 - \frac{1}{N}\sum_{i=1}^{N}\sum_{\hat{c}_1,\ldots\hat{c}_k}\delta_{\hat{\boldsymbol{c}},\boldsymbol{c}^{(i)}}\sum_{k}\delta_{k,k_i}\prod_{j=1}^{k}\left[(1-\hat{c}_j)\right] \tag{A.7}$$

where $\hat{\boldsymbol{c}} = (\hat{c}_1,\ldots,\hat{c}_k)$ and $\boldsymbol{c}^{(i)} = (c_1^{(i)},\ldots,c_k^{(i)})$. We now define the distribution,

$$\mathrm{P}(k,\hat{\mathbf{c}}|\boldsymbol{A}) = \lim_{N\to\infty}\frac{1}{N}\sum_{i=1}^{N}\delta_{k,k_i}\prod_{j=1}^{k}\delta_{\hat{c}_j,c_j^{(i)}(\mathbf{A})} \tag{A.8}$$

which is the probability to select a node at random which has degree k and neighbours with cavity fields $\hat{\mathbf{c}} = (\hat{c}_1, \hat{c}_2, \ldots, \hat{c}_k)$. With this distribution defined we may write,

$$m(\boldsymbol{A}) = 1 - \sum_{k} \sum_{\hat{c}_1,\ldots,\hat{c}_k} \mathrm{P}(k, \hat{\mathbf{c}}|\boldsymbol{A}) \prod_{j=1}^{k} \left[\left(1 - \hat{c}_j(\boldsymbol{A})\right) \right]. \tag{A.9}$$

We now make the assumption that the degrees of nodes are uncorrelated. If we consider again Figure A.1.1 we can argue that the cavity fields $c_j^{(i)}$ are independent of the degree of node i. The cavity field $c_j^{(i)}$ will depend upon the degree of node j, since nodes with more links are more likely to be a member of a GCC. Likewise $c_j^{(i)}$ will depend on the degree of its neighbours, and their neighbours, and so on. Since node i is absent from the network, the degree of node i should have no influence on $c_j^{(i)}$. However, this is only the case if the degree of nodes are uncorrelated. If the degree of nodes are correlated, then the degree of node i would be correlated with the degree of node j, which does influence $c_j^{(i)}$, and hence $c_j^{(i)}$ would not be independent of the degree of node i. Hence, by assuming that degrees are uncorrelated we may write that the degree of a randomly selected node is independent of the cavity fields of its neighbours $\mathrm{P}(k, \hat{\mathbf{c}}|\boldsymbol{A}) = \mathrm{P}(k|\boldsymbol{A})\mathrm{P}(\hat{\mathbf{c}}|\boldsymbol{A})$. Furthermore, as shown on the right of Figure A.1.1, when a node is removed from the network, the network splits into several trees, such that the cavity fields of these nodes will be independent of each other and we may write $\mathrm{P}(\hat{\mathbf{c}}|\boldsymbol{A}) = \prod_{j=1}^{k} \mathrm{P}(\hat{c}_j|\boldsymbol{A})$. Therefore, under the assumption that degrees are uncorrelated, equation (A.9)

becomes,

$$m(\boldsymbol{A}) = 1 - \sum_k \mathrm{P}(k|\boldsymbol{A}) \prod_{j=1}^{k} \sum_{\hat{c}_j} \mathrm{P}(\hat{c}_j|\boldsymbol{A}) \left[\left(1 - \hat{c}_j(\boldsymbol{A})\right) \right] \tag{A.10}$$

$$= 1 - \sum_k \mathrm{P}(k|\boldsymbol{A}) \left[\left(1 - \hat{m}(\boldsymbol{A})\right)^k \right] \tag{A.11}$$

where we have defined $\hat{m}(\boldsymbol{A}) = \sum_{\hat{c}} \mathrm{P}(\hat{c}|\boldsymbol{A})\hat{c}$ which is the average cavity field in the network $\boldsymbol{A}$. We must then find an expression for $\hat{m}(\boldsymbol{A})$.

From its definition we may write,

$$\hat{m}(\boldsymbol{A}) = \sum_{\hat{c}} \mathrm{P}(\hat{c}|\boldsymbol{A})\hat{c} \tag{A.12}$$

$$= \sum_k \sum_{\hat{c}} \mathrm{P}(k, \hat{c}|\boldsymbol{A})\hat{c} \tag{A.13}$$

$$= \sum_k \sum_{\hat{c}_1,\ldots,\hat{c}_k} \mathrm{P}(k, \hat{\mathbf{c}}|\boldsymbol{A}) \frac{1}{k} \sum_{j=1}^{k} \hat{c}_j \tag{A.14}$$

$$= \frac{1}{N} \sum_i \sum_k \sum_{\hat{c}_1,\ldots,\hat{c}_k} \delta_{k,k_i} \left[\prod_{j=1}^{k} \delta_{\hat{c}_j, c_j^{(i)}(\boldsymbol{A})} \right] \frac{1}{k} \sum_{j=1}^{k} \hat{c}_j \tag{A.15}$$

$$= \frac{1}{N} \sum_{i,j=1}^{N} \frac{A_{ij}}{k_i} c_j^{(i)}(\boldsymbol{A}). \tag{A.16}$$

By inserting equation (A.3) into (A.16) we may write,

$$\hat{m}(\boldsymbol{A}) = 1 - \frac{1}{N} \sum_{i,j=1}^{N} \frac{A_{ij}}{k_i} \prod_{\ell \in \partial_j^{\boldsymbol{A}} \setminus i} (1 - c_\ell^{(j)}(\boldsymbol{A})) \tag{A.17}$$

where we then insert $1 = \sum_{k,k'} \delta_{k,k_i}\delta_{k',k_j}$ and $1 = \sum_{\hat{c}'_\ell} \delta_{\hat{c}'_\ell, c^{(j)}_\ell(\mathbf{A})}$ in the above,

$$\hat{m}(\boldsymbol{A}) = 1 - \frac{1}{kN}\sum_{i,j=1}^{N} A_{ij}\delta_{k,k_i}\delta_{k',k_j} \sum_{\hat{c}'_1,\ldots,\hat{c}'_{k'-1}} \prod_{\ell\in\partial_j^A\setminus i} \delta_{\hat{c}'_\ell, c^{(j)}_\ell(\mathbf{A})}(1-\hat{c}'_\ell). \tag{A.18}$$

We then define the distribution,

$$W(k,k',\hat{\mathbf{c}}'|\boldsymbol{A}) = \frac{\sum_{i,j=1}^{N} A_{ij}\delta_{k,k_i}\delta_{k',k_j}\left[\prod_{\ell\in\partial_j^A\setminus i}\delta_{\hat{c}'_\ell, c^{(j)}_\ell(\mathbf{A})}\right]}{\sum_{ij} A_{ij}} \tag{A.19}$$

where we note that $\sum_{ij} A_{ij} = \bar{k}N$ where $\bar{k} = \sum_k k\mathrm{P}(k|\boldsymbol{A})$ is the average degree of nodes in the network. This distribution is the probability to select a link at random in the network $\boldsymbol{A}$ with a node of degree k at one end and k' at the other, where the node with degree k' has $k'-1$ neighbours, excluding the node with degree k, which have cavity fields $\hat{\mathbf{c}}' = (\hat{c}'_1,\ldots,\hat{c}'_{k'-1})$. We may now rewrite (A.18) as,

$$\hat{m}(\boldsymbol{A}) = 1 - \sum_k \sum_{\hat{c}'_1,\ldots,\hat{c}'_{k'-1}} \frac{\bar{k}}{k} W(k,k',\hat{\mathbf{c}}'|\boldsymbol{A}) \prod_{\ell=1}^{k'-1}(1-\hat{c}'_\ell(\boldsymbol{A})). \tag{A.20}$$

As we have previously argued, by assuming that degrees are uncorrelated, it follows that the cavity fields $\hat{\mathbf{c}}'$ are independent of k and k'. Hence we may write, $W(k,k',\hat{\mathbf{c}}'|\boldsymbol{A}) = W(k,k'|\boldsymbol{A})\mathrm{P}(\hat{\mathbf{c}}'|\boldsymbol{A})$. Here we have defined $W(k,k'|\boldsymbol{A})$, the degree correlation function, which is the probability to select a link from $\mathbf{A}$ at random with a node of degree k and k' at either end. Additionally, we again state that by assuming the network is a tree, the cavity fields are independent of each other and, hence, we may write $\mathrm{P}(\hat{\mathbf{c}}'|\boldsymbol{A}) = \prod_{j=1}^{k}\mathrm{P}(\hat{c}'_j|\boldsymbol{A})$.

Under these assumptions equation (A.20) may then be written,

$$\hat{m}(\boldsymbol{A}) = 1 - \sum_k \frac{\bar{k}}{k} W(k,k'|\boldsymbol{A}) \prod_{\ell=1}^{k'-1} \sum_{\hat{c}'_\ell} \mathrm{P}(\hat{c}'_\ell|\boldsymbol{A})(1-\hat{c}'_\ell(\boldsymbol{A})) \tag{A.21}$$

$$= 1 - \sum_k \frac{\bar{k}}{k} W(k,k'|\boldsymbol{A})(1-\hat{m}(\boldsymbol{A}))^{k'-1}. \tag{A.22}$$

Since degrees are assumed to be uncorrelated $W(k,k'|\boldsymbol{A}) = W(k|\boldsymbol{A})W(k'|\boldsymbol{A})$. From its definition $W(k|\boldsymbol{A}) = \sum_k W(k,k'|\boldsymbol{A}) = \frac{\sum_{k'}\sum_{ij} A_{ij}\delta_{k_i,k}\delta_{k_j,k'}}{\bar{k}N} = \frac{kP(k|\boldsymbol{A})}{\bar{k}}$. Therefore, we find our final expression for the average cavity field,

$$\hat{m}(\boldsymbol{A}) = 1 - \sum_k \frac{k'\mathrm{P}(k'|\boldsymbol{A})}{\bar{k}}(1-\hat{m}(\boldsymbol{A}))^{k'-1}. \tag{A.23}$$

Equation (A.23) is a self-consistent equation that may be solved by numerical iteration, starting with a random initial condition and iterating until convergence. Its solution may then be inserted into (A.11) to find the fraction of nodes in a GCC in $\boldsymbol{A}$.

Lastly, it should be noted that the dependence on the specific realisation of $\boldsymbol{A}$ is only through the degree distribution $\mathrm{P}(k|\boldsymbol{A})$. It is expected of extensive properties of networks, in the limit $N \to \infty$, that their fluctuations between specific realisations of the network $\boldsymbol{A}$ will vanish, and their value for a specific realisation of the network will be equal to the ensemble averaged value. Hence, in the limit $N \to \infty$, we may assume that the degree distribution is independent of the specific realisation of the network $\mathrm{P}(k|\boldsymbol{A}) = \mathrm{P}(k)$. In this

case, (A.11) and (A.23) no longer depend on $\boldsymbol{A}$ and we may write,

$$m = 1 - \sum_k \mathrm{P}(k)(1-\hat{m})^k \tag{A.24}$$

$$\hat{m} = 1 - \sum_{k'} \frac{k'\mathrm{P}(k')}{\bar{k}}(1-\hat{m})^{k'-1} = f(\hat{m}). \tag{A.25}$$

So far, we have derived the cavity equations (A.2) and (A.3) for node-specific, microscopic, quantities $c_i(\boldsymbol{A})$, and the cavity equations (A.24) and (A.25) for the node-averaged, macroscopic, quantity m. In both cases, the cavity equations are derived under the assumption that the network is a tree, and are exact when this is the case. The cavity equations have also been shown to be a good approximation for large random networks. It is a general property of random networks that the length of a typical cycle, a closed path between any two nodes, grows as $\mathcal{O}(\log N)$ (224). For large N one then expects there to be an absence of short cycles, in which case we say the network is *locally tree-like*, and hence the cavity equations, which assume that the network under consideration is a tree, are a good approximation. Furthermore, in the limit $N \to \infty$, the length of a typical cycle will diverge to infinity, and the cavity method becomes exact.

We can now find a condition for the existence of a GCC if we consider a *graphical solution* to the self-consistent equation (A.25). The idea behind the graphical solution is as follows. We first take the derivative of $f(\hat{m})$ with

respect to $\hat{m}$,

$$f'(\hat{m}) = \sum_{k'} \frac{k'(k'-1)\mathrm{P}(k')}{\bar{k}}(1-\hat{m})^{k'-2} \tag{A.26}$$

which is strictly positive, $f'(\hat{m}) \geq 0$, since $\hat{m} \in [0,1]$. Similarly, the second derivative,

$$f''(\hat{m}) = -\sum_{k'} \frac{k'(k'-1)(k'-2)\mathrm{P}(k')}{\bar{k}}(1-\hat{m})^{k'-3} \tag{A.27}$$

is strictly negative $f''(\hat{m}) \leq 0$. In combination, this tells us that $f(\hat{m})$ is a monotonically increasing, $f'(\hat{m}) \geq 0$, and concave, $f''(\hat{m}) \leq 0$, function. We next note that there is a trivial solution when $\hat{m} = 0$ which, when substituted into (A.11), corresponds to $m = 0$ where there is no GCC. In Figure A.1.2 we illustrate that the solution to (A.25) is given by the intersection of the curve $y = f(\hat{m})$ with the diagonal $y = \hat{m}$. Due to the monotonically increasing and concave nature of $f(\hat{m})$ there are two scenarios to consider. Either the curve $y = f(\hat{m})$ passes below the diagonal at $\hat{m} = 0$, thus it only intersects the diagonal at $\hat{m} = 0$, or $y = f(\hat{m})$ passes above the diagonal at $\hat{m} = 0$, in which case the curve will eventually cross the diagonal again and hence there is a non-zero solution to (A.25). Therefore, the condition for there to be a non-zero solution is given by, $f'(0) > 0$ which from (A.26) we find to be equivalent to,

$$\sum_{k'} \frac{k'(k'-1)\mathrm{P}(k')}{\bar{k}} > 1. \tag{A.28}$$

If we denote the second moment of the degree distribution $\overline{k^2} = \sum_k k^2 \mathrm{P}(k)$,

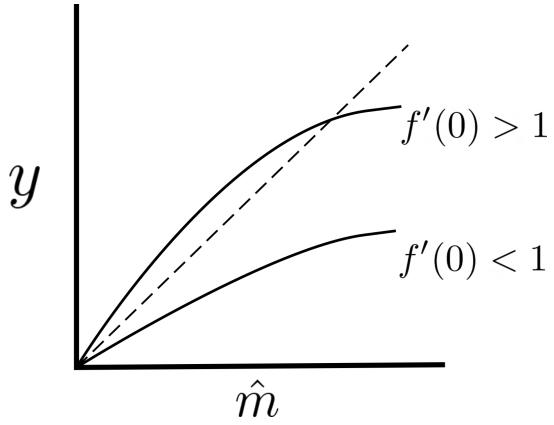

Figure A.1.2: A sketch of the graphical solution to equation (A.25). The dashed line indicates $y = \hat{m}$ and the solid lines indicate $y = f(\hat{m})$ for two different parameterisations where i) $f'(0) < 1$ such that $y = f(\hat{m})$ intersects with $y = \hat{m}$ only at $\hat{m} = 0$ and ii) where $f'(0) > 1$ such that there is an additional intersection at $\hat{m} > 0$.

the condition above is equivalent to,

$$\frac{\overline{k^2} - \bar{k}}{\bar{k}} > 1. \tag{A.29}$$

Hence, the cavity method states that networks which meet the condition (A.29) contain a GCC.

A.2 Dynamical processes on networks

The arguments that the cavity method rely on to analyse static properties of networks may also be applied to the analysis of dynamical processes on networks. As an example, we shall consider a network with N nodes, where each node is described by a binary state variable $\sigma_i \in \{0, 1\}\ \forall\ i = 1, \ldots, N$. We consider a system that evolves in discrete time steps according to the

following equation,

$$\mathrm{P}(\boldsymbol{\sigma}^{t+1}) = \sum_{\boldsymbol{\sigma}^t} \mathrm{W}(\boldsymbol{\sigma}^{t+1}|\boldsymbol{\sigma}^t)\mathrm{P}(\boldsymbol{\sigma}^t) \tag{A.30}$$

where $\mathrm{P}(\boldsymbol{\sigma}^t)$ is the probability to observe, at time t, a configuration of the network $\boldsymbol{\sigma}^t = (\sigma_1^t, \ldots, \sigma_N^t)$, where σ_i^t is the state of node i at time t, and $\mathrm{W}(\boldsymbol{\sigma}^{t+1}|\boldsymbol{\sigma}^t)$ is the probability to transition from configuration $\boldsymbol{\sigma}^t$ to $\boldsymbol{\sigma}^{t+1}$. We choose the transition probabilities to be of the following form,

$$\mathrm{W}(\boldsymbol{\sigma}^{t+1}|\boldsymbol{\sigma}^t) = \prod_{i=1}^{N} \mathrm{W}(\sigma_i^{t+1}|h_i(\boldsymbol{\sigma}^t_{\partial_i^A})) \tag{A.31}$$

where we define,

$$\mathrm{W}(\sigma_i^{t+1}|h_i(\boldsymbol{\sigma}^t_{\partial_i})) = \frac{\mathrm{e}^{\beta(2\sigma_i^{t+1}-1)h_i(\boldsymbol{\sigma}^t_{\partial_i})}}{2\cosh \beta h_i(\boldsymbol{\sigma}^t_{\partial_i})} \tag{A.32}$$

and $h_i(\boldsymbol{\sigma}^t_{\partial_i}) = \sum_{j\in\partial_i} J_{ij}\sigma_j^t$ is the *local field* that acts on node i. This local field is a sum over the state of the neighbours of node i, which we denote by $\boldsymbol{\sigma}^t_{\partial_i} = \{\sigma_j^t \ \forall\ j \in \partial_i\}$, multiplied by the interaction matrix J_{ij}. This interaction matrix is a *weighted* adjacency matrix, if $J_{ij} = 0$ there is no link from node j to i, if $J_{ij} > 0$ then there is a link from j to i and node j promotes the activation of node i, i.e $\sigma_i^t = 1$, and if $J_{ij} < 0$ then there is also a link from j to i but node j inhibits the activation of node i. This choice of dynamics is known as *synchronous Glauber dynamics*. The dynamics are said to be synchronous because the transition probabilities $\mathrm{W}(\boldsymbol{\sigma}^{t+1}|\boldsymbol{\sigma}^t)$ factorise over the nodes in the network, such that in a given time step all nodes update their state based

on the state of the network at the previous point in time. The term Glauber dynamics refers to the specific choice of $\mathrm{W}(\sigma_i^{t+1}|h_i(\boldsymbol{\sigma}_{\partial_i}^t))$ we have made, and is a well studied model of statistical mechanics.

The equation of evolution (A.30) is intractable, involving a sum over $|\boldsymbol{\sigma}^t| = 2^N$ variables. However, knowing that the state of a node at any given point in time will be updated only according to the state of its neighbours at the previous time point, one may ask if the cavity arguments we used to study static properties of networks can be used to derive a simpler expression that describes the dynamics of the system. Specifically, we seek to derive an expression for single node quantities, as oppose to the joint distribution of all nodes in the network that is described by equation (A.30). To begin, as in the static cavity method, we assume our network is a tree. As sketched in Figure A.1.1, node i shares a link with nodes j, k and ℓ, and therefore the state of node i at some time $t+1$, σ_i^{t+1}, will depend on the state of its neighbours at time t, σ_j^t, σ_k^t and σ_ℓ^t, or using our shorthand $\boldsymbol{\sigma}_{\partial_i}^t = (\sigma_j^t, \sigma_k^t, \sigma_\ell^t)$.

When we considered the static properties of networks, we stated that the membership of node i to a GCC, c_i, was dependent on the membership of its neighbours to a GCC c_j, c_k, c_ℓ, i.e if one of its neighbours is in a GCC, by definition so is node i. We then noted that because the network is assumed to be a tree, it is also true that if one of the neighbours of node i is in a GCC in the i-cavity graph, then node i is in a GCC in the original network. The cavity fields $c_j^{(i)}$, $c_k^{(i)}$ and $c_\ell^{(i)}$ are independent of c_i since i is absent from the i-cavity graph. Hence, we write an expression, equation (A.2) for c_i that was dependent on the cavity fields $c_j^{(i)}$, $c_k^{(i)}$ and $c_\ell^{(i)}$. In the context of the dynamics of networks such an argument *cannot* be made for the state of a node σ_i^t; the

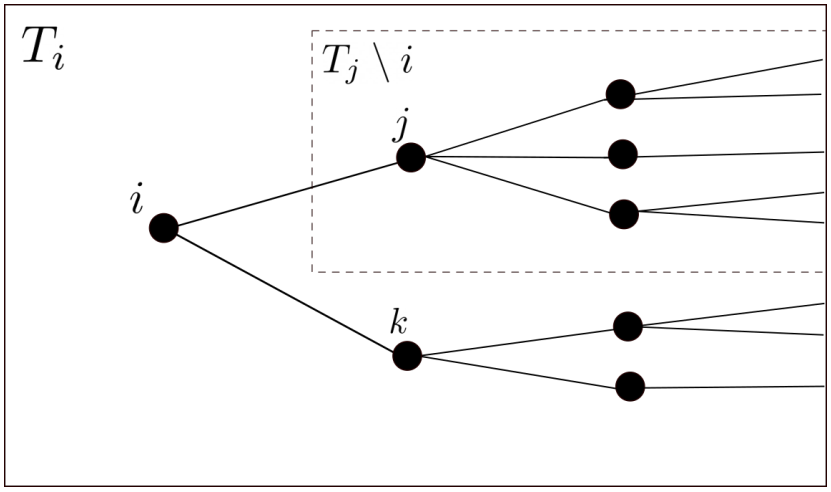

Figure A.2.1: A sketch of a network which is a tree. Here the tree is rooted at node i, which has neighbours j and k. Nodes j and k are shown to have several neighbours, which themselves are connected to further nodes in the network, not sketched. The large black box contains the set of nodes T_i, which are all nodes in the tree rooted at node i. The dashed black box contains all the nodes belonging to the set $T_j \setminus i$, which are the nodes in the sub-tree rooted at node j when node i is removed from the network.

state of the neighbours of node i in the i-cavity graph at some time t, $\sigma_j^{(i),t}$, $\sigma_k^{(i),t}$ and $\sigma_\ell^{(i),t}$ are not independent of node i. This is because each of them will be influenced by the state of node i at the previous time point σ_i^{t-1}. Although we have assumed that the network is a tree, correlations between the state of nodes at different time points prevent us from applying the cavity argument directly to the state of each node at a given point in time σ_i^t, and we can not formulate an expression relating σ_i^t to $\boldsymbol{\sigma}_{\partial_i}^{(i),t}$.

However, as we shall now show, the cavity argument can still be used to derive a set of expressions describing single node quantities, if one considers not the state of a node at an arbitrary point in time, but its entire trajectory. The probability to observe a trajectory of the network from time $t = 0, \ldots, t_m$

$\boldsymbol{\sigma}^0 \to \boldsymbol{\sigma}^1 \to \cdots \to \boldsymbol{\sigma}^{t_m}$ is given by,

$$\mathrm{P}(\boldsymbol{\sigma}^0, \ldots, \boldsymbol{\sigma}^{t_m}) = \mathrm{P}(\boldsymbol{\sigma}^0) \prod_{t=0}^{t_m-1} \mathrm{W}(\boldsymbol{\sigma}^{t+1}|\boldsymbol{\sigma}^t) \tag{A.33}$$

$$= \mathrm{P}(\boldsymbol{\sigma}^0) \prod_{t=0}^{t_m-1} \prod_{i=1}^{N} \mathrm{W}(\sigma_i^{t+1}|h_i(\boldsymbol{\sigma}_{\partial_i}^t)). \tag{A.34}$$

From the above we can find the probability of a trajectory of a single node i by taking the sum over $\boldsymbol{\sigma}^t \setminus \sigma_i^t \;\forall\; t = 0, \ldots, t_m$,

$$\mathrm{P}(\sigma_i^0, \ldots, \sigma_i^{t_m}) = \sum_{\boldsymbol{\sigma}^0, \ldots, \boldsymbol{\sigma}^{t_m} \setminus \sigma_i^0, \ldots, \sigma_i^{t_m}} \mathrm{P}(\boldsymbol{\sigma}^0) \prod_{t=0}^{t_m-1} \prod_{i=1}^{N} \mathrm{W}(\sigma_i^{t+1}|h_i(\boldsymbol{\sigma}_{\partial_i}^t)). \tag{A.35}$$

We then separate the terms containing node i,

$$\mathrm{P}(\sigma_i^0, \ldots, \sigma_i^{t_m}) = \sum_{\boldsymbol{\sigma}^0, \ldots, \boldsymbol{\sigma}^{t_m} \setminus \sigma_i^0, \ldots, \sigma_i^{t_m}} \mathrm{P}(\boldsymbol{\sigma}^0) \tag{A.36}$$

$$\times \prod_{t=0}^{t_m-1} \mathrm{W}(\sigma_i^{t+1}|h_i(\boldsymbol{\sigma}_{\partial_i}^t)) \prod_{j \in T_i \setminus i} \mathrm{W}(\sigma_j^{t+1}|h_j(\boldsymbol{\sigma}_{\partial_j}^t)) \tag{A.37}$$

where we have defined T_i as the set of nodes that describe the tree rooted at node i, which we sketch in Figure A.2.1. We may now separate the terms in T_i, into a product over the neighbours of node i, and a product over the sub-trees, rooted at each of the neighbours of node i, which are formed when

node i is removed from the network,

$$\prod_{j\in T_i\setminus i} \mathrm{W}(\sigma_j^{t+1}|h_j(\boldsymbol{\sigma}_{\partial_j}^t)) \tag{A.38}$$

$$= \prod_{j\in\partial_i}\left[\mathrm{W}(\sigma_j^{t+1}|h_j(\boldsymbol{\sigma}_{\partial_j}^t)\prod_{k\in T_j\setminus i,j}\mathrm{W}(\sigma_k^{t+1}|h_k(\boldsymbol{\sigma}_{\partial_k}^t))\right]. \tag{A.39}$$

The expression above contains a product over $T_j\setminus i,j$, which is the sub-tree rooted at node j when node i is removed from the network, $T_j\setminus i$, as sketched in Figure A.2.1, with node j also removed from this set. We may also write the local field acting on node j as,

$$h_j(\boldsymbol{\sigma}_{\partial_j}^t) = \sum_k J_{jk}\sigma_k^t = \sum_{k\in\partial_j\setminus i} J_{jk}\sigma_k^t + J_{ji}\sigma_i^t = h_j^{(i)}(\boldsymbol{\sigma}_{\partial_j}^t) + J_{ji}\sigma_i^t) \tag{A.40}$$

where we have defined the *local cavity field* $h_j^{(i)}(\boldsymbol{\sigma}_{\partial_j}^t) = \sum_{k\in\partial_j\setminus i} J_{jk}\sigma_k^t$. This allows us to write,

$$\mathrm{P}_i(\sigma_i^{0\ldots t_m}) = \mathrm{P}_i(\sigma_i^0)\sum_{\boldsymbol{\sigma}_{\partial_i}^{0\ldots t_m}\setminus\sigma_i^{0\ldots t_m}}\left[\prod_{t=0}^{t_m-1}\mathrm{W}(\sigma_i^{t+1}|h_i(\boldsymbol{\sigma}_{\partial_i}^t))\right] \tag{A.41}$$

$$\times\sum_{\boldsymbol{\sigma}^{0\ldots t_m}\setminus\sigma_i^{0\ldots t_m},\sigma_{\partial_i}^{0\ldots t_m}}\mathrm{P}(\boldsymbol{\sigma}^0\setminus\sigma_i^0) \tag{A.42}$$

$$\times\prod_{t=0}^{t_m-1}\prod_{j\in\partial_i}\left[\mathrm{W}(\sigma_j^{t+1}|h_j^{(i)}(\boldsymbol{\sigma}_{\partial_j}^t)+J_{ji}\sigma_i^t)\prod_{k\in T_j\setminus i,j}\mathrm{W}(\sigma_k^{t+1}|h_k(\boldsymbol{\sigma}_{\partial_k}^t))\right]. \tag{A.43}$$

We then move the sum over the nodes which are *not* in the neighbourhood of

i inside the product over $j \in \partial_i$

$$\mathrm{P}_i(\sigma_i^{0\dots t_m}) = \mathrm{P}_i(\sigma_i^0) \sum_{\boldsymbol{\sigma}_{\partial_i}^{0\dots t_m} \setminus \sigma_i^{0\dots t_m}} \left[\prod_{t=0}^{t_m-1} \mathrm{W}(\sigma_i^{t+1} | h_i(\boldsymbol{\sigma}_{\partial_i}^t)) \right] \tag{A.44}$$

$$\times \prod_{j \in \partial_i} \left\{ \sum_{\boldsymbol{\sigma}_{T_j}^{0\dots t_m} \setminus \sigma_i^{0\dots t_m}, \sigma_j^{0\dots t_m}} \mathrm{P}(\boldsymbol{\sigma}_{T_j}^0 \setminus \sigma_i^0) \right. \tag{A.45}$$

$$\left. \times \prod_{t=0}^{t_m-1} \left[\mathrm{W}(\sigma_j^{t+1} | h_j^{(i)}(\boldsymbol{\sigma}_{\partial_j}^t) + J_{ji}\sigma_i^t) \prod_{k \in T_j \setminus i,j} \mathrm{W}(\sigma_k^{t+1} | h_k(\boldsymbol{\sigma}_{\partial_k}^t)) \right] \right\}. \tag{A.46}$$

At this stage we can see that we can take the external sum over $\sigma_{\partial_i}^{t_m}$ and the internal sums over $\sigma_{T_j}^{t_m}$

$$\mathrm{P}_i(\sigma_i^{0\dots t_m}) = \mathrm{P}_i(\sigma_i^0) \sum_{\boldsymbol{\sigma}_{\partial_i}^{0\dots t_m-1} \setminus \sigma_i^{0\dots t_m-1}} \left[\prod_{t=0}^{t_m-1} \mathrm{W}(\sigma_i^{t+1} | h_i(\boldsymbol{\sigma}_{\partial_i}^t)) \right] \tag{A.47}$$

$$\times \prod_{j \in \partial_i} \left\{ \sum_{\boldsymbol{\sigma}_{T_j}^{0\dots t_m-1} \setminus \sigma_i^{0\dots t_m-1}, \sigma_j^{0\dots t_m-1}} \mathrm{P}(\boldsymbol{\sigma}_{T_j}^0 \setminus \sigma_i^0) \right. \tag{A.48}$$

$$\left. \times \prod_{t=0}^{t_m-1} \left[\mathrm{W}(\sigma_j^{t+1} | h_j^{(i)}(\boldsymbol{\sigma}_{\partial_j}^t) + J_{ji}\sigma_i^t) \prod_{k \in T_j \setminus i,j} \mathrm{W}(\sigma_k^{t+1} | h_k(\boldsymbol{\sigma}_{\partial_k}^t)) \right] \right\}. \tag{A.49}$$

The next step is to notice that the terms inside the curly brackets above are a marginalisation of some joint probability distribution, and when the internal sum $\sum_{\boldsymbol{\sigma}_{T_j}^{0\dots t_m-1} \setminus \sigma_i^{0\dots t_m-1}, \sigma_j^{0\dots t_m-1}}$ is taken, what remains will be the joint distribution $\mathrm{P}_j^{(i)}(\sigma_i^{0\dots t_m-1} | \zeta_j^{(i),0\dots t_m-1})$ which is interpreted as the probability to observe the trajectory $\sigma_j^{0\dots t_m}$ in the i-cavity graph, given that node i exerts an external field $\zeta_j^{(i),t} = J_{ji}\sigma_i^{t-1}$ on node j in the i-cavity graph. By defining the contents of the curly brackets above as $\mathrm{P}_j^{(i)}(\sigma_i^{0\dots t_m-1} | \zeta_j^{(i),0\dots t_m-1})$, the probability of the

trajectory of a single node is given by,

$$\mathrm{P}_i(\sigma_i^{0\ldots t_m}) = \mathrm{P}_i(\sigma_i^0) \sum_{\boldsymbol{\sigma}_{\partial_i}^{0\ldots t_m-1}} \left[\prod_{t=0}^{t_m-1} \mathrm{W}(\sigma_i^{t+1}|h_i(\boldsymbol{\sigma}_{\partial_i}^t)) \right] \times \prod_{j\in\partial_i} \mathrm{P}_j^{(i)}(\sigma_i^{0\ldots t_m-1}|\zeta_j^{(i),0\ldots t_m-1}). \tag{A.50}$$

A similar expression can be derived for the cavity distribution $\mathrm{P}_i^{(j)}(\sigma_i^{0\ldots t_m})$ if we consider removing a node ℓ from the above expression,

$$\mathrm{P}_i^{(\ell)}(\sigma_i^{0\ldots t_m}) = \mathrm{P}_i(\sigma_i^0) \sum_{\boldsymbol{\sigma}_{\partial_i}^{0\ldots t_m-1}\setminus\sigma_\ell^{0\ldots t_m-1}} \left[\prod_{t=0}^{t_m-1} \mathrm{W}(\sigma_i^{t+1}|h_i^{(\ell)}(\boldsymbol{\sigma}_{\partial_i}^t)) \right] \times \prod_{j\in\partial_i\setminus\ell} \mathrm{P}_j^{(i)}(\sigma_i^{0\ldots t_m-1}|\zeta_j^{(i),0\ldots t_m-1}). \tag{A.51}$$

We are yet to find an expression for the cavity distribution where the node that is removed exerts a time dependent external field $\zeta_i^{(\ell),t}$, denoted by $\mathrm{P}_i^{(\ell)}(\sigma_i^{0\ldots t_m}|\zeta_i^{(\ell),0\ldots t_m})$. However, it is by definition that this external field will alter the local field $h_i^{(\ell)}(\boldsymbol{\sigma}_{\partial_i}^t) \to h_i^{(\ell)}(\boldsymbol{\sigma}_{\partial_i}^t) + \zeta_i^{(\ell),t} = h_i(\boldsymbol{\sigma}_{\partial_i}^t)$. Hence, we condition the distribution in equation (A.51) on $\zeta_i^{(\ell),0\ldots t_m}$ and replace $h_i^{(\ell)}(\boldsymbol{\sigma}_{\partial_i}^t)$ with $h_i(\boldsymbol{\sigma}_{\partial_i}^t)$ to find,

$$\mathrm{P}_i^{(\ell)}(\sigma_i^{0\ldots t_m}|\zeta_i^{(\ell),0\ldots t_m}) = \mathrm{P}_i(\sigma_i^0) \sum_{\boldsymbol{\sigma}_{\partial_i}^{0\ldots t_m-1}\setminus\sigma_\ell^{0\ldots t_m-1}} \left[\prod_{t=0}^{t_m-1} \mathrm{W}(\sigma_i^{t+1}|h_i(\boldsymbol{\sigma}_{\partial_i}^t)) \right] \times \prod_{j\in\partial_i\setminus\ell} \mathrm{P}_j^{(i)}(\sigma_i^{0\ldots t_m-1}|\zeta_j^{(i),0\ldots t_m-1}). \tag{A.52}$$

By considering the trajectory of single nodes, we have shown that by assuming the network is a tree, the cavity method may be used to derive equations (A.50) and (A.52), a closed set of equations that can be solved recursively. As they rely on the same assumptions as the static cavity method, they are exact on trees, and locally tree-like networks in the limit $N \to \infty$.

To demonstrate the utility of the dynamical cavity method, we can consider a particular choice for the interaction matrix J_{ij} where these equations can be simplified. Namely, we will assume that the network is *unidirectional* such that if there is a link from j to i, $J_{ij} \neq 0$, there will not be a link from i to j, $J_{ji} = 0$. In this case the external field on the right hand side of equation (A.50) becomes is zero $\zeta_j^{(i)} = J_{ji}\sigma_i^t$ =0, such that,

$$\mathrm{P}_i(\sigma_i^{0\ldots t_m}) = \mathrm{P}_i(\sigma_i^0) \sum_{\boldsymbol{\sigma}_{\partial_i}^{0\ldots t_m-1}} \left[\prod_{t=0}^{t_m-1} \mathrm{W}(\sigma_i^{t+1}|h_i(\boldsymbol{\sigma}_{\partial_i}^t)) \right] \times \prod_{j\in\partial_i} \mathrm{P}_j^{(i)}(\sigma_i^{0\ldots t_m-1}|0) \tag{A.53}$$

which from (A.52) is equal to,

$$\mathrm{P}_j^{(i)}(\sigma_j^{0\ldots t_m}|0) = \mathrm{P}_i(\sigma_i^0) \sum_{\boldsymbol{\sigma}_{\partial_i}^{0\ldots t_m-1}\setminus\sigma_i^{0\ldots t_m-1}} \left[\prod_{t=0}^{t_m-1} \mathrm{W}(\sigma_i^{t+1}|h_j^{(i)}(\boldsymbol{\sigma}_{\partial_j}^t)) \right] \times \prod_{\ell\in\partial_j\setminus i} \mathrm{P}_\ell^{(j)}(\sigma_\ell^{0\ldots t_m-1}|\zeta_\ell^{(j),0\ldots t_m-1}) \tag{A.54}$$

$$= \mathrm{P}_j^{(i)}(\sigma_j^{0\ldots t_m}). \tag{A.55}$$

Hence, for networks with unidirectional interactions, the single node trajec-

tory is described by

$$\mathrm{P}_i(\sigma_i^{0\ldots t_m}) = \mathrm{P}_i(\sigma_i^0) \sum_{\boldsymbol{\sigma}_{\partial_i}^{0\ldots t_m-1}} \left[\prod_{t=0}^{t_m-1} \mathrm{W}(\sigma_i^{t+1}|h_i(\boldsymbol{\sigma}_{\partial_i}^t)) \right] \times \prod_{j\in\partial_i} \mathrm{P}_j^{(i)}(\sigma_i^{0\ldots t_m-1}) \tag{A.56}$$

which we can take the sum over $\sigma_i^{0\ldots t_m-1}$ to find an expression for $\sigma_i^{t_m}$,

$$\begin{aligned}
\mathrm{P}_i(\sigma_i^{t_m}) &= \sum_{\sigma_i^{0\ldots t_m-1}} \mathrm{P}_i(\sigma_i^0) \sum_{\boldsymbol{\sigma}_{\partial_i}^{0\ldots t_m-1}} \left[\prod_{t=0}^{t_m-1} \mathrm{W}(\sigma_i^{t+1}|h_i(\boldsymbol{\sigma}_{\partial_i}^t)) \right] \\
&\quad \times \prod_{j\in\partial_i} \mathrm{P}_j^{(i)}(\sigma_j^{0\ldots t_m-1}) && \text{(A.57)} \\
&= \sum_{\boldsymbol{\sigma}_{\partial_i}^{0\ldots t_m-1}} \mathrm{W}(\sigma_i^{t_m}|h_i(\boldsymbol{\sigma}_{\partial_i}^{t_m-1})) \prod_{j\in\partial_i} \mathrm{P}_j^{(i)}(\sigma_j^{0\ldots t_m-1}) && \text{(A.58)} \\
&= \sum_{\boldsymbol{\sigma}_{\partial_i}^{t_m-1}} \mathrm{W}(\sigma_i^{t_m}|h_i(\boldsymbol{\sigma}_{\partial_i}^{t_m-1})) \prod_{j\in\partial_i} \mathrm{P}_j^{(i)}(\sigma_j^{t_m-1}) && \text{(A.59)}
\end{aligned}$$

where in the last line we have related the distribution for the state of a single node, $\mathrm{P}_i(\sigma_i^{t_m})$, to the cavity fields of its neighbouring nodes $\mathrm{P}_j^{(i)}(\sigma_i^{t_m-1})$. Lastly, we note that since the interactions are unidirectional, in the above expression $\mathrm{P}_j^{(i)}(\sigma_j^{t_m-1}) = \mathrm{P}_j(\sigma_j^{t_m-1})$ since the existence of $\mathrm{P}_j^{(i)}(\sigma_j^{t_m-1})$ implies that there is a node from j to i, and hence, there is not a link from i to j, and node i has no influence on node j. Hence, for unidirectional networks we have that the probability to observe a node in state σ_i at time t_m is given by,

$$\mathrm{P}_i(\sigma_i^{t_m}) = \sum_{\boldsymbol{\sigma}_{\partial_i}^{t_m-1}} \mathrm{W}(\sigma_i^{t_m}|h_i(\boldsymbol{\sigma}_{\partial_i}^{t_m-1})) \prod_{j\in\partial_i} \mathrm{P}_j(\sigma_j^{t_m-1}) \tag{A.60}$$

which reveals that the evolution of the state of each node in unidirectional networks is Markovian. For unidirectional networks the dynamical cavity equations (A.60) are simpler to solve at long times than equation (A.50). This is because equation (A.60) does not contain the sum over a set of $|\sigma_{\partial_i}^{0\ldots t_m-1}| = 2^{|\partial_i| t_m}$ variables, that appears in equation (A.50), the size of which is exponentially increasing with time. It should, however, be noted that although the dynamical cavity equations reduce in computational complexity for unidirectional networks, equation (A.60) still contains a sum over a set of $|\sigma_{\partial_i}^{t_m-1}| = 2^{|\partial_i|}$ variables, the size of which increases exponentially with the size of neighbourhood of node i, $|\partial_i|$. Therefore, for networks with nodes of large degree, these equations will also suffer from high computational complexity, although methods to overcome this have been addressed recently (249).

References

[1] Alexandra J Stewart and Phillip M Devlin. **The history of the smallpox vaccine**. *Journal of infection*, **52**[5]:329–334, 2006. 13

[2] Cary P Gross and Kent A Sepkowitz. **The myth of the medical breakthrough: smallpox, vaccination, and Jenner reconsidered**. *International journal of infectious diseases*, **3**[1]:54–60, 1998. 13

[3] Donald A Henderson. **Principles and lessons from the smallpox eradication programme**. *Bulletin of the World Health Organization*, **65**[4]:535, 1987. 14

[4] Frank Fenner, Donald Ainslie Henderson, Isao Arita, Zdenek Jezek, Ivan Danilovich Ladnyi, et al. *Smallpox and its eradication*, **6**. World Health Organization Geneva, 1988. 14

[5] Donald A Henderson. **The eradication of smallpox–an overview of the past, present, and future**. *Vaccine*, **29**:D7–D9, 2011. 14

[6] Minal K Patel, Marta Gacic-Dobo, Peter M Strebel, Alya Dabbagh, Mick N Mulders, Jean-Marie Okwo-Bele, Laure Dumolard, Paul A Rota, Katrina Kretsinger, and James L Goodson. **Progress toward regional measles elimination—worldwide, 2000–2015**. *Morbidity and Mortality Weekly Report*, **65**[44]:1228–1233, 2016. 14

[7] David N Durrheim. **Measles eradication—retreating is not an option**. *The Lancet Infectious Diseases*, **20**[6]:e138–e141, 2020. 14

[8] World Health Organization et al. **Decade of Vaccines—Global Vaccine Action Plan 2011–2020**, 2014. 14

[9] Elena Bozzola, Giulia Spina, Alberto Eugenio Tozzi, and Alberto Villani. **Global measles epidemic risk: Current perspectives on the growing need for implementing digital communication strategies**. *Risk Management and Healthcare Policy*, **13**:2819, 2020. 14

[10] Anat Gesser-Edelsburg, Alon Diamant, Rana Hijazi, and Gustavo S Mesch. **Correcting misinformation by health organizations during measles outbreaks: a controlled experiment**. *PloS one*, **13**[12]:e0209505, 2018. 14

[11] Delphine Planas, David Veyer, Artem Baidaliuk, Isabelle Staropoli, Florence Guivel-Benhassine, Maaran Michael Rajah, Cyril Planchais, Françoise Porrot, Nicolas Robillard, Julien Puech, et al. **Reduced sensitivity of SARS-CoV-2 variant Delta to antibody neutralization**. *Nature*, **596**[7871]:276–280, 2021. 15

[12] Diana Duong. **Alpha, Beta, Delta, Gamma: What's important to know about SARS-CoV-2 variants of concern?**, 2021. 15

[13] Frederic Grabowski, Marek Kochańczyk, and Tomasz Lipniacki. **The spread of SARS-CoV-2 variant Omicron with a doubling time of 2.0–3.3 days can be explained by immune evasion**. *Viruses*, **14**[2]:294, 2022. 15

[14] David Skegg, Peter Gluckman, Geoffrey Boulton, Heide Hackmann, Salim S Abdool Karim, Peter Piot, and Christiane Woopen. **Future scenarios for the COVID-19 pandemic**. *The Lancet*, **397**[10276]:777–778, 2021. 15

[15] Aaron Kofman, Rami Kantor, and Eli Y Adashi. **Potential COVID-19 endgame scenarios: eradication, elimination, cohabitation, or conflagration?** *JAMA*, **326**[4]:303–304, 2021. 15

[16] Kenneth Murphy and Casey Weaver. *Janeway's immunobiology*, chapter 1. Garland science, 2016. 15, 16, 17

[17] Max D Cooper, Raymond DA Peterson, and Robert A Good. **Delineation of the thymic and bursal lymphoid systems in the chicken**. *Nature*, **205**[4967]:143–146, 1965. 16

[18] AM DiGeorge. **Congenital absence of the thymus and its immunologic consequences: Concurrense with congenital hypoparathyRoidism**. *Immunologic Deficiency Disease in Man, Birth Defects*, pages 116–121, 1969. 16

[19] Max D Cooper. **The early history of B cells**. *Nature Reviews Immunology*, **15**[3]:191–197, 2015. 16

[20] Yusuke Yanagi, Yasunobu Yoshikai, Kathleen Leggett, Stephen P Clark, Ingrid Aleksander, and Tak W Mak. **A human T cell-specific cDNA clone encodes a protein having extensive homology to immunoglobulin chains**. *Nature*, **308**[5955]:145–149, 1984. 16

[21] Stephen M Hedrick, David I Cohen, Ellen A Nielsen, and Mark M Davis. **Isolation of cDNA clones encoding T cell-specific membrane-associated proteins**. *Nature*, **308**[5955]:149–153, 1984. 16

[22] F.M. Burnet and M.F. Burnet. *The Clonal Selection Theory of Acquired Immunity*. Abraham Flexner lectures of Vanderbilt University 1958. Vanderbilt University Press, 1959. 16

[23] Abul K Abbas, Andrew H Lichtman, and Shiv Pillai. *Cellular and molecular immunology*, chapter 12. Elsevier Health Sciences, 2021. 16, 41, 42

REFERENCES

[24] Abul K Abbas, Andrew H Lichtman, and Shiv Pillai. *Cellular and molecular immunology*, chapter 10. Elsevier Health Sciences, 2021. 17, 41, 43

[25] Abul K Abbas, Andrew H Lichtman, and Shiv Pillai. *Cellular and molecular immunology*, chapter 11. Elsevier Health Sciences, 2021. 17

[26] Abul K Abbas, Andrew H Lichtman, and Shiv Pillai. *Cellular and molecular immunology*, chapter 15. Elsevier Health Sciences, 2021. 17

[27] William B Coley. **II. Contribution to the knowledge of sarcoma**. *Annals of surgery*, **14**[3]:199, 1891. 17

[28] WB Coley. **Treatment of malignant tumors by repeated inoculations of erysipelas with a report of 10 cases**. *Med Rec*, **43**:60, 1893. 17

[29] George Klein and Eva Klein. **Immune surveillance against virus-induced tumors and nonrejectability of spontaneous tumors: contrasting consequences of host versus tumor evolution**. *Proceedings of the National Academy of Sciences*, **74**[5]:2121–2125, 1977. 17

[30] Mary E Connor and Peter L Stern. **Loss of MHC class-I expression in cervical carcinomas**. *International journal of cancer*, **46**[6]:1029–1034, 1990. 17

[31] Federico Garrido. **MHC/HLA class I loss in cancer cells**. *MHC Class-I Loss and Cancer Immune Escape*, pages 15–78, 2019. 17

[32] Nicholas McGranahan and Charles Swanton. **Clonal heterogeneity and tumor evolution: past, present, and the future**. *Cell*, **168**[4]:613–628, 2017. 17

[33] Mariam Jamal-Hanjani, Gareth A Wilson, Nicholas McGranahan, Nicolai J Birkbak, Thomas BK Watkins, Selvaraju Veeriah, Seema Shafi, Diana H Johnson, Richard Mitter, Rachel Rosenthal, et al. **Tracking the evolution of non–small-cell lung cancer**. *New England Journal of Medicine*, **376**[22]:2109–2121, 2017. 17

[34] Jeffrey W Pollard. **Tumour-educated macrophages promote tumour progression and metastasis**. *Nature Reviews Cancer*, **4**[1]:71–78, 2004. 18

[35] Valeria Quaranta and Michael C Schmid. **Macrophage-mediated subversion of anti-tumour immunity**. *Cells*, **8**[7]:747, 2019. 18

[36] Theresa L Whiteside. **What are regulatory T cells (Treg) regulating in cancer and why?** In *Seminars in cancer biology*, **22**, pages 327–334. Elsevier, 2012. 18

[37] Magdalena Frydrychowicz, Maciej Boruczkowski, Agata Kolecka-Bednarczyk, and Grzegorz Dworacki. **The dual role of Treg in cancer**. *Scandinavian journal of immunology*, **86**[6]:436–443, 2017. 18

[38] Masoud Najafi, Bagher Farhood, and Keywan Mortezaee. **Contribution of regulatory T cells to cancer: A review**. *Journal of cellular physiology*, **234**[6]:7983–7993, 2019. 18

[39] Gideon Gross, Tova Waks, and Zelig Eshhar. **Expression of immunoglobulin-T-cell receptor chimeric molecules as functional receptors with antibody-type specificity**. *Proceedings of the National Academy of Sciences*, **86**[24]:10024–10028, 1989. 18

[40] Renier J Brentjens, Marco L Davila, Isabelle Riviere, Jae Park, Xiuyan Wang, Lindsay G Cowell, Shirley Bartido, Jolanta Stefanski, Clare Taylor, Malgorzata Olszewska, et al. **CD19-targeted T cells rapidly induce molecular remissions in adults with chemotherapy-refractory acute lymphoblastic leukemia**. *Science translational medicine*, **5**[177]:177ra38–177ra38, 2013. 18

[41] Marcela V Maus, Stephan A Grupp, David L Porter, and Carl H June. **Antibody-modified T cells: CARs take the front seat for hematologic malignancies**. *Blood, The Journal of the American Society of Hematology*, **123**[17]:2625–2635, 2014. 18

[42] James N Kochenderfer, Mark E Dudley, Sadik H Kassim, Robert P T Somerville, Robert O Carpenter, Maryalice Stetler-Stevenson, James C Yang, Giao Q Phan, Marybeth S Hughes, Richard M Sherry, Mark Raffeld, Steven Feldman, Lily Lu, Yong F Li, Lien T Ngo, Andre Goy, Tatyana Feldman, David E Spaner, Michael L Wang, Clara C Chen, Sarah M Kranick, Avindra Nath, Debbie-Ann N Nathan, Kathleen E Morton, Mary Ann Toomey, and Steven A Rosenberg. **Chemotherapy-Refractory Diffuse Large B-Cell Lymphoma and Indolent B-Cell Malignancies Can Be Effectively Treated With Autologous T Cells Expressing an Anti-CD19 Chimeric Antigen Receptor**. *J Clin Oncol*, **33**:540–549, 2014. 18, 29

[43] Sunitha Kakarla and Stephen Gottschalk. **CAR T cells for solid tumors: armed and ready to go?** *Cancer Journal (Sudbury, Mass.)*, **20**[2]:151, 2014. 18

[44] Leonid Cherkassky, Aurore Morello, Jonathan Villena-Vargas, Yang Feng, Dimiter S Dimitrov, David R Jones, Michel Sadelain, Prasad S Adusumilli, et al. **Human CAR T cells with cell-intrinsic PD-1 checkpoint blockade resist tumor-mediated inhibition**. *The Journal of clinical investigation*, **126**[8]:3130–3144, 2016. 18

[45] Andras Heczey, Chrystal U Louis, Barbara Savoldo, Olga Dakhova, April Durett, Bambi Grilley, Hao Liu, Mengfeng F Wu, Zhuyong Mei, Adrian Gee, et al. **CAR T cells administered in combination with lymphodepletion and PD-1 inhibition to patients with neuroblastoma**. *Molecular therapy*, **25**[9]:2214–2224, 2017. 18

[46] Michael JT Stubbington, Orit Rozenblatt-Rosen, Aviv Regev, and Sarah A Teichmann. **Single-cell transcriptomics to explore the immune system in health and disease**. *Science*, **358**[6359]:58–63, 2017. 19

[47] Ananda L Roy. **Transcriptional regulation in the immune system: one cell at a time**. *Frontiers in immunology*, **10**:1355, 2019. 19

[48] Svetoslav Chakarov, Hwee Ying Lim, Leonard Tan, Sheau Yng Lim, Peter See, Josephine Lum, Xiao-Meng Zhang, Shihui Foo, Satoshi Nakamizo, Kaibo Duan, et al. **Two distinct interstitial macrophage populations coexist across tissues in specific subtissular niches**. *Science*, **363**[6432]:eaau0964, 2019. 19

[49] K.M. Murphy and C. Weaver. *Janeway's Immunobiology: Ninth International Student Edition*. Garland Science, 2016. 19

[50] Arne B Gjuvsland, Jon Olav Vik, Daniel A Beard, Peter J Hunter, and Stig W Omholt. **Bridging the genotype–phenotype gap: what does it take?** *The Journal of physiology*, **591**[8]:2055–2066, 2013. 20

[51] Marylyn D Ritchie, Emily R Holzinger, Ruowang Li, Sarah A Pendergrass, and Dokyoon Kim. **Methods of integrating data to uncover genotype–phenotype interactions**. *Nature Reviews Genetics*, **16**[2]:85–97, 2015. 20

[52] Anthony J Brookes and Peter N Robinson. **Human genotype–phenotype databases: aims, challenges and opportunities**. *Nature Reviews Genetics*, **16**[12]:702–715, 2015. 20

[53] G Tancini, S Barni, R Rescaldani, G Fiorelli, S Viviani, and P Lissoni. **Analysis of T helper and suppressor lymphocyte subsets in relation to the clinical stage of solid neoplasms**. *Oncology*, **47**[5]:381–384, 1990. 21, 33

[54] Axel C. P. Diederichsen, J. v. B. Hjelmborg, Per B. Christensen, Jesper Zeuthen, and Claus Fenger. **Prognostic value of the CD4+/CD8+ ratio of tumour infiltrating lymphocytes in colorectal cancer and HLA-DR expression on tumour cells**. *Cancer Immunology, Immunotherapy*, **52**[7]:423–428, Jul 2003. 21, 34

[55] E. Sato, S. H. Olson, J. Ahn, B. Bundy, H. Nishikawa, F. Qian, A. A. Jungbluth, D. Frosina, S. Gnjatic, C. Ambrosone, J. Kepner, T. Odunsi, G. Ritter, S. Lele, Y.-T. Chen, H. Ohtani, L. J. Old, and K. Odunsi. **Intraepithelial CD8+ tumor-infiltrating lymphocytes and a high CD8+/regulatory T cell ratio are associated with favorable prognosis in ovarian cancer**. *Proceedings of the National Academy of Sciences*, **102**[51]:18538–18543, Dec 2005. 21, 34

[56] Jeremy M.G. Taylor, John L. Fahey, Roger Detels, and Janis V. Giorgi. **Cd4 percentage, cd4 number, and cd4:Cd8 ratio in hiv infection: Which to choose and how to use**. *Journal of Acquired Immune Deficiency Syndromes*, **2**[2]:114–124, jan 1989. 21, 30

[57] Sergio Serrano-Villar, Talia Sainz, Sulggi A. Lee, Peter W. Hunt, Elizabeth Sinclair, Barbara L. Shacklett, April L. Ferre, Timothy L. Hayes, Ma Somsouk, Priscilla Y. Hsue, Mark L. Van Natta, Curtis L. Meinert, Michael M. Lederman, Hiroyu Hatano, Vivek Jain, Yong Huang, Frederick M. Hecht, Jeffrey N. Martin, Joseph M. McCune, Santiago Moreno, and Steven G. Deeks. **HIV-Infected Individuals with Low CD4/CD8 Ratio despite Effective Antiretroviral Therapy Exhibit Altered T Cell Subsets, Heightened CD8+ T Cell Activation, and Increased Risk of Non-AIDS Morbidity and Mortality**. *PLoS Pathogens*, **10**[5], 2014. 21, 30

[58] Anders Wikby, Pamela Maxson, Jadwiga Olsson, Boo Johansson, and Frederick G. Ferguson. **Changes in CD8 and CD4 lymphocyte subsets, T cell proliferation responses and non-survival in the very old: The Swedish longitudinal OCTO-immune study**. In *Mechanisms of Ageing and Development*, **102**, pages 187–198. Elsevier, May 1998. 21, 31

[59] Jadwiga Olsson, Anders Wikby, Boo Johansson, Sture Löfgren, Bengt Olof Nilsson, and Frederick G. Ferguson. **Age-related change in peripheral blood T-lymphocyte subpopulations and cytomegalovirus infection in the very old: The Swedish longitudinal OCTO immune study**. *Mechanisms of Ageing and Development*, **121**[1-3]:187–201, jan 2001. 21, 31

[60] Angel Garcia-Lora, Ignacio Algarra, and Federico Garrido. **MHC class I antigens, immune surveillance, and tumor immune escape**, Jun 2003. 21, 34

[61] Nicholas F.S. Watson, Judith M. Ramage, Zahra Madjd, Ian Spendlove, Ian O. Ellis, John H. Scholefield, and Lindy G. Durrant. **Immunosurveillance is active in colorectal cancer as downregulation but not complete loss of MHC class I expression correlates with a poor prognosis**. *International Journal of Cancer*, **118**[1]:6–10, jan 2006. 21, 34, 35

[62] Jonathan A D Simpson, Ahmad Al-Attar, Nicholas F S Watson, John H Scholefield, Mohammad Ilyas, and Lindy G Durrant. **Intratumoral T cell infiltration, MHC class I and STAT1 as biomarkers of good prognosis in colorectal cancer**. *Gut*, **59**[7]:926–933, Jul 2010. 21, 34

[63] V Kuznetsov, I Makalkin, M Taylor, and A Perelson. **Nonlinear dynamics of immunogenic tumors: Parameter estimation and global bifurcation analysis**. *Bulletin of Mathematical Biology*, **56**[2]:295–321, Mar 1994. 22, 36

[64] Heidi Dritschel, Sarah L Waters, Andreas Roller, and Helen M Byrne. **A mathematical model of cytotoxic and helper T cell interactions in a tumour microenvironment**. *Letters in Biomathematics*, 2018. 22, 36, 73

[65] M. E. J. Newman. **Assortative Mixing in Networks**. *Phys Rev Lett*, **89**[20]:208701, 2002. 22, 23, 24, 110

[66] M. E.J. Newman. **Spread of epidemic disease on networks**. *Phys Rev E Stat Phys Plasmas Fluids Relat Interdiscip Topics*, **66**[1], 2002. 22, 23, 96, 98

[67] Mark Newman. *Networks*. Oxford university press, 2018. 22, 23

[68] Romualdo Pastor-Satorras and Alessandro Vespignani. **Immunization of complex networks**. *Phys Rev E Stat Phys Plasmas Fluids Relat Interdiscip Topics*, **65**[3]:036104, 2002. 23

[69] Joel C. Miller and James M. Hyman. **Effective vaccination strategies for realistic social networks**. *Physica A*, **386**[2]:780–785, 2007. 23, 97

[70] Junling Ma, P. Van Den Driessche, and Frederick H. Willeboordse. **The importance of contact network topology for the success of vaccination strategies**. *J Theor Biol*, **325**:12–21, 2013. 23, 97

[71] Leo Torres, Kevin S Chan, Hanghang Tong, and Tina Eliassi-Rad. **Nonbacktracking Eigenvalues under Node Removal: X-Centrality and Targeted Immunization**. *SIAM J Math Data Sci*, **3**[2]:656–675, 2021. 23, 97

[72] Romualdo Pastor-Satorras and Alessandro Vespignani. **Epidemic dynamics and endemic states in complex networks**. *Physical Review E*, **63**[6]:066117, 2001. 24

[73] Robert M May and Alun L Lloyd. **Infection dynamics on scale-free networks**. *Physical Review E*, **64**[6]:066112, 2001. 24

[74] Yamir Moreno, Romualdo Pastor-Satorras, and Alessandro Vespignani. **Epidemic outbreaks in complex heterogeneous networks**. *The European Physical Journal B-Condensed Matter and Complex Systems*, **26**[4]:521–529, 2002. 24

[75] Byungjoon Min and Claudio Castellano. **Message-passing theory for cooperative epidemics**. *Chaos*, **30**[2]:023131, 2020. 24, 96, 249

[76] S. Moore and T. Rogers. **Heterogeneous node responses to multi-type epidemics on networks**. *Proc R Soc Lond A Math Phys Sci*, **476**[2243], 2020. 24, 96, 249

[77] Hanlin Sun, David Saad, and Andrey Y Lokhov. **Competition, Collaboration, and Optimization in Multiple Interacting Spreading Processes**. *Phys Rev X*, **11**, 2021. 24, 96, 249

[78] Clara Granell, Sergio Gómez, and Alex Arenas. **Dynamical interplay between awareness and epidemic spreading in multiplex networks**. *Physical review letters*, **111**[12]:128701, 2013. 24

[79] Clara Granell, Sergio Gómez, and Alex Arenas. **Competing spreading processes on multiplex networks: awareness and epidemics**. *Physical review E*, **90**[1]:012808, 2014. 24

[80] Ginestra Bianconi, Hanlin Sun, Giacomo Rapisardi, and Alex Arenas. **Message-passing approach to epidemic tracing and mitigation with apps**. *Phys Rev Res*, **3**[1]:L012014, 2021. 24, 96

[81] GJ Baxter and G Timár. **Degree dependent transmission rates in epidemic processes**. *Journal of Statistical Mechanics: Theory and Experiment*, **2021**[10]:103501, 2021. 24, 98

[82] Stuart A Kauffman. **Metabolic stability and epigenesis in randomly constructed genetic nets**. *Journal of theoretical biology*, **22**[3]:437–467, 1969. 25, 169

[83] Stuart Kauffman. **Homeostasis and differentiation in random genetic control networks**. *Nature*, **224**[5215]:177–178, 1969. 25, 169

[84] CC Walker and William Ross Ashby. **On temporal characteristics of behavior in certain complex systems**. *Kybernetik*, **3**[2]:100–108, 1966. 26

[85] Réka Albert and Albert-László Barabási. **Dynamics of complex systems: Scaling laws for the period of Boolean networks**. *Physical Review Letters*, **84**[24]:5660, 2000. 26

[86] Hamed Mahmoudi and David Saad. **Generalized mean field approximation for parallel dynamics of the Ising model**. *Journal of Statistical Mechanics: Theory and Experiment*, **2014**[7]:P07001, 2014. 26

[87] Erik Aurell and Hamed Mahmoudi. **Dynamic mean-field and cavity methods for diluted Ising systems**. *Physical Review E*, **85**[3]:031119, 2012. 26, 173, 179, 180, 184, 194, 201

REFERENCES

[88] Haiping Huang and Yoshiyuki Kabashima. **Dynamics of asymmetric kinetic Ising systems revisited**. *Journal of Statistical Mechanics: Theory and Experiment*, **2014**[5]:P05020, 2014. 26

[89] ACC Coolen, SN Laughton, and D Sherrington. **Dynamical replica theory for disordered spin systems**. *Physical Review B*, **53**[13]:8184, 1996. 26

[90] JPL Hatchett, I Pérez Castillo, ACC Coolen, and NS Skantzos. **Dynamical replica analysis of disordered Ising spin systems on finitely connected random graphs**. *Physical review letters*, **95**[11]:117204, 2005. 26

[91] Alexander Mozeika and ACC Coolen. **Dynamical replica analysis of processes on finitely connected random graphs: I. Vertex covering**. *Journal of Physics A: Mathematical and Theoretical*, **41**[11]:115003, 2008. 26

[92] Alexander Mozeika and ACC2599315 Coolen. **Dynamical replica analysis of processes on finitely connected random graphs: II. Dynamics in the Griffiths phase of the diluted Ising ferromagnet**. *Journal of Physics A: Mathematical and Theoretical*, **42**[19]:195006, 2009. 26

[93] JPL Hatchett, B Wemmenhove, I Pérez Castillo, T Nikoletopoulos, NS Skantzos, and ACC Coolen. **Parallel dynamics of disordered Ising spin systems on finitely connected random graphs**. *Journal of Physics A: Mathematical and General*, **37**[24]:6201, 2004. 26, 210, 214

[94] Kazushi Mimura and ACC Coolen. **Parallel dynamics of disordered Ising spin systems on finitely connected directed random graphs with arbitrary degree distributions**. *Journal of Physics A: Mathematical and Theoretical*, **42**[41]:415001, 2009. 26, 210, 214, 239

[95] Ton Coolen, Alessia Annibale, and Ekaterina Roberts. *Generating random networks and graphs*. Oxford university press, 2017. 26, 122

[96] Izaak Neri and Désiré Bollé. **The cavity approach to parallel dynamics of Ising spins on a graph**. *Journal of Statistical Mechanics: Theory and Experiment*, **2009**[08]:P08009, 2009. 26, 173, 179, 180, 184, 185, 194, 214

[97] Erik Aurell and Hamed Mahmoudi. **A message-passing scheme for non-equilibrium stationary states**. *Journal of Statistical Mechanics: Theory and Experiment*, **2011**[04]:P04014, 2011. 26, 173, 179, 180, 184, 194, 201

[98] Giuseppe Torrisi, Reimer Kühn, and Alessia Annibale. **Uncovering the non-equilibrium stationary properties in sparse Boolean networks**. *Journal of Statistical Mechanics: Theory and Experiment*, **2022**[5]:053303, 2022. 26, 170, 171, 172, 174, 175, 176, 178, 179, 180, 184, 185, 186, 193, 194, 199

[99] Renier J Brentjens, Marco L Davila, Isabelle Riviere, Jae Park, Xiuyan Wang, Lindsay G Cowell, Shirley Bartido, Jolanta Stefanski, Clare Taylor, Malgorzata Olszewska, Oriana Borquez-Ojeda, Jinrong Qu, Teresa Wasielewska, Qing He, Yvette Bernal, Ivelise V Rijo, Cyrus Hedvat, Rachel Kobos, Kevin Curran, Peter Steinherz, Joseph Jurcic, Todd Rosenblat, Peter Maslak, Mark Frattini, and Michel Sadelain. **CD19-targeted T cells rapidly induce molecular remissions in adults with chemotherapy-refractory acute lymphoblastic leukemia.** *Science translational medicine*, **5**[177]:177ra38, Mar 2013. 29

[100] D. R. Leach, M. F. Krummel, and J. P. Allison. **Enhancement of Antitumor Immunity by CTLA-4 Blockade**. *Science*, **271**[5256]:1734–1736, Mar 1996. 29

[101] David F. McDermott, Charles G. Drake, Mario Sznol, Toni K. Choueiri, John D. Powderly, David C. Smith, Julie R. Brahmer, Richard D. Carvajal, Hans J. Hammers, Igor Puzanov, F. Stephen Hodi, Harriet M. Kluger, Suzanne L. Topalian, Drew M. Pardoll, Jon M. Wigginton, Georgia D. Kollia, Ashok Gupta, Dan McDonald, Vindira Sankar, Jeffrey A. Sosman, and Michael B. Atkins. **Survival, Durable Response, and Long-Term Safety in Patients With Previously Treated Advanced Renal Cell Carcinoma Receiving Nivolumab**. *Journal of Clinical Oncology*, **33**[18]:2013–2020, Jun 2015. 29

[102] F. Stephen Hodi, Steven J. O'Day, David F. McDermott, Robert W. Weber, Jeffrey A. Sosman, John B. Haanen, Rene Gonzalez, Caroline Robert, Dirk Schadendorf, Jessica C. Hassel, Wallace Akerley, Alfons J.M. van den Eertwegh, Jose Lutzky, Paul Lorigan, Julia M. Vaubel, Gerald P. Linette, David Hogg, Christian H. Ottensmeier, Celeste Lebbé, Christian Peschel, Ian Quirt, Joseph I. Clark, Jedd D. Wolchok, Jeffrey S. Weber, Jason Tian, Michael J. Yellin, Geoffrey M. Nichol, Axel Hoos, and Walter J. Urba. **Improved Survival with Ipilimumab in Patients with Metastatic Melanoma**. *New England Journal of Medicine*, **363**[8]:711–723, Aug 2010. 29

[103] Sunitha Kakarla and Stephen Gottschalk. **CAR T Cells for Solid Tumors**. *The Cancer Journal*, **20**[2]:151–155, 2014. 29

[104] Andrew K Sewell. **Why must T cells be cross-reactive?** *Nature Reviews Immunology*, **12**[9]:669–677, 2012. 30

[105] Galina Petrova, Andrea Ferrante, and Jack Gorski. **Cross-reactivity of T cells and its role in the immune system**. *Critical Reviews™ in Immunology*, **32**[4], 2012. 30

[106] Nicholas P. Restifo, Mark E. Dudley, and Steven A. Rosenberg. **Adoptive immunotherapy for cancer: Harnessing the T cell response**, Apr 2012. 30, 32

[107] Ting-Jun Jiang, Xue-Liang Cao, Sha Luan, Wan-Hui Cui, Si-Huang Qiu, Yi-Chao Wang, Chang-Jiu Zhao, and Peng Fu. **Percentage and function of CD4+ CD25+ regulatory T cells in patients with hyperthyroidism**. *Molecular Medicine Reports*, **17**[2]:2137–2144, 2018. 31

[108] Yoshiko Takeuchi and Hiroyoshi Nishikawa. **Roles of regulatory T cells in cancer immunity**. *International immunology*, **28**[8]:401–409, 2016. 31

[109] Dounia Chraa, Asmaa Naim, Daniel Olive, and Abdallah Badou. **T lymphocyte subsets in cancer immunity: friends or foes**. *Journal of leukocyte biology*, **105**[2]:243–255, 2019. 31

[110] SUZANNE L Topalian, DIANE Solomon, and STEVEN A Rosenberg. **Tumor-specific cytolysis by lymphocytes infiltrating human melanomas.** *Journal of immunology (Baltimore, Md.: 1950)*, **142**[10]:3714–3725, 1989. 31

[111] Sophia S Horn, Suzanne L Topalian, Toni Simonis, Marie Mancini, and Steven A Rosenberg. **Common expression of melanoma tumor-associated antigens recognized by human tumor infiltrating lymphocytes: analysis by human lymphocyte antigen restriction**. *Journal of immunotherapy*, **10**[3]:152–164, 1991. 31

[112] Fathia Mami-Chouaib, Hamid Echchakir, Guillaume Dorothée, Isabelle Vergnon, and Salem Chouaib. **Antitumor cytotoxic T-lymphocyte response in human lung carcinoma: identification of a tumor-associated antigen**. *Immunological reviews*, **188**[1]:114–121, 2002. 31

[113] Andreas Mackensen, Laurent Ferradini, Guislaine Carcelain, Frederic Triebel, Florence Faure, Sophie Viel, and Thierry Hercend. **Evidence for in situ amplification of cytotoxic T-lymphocytes with antitumor activity in a human regressive melanoma**. *Cancer research*, **53**[15]:3569–3573, 1993. 31

[114] Hans Raskov, Adile Orhan, Jan Pravsgaard Christensen, and Ismail Gögenur. **Cytotoxic CD8+ T cells in cancer and cancer immunotherapy**. *British journal of cancer*, **124**[2]:359–367, 2021. 31

[115] Keith L Knutson and ML Disis. **Tumor antigen-specific T helper cells in cancer immunity and immunotherapy**. *Cancer Immunology, Immunotherapy*, **54**:721–728, 2005. 31

[116] Takashi Nishimura, Kenji Iwakabe, Masashi Sekimoto, Yasushi Ohmi, Takashi Yahata, Minoru Nakui, Takehito Sato, Sonoko Habu, Hiroyuki Tashiro, Marimo Sato, et al. **Distinct role of antigen-specific T helper type 1 (Th1) and Th2 cells in tumor eradication in vivo**. *The Journal of experimental medicine*, **190**[5]:617–628, 1999. 32, 41, 42, 43

[117] Aris Giannopoulos, Constantinos Constantinides, Eleftherios Fokaeas, Constantinos Stravodimos, Myrto Giannopoulou, Aspasia Kyroudi, and Antonia Gounaris. **The immunomodulating effect of interferon-γ intravesical instillations in preventing bladder cancer recurrence**. *Clinical Cancer Research*, **9**[15]:5550–5558, 2003. 32

[118] Hye-Jung Kim and Harvey Cantor. **CD4 T-cell subsets and tumor immunity: the helpful and the not-so-helpful**. *Cancer immunology research*, **2**[2]:91–98, 2014. 32

[119] Weiping Zou. **Regulatory T cells, tumour immunity and immunotherapy**. *Nature Reviews Immunology*, **6**[4]:295–307, 2006. 32

[120] K Oleinika, RJ Nibbs, GJ Graham, and AR Fraser. **Suppression, subversion and escape: the role of regulatory T cells in cancer progression**. *Clinical & Experimental Immunology*, **171**[1]:36–45, 2013. 32

[121] Mary Jo Turk, José A Guevara-Patiño, Gabrielle A Rizzuto, Manuel E Engelhorn, and Alan N Houghton. **Concomitant tumor immunity to a poorly immunogenic melanoma is prevented by regulatory T cells**. *The Journal of experimental medicine*, **200**[6]:771–782, 2004. 32

[122] Deepali V Sawant, Hiroshi Yano, Maria Chikina, Qianxia Zhang, Mengting Liao, Chang Liu, Derrick J Callahan, Zhe Sun, Tao Sun, Tracy Tabib, et al. **Adaptive plasticity of IL-10+ and IL-35+ Treg cells cooperatively promotes tumor T cell exhaustion**. *Nature immunology*, **20**[6]:724–735, 2019. 32

[123] Chunxiao Li, Ping Jiang, Shuhua Wei, Xiaofei Xu, and Junjie Wang. **Regulatory T cells in tumor microenvironment: new mechanisms, potential therapeutic strategies and future prospects**. *Molecular cancer*, **19**:1–23, 2020. 32

[124] Kristina Berg Lorvik, Clara Hammarström, Marte Fauskanger, Ole Audun Werner Haabeth, Michael Zangani, Guttorm Haraldsen, Bjarne Bogen, and Alexandre Corthay. **Adoptive Transfer of Tumor-Specific Th2 Cells Eradicates Tumors by Triggering an In Situ Inflammatory Immune ResponseCancer Immunotherapy by Adoptive Transfer of Th2 Cells**. *Cancer research*, **76**[23]:6864–6876, 2016. 32

[125] Julia I Ellyard, Ljubov Simson, and Christopher R Parish. **Th2-mediated anti-tumour immunity: friend or foe?** *Tissue antigens*, **70**[1]:1–11, 2007. 33

[126] Xinming Su, Jian Ye, Eddy C Hsueh, Yanping Zhang, Daniel F Hoft, and Guangyong Peng. **Tumor microenvironments direct the recruitment and expansion of human Th17 cells**. *The Journal of Immunology*, **184**[3]:1630–1641, 2010. 33

[127] Zahra Asadzadeh, Hamed Mohammadi, Elham Safarzadeh, Maryam Hemmatzadeh, Ahmad Mahdian-Shakib, Farhad Jadidi-Niaragh, Gholamreza Azizi, and Behzad Baradaran. **The paradox of Th17 cell functions in tumor immunity**. *Cellular Immunology*, **322**:15–25, 2017. 33

[128] Bor-Ching Sheu, Su-Ming Hsu, Hong-Nerng Ho, Rong-Hwa Lin, Pao-Ling Torng, and Su-Cheng Huang. **Reversed CD4/CD8 ratios of tumor-infiltrating lymphocytes are correlated with the progression of human cervical carcinoma**. *Cancer*, **86**[8]:1537–1543, Oct 1999. 33

[129] Bor Ching Sheu, Wen Hung Kuo, Ruey Jien Chen, Su Cheng Huang, King Jen Chang, and Song Nan Chow. **Clinical significance of tumor-infiltrating lymphocytes in neoplastic progression and lymph node metastasis of human breast cancer**. *Breast*, **17**[6]:604–610, 2008. 33

[130] L Sevcíková, L Hunáková, B Chorváth, M Turzová, and E Bolesíková. **T-lymphocyte subsets (CD4/CD8 ratio) in breast cancer patients.** *Neoplasma*, **39**[4]:219–22, 1992. 33

[131] Claudia Nunes, Ryan Wong, Malcolm Mason, Chris Fegan, Stephen Man, and Chris Pepper. **Expansion of a CD8$^+$PD-1$^+$ Replicative Senescence Phenotype in Early Stage CLL Patients Is Associated with Inverted CD4:CD8 Ratios and Disease Progression**. *Human Cancer Biology*, 2012. 33

[132] S Ménard, G Tomasic, P Casalini, A Balsari, S Pilotti, N Cascinelli, B Salvadori, M I Colnaghi, F Rilke, Markus W. Büchler, and Jan Schmidt. **Lymphoid infiltration as a prognostic variable for early-onset breast carcinomas.** *Clinical cancer research : an official journal of the American Association for Cancer Research*, **3**[5]:817–9, May 1997. 34

[133] E Ryschich, T Nötzel, U Hinz, F Autschbach, J Ferguson, I Simon, J Weitz, B Fröhlich, E Klar, MW Büchler, and J Schmidt. **Control of T-cell-mediated immune response by HLA class I in human pancreatic carcinoma.** *Clinical cancer research : an official journal of the American Association for Cancer Research*, **11**[2 Pt 1]:498–504, 2005. 34, 35

[134] Wouter Scheper, Sander Kelderman, Lorenzo F. Fanchi, Carsten Linnemann, Gavin Bendle, Marije A.J. de Rooij, Christian Hirt, Riccardo Mezzadra, Maarten Slagter, Krijn Dijkstra, Roelof J.C. Kluin, Petur Snaebjornsson, Katy Milne, Brad H. Nelson, Henry Zijlmans, Gemma Kenter, Emile E. Voest, John B.A.G. Haanen, and Ton N. Schumacher. **Low and variable tumor reactivity of the intratumoral TCR repertoire in human cancers**. *Nature Medicine*, **25**[1]:89–94, Dec 2019. 34, 81

[135] Zahra Madjd, Ian Spendlove, Sarah E. Pinder, Ian O. Ellis, and Lindy G. Durrant. **Total loss of MHC class I is an independent indicator of good prognosis in breast cancer**. *International Journal of Cancer*, **117**[2]:248–255, Nov 2005. 34

[136] Simon Turcotte, Steven C Katz, Jinru Shia, William R Jarnagin, T Peter Kingham, Peter J Allen, Yuman Fong, Michael I D'Angelica, and Ronald P DeMatteo. **Tumor MHC class I expression improves the prognostic value of T-cell density in resected colorectal liver metastases.** *Cancer immunology research*, **2**[6]:530–7, Jun 2014. 35, 65, 67, 80

[137] Grace E Mahlbacher, Kara C Reihmer, and Hermann B Frieboes. **Mathematical modeling of tumor-immune cell interactions**. *Journal of Theoretical Biology*, **469**:47–60, 2019. 36

[138] Mohammad El Wajeh, Falco Jung, Dominik Bongartz, Chrysoula Dimitra Kappatou, Narmin Ghaffari Laleh, Alexander Mitsos, and Jakob Nikolas Kather. **Can the Kuznetsov Model Replicate and Predict Cancer Growth in Humans?** *Bulletin of Mathematical Biology*, **84**[11]:130, 2022. 36

[139] Katherine Owens and Ivana Bozic. **Modeling CAR T-cell therapy with patient preconditioning**. *Bulletin of Mathematical Biology*, **83**:1–36, 2021. 36

[140] Motahareh Moghtadaei, Mohammad Reza Hashemi Golpayegani, and Reza Malekzadeh. **Periodic and chaotic dynamics in a map-based model of tumor–immune interaction**. *Journal of theoretical biology*, **334**:130–140, 2013. 36

[141] Kathleen P Wilkie and Philip Hahnfeldt. **Mathematical models of immune-induced cancer dormancy and the emergence of immune evasion**. *Interface Focus*, **3**[4]:20130010, 2013. 36

[142] Yueping Dong, Rinko Miyazaki, and Yasuhiro Takeuchi. **MATHEMATICAL MODELING ON HELPER T CELLS IN A TUMOR IMMUNE SYSTEM.** *Discrete & Continuous Dynamical Systems-Series B*, **19**[1], 2014. 36

[143] Mark Robertson-Tessi, Ardith El-Kareh, and Alain Goriely. **A mathematical model of tumor–immune interactions**. *Journal of theoretical biology*, **294**:56–73, 2012. 37

[144] Zhongtao Yang, Cuihong Yang, Yueping Dong, and Yasuhiro Takeuchi. **Mathematical modelling of the inhibitory role of regulatory T cells in tumor immune response**. *Complexity*, **2020**:1–21, 2020. 37

[145] Luis De la Higuera Romero. *Stochastic models for CD4+ T cells*. PhD thesis, University of Leeds, 2017. 37

REFERENCES

[146] A Annibale, L A Dziobek-Garrett, and H Tari. **The role of the T-helper/T-suppressor ratio in the adaptive immune response: a dynamical model**. *Journal of Physics A: Mathematical and Theoretical*, 2018. 37, 47

[147] Alan S. Perelson and Gérard Weisbuch. **Immunology for physicists**. *Reviews of Modern Physics*, **69**[4]:1219–1267, Oct 1997. 38

[148] U. Lucia and G. Maino. **Thermodynamical analysis of the dynamics of tumor interaction with the host immune system**. *Physica A: Statistical Mechanics and its Applications*, **313**[3-4]:569–577, Oct 2002. 38

[149] Arup K. Chakraborty and Andrej Košmrlj. **Statistical Mechanical Concepts in Immunology**. *Annual Review of Physical Chemistry*, **61**[1]:283–303, Mar 2010. 38

[150] Thierry Mora, Aleksandra M. Walczak, William Bialek, and Curtis G. Callan. **Maximum entropy models for antibody diversity**. *Proceedings of the National Academy of Sciences of the United States of America*, **107**[12]:5405–5410, Mar 2010. 38

[151] Elena Agliari, Alessia Annibale, Adriano Barra, A. C. C. Coolen, and Daniele Tantari. **Immune networks: multitasking capabilities near saturation**. *Journal of Physics A: Mathematical and Theoretical*, **46**[41], May 2013. 38, 47

[152] Silvia Bartolucci, Alexander Mozeika, and Alessia Annibale. **The role of idiotypic interactions in the adaptive immune system: A belief-propagation approach**. *Journal of Statistical Mechanics: Theory and Experiment*, **2016**[8], Aug 2016. 38

[153] R. Eftimie and G. Eftimie. **Tumour-associated macrophages and oncolytic virotherapies: a mathematical investigation into a complex dynamics**. *Letters in Biomathematics*, **5**[sup1]:S6–S35, Jun 2018. 38

[154] Elisa Peranzoni, Jean Lemoine, Lene Vimeux, Vincent Feuillet, Sarah Barrin, Chahrazade Kantari-Mimoun, Nadège Bercovici, Marion Guérin, Jérôme Biton, Hanane Ouakrim, et al. **Macrophages impede CD8 T cells from reaching tumor cells and limit the efficacy of anti–PD-1 treatment**. *Proceedings of the National Academy of Sciences*, **115**[17]:E4041–E4050, 2018. 38

[155] Pierre G Coulie, Benoît J Van den Eynde, Pierre Van Der Bruggen, and Thierry Boon. **Tumour antigens recognized by T lymphocytes: at the core of cancer immunotherapy**. *Nature Reviews Cancer*, **14**[2]:135–146, 2014. 40

[156] Daniel S Chen and Ira Mellman. **Oncology meets immunology: the cancer-immunity cycle**. *immunity*, **39**[1]:1–10, 2013. 40

[157] Joseph Wolfers, Anne Lozier, Graça Raposo, Armelle Regnault, Clotilde Théry, Carole Masurier, Caroline Flament, Stéphanie Pouzieux, Florence Faure, Thomas Tursz, et al. **Tumor-derived exosomes are a source of shared tumor rejection antigens for CTL cross-priming**. *Nature medicine*, **7**[3]:297–303, 2001. 40

[158] Fabrice Andre, Noel EC Schartz, Mojgan Movassagh, Caroline Flament, Patricia Pautier, Philippe Morice, Christophe Pomel, Catherine Lhomme, Bernard Escudier, Thierry Le Chevalier, et al. **Malignant effusions and immunogenic tumour-derived exosomes**. *The Lancet*, **360**[9329]:295–305, 2002. 40

[159] M Iero, R Valenti, V Huber, P Filipazzi, G Parmiani, S Fais, and L Rivoltini. **Tumour-released exosomes and their implications in cancer immunity**. *Cell Death & Differentiation*, **15**[1]:80–88, 2008. 40

[160] Shu Wen Wen, Jaclyn Sceneay, Luize Goncalves Lima, Christina SF Wong, Melanie Becker, Sophie Krumeich, Richard J Lobb, Vanessa Castillo, Ke Ni Wong, Sarah Ellis, et al. **The Biodistribution and Immune Suppressive Effects of Breast Cancer–Derived ExosomesExosomes Regulate Immune Composition in Metastatic Organs**. *Cancer research*, **76**[23]:6816–6827, 2016. 40

[161] Sonam Mittal, Prachi Gupta, Pradeep Chaluvally-Raghavan, and Sunila Pradeep. **Emerging role of extracellular vesicles in immune regulation and cancer progression**. *Cancers*, **12**[12]:3563, 2020. 40

[162] Abul K Abbas, Andrew H Lichtman, and Shiv Pillai. *Cellular and molecular immunology*, chapter 6. Elsevier Health Sciences, 2021. 40, 42, 51

[163] Abul K Abbas, Andrew H Lichtman, and Shiv Pillai. *Cellular and molecular immunology*, chapter 18. Elsevier Health Sciences, 2021. 40, 41, 42, 43

[164] Troels R Petersen, Nina Dickgreber, and Ian F Hermans. **Tumor antigen presentation by dendritic cells**. *Critical Reviews™ in Immunology*, **30**[4], 2010. 40, 41, 42, 43

[165] Alycia Gardner and Brian Ruffell. **Dendritic cells and cancer immunity**. *Trends in immunology*, **37**[12]:855–865, 2016. 40, 42

[166] Tullia C Bruno, Peggy J Ebner, Brandon L Moore, Olivia G Squalls, Katherine A Waugh, Evgeniy B Eruslanov, Sunil Singhal, John D Mitchell, Wilbur A Franklin, Daniel T Merrick, et al. **Antigen-Presenting Intratumoral B Cells Affect CD4+ TIL Phenotypes in Non–Small Cell Lung Cancer PatientsTIL-Bs Present Antigen to CD4 TILs in NSCLC**. *Cancer immunology research*, **5**[10]:898–907, 2017. 40, 42

[167] Soizic Garaud, Laurence Buisseret, Cinzia Solinas, Chunyan Gu-Trantien, Alexandre de Wind, Gert Van den Eynden, Celine Naveaux, Jean-Nicolas Lodewyckx, Anaïs Boisson, Hughes Duvillier, et al. **Tumor-infiltrating B cells signal functional humoral immune responses in breast cancer**. *JCI insight*, **4**[18], 2019. 40, 42

[168] Kerstin Wennhold, Martin Thelen, Jonas Lehmann, Simon Schran, Ella Preugszat, Maria Garcia-Marquez, Axel Lechner, Alexander Shimabukuro-Vornhagen, Meryem S Ercanoglu, Florian Klein, et al. **CD86+ Antigen-Presenting B Cells Are Increased in Cancer, Localize in Tertiary Lymphoid Structures, and Induce Specific T-cell ResponsesB Cells Are Important Antigen-Presenting Cells in Cancer**. *Cancer immunology research*, **9**[9]:1098–1108, 2021. 40, 42

[169] Abul K Abbas, Andrew H Lichtman, and Shiv Pillai. *Cellular and molecular immunology*, chapter 9. Elsevier Health Sciences, 2021. 40, 42

[170] Karen M Smith, Lindsay Pottage, Elaine R Thomas, Andrew J Leishman, Tamsin N Doig, Damo Xu, Foo Y Liew, and Paul Garside. **Th1 and Th2 CD4+ T cells provide help for B cell clonal expansion and antibody synthesis in a similar manner in vivo**. *The Journal of Immunology*, **165**[6]:3136–3144, 2000. 41, 42

[171] Flávia Castro, Ana Patrícia Cardoso, Raquel Madeira Gonçalves, Karine Serre, and Maria José Oliveira. **Interferon-gamma at the crossroads of tumor immune surveillance or evasion**. *Frontiers in immunology*, **9**:847, 2018. 41, 43

[172] Loredana Frasca, Maria Nasso, Fabiana Spensieri, Giorgio Fedele, Raffaella Palazzo, Fabio Malavasi, and Clara Maria Ausiello. **IFN-γ arms human dendritic cells to perform multiple effector functions**. *The Journal of Immunology*, **180**[3]:1471–1481, 2008. 41, 43

[173] Jason G Cyster. **Chemokines and cell migration in secondary lymphoid organs**. *Science*, **286**[5447]:2098–2102, 1999. 41, 43

[174] Jannie Borst, Tomasz Ahrends, Nikolina Babała, Cornelis JM Melief, and Wolfgang Kastenmüller. **CD4+ T cell help in cancer immunology and immunotherapy**. *Nature Reviews Immunology*, **18**[10]:635–647, 2018. 41, 42

[175] Kenneth Murphy and Casey Weaver. *Janeway's immunobiology*, chapter 16. Garland science, 2016. 41, 43

[176] Mathilde Allard, Barbara Couturaud, Laura Carretero-Iglesia, Minh Ngoc Duong, Julien Schmidt, Gwennaëlle C. Monnot, Pedro Romero, Daniel E. Speiser, Michael Hebeisen, and Nathalie Rufer. **TCR-ligand dissociation rate is a robust and stable biomarker of CD8+ T cell potency**. *JCI insight*, **2**[14], Jul 2017. 47

[177] Shaomin Tian, Robert Maile, Edward J. Collins, and Jeffrey A. Frelinger. **CD8 + T Cell Activation Is Governed by TCR-Peptide/MHC Affinity, Not Dissociation Rate** . *The Journal of Immunology*, **179**[5]:2952–2960, Sep 2007. 47

[178] Philippe Robert, Milos Aleksic, Omer Dushek, Vincenzo Cerundolo, Pierre Bongrand, and P. Anton Van Der Merwe. **Kinetics and mechanics of two-dimensional interactions between T cell receptors and different activating ligands**. *Biophysical Journal*, **102**[2]:248–257, jan 2012. 47

[179] Karen Tkach and Grégoire Altan-Bonnet. **T cell responses to antigen: Hasty proposals resolved through long engagements**, Feb 2013. 47

[180] Milos Aleksic, Omer Dushek, Hao Zhang, Eugene Shenderov, Ji Li Chen, Vincenzo Cerundolo, Daniel Coombs, and P. Anton van der Merwe. **Dependence of T Cell Antigen Recognition on T Cell Receptor-Peptide MHC Confinement Time**. *Immunity*, **32**[2]:163–174, Feb 2010. 47

[181] J. R. Wedagedera and N. J. Burroughs. **T-cell activation: A queuing theory analysis at low agonist density**. *Biophysical Journal*, **91**[5]:1604–1618, Sep 2006. 47, 52

[182] Tomasz Lipniacki, Beata Hat, James R. Faeder, and William S. Hlavacek. **Stochastic effects and bistability in T cell receptor signaling**. *Journal of Theoretical Biology*, **254**[1]:110–122, Sep 2008. 47

[183] Marina Cella, Anneke Engering, Valerie Pinet, Jean Pieters, and Antonio Lanzavecchia. **Inflammatory stimuli induce accumulation of MHC class II complexes on dendritic cells**. *Nature*, **388**[6644]:782–787, 1997. 51

[184] Clifford V Harding and Emil R Unanue. **Quantitation of antigen-presenting cell MHC class II/peptide complexes necessary for T-cell stimulation**. *Nature*, **346**[6284]:574–576, 1990. 51

[185] Jingwen Li, Wei Yin, Yukai Jing, Danqing Kang, Lu Yang, Jiali Cheng, Ze Yu, Zican Peng, Xingbo Li, Yue Wen, et al. **The coordination between B cell receptor signaling and the actin cytoskeleton during B cell activation**. *Frontiers in immunology*, **9**:3096, 2019. 51

[186] Darrell J. Irvine, Marco A. Purbhoo, Michelle Krogsgaard, and Mark M. Davis. **Direct observation of ligand recognition by T cells**. *Nature*, **419**[6909]:845–849, Oct 2002. 52

[187] Nigel J. Burroughs and P. Anton Van Der Merwe. **Stochasticity and spatial heterogeneity in T-cell activation**. *Immunological Reviews*, **216**[1]:69–80, Apr 2007. 52

[188] Nicholas S Wilson, Dima El-Sukkari, and José A Villadangos. **Dendritic cells constitutively present self antigens in their immature state in vivo and regulate antigen presentation by controlling the rates of MHC class II synthesis and endocytosis**. *Blood*, **103**[6]:2187–2195, 2004. 58

[189] Scott B Drutman and E Sergio Trombetta. **Dendritic cells continue to capture and present antigens after maturation in vivo**. *The Journal of Immunology*, **185**[4]:2140–2146, 2010. 58

[190] Sachiko Sato, Ann Rancourt, Yukiko Sato, and Masahiko S Satoh. **Single-cell lineage tracking analysis reveals that an established cell line comprises putative cancer stem cells and their heterogeneous progeny**. *Scientific Reports*, **6**[1]:1–11, 2016. 58

[191] Ridha Limame, An Wouters, Bea Pauwels, Erik Fransen, Marc Peeters, Filip Lardon, Olivier De Wever, and Patrick Pauwels. **Comparative analysis of dynamic cell viability, migration and invasion assessments by novel real-time technology and classic endpoint assays**. 2012. 58

[192] Mark J Miller, Arsalan S Hejazi, Sindy H Wei, Michael D Cahalan, and Ian Parker. **T cell repertoire scanning is promoted by dynamic dendritic cell behavior and random T cell motility in the lymph node**. *Proceedings of the National Academy of Sciences*, **101**[4]:998–1003, 2004. 59

[193] E. S. Jordanova, A. Gorter, O. Ayachi, F. Prins, L. G. Durrant, G. G. Kenter, S. H. van der Burg, and G. J. Fleuren. **Human Leukocyte Antigen Class I, MHC Class I Chain-Related Molecule A, and CD8+/Regulatory T-Cell Ratio: Which Variable Determines Survival of Cervical Cancer Patients?** *Clinical Cancer Research*, **14**[7]:2028–2035, Apr 2008. 67

[194] Gavin P. Dunn, Lloyd J. Old, and Robert D. Schreiber. **The Three Es of Cancer Immunoediting**. *Annual Review of Immunology*, **22**[1]:329–360, Apr 2004. 72

[195] Ilya M Sobol. **Global sensitivity indices for nonlinear mathematical models and their Monte Carlo estimates**. *Mathematics and computers in simulation*, **55**[1-3]:271–280, 2001. 74

[196] Jiri Nossent, Pieter Elsen, and Willy Bauwens. **Sobol'sensitivity analysis of a complex environmental model**. *Environmental Modelling & Software*, **26**[12]:1515–1525, 2011. 74

[197] X-Y Zhang, Mirjam N Trame, Lawrence J Lesko, and Stephan Schmidt. **Sobol sensitivity analysis: a tool to guide the development and evaluation of systems pharmacology models**. *CPT: pharmacometrics & systems pharmacology*, **4**[2]:69–79, 2015. 74

[198] Jon Herman and Will Usher. **SALib: An open-source Python library for sensitivity analysis**. *Journal of Open Source Software*, **2**[9]:97, 2017. 76

[199] Yong Tang, Patrick Reed, Thibaut Wagener, and K Van Werkhoven. **Comparing sensitivity analysis methods to advance lumped watershed model identification and evaluation**. *Hydrology and Earth System Sciences*, **11**[2]:793–817, 2007. 77

[200] ACC Coolen and Th W Ruijgrok. **Image evolution in Hopfield networks**. *Physical Review A*, **38**[8]:4253, 1988. 82

[201] Haim Sompolinsky, Andrea Crisanti, and Hans-Jurgen Sommers. **Chaos in random neural networks**. *Physical review letters*, **61**[3]:259, 1988. 82, 207

[202] Hidetoshi Nishimori, Tota Nakamura, and Masatoshi Shiino. **Retrieval of spatio-temporal sequence in asynchronous neural network**. *Physical Review A*, **41**[6]:3346, 1990. 82

[203] ACC Coolen and D Sherrington. **Dynamics of fully connected attractor neural networks near saturation**. *Physical review letters*, **71**[23]:3886, 1993. 82

[204] Marcel Salathé, Maria Kazandjieva, Jung Woo Lee, Philip Levis, Marcus W. Feldman, and James H. Jones. **A high-resolution human contact network for infectious disease transmission**. *Proc Natl Acad Sci U S A*, **107**[51]:22020–22025, 2010. 95

[205] Luca Dall'Asta. **Inhomogeneous percolation models for spreading phenomena in random graphs**. *J Stat Mech*, **2005**[08]:P08011, 2005. 96

[206] James P. Gleeson. **Cascades on correlated and modular random networks**. *Phys Rev E Stat Nonlin Soft Matter Phys*, **77**[4]:046117, 2008. 96

[207] Brian Karrer and M. E.J. Newman. **Message passing approach for general epidemic models**. *Phys Rev E*, **82**[1], 2010. 96, 107

[208] Alexei Vázquez and Yamir Moreno. **Resilience to damage of graphs with degree correlations**. *Phys Rev E*, **67**[1]:015101, 2003. 96, 107

REFERENCES

[209] Yoshifumi Shiraki and Yoshiyuki Kabashima. **Cavity analysis on the robustness of random networks against targeted attacks: Influences of degree-degree correlations**. *Phys Rev E*, **82**[3]:036101, 2010. 96

[210] Marc Mézard, Giorgio Parisi, and Miguel Angel Virasoro. *Spin glass theory and beyond: An Introduction to the Replica Method and Its Applications*, **9**. World Scientific Publishing Company, 1987. 96, 105

[211] Romualdo Pastor-Satorras and Alessandro Vespignani. **Immunization of complex networks**. *Phys Rev E*, **65**[3]:036104, 2002. 97

[212] Kathleen E. Hamilton and Leonid P. Pryadko. **Tight Lower Bound for Percolation Threshold on an Infinite Graph**. *Phys Rev Lett*, **113**[20]:208701, Nov 2014. 97

[213] Brian Karrer, M.E.J. Newman, and Lenka Zdeborová. **Percolation on Sparse Networks**. *Phys Rev Lett*, **113**[20]:208702, 2014. 97

[214] T. Rogers. **Assessing node risk and vulnerability in epidemics on networks**. *Europhys Lett*, **109**[2], 2015. 97, 98, 101, 128, 131

[215] Michele Starnini, Anna Machens, Ciro Cattuto, Alain Barrat, and Romualdo Pastor-Satorras. **Immunization strategies for epidemic processes in time-varying contact networks**. *Journal of theoretical biology*, **337**:89–100, 2013. 97

[216] Urszula Ledzewicz and Heinz Schättler. **On optimal singular controls for a general SIR-model with vaccination and treatment**. In *Conference Publications*, **2011**, page 981. American Institute of Mathematical Sciences, 2011. 97

[217] Rinaldo M Colombo and Mauro Garavello. **Optimizing vaccination strategies in an age structured SIR model**. *Math Biosci Eng*, **17**[2]:1074–1089, 2020. 97

[218] Joël Mossong, Niel Hens, Mark Jit, Philippe Beutels, Kari Auranen, Rafael Mikolajczyk, Marco Massari, Stefania Salmaso, Gianpaolo Scalia Tomba, Jacco Wallinga, et al. **Social contacts and mixing patterns relevant to the spread of infectious diseases**. *PLoS Med*, **5**[3]:e74, 2008. 98

[219] Dina Mistry et al. **Inferring high-resolution human mixing patterns for disease modeling**. *Nat Commun*, **12**[1], 2021. 98

[220] Linhua Zhou, Yan Wang, Yanyu Xiao, and Michael Y Li. **Global dynamics of a discrete age-structured SIR epidemic model with applications to measles vaccination strategies**. *Math Biosci*, **308**:27–37, 2019. 98

[221] Roy M. Anderson and Robert M. May. **Spatial, Temporal, and Genetic Heterogeneity in Host Populations And the Design of Immunization Programmes**. *Math Med Biol*, **1**[3]:233–266, 1984. 98

[222] Wei Gou and Zhen Jin. **How heterogeneous susceptibility and recovery rates affect the spread of epidemics on networks**. *Infect Dis Model*, **2**[3]:353–367, 2017. 98

[223] Reimer Kühn and Tim Rogers. **Heterogeneous micro-structure of percolation in sparse networks**. *Europhys Lett*, **118**[6]:68003, 2017. 98, 99, 131, 134, 138

[224] Sergey Melnik, Adam Hackett, Mason A. Porter, Peter J. Mucha, and James P. Gleeson. **The unreasonable effectiveness of tree-based theory for networks with clustering**. *Phys Rev E Stat Nonlin Soft Matter Phys*, **83**[3]:036112, 2011. 105, 262

[225] Mark Newman. *Networks*. Oxford university press, 2018. 109

[226] Daniel T Gillespie. **Exact stochastic simulation of coupled chemical reactions**. *J Phys Chem*, **81**[25]:2340–2361, 1977. 110, 156

[227] István Z Kiss, Joel C Miller, Péter L Simon, et al. **Mathematics of epidemics on networks**. *Cham: Springer*, **598**, 2017. 110, 156

[228] Joel C. Miller and Tony Ting. **EoN (Epidemics on Networks): a fast, flexible Python package for simulation, analytic approximation, and analysis of epidemics on networks**. *J Open Source Softw*, **4**[44]:1731, 2019. 110, 156

[229] A. Annibale, A. C.C. Coolen, L. P. Fernandes, F. Fraternali, and J. Kleinjung. **Tailored graph ensembles as proxies or null models for real networks I: Tools for quantifying structure**. *J Phys A Math Theor*, **42**[48], 2009. 110

[230] Istvan Z. Kiss, Gergely Röst, and Zsolt Vizi. **Generalization of Pairwise Models to non-Markovian Epidemics on Networks**. *Phys Rev Lett*, **115**[7]:078701, 2015. 112

[231] Guido Caldarelli, Andrea Capocci, Paolo De Los Rios, and Miguel A Munoz. **Scale-free networks from varying vertex intrinsic fitness**. *Phys Rev Lett*, **89**[25]:258702, 2002. 122

[232] Marc Mézard and Giorgio Parisi. **The Bethe lattice spin glass revisited**. *Eur Phys J B*, **20**[2]:217–233, 2001. 132

[233] Marc Mezard and Andrea Montanari. *Information, physics, and computation*. Oxford University Press, 2009. 133

[234] Ido Tishby, Ofer Biham, Eytan Katzav, and Reimer Kühn. **Revealing the microstructure of the giant component in random graph ensembles**. *Physical Review E*, **97**[4]:042318, 2018. 137

[235] Tomokatsu Onaga, James P Gleeson, and Naoki Masuda. **Concurrency-induced transitions in epidemic dynamics on temporal networks**. *Phys Rev Lett*, **119**[10]:108301, 2017. 148

[236] Tiago P. Peixoto and Laetitia Gauvin. **Change points, memory and epidemic spreading in temporal networks**. *Sci Rep*, **8**[1]:1–10, 2018. 148

[237] Jinghang Liang and Jie Han. **Stochastic Boolean networks: an efficient approach to modeling gene regulatory networks**. *BMC systems biology*, **6**[1]:1–21, 2012. 170

[238] Jon PL Hatchett and Reimer Kühn. **Credit contagion and credit risk**. *Quantitative Finance*, **9**[4]:373–382, 2009. 170

[239] Jia-Wen Gu, Wai-Ki Ching, Tak-Kuen Siu, and Harry Zheng. **On modeling credit defaults: A probabilistic Boolean network approach**. *Risk and Decision Analysis*, **4**[2]:119–129, 2013. 170

[240] Ruochen Liang, Yushan Qiu, and Wai Ki Ching. **Construction of probabilistic Boolean network for credit default data**. In *2014 Seventh International Joint Conference on Computational Sciences and Optimization*, pages 11–15. IEEE, 2014. 170

[241] Peican Zhu, Xiaogang Song, Leibo Liu, Zhen Wang, and Jie Han. **Stochastic analysis of multiplex Boolean networks for understanding epidemic propagation**. *IEEE access*, **6**:35292–35304, 2018. 170

[242] David G Green, Tania G Leishman, and Suzanne Sadedin. **The emergence of social consensus in Boolean networks**. In *2007 IEEE Symposium on Artificial Life*, pages 402–408. IEEE, 2007. 170

[243] Bo Li, Junfeng Wu, Hongsheng Qi, Alexandre Proutiere, and Guodong Shi. **Boolean gossip networks**. *IEEE/ACM Transactions on Networking*, **26**[1]:118–130, 2017. 170

[244] Ryan Hannam, Reimer Kuehn, and Alessia Annibale. **Percolation in bipartite Boolean networks and its role in sustaining life**. *Journal of Physics A: Mathematical and Theoretical*, **52**[33]:334002, 2019. 170, 171, 172, 173, 174, 175, 176, 178, 179, 199

[245] Giuseppe Torrisi, Reimer Kühn, and Alessia Annibale. **Percolation on the gene regulatory network**. *Journal of Statistical Mechanics: Theory and Experiment*, **2020**[8]:083501, 2020. 170, 171, 172, 174, 175, 176, 178, 179

[246] Viola Folli, Giorgio Gosti, Marco Leonetti, and Giancarlo Ruocco. **Effect of dilution in asymmetric recurrent neural networks**. *Neural Networks*, **104**:50–59, 2018. 171, 207

[247] Dmitry Panchenko. **The Parisi formula for mixed p-spin models**. *The Annals of Probability*, **42**[3]:946–958, 2014. 172

[248] Pan Zhang. **Inference of kinetic Ising model on sparse graphs**. *Journal of Statistical Physics*, **148**[3]:502–512, 2012. 173, 179, 180, 184, 185, 186, 194, 211, 226

[249] Giuseppe Torrisi, Alessia Annibale, and Reimer Kühn. **Overcoming the complexity barrier of the dynamic message-passing method in networks with fat-tailed degree distributions**. *Physical Review E*, **104**[4]:045313, 2021. 178, 274

[250] Alexander Mozeika and David Saad. **Phase transitions and memory effects in the dynamics of Boolean networks**. *Philosophical Magazine*, **92**[1-3]:210–229, 2012. 178

[251] P Peretto. **Collective properties of neural networks: a statistical physics approach**. *Biological cybernetics*, **50**[1]:51–62, 1984. 188

[252] NS Skantzos and ACC Coolen. **Random field Ising chains with synchronous dynamics**. *Journal of Physics A: Mathematical and General*, **33**[9]:1841, 2000. 188

[253] NS Skantzos and ACC Coolen. **Random field Ising chain and neutral networks with synchronous dynamics**. In *AIP Conference Proceedings*, **553**, pages 101–106. American Institute of Physics, 2001. 188

[254] JF Fontanari and R Köberle. **Information processing in synchronous neural networks**. *Journal de Physique*, **49**[1]:13–23, 1988. 188, 189, 227

[255] I Pérez Castillo and NS Skantzos. **The Little–Hopfield model on a sparse random graph**. *Journal of Physics A: Mathematical and General*, **37**[39]:9087, 2004. 188, 189, 227

[256] Marc Mézard and Giorgio Parisi. **The Bethe lattice spin glass revisited**. *The European Physical Journal B-Condensed Matter and Complex Systems*, **20**[2]:217–233, 2001. 192, 212, 250

[257] Giorgio Parisi, Federico Ricci-Tersenghi, and Tommaso Rizzo. **Diluted mean-field spin-glass models at criticality**. *Journal of Statistical Mechanics: Theory and Experiment*, **2014**[4]:P04013, 2014. 192

[258] Ada Altieri, Maria Chiara Angelini, Carlo Lucibello, Giorgio Parisi, Federico Ricci-Tersenghi, and Tommaso Rizzo. **Loop expansion around the Bethe approximation through the M-layer construction**. *Journal of Statistical Mechanics: Theory and Experiment*, **2017**[11]:113303, 2017. 192

[259] DJ Thouless. **Spin-glass on a Bethe lattice**. *Physical review letters*, **56**[10]:1082, 1986. 192, 215

[260] JM Carlson, JT Chayes, L Chayes, JP Sethna, and DJ Thouless. **Bethe lattice spin glass: the effects of a ferromagnetic bias and external fields. I. Bifurcation analysis**. *Journal of statistical physics*, **61**[5]:987–1067, 1990. 192

[261] JM Carlson, JT Chayes, James P Sethna, and DJ Thouless. **Bethe lattice spin glass: the effects of a ferromagnetic bias and external fields. II. Magnetized spin-glass phase and the de Almeida-Thouless line**. *Journal of statistical physics*, **61**[5]:1069–1084, 1990. 192

[262] H Rieger, M Schreckenberg, and J Zittartz. **Glauber dynamics of the asymmetric SK-model**. *Zeitschrift für Physik B Condensed Matter*, **74**[4]:527–538, 1989. 207

[263] Yu-Qiang Ma, Yue-Ming Zhang, and Chang-De Gong. **Suppression of Retrieval States in Spin-Glass-Like Model of Neural Networks with Random Neuronal Threshold1**. *Communications in Theoretical Physics*, **18**[4]:491, 1992. 207

[264] Silvio Franz, Michele Leone, Federico Ricci-Tersenghi, and Riccardo Zecchina. **Exact solutions for diluted spin glasses and optimization problems**. *Physical Review Letters*, **87**[12]:127209, 2001. 208

[265] Federico Ricci-Tersenghi, Martin Weigt, and Riccardo Zecchina. **Simplest random K-satisfiability problem**. *Physical Review E*, **63**[2]:026702, 2001. 208

[266] M Mézard, F Ricci-Tersenghi, and R Zecchina. **Alternative solutions to diluted p-spin models and XORSAT problems**. *Jour. of Statistical Physics*, **111**:105, 2002. 208

[267] Tommaso Castellani and Andrea Cavagna. **Spin-glass theory for pedestrians**. *Journal of Statistical Mechanics: Theory and Experiment*, **2005**[05]:P05012, 2005. 208

[268] Christian John Hurry, Alexander Mozeika, and Alessia Annibale. **Vaccination with partial transmission and social distancing on contact networks**. *Journal of Statistical Mechanics: Theory and Experiment*, **2022**[3]:033302, 2022. 212, 214

[269] Jairo RL de Almeida and David J Thouless. **Stability of the Sherrington-Kirkpatrick solution of a spin glass model**. *Journal of Physics A: Mathematical and General*, **11**[5]:983, 1978. 215

[270] Marc Mézard and Riccardo Zecchina. **Random k-satisfiability problem: From an analytic solution to an efficient algorithm**. *Physical Review E*, **66**[5]:056126, 2002. 250

[271] Stephan Mertens, Marc Mézard, and Riccardo Zecchina. **Threshold values of random K-SAT from the cavity method**. *Random Structures & Algorithms*, **28**[3]:340–373, 2006. 250

[272] Diane R Mould and RN Upton. **Basic concepts in population modeling, simulation, and model-based drug development**. *CPT: pharmacometrics & systems pharmacology*, **1**[9]:1–14, 2012. 251

[273] Diane R Mould and Richard Neil Upton. **Basic concepts in population modeling, simulation, and model-based drug development—part 2: introduction to pharmacokinetic modeling methods**. *CPT: pharmacometrics & systems pharmacology*, **2**[4]:1–14, 2013. 251

[274] RN Upton and DR Mould. **Basic concepts in population modeling, simulation, and model-based drug development: part 3—introduction to pharmacodynamic modeling methods**. *CPT: pharmacometrics & systems pharmacology*, **3**[1]:1–16, 2014. 251

[275] Sophie J Rhodes, Gwenan M Knight, Denise E Kirschner, Richard G White, and Thomas G Evans. **Dose finding for new vaccines: The role for immunostimulation/immunodynamic modelling**. *Journal of theoretical biology*, **465**:51–55, 2019. 251